ADVANCED PHOTONICS METASURFACES: DESIGN, FABRICATION, AND APPLICATIONS

EDITED BY: Xufeng Jing, Haiyong Gan, Zhi Hong and Chee Leong Tan
PUBLISHED IN: Frontiers in Physics

frontiers Research Topics

ISSN 1664-8714
ISBN 978-2-88971-050-8
DOI 10.3389/978-2-88971-050-8

About Frontiers

Frontiers is more than just an open-access publisher of scholarly articles: it is a pioneering approach to the world of academia, radically improving the way scholarly research is managed. The grand vision of Frontiers is a world where all people have an equal opportunity to seek, share and generate knowledge. Frontiers provides immediate and permanent online open access to all its publications, but this alone is not enough to realize our grand goals.

Frontiers Journal Series

The Frontiers Journal Series is a multi-tier and interdisciplinary set of open-access, online journals, promising a paradigm shift from the current review, selection and dissemination processes in academic publishing. All Frontiers journals are driven by researchers for researchers; therefore, they constitute a service to the scholarly community. At the same time, the Frontiers Journal Series operates on a revolutionary invention, the tiered publishing system, initially addressing specific communities of scholars, and gradually climbing up to broader public understanding, thus serving the interests of the lay society, too.

Dedication to Quality

Each Frontiers article is a landmark of the highest quality, thanks to genuinely collaborative interactions between authors and review editors, who include some of the world's best academicians. Research must be certified by peers before entering a stream of knowledge that may eventually reach the public - and shape society; therefore, Frontiers only applies the most rigorous and unbiased reviews.
Frontiers revolutionizes research publishing by freely delivering the most outstanding research, evaluated with no bias from both the academic and social point of view. By applying the most advanced information technologies, Frontiers is catapulting scholarly publishing into a new generation.

What are Frontiers Research Topics?

Frontiers Research Topics are very popular trademarks of the Frontiers Journals Series: they are collections of at least ten articles, all centered on a particular subject. With their unique mix of varied contributions from Original Research to Review Articles, Frontiers Research Topics unify the most influential researchers, the latest key findings and historical advances in a hot research area! Find out more on how to host your own Frontiers Research Topic or contribute to one as an author by contacting the Frontiers Editorial Office: frontiersin.org/about/contact

ADVANCED PHOTONICS METASURFACES: DESIGN, FABRICATION, AND APPLICATIONS

Topic Editors:
Xufeng Jing, China Jiliang University, China
Haiyong Gan, National Institute of Metrology, China
Zhi Hong, China Jiliang University, China
Chee Leong Tan, University of Malaya, Malaysia

Citation: Jing, X., Gan, H., Hong, Z., Tan, C. L., eds. (2021). Advanced Photonics Metasurfaces: Design, Fabrication, and Applications. Lausanne: Frontiers Media SA. doi: 10.3389/978-2-88971-050-8

Table of Contents

frontiers in Physics

EDITORIAL
published: 21 May 2021
doi: 10.3389/fphy.2021.694972

Editorial: Advanced Photonics Metasurfaces: Design, Fabrication, and Applications

Yan Shi[1], *Xufeng Jing*[1,2]*, *Chenxia Li*[1] *and Zhi Hong*[1,2]*

[1] *Institute of Optoelectronic Technology, China Jiliang University, Hangzhou, China,* [2] *Centre for Terahertz Research, China Jiliang University, Hangzhou, China*

Keywords: metasurface, optics, metamaterial, meta-optics, metadevices

Editorial on the Research Topic:

Advanced Photonics Metasurfaces: Design, Fabrication, and Applications

Metasurface refers to an artificial layered material with a thickness than the wavelength, which can be considered as a two-dimensional metamaterial [1–10]. Due to the novel properties that natural materials do not have, metasurfaces have shown great application potential in many fields such as optical integration, optical communication, micro-nano optics, stealth, super-resolution imaging and sensing, etc., [11–20] and are a hot research field [21–30]. The metasurface was first proposed in the field of optics, it has been rapidly expanded to many fields, such as acoustic wave, elastic wave, thermal field, etc. [31–33]. Metasurface can realize flexible and effective regulation of electromagnetic wave characteristics such as polarization, amplitude, phase, polarization mode, and propagation mode [34–40]. According to the types of regulated electromagnetic waves, metasurfaces can be divided into optical, acoustic, and mechanical metasurfaces. Optical metasurface is the most common type, which can regulate the characteristics of polarization, phase, amplitude, and frequency of electromagnetic wave through the subwavelength microstructure. It is an emerging technology that combines optics and nanotechnology.

In terms of polarization regulation, the metasurface can realize polarization conversion, optical rotation, vector beam generation, and other functions [41–43]. In terms of the amplitude regulation of the metasurface, the metasurface can realize asymmetric transmission of light, anti-reflection, increased transmission, magnetic mirror, EIT-like effect, etc. In terms of frequency regulation of the metasurface, researchers can realize free regulation of the color of the metasurface by changing geometric parameters such as the size and shape of its structural units, which can be used in high pixel imaging, visual biosensors, and other fields [44–46]. Phase is a core property of electromagnetic wave. The phase plane determines the propagation direction of the electromagnetic wave, and the phase of an image contains its three-dimensional information. By controlling the phase of electromagnetic waves, functions such as beam deflection, meta-lens, hyperholography, vortex generation, coding, cloaking, and phantom can be realized [47–50]. In addition, metasurface can control the phase, amplitude, and polarization of electromagnetic waves simultaneously. For example, by adjusting the phase and amplitude of electromagnetic waves, stereo super holography can be realized. By adjusting the phase and polarization of electromagnetic waves, vector vorticity can be realized. By adjusting the phase and frequency of electromagnetic waves, some functions such as non-linear superlens can be realized.

Through this Research Topic, our purpose is to show the progress of metasurface in the design, fabrication, and applications of metasurfaces. With the continuous development of semiconductor

Edited and reviewed by:
Lorenzo Pavesi,
University of Trento, Italy

***Correspondence:**
Xufeng Jing
jingxufeng@cjlu.edu.cn
Zhi Hong
hongzhi@cjlu.edu.cn

Specialty section:
This article was submitted to Optics and Photonics, a section of the journal Frontiers in Physics

Received: *14 April 2021*
Accepted: *26 April 2021*
Published: *21 May 2021*

Citation:
Shi Y, Jing X, Li C and Hong Z (2021) Editorial: Advanced Photonics Metasurfaces: Design, Fabrication, and Applications. Front. Phys. 9:694972. doi: 10.3389/fphy.2021.694972

technology, metasurface technology has found some important applications which are expected to transform the research into practical products. In turn, metasurfaces will also become a new opportunity for the semiconductor industry, thus changing the design flexibility of some important devices. It is our hope that the contributed papers to this Research Topic will contribute to international cooperation in the field of metasurfaces and accelerate progress in their design, preparation, and application.

One of the sub-topical areas of this topic covers a review on metasurfaces from principle to smart metadevices. The paper by Hu et al. follows current trends on advanced photonics metasurface, and they demonstrate the concepts of anomalous reflection and refraction, applications of metasurfaces with the Pancharatanm-Berry Phase, and Huygens metasurface. The progress of soft metasurface has also been discussed in this review. Zhang et al. show that a systematic scheme for fabricating spiral-structure metasurface is proposed by employing the metal mold making with diamond-based ultra-precision turning technique and then molding replication method. Finally, Xu et al. numerically and experimentally demonstrated double Fano resonances in a simple S-shaped plasmonic metasurface in the terahertz frequency range.

AUTHOR CONTRIBUTIONS

All authors listed have made a substantial, direct and intellectual contribution to the work, and approved it for publication.

FUNDING

This work was supported by Natural Science Foundation of Zhejiang Province (Nos. LZ21A040003 and LY20F050007) and National Natural Science Foundation of China (NSFC) (Nos. 61904169, 61904168, and 61875179).

REFERENCES

1. Arbabi A, Horie Y, Bagheri M, Faraon A. Dielectric metasurfaces for complete control of phase and polarization with subwavelength spatial resolution and high transmission. *Nat Nanotechnol.* (2015) 10:937–43. doi: 10.1038/nnano.2015.186
2. Zhang J, Zhang H, Yang W, Chen K, Wei X, Feng Y, et al. Dynamic scattering steering with graphene-based coding meta-mirror. *Adv Optical Mater.* (2020) 8:2000683. doi: 10.1002/adom.202000683
3. Bai X, Kong F, Sun Y, Wang F, Qian J, Li X, et al. High-efficiency transmissive programable metasurface for multi-mode OAM generations. *Adv Optical Mater.* (2020) 8:2000570. doi: 10.1002/adom.202000570
4. Huang LG, Takabe H, Cowan TE. Maximizing magnetic field generation in high power laser–solid interactions. *High Power Laser Sci Eng.* (2019) 7:02000e22. doi: 10.1017/hpl.2019.9
5. Teng S, Zhang Q, Wang H, Liu L, Lv H. Conversion between polarization states based on metasurface. *Photonics Res.* (2019) 7:246–50. doi: 10.1364/PRJ.7.000246
6. Luo X, Tan Z, Wang C, Cao J. A reflecting-type highly efficient terahertz cross-polarization converter based on metamaterials. *Chin Opt Lett*. (2019) 17:0931101. doi: 10.3788/COL201917.093101
7. Liang W, Li Z, Wang Y, Chen W, Li Z. All-angle optical switch based on the zero reflection effect of graphene–dielectric hyperbolic metamaterials. *Photon Res*. (2019) 7:318–24. doi: 10.1364/PRJ.7.000318
8. Cui Y, Zheng G, Chen M, Zhang Y, Yang Y, Tao J, et al. Reconfigurable continuous-zoom meta-lens in visible band. *Chin Opt Lett*. (2019) 17:111603. doi: 10.3788/COL201917.111603
9. Jing X, Gui X, Zhou P, Hong Z. Physical explanation of Fabry-Pérot cavity for broadband bilayer metamaterials polarization converter. *J Lightw Technol.* (2018) 36:2322–7. doi: 10.1109/JLT.2018.2808339
10. Xia R, Jing X, Gui X, Tian Y. Broadband terahertz half-wave plate based on anisotropic polarization conversion metamaterials. *Optics Materials Express*. (2017) 7:977–88. doi: 10.1364/OME.7.000977
11. Akram MR, Ding G, Chen K, Feng Y, Zhu W. Ultra-thin single layer metasurfaces with ultra-wideband operation for both transmission and reflection. *Adv Mater.* (2020) 32:1907308. doi: 10.1002/adma.201907308
12. Zhang J, Wei X, Rukhlenko ID, Chen H-T, Zhu W. Electrically tunable metasurface with independent frequency and amplitude modulations. *ACS Photonics.* (2020) 7:265–71. doi: 10.1021/acsphotonics.9b01532
13. Akram MR, Mehmood MQ, Bai X, Jin R, Premaratne M, Zhu W. High efficiency ultra-thin transmissive metasurfaces. *Adv Optical Mater.* (2019) 7:1801628. doi: 10.1002/adom.201801628
14. Akram MR, Bai X, Jin R, Vandenbosch GAE, Premaratne M, Zhu W. Photon spin Hall effect based ultra-thin transmissive metasurface for efficient generation of OAM waves. *IEEE Trans Antennas Propag.* (2019) 67:4650–8. doi: 10.1109/TAP.2019.2905777
15. Zhao J, Jing X, Wang W, Tian Y, Zhu D, Shi G. Steady method to retrieve effective electromagnetic parameters of bianisotropic metamaterials at one incident direction in the terahertz region. *Optics Laser Technol.* (2017) 95:56–62. doi: 10.1016/j.optlastec.2017.04.001
16. Tian Y, Jing X, Gan H, Li X, Hong Z. Free control of far-field scattering angle of transmission terahertz wave using multilayer split-ring resonators' metasurfaces. *Front Phys.* (2020) 15:62502. doi: 10.1007/s11467-020-1013-1
17. Fu Y, Fei Y, Dong D, Liu Y. Photonic spin Hall effect in PT symmetric metamaterials. *Front Phys.* (2019) 14:62601. doi: 10.1007/s11467-019-0938-8
18. Fu Y, Tao J, Song A, Liu Y, Xu Y. Controllably asymmetric beam splitting via gap-induced diffraction channel transition in dual-layer binary metagratings. *Front Phys.* (2020) 15:52502. doi: 10.1007/s11467-020-0968-2
19. Li J, Jin R, Geng J, Liang X, Wang K, Premaratne M, et al. Design of a broadband metasurface Luneburg lens for full-angle operation. *IEEE Trans Antennas Propag.* (2019) 67:2442–51. doi: 10.1109/TAP.2018.2889006
20. Lu X, Zeng X, Lv H, Han Y, Mou Z, Liu C, et al. Polarization controllable plasmonic focusing based on nanometer holes. *Nanotechnology.* (2020) 31:135201. doi: 10.1088/1361-6528/ab62d0
21. Lv H, Lu X, Han Y, Mou Z, Zhou C, Wang S, et al. Metasurface cylindrical vector light generators based on nanometer holes. *New J Phys.* (2019) 21:123047. doi: 10.1088/1367-2630/ab5f44
22. Lv H, Lu X, Han Y, Mou Z, Teng S. Multifocal metalens with a controllable intensity ratio. *Optics Lett.* (2019) 44:2518–21. doi: 10.1364/OL.44.002518
23. Wang H, Liu L, Zhou C, Xu J, Zhang M, Teng S, et al. Vortex beam generation with variable topological charge based on a spiral slit. *Nanophotonics.* (2019) 8:317–24. doi: 10.1515/nanoph-2018-0214
24. Jing X, Jin S, Tian Y, Liang P, Dong Q, Wang L. Analysis of the sinusoidal nanopatterning grating structure. *Optics Laser Technol.* (2013) 48:160–6. doi: 10.1016/j.optlastec.2012.10.008
25. Jing X, Xu Y, Gan H, He Y, Hong Z. High refractive index metamaterials by using higher order modes resonances of hollow cylindrical nanostructure in visible region. *IEEE Access*. (2019) 7:144945–56. doi: 10.1109/ACCESS.2019.2945119
26. Jiang L, Fang B, Yan Z, Fan J, Qi C, Liu J, et al. Terahertz high and near-zero refractive index metamaterials by double layer metal ring microstructure. *Optics Laser Technol*. (2020) 123:105949. doi: 10.1016/j.optlastec.2019.105949
27. He X. Tunable terahertz graphene metamaterials. *Carbon.* (2015) 82:229–37. doi: 10.1016/j.carbon.2014.10.066

28. He X, Zhong X, Lin F, Shi W. Investigation of graphene assisted tunable terahertz metamaterials absorber. *Opt. Mater. Express.* (2016) 6:331–42. doi: 10.1364/OME.6.000331
29. Koirala L, Park C, Lee S, Choi D. Angle tolerant transmissive color filters exploiting metasurface incorporating hydrogenated amorphous silicon nanopillars. *Chin Opt Lett.* (2019) 17:082301. doi: 10.3788/COL201917.082301
30. Hou T, An Y, Chang Q, Ma P, Li J, Zhi D, et al. Deep-learning-based phase control method for tiled aperture coherent beam combining systems. *High Power Laser Sci Eng.* (2019) 7:04000e59. doi: 10.1017/hpl.2019.46
31. Estakhri NM, Alù A. Recent progress in gradient metasurfaces. *J Opt Soc Am B.* (2015) 33:A21. doi: 10.1364/JOSAB.33.000A21
32. Fan Y, Shen N-H, Zhang F, Zhao Q, Wei Z, Zhang P, et al. Photoexcited graphene metasurfaces: significantly enhanced and tunable magnetic resonances. *ACS Photonics.* (2018) 5:1612–8. doi: 10.1021/acsphotonics.8b00057
33. Gutruf P, Zou C, Withayachumnankul W, Bhaskaran M, Sriram S, Fumeaux C. Mechanically tunable dielectric resonator metasurfaces at visible frequencies. *ACS Nano.* (2016) 10:133–41. doi: 10.1021/acsnano.5b05954
34. High AA, Devlin RC, Dibos A, Polking M, Wild DS, Perczel J, et al. Visiblefrequency hyperbolic metasurface. *Nature.* (2015) 522:192–6. doi: 10.1038/nature14477
35. Hsiao H-H, Chu CH, Tsai DP. Fundamentals applications ofmetasurfaces. *Small Methods.* (2017) 1:1600064. doi: 10.1002/smtd.201600064
36. Ma Q, Bai GD, Jing HB, Yang C, Li L, Cui TJ. Smart metasurface with selfadaptively reprogrammable functions. *Light Sci Appl.* (2019) 8:98. doi: 10.1038/s41377-019-0205-3
37. Meinzer N, Barnes WL, Hooper IR. Plasmonic meta-atoms and metasurfaces. *Nat Photon.* (2014) 8:889–98. doi: 10.1038/nphoton.2014.247
38. Wu Z, Zhou M, Khoram E, Liu B, Yu Z. Neuromorphic metasurface. *Photonics Res.* (2020) 8:46–50. doi: 10.1364/PRJ.8.000046
39. Qian C, Zheng B, Shen Y, Jing L, Li E, Shen L, et al. Deep-learning-enabled self-adaptive microwave cloak without human intervention. *Nat Photon.* (2020) 14:383–90. doi: 10.1038/s41566-020-0604-2
40. Shrestha S, Overvig AC, Lu M, Stein A, Yu N. Broadband achromatic dielectric metalenses. *Light Sci Appl.* (2018) 7:85. doi: 10.1038/s41377-018-0078-x
41. Su VC, Chu CH, Sun G, Tsai DP. Advances in optical metasurfaces: fabrication and applications. *Opt Express.* (2018) 26: 13148–82. doi: 10.1364/OE.26.013148
42. Sun S, Yang KY, Wang CM, Juan TK, Chen WT, Liao CY, et al. High efficiency broadband anomalous reflection by gradient meta-surfaces. *Nano Lett.* (2012) 12:6223–9. doi: 10.1021/nl3032668
43. Walia S, Shah CM, Gutruf P, Nili H, Chowdhury DR, Withayachumnankul W, et al. Flexible metasurfaces and metamaterials: a review of materials and fabrication processes at micro- and nano-scales. *Appl Phys Rev.* (2015) 2:011303. doi: 10.1063/1.4913751
44. Wang Y, Liu F, Zhang X. Flexible transfer of plasmonic photonic structures onto fiber tips for sensor applications in liquids. *Nanoscale.* (2018) 10:16193–200. doi: 10.1039/C8NR05871G
45. Zhu Y, Li Z, Hao Z, DiMarco C, Maturavongsadit P, Hao Y, et al. Optical conductivity-based ultrasensitive mid-infrared biosensing on a hybrid metasurface. *Light Sci Appl.* (2018) 7:67. doi: 10.1038/s41377-018-0066-1
46. Ye W, Zeuner F, Li X, Reineke B, He S, Qiu CW, et al. Spin and wavelength multiplexed nonlinear metasurface holography. *Nat Commun.* (2016) 7:11930. doi: 10.1038/ncomms11930
47. Yang Y, Kravchenko II, Briggs DP, Valentine J. All-dielectric metasurface analogue of electromagnetically induced transparency. *Nat Commun.* (2014) 5:5753. doi: 10.1038/ncomms6753
48. Yu YF, Zhu AY, Paniagua-Domínguez R, Fu YH, Luk'yanchuk B, Kuznetsov AI. High-transmission dielectric metasurface with 2π phase control at visible wavelengths. *Laser Photon Rev.* (2015) 9:412–8. doi: 10.1002/lpor.201500041
49. Yue F, Wen D, Xin J, Gerardot BD, Li J, Chen X. Vector vortex beam generation with a single plasmonic metasurface. *ACS Photonics.* (2016) 3:1558–63. doi: 10.1021/acsphotonics.6b00392
50. Zuo R, Liu W, Cheng H, Chen S, Tian J. Breaking the diffraction limit with radially polarized light based on dielectric metalenses. *Adv Opt Mater.* (2018) 6:1800795. doi: 10.1002/adom.201800795

Conflict of Interest: The authors declare that the research was conducted in the absence of any commercial or financial relationships that could be construed as a potential conflict of interest.

frontiers in Physics

ORIGINAL RESEARCH
published: 30 June 2020
doi: 10.3389/fphy.2020.00231

Wideband Absorbing Plasmonic Structures via Profile Optimization Based on Genetic Algorithm

Ruichao Zhu, Jiafu Wang, Sai Sui*, Yueyu Meng, Tianshuo Qiu, Yuxiang Jia, Xiaofeng Wang, Yajuan Han, Mingde Feng, Lin Zheng and Shaobo Qu*

Department of Basic Sciences, Air Force Engineering University, Xi'an, China

Plasmonic structures that support the spoof surface plasmon polariton (SSPP) mode can be tailored to achieve strong absorption of electromagnetic (EM) waves. In particular, the profile of an absorbing plasmonic structure (APS) plays an important role in realizing its wideband absorption performance. In this paper, we propose a method of optimizing the longitudinal profile of APS based on Genetic Algorithm (GA), with the aim of obtaining high-efficiency wideband absorption of EM waves. The APS unit cell is composed of a longitudinal array of metallic strips, the length profile of which can be optimized to improve *k*-matching between free-space waves and SSPPs and meanwhile to customize absorption at each frequency within a wide band. Our investigation shows that non-linear variation of the strip lengths will make better *k*-matching and wideband absorption. As an example, a wideband APS is demonstrated using this method. The simulated and measured results show that the absorbance is higher than 90% in 10–30 GHz, which convincingly verifies the effectiveness of this method. This method provides an efficient approach to the design of radar absorbing structures and can also be extended to optimized design of other metamaterials.

Keywords: metamaterial, absorbing plasmonic structure, spoof surface plasmon polariton, wideband absorption, genetic algorithm

OPEN ACCESS

Edited by:
Zhi Hong,
China Jiliang University, China

Reviewed by:
Weiqiang Ding,
Harbin Institute of Technology, China
Ilia L. Rasskazov,
University of Rochester, United States

****Correspondence:***
Jiafu Wang
wangjiafu1981@126.com
Sai Sui
suisai_mail@foxmail.com

Specialty section:
This article was submitted to Optics and Photonics, a section of the journal Frontiers in Physics

Received: *05 May 2020*
Accepted: *28 May 2020*
Published: *30 June 2020*

Citation:
Zhu R, Wang J, Sui S, Meng Y, Qiu T, Jia Y, Wang X, Han Y, Feng M, Zheng L and Qu S (2020) Wideband Absorbing Plasmonic Structures via Profile Optimization Based on Genetic Algorithm. Front. Phys. 8:231. doi: 10.3389/fphy.2020.00231

INTRODUCTION

The electromagnetic wave transmission can be effectively suppressed by electromagnetic absorbers, which is why they can be widely applied in radar stealth techniques [1–3], electromagnetic protection [4, 5], and wireless transmission [6]. Metamaterials composed of artificially engineered subwavelength inclusions exhibit novel properties that cannot be found in nature or difficult to achieve [7, 8]. A significant breakthrough has been made for wave absorption thanks to the rapid development of electromagnetic metamaterials [9, 10]. Originated from optics, Surface Plasmon Polariton (SPP) is a transmission mode that is generated by the tight coupling between the electromagnetic (EM) wave and surface electron [11, 12]. On this basis, Pendry first proposed Spoof Surface Plasmon Polariton (SSPP) in earlier researches [13]. Exhibiting similar properties to Surface Plasmon Polariton (SPP) in optics, SSPP is an electromagnetic mode excited by artificial electromagnetic medium or structure in the microwave band [14, 15]. Subsequently, the SSPP of Transverse Magnetic(TM) and Transverse Electric(TE) were obtained by metamaterial [16, 17]. With the development of researches, the properties in the local field enhancement, strong dispersion and deep subwavelength characteristics of SSPP are widely

applied in microwave absorbing, stealth and dispersion engineering [18–20]. Additionally, SSPP as absorbing metamaterial has also been applied in terahertz and infrared stealth [21, 22]. Therefore, SSPP has been extensively used as absorbing metamaterials by a lot of researchers.

It is worth noting that a longitudinal array of metallic strips overlapping with periodic arrangement can be combined with adjacent absorption peaks into a continuous adsorption peak [23, 24]. As metal strips increase, absorption bandwidth increases and metamaterials get thicker. Hence, a number of methods for reducing thickness of metamaterials were proposed such as introducing meandered strip structure, increasing high duty ratio of metal strips and loading other absorbing materials [25–28]. The SSPP performance can be affected by adjusting and controlling the length of horizontal metallic strip affects the impedance matching of electromagnetic wave, so its adjustment and control will also affect the SSPP performance, which, therefore can be improved by optimizing the longitudinal profile of strips. The conventional optimization algorithm includes heuristic algorithms such as Genetic Algorithm (GA) and Particle Swarm Optimization (PSO) [29–31], all of which has been widely applied in designing metamaterial and especially metasurface. The topology optimization in metasurface is currently restricted to the horizontal two-dimensional (2D) surface [32, 33]. However, optimization algorithm can also be expanded in vertical space. Therefore, we discuss the longitudinal profile of the Absorbing Plasmonic Structure (APS) and propose an optimization scheme adapted to the longitudinal profile's structure.

In this paper, we proposed the method that using GA to optimize the longitudinal profile of APS. This process is shown in **Figure 1**. The length of the horizontal metal strips in a specified thickness is simplified to a cubic function in the longitudinal direction. The coefficient matrix of polynomials was then regarded as the parameters to be optimized. The corresponding structural model can be built according to different curve functions. And then the mapping between the coefficient matrix and structure is established. Thus, the digital analysis of APS is realized. A large number of random samples were cross-iterated and selected according to the rules of GA. After optimization, the optimal coefficient matrix is obtained, the optimal structure is established, and the wideband absorber is realized. And finally, the wideband absorption with an efficiency of more than 90% in the frequency range of 10–30 GHz at the specified thickness was optimized. More importantly, when the objective function of GA is modified, the algorithm can also be applied to phase gradient design, dispersion engineering and other fields.

ABSORBER DESIGN AND OPTIMIZATION STRATEGY

Design of Absorber

The APS with straight strips is designed as shown in **Figure 2A**, in which structural parameters are listed as follows: the height of

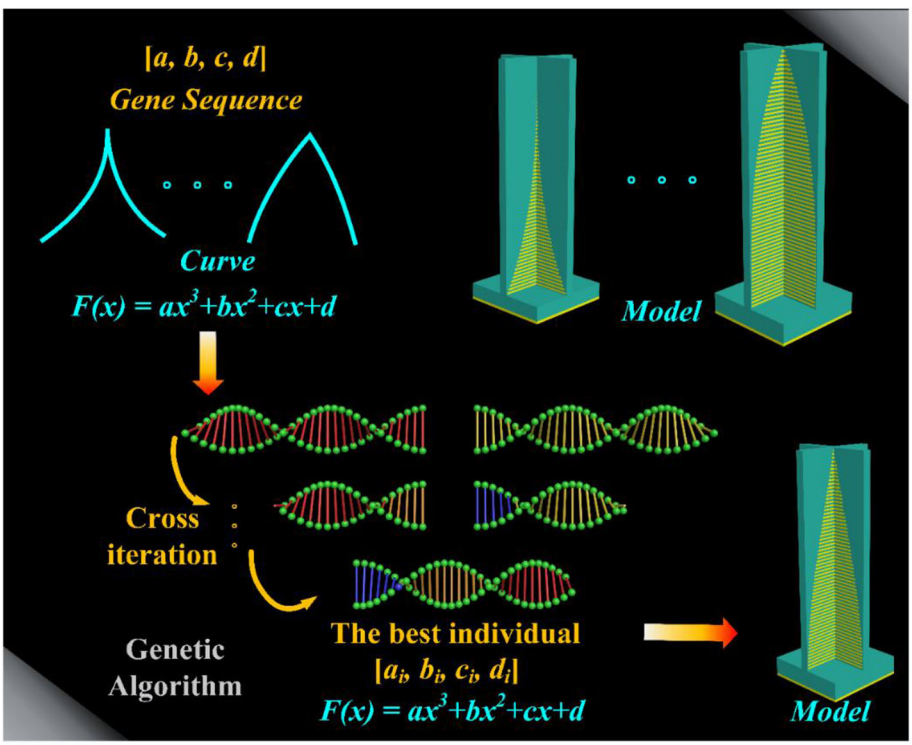

FIGURE 1 | Schematic diagram of this work.

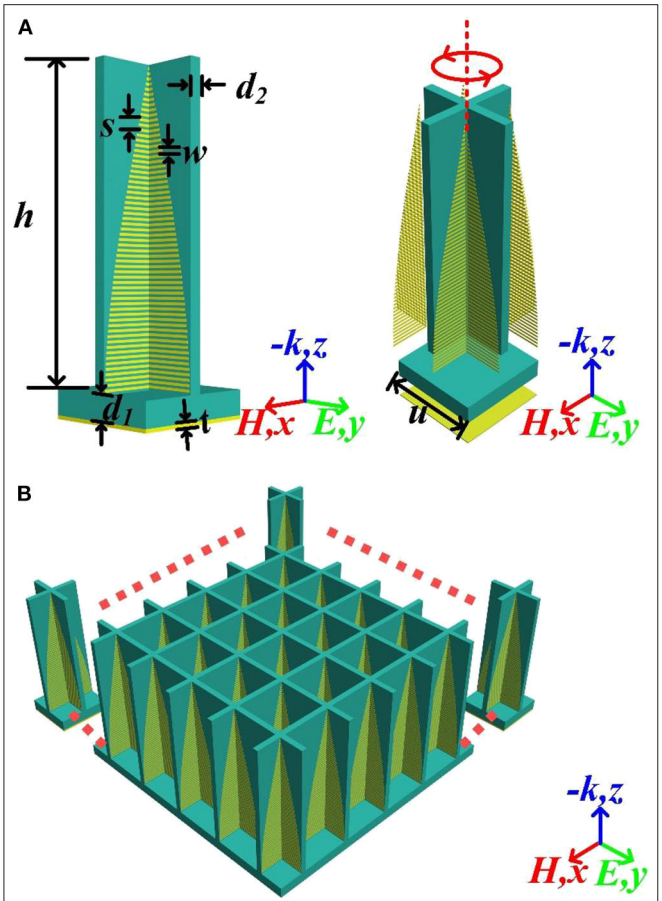

FIGURE 2 | Schematic of straight-strip-shaped APS. **(A)** The design of absorber unit and **(B)** the complete absorber is consisted of absorber units.

vertical substrate $h = 25.0$ mm and the thickness $d_2 = 1.0$ mm; the periodic distance of parallel straight strips s =0.4 mm and the width of strips $w = 0.2$ mm; the thickness of horizontal substrate $d_1 = 2.0$ mm, the metal is copper with an electric conductivity of 5.8×10^7 S/m and a thickness of $t = 0.017$ mm; the periodical length of absorber unit $u = 10.0$ mm. These parameters can be obtained in previous work [14, 34, 35]. The parallel straight copper strips with gradually varied length are bent, assembled and attached to the junction of dielectric substrates. The parallel straight strips lead electromagnetic(EM) waves from free space into absorber and form a standing wave between strips. In order to increase the loss of EM wave, a commercial dielectric substrate FR4 with a dielectric constant $\varepsilon_r = 4.2$ and a loss tangent $\tan\delta = 0.025$ is used as carrier of copper. The bottom of the absorber is consisted by a FR4 dielectric substrate backed with a copper reflector. The complete structure of the absorber is composed of design units, as shown in **Figure 2B**.

Profile Optimization and Analysis

According to some researches, the longer length of the strip, the better it matches the low-frequency EM wave, and vice versa [13, 34, 36]. Based on the theory of APS, the impedance matching between the wave vector and absorber can be affected by the length of strip. Therefore, APS profile can be optimized for better wave absorption. The gradually varying external edges of these parallel straight strips can be regarded as some discrete points in a continuous curve. Because the structure is highly symmetrical, only one eighth of the structure needs to be designed. The value range of external edges of these parallel straight strips can be expressed as: x-axis in [0.5], y-axis in [0.25]. Within this range, a cubic function can fit arbitrary gradually changed curve. Thus, the optimization of parallel straight strips is transformed to the profile curve optimization of strip's external edge which is set as a cubic function as follows:

$$f(x) = ax^3 + bx^2 + cx + d \tag{1}$$

Where [***a, b, c, d***] is the coefficient matrix of the function *f(x)*, and *f(x)* represents the curve of the longitudinal profile of APS. The curvilinear function *f(x)* affects the length of strip, as shown in **Figure 3**.

As shown in **Figure 3**, a variety of curves are generated by the cubic function *f(x)* with different coefficients. The curves are normalized to a specified region of the dielectric substrate, and the external edges of parallel straight strips vary gradually based on the function line *f(x)*. The profile of APSs was then modeled by the curves in **Figure 3A** and the corresponding structure in **Figure 3B**. Therefore, the absorption effect of the parallel straight strips will be affected if the coefficient matrix [***a, b, c, d***] is adjusted. Hence, the optimization objective can be illustrated as Equation (2):

$$\begin{aligned} &\min F(\mathrm{X}) = -\frac{\sum_{i=1}^{n} \Delta F_i}{f_{\max} - f_{\min}} \\ &S.t. \begin{cases} X = \{a, b, c, d\} \in [-1, 1] \\ f_{\max} > f_{\min} \end{cases} \end{aligned} \tag{2}$$

Where ΔF_i is the continuous bandwidth in the desired frequency range [f_{min} f_{max}], which is 10–30 GHz in this paper. If the absorbance is >90%, the current frequency satisfies the requirements. The optimization objective is to achieve the absorbance that is >90% under normal incidence.

Equation (2) reveals that the wider the absorbing bandwidth, the less the fitness function value is. The optimization process is based on MATLAB-CST co-simulation and MATLAB optimization toolbox is applied as GA optimizer. The optimization process and result are shown in **Figure 4**.

The results of the absorber optimized by GA were obtained by comprehensive simulation after 15 iterative evolutions, as shown in **Figure 4**. According to Equation (2), we can calculate the ratio of the current absorbing bandwidth in the total bandwidth. **Figure 4A** shows the process of GA optimization, the red line represents the variation of best fitness and the blue line represents the variation of mean fitness. The fitness is the value of function calculated by Equation (2). The best fitness is the optimal individual in the current generation. The mean fitness is the mean of all individuals in the current generation. According to the mean fitness, it can be seen intuitively that the population generated by GA is in a downward trend. Meanwhile, the best

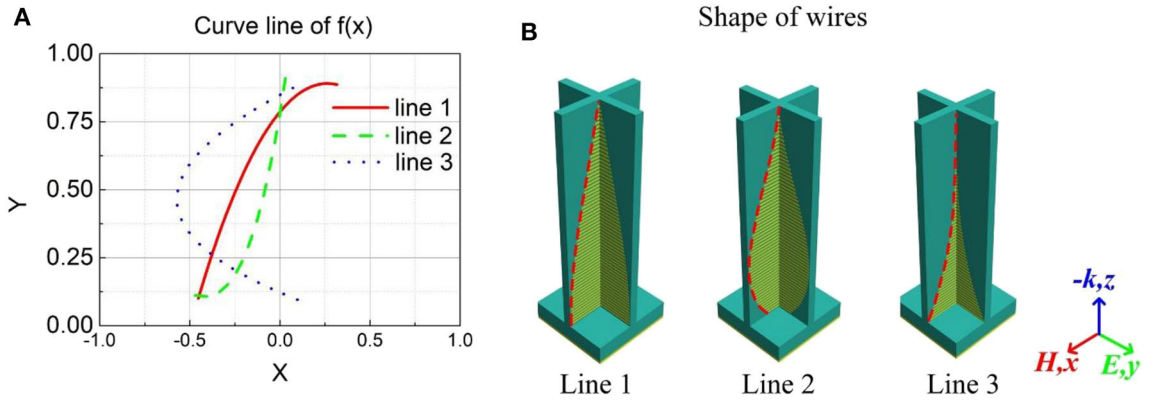

FIGURE 3 | Curve and shape of strips. **(A)** Different curves generated by function *f(x)* and **(B)** the corresponding structure of SSPPs.

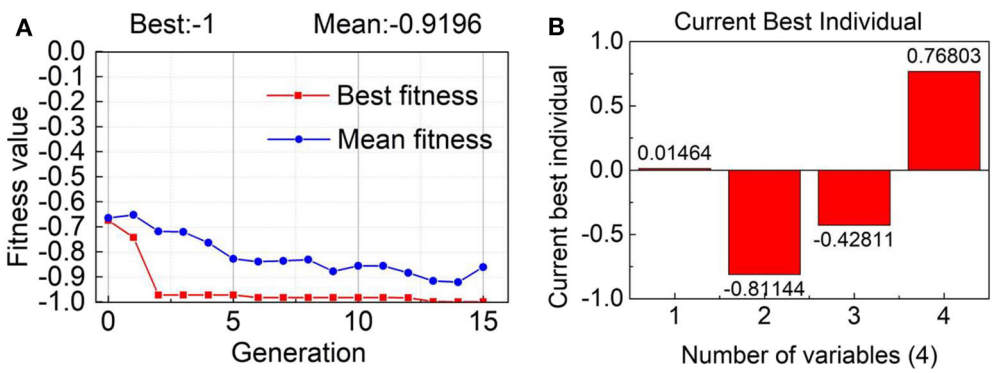

FIGURE 4 | GA optimization. **(A)** The process of GA optimization and **(B)** the current best individual.

fitness also keeps a downward trend and gradually approaches the optimal value. The optimized wideband absorber is illustrated in **Figure 4A**, in which the best fitness value is −1, indicating that the best individual has been obtained. The coefficient matrix [***a, b, c, d***] of the current best individual is shown in **Figure 4B**. According to the optimization and simulation result, the best fitness is −1, implying that the absorber can achieve more than 90% of the absorbance in the frequency range of 10–30 GHz. The current best individual is [0.01464, −0.81144, −0.42811, 0.76803], therefore, the best curve function is $f(x) = 0.01464^{*}x^{3} - 0.81144^{*}x^{2} - 0.42811^{*}x + 0.76803$. The parallel straight strips vary gradually based on above curve function and achieve better absorbing performance.

The parallel straight strips can be modified by the best line function, and the APS can be then modeled, as shown in **Figure 5A**. In order to verify the performance of the optimized APS, full-wave EM simulations were carried out using the time-domain solver in CST Microwave Studio. The simulation setups are as follows. The APS lies on XOY plane and the X-polarized waves are normally incident from the -Z direction. Remarkably, the structural unit is completely symmetric in the X and Y directions. In order to simulate an infinite continuous array while improving computing speed, the boundary conditions are introduced as follows: The X boundary condition is set to electric (Et = 0), the Y boundary condition is set to magnetic (Ht = 0). The Z boundary condition is set to open (add space). According to the simulation result in **Figure 5B**, the S_{11} is >10 dB in 10–30 GHz, implying that the absorbance is >90% in the work band. To understand the physical principle better, the distributions of surface current and power loss of the optimized model under different absorption frequencies are depicted in **Figures 5C,D**. It can be concluded that the different lengths of parallel straight strips produce resonance of different frequencies. Hence, the distribution of power loss is similar to that of surface current. The SSPPs transform EM waves in free space into surface waves and form standing waves, and the energy of EM wave is absorbed through a loss dielectric substrate. The resonance frequency is highly correlated to the length of parallel straight strips. Hence, the superposition of multiple resonant frequencies is achieved through the gradually varying strips, and then the wideband absorbing is achieved.

The optimized absorber is theoretically analyzed to explore the causes of this model. In fact, the parallel straight strips can be equivalent to dipole [34]. The straight strips produce Lorentz resonance under the effect of the electromagnetic field. The upper boundary of the linear region is the cut-off frequency of the

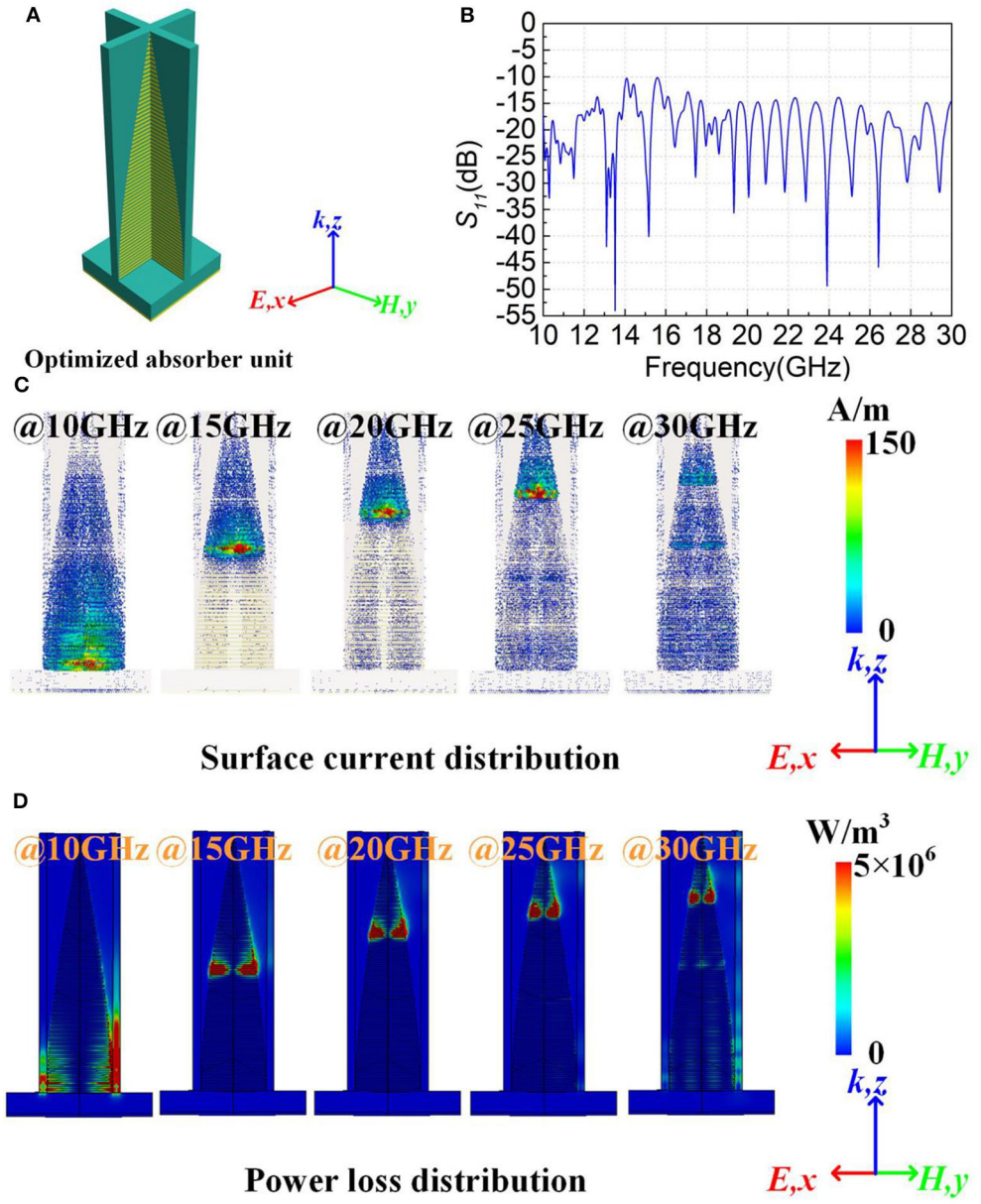

FIGURE 5 | Electromagnetic response of the APS. **(A)** The model of optimized APS, **(B)** the simulation result of this model, **(C)** surface current distributions of the parallel straight strips in 10, 15, 20, 25, and 30 GHz, and **(D)** power loss distributions of the parallel straight strips in 10, 15, 20, 25, and 30 GHz.

metal bar. With the increased frequency, the dispersion curves will gradually drift away from the light line and then get cut-off at certain frequencies. When the frequency is infinitely close to the cut-off, the maximum value of *k*-vector will produce the strongly localized surface wave, and the strongly localized surface wave always equipped with electric field enhancement, which makes the highly effective absorption close to the cutoff frequency [25].

CST Microwave Studio eigenmode solver is used to solve the dispersion relations for the electric dipole model with all the boundaries being set to period. **Figure 6A** illustrates the different lengths of strips corresponding to dispersion curves in the first Brillouin region. In order to further obtain the relations between strip length and cut-off frequency, their relations diagram shown in **Figure 6B** indicates that the length of strip *l* and frequency is non-linear. Long strip has a better match with high frequency, while short strip has a better match with low frequency. Therefore, if strip of corresponding length is matched with it in the appropriate frequency interval, the wideband matching effect can be obtained. When multiple electric dipoles are cascaded, the gradient structure of the parallel straight strips can facilitate the matching of the wave vector of SSPP and wave in free space and improve the coupling efficiency. As shown in **Figure 6**, the

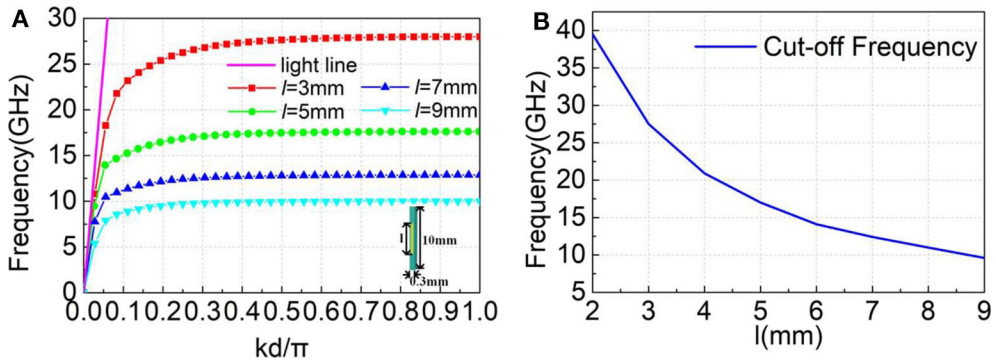

FIGURE 6 | Dispersion diagram and cut-off frequency. **(A)** The dispersion diagram of the equivalent electric dipole of a short metallic strip patterned on a dielectric substrate and **(B)** the fitting curve between the unit length and frequency.

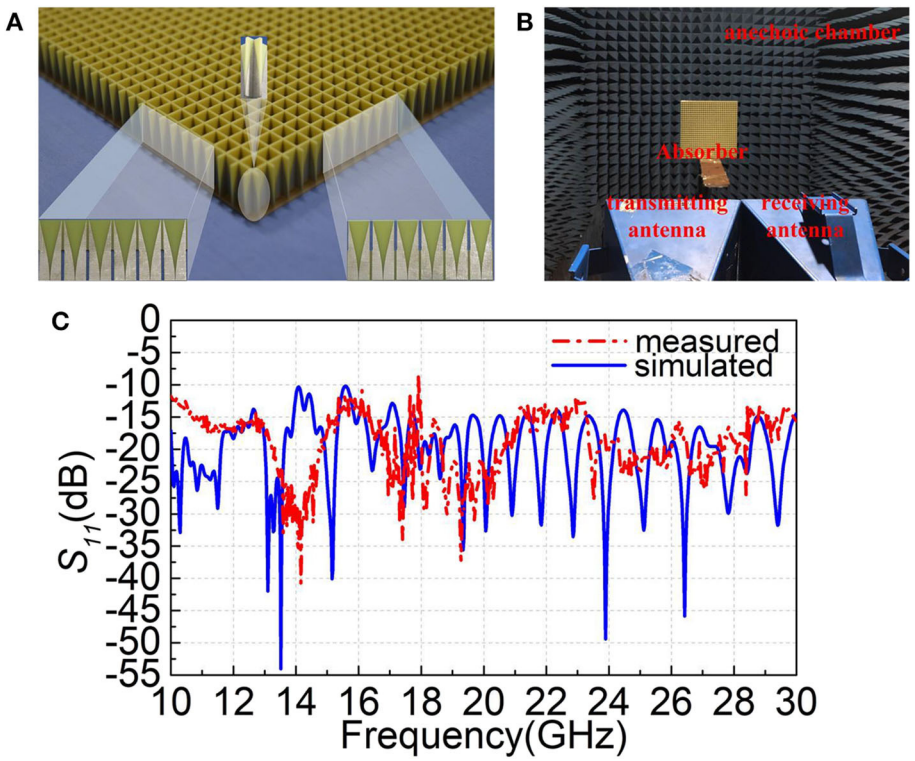

FIGURE 7 | Measurement and results. **(A)** The photograph of the fabricated APS prototype, **(B)** the experiment measuring systems, and **(C)** the measured and simulated results of this APS.

variation between strip length and cut-off frequency is non-linear. The APS can achieve a better absorbing performance because the profiles of parallel straight strips are also non-linear.

EXPERIMENT AND VERIFICATION

In order to further verify the model, we fabricated a prototype of the optimized APS using conventional Printed Circuit Board (PCB) techniques. The photograph of the fabricated APS prototype is shown in **Figure 7A**. The size of APS array is 300 × 300 mm including 900 absorber units. **Figure 7B** illustrates the experiment measuring systems. The measurements were carried out in a microwave anechoic chamber based on a network analyzer (Agilent E8363B) with three pairs of broadband antenna horns with the frequency bands of 10–12 GHz, 12–18 GHz and 18–30 GHz. The measured results and simulated absorption spectra are shown in **Figure 7C**. It can be concluded from the measured results that all the test results are <-10 dB. However, some test results are not consistent, especially in the

low frequency range. And the positions of the peaks and dips do not coincident at all, which is due to the error of machining and testing. As shown in **Figure 7A**, the APS is consisted by some components and the splicing of the modules results in poor electrical connectivity of the parallel straight strips at some intermediate junctions. However, the measured results are basically consistent with the simulation results. Additionally, the experience results demonstrate a better absorbing performance in the work band, thus proving that our method is effective.

CONCLUSION AND PERSPECTIVES

In summary, we proposed a wideband absorber based on GA to achieve a better absorbing performance in the work band. The profile of parallel straight strips is regarded as a cubic function and the curve function is optimized by GA. Subsequently, the APS is optimized by GA with 15 generations, and then a best absorber is simulated, fabricated and measured. All the tested results are <-10 dB in the work band, thus proving that this method is effective. What's more, by analyzing the relation between the cut-off frequency and the length of parallel straight strip, we concluded that the non-linearly varying parallel straight strips can be better matched with wave vector. More importantly, this paper provides an idea for optimizing non-planar structure and a method to improve the performance in the specified thickness. And this method has a wide application prospect in electromagnetic protection and metamaterial design.

DATA AVAILABILITY STATEMENT

The original contributions presented in the study are included in the article/supplementary material, further inquiries can be directed to the corresponding author/s.

AUTHOR CONTRIBUTIONS

JW, SS, and SQ were the leaders of the work. RZ and TQ were responsible for the main of experiment and paper writing. YM, YJ, XW, and YH assisted in the experiment. MF and LZ were responsible for single step of the fabrication. All authors contributed to the article and approved the submitted version.

FUNDING

The authors are grateful to the support from the National Natural Science Foundation of China under Grant Nos. 61971435, 61971437, 61901508, 61671466, and 61671467, the Graduate Scientific Research Foundation of Department of Basic Sciences, the National Key Research and Development Program of China (Grant No.: SQ2017YFA0700201).

REFERENCES

1. Zhong S, Jiang W, Xu P, Liu T, Huang J, Ma Y. A radar-infrared bi-stealth structure based on metasurfaces. *Appl Phys Lett*. (2017) **110**:6–11. doi: 10.1063/1.4975781
2. Iwaszczuk K, Strikwerda AC, Fan K, Zhang X, Averitt RD, Jepsen PU. Flexible metamaterial absorbers for stealth applications at terahertz frequencies. *Opt Express*. (2012) **20**:635. doi: 10.1364/oe.20.000635
3. Yang Y, Yoke Leng L, Wang N, Ma Y, Ong CK. Electromagnetic field attractor made of gradient index metamaterials. *J Opt Soc Am A*. (2012) **29**:473. doi: 10.1364/josaa.29.000473
4. Fan C, Tian Y, Ren P, Jia W. Realization of THz dual-band absorber with periodic cross-shaped graphene metamaterials. *Chinese Phys B*. (2019) **28**:076105. doi: 10.1088/1674-1056/28/7/076105
5. Albano M, Micheli D, Gradoni G, Morles RB, Marchetti M, Moglie F, et al. Electromagnetic shielding of thermal protection system for hypersonic vehicles. *Acta Astronaut*. (2013) **87**:30–9. doi: 10.1016/j.actaastro.2013.02.003
6. Wang B, Teo KH, Nishino T, Yerazunis W, Barnwell J, Zhang J. Experiments on wireless power transfer with metamaterials. *Appl Phys Lett*. (2011) **98**:254101. doi: 10.1063/1.3601927
7. Zhang S, Genov DA, Wang Y, Liu M, Zhang X. Plasmon-induced transparency in metamaterials. *Phys Rev Lett*. (2008) **101**:1–4. doi: 10.1103/PhysRevLett.101.047401
8. Boltasseva A, Atwater HA. Low-loss plasmonic metamaterials. *Science*. (2011) **331**:290–1. doi: 10.1126/science.1198258
9. Landy NI, Sajuyigbe S, Mock JJ, Smith DR, Padilla WJ. Perfect metamaterial absorber. *Phys Rev Lett*. (2008) **100**:1–4. doi: 10.1103/PhysRevLett.100.207402
10. Egorov V, Eitan M, Scheuer J. Genetically optimized all-dielectric metasurfaces. *Opt Express*. (2017) **25**:2583. doi: 10.1364/oe.25.002583
11. Maier SA. Gain-assisted propagation of electromagnetic energy in subwavelength surface plasmon polariton gap waveguides. *Opt Commun*. (2006) **258**:295–99. doi: 10.1016/j.optcom.2005.07.064
12. Lim SH, Mar W, Matheu P, Derkacs D, Yu ET. Photocurrent spectroscopy of optical absorption enhancement in silicon photodiodes via scattering from surface plasmon polaritons in gold nanoparticles. *J Appl Phys*. (2007) **101**:2733649. doi: 10.1063/1.2733649
13. Pendry JB, Martín-Moreno L, Garcia-Vidal FJ. Mimicking surface plasmons with structured surfaces. *Science*. (2004) **305**:847–8. doi: 10.1126/science.1098999
14. Yang J, Wang J, Feng M, Li Y, Wang X, Zhou X, et al. Achromatic flat focusing lens based on dispersion engineering of spoof surface plasmon polaritons. *Appl Phys Lett*. (2017) **110**:1–6. doi: 10.1063/1.4983831
15. Ding F, Cui Y, Ge X, Jin Y, He S. Ultra-broadband microwave metamaterial absorber. *Appl Phys Lett*. (2012) **100**:2010–4. doi: 10.1063/1.3692178
16. Lockyear MJ, Hibbins AP, Sambles JR. Microwave surface-plasmon-like modes on thin metamaterials. *Phys Rev Lett*. (2009) **102**:073901 doi: 10.1103/PhysRevLett.102.073901
17. Liu N, Liu H, Zhu S, Giessen H. Stereo metamaterials. *Nat Photonics*. (2009) **3**:157–62. doi: 10.1038/nphoton.2009.4
18. Shen Y, Zhang J, Meng Y, Wang Z, Pang Y, Wang J, et al. Merging absorption bands of plasmonic structures via dispersion engineering. *Appl Phys Lett*. (2018) **112**:5040067. doi: 10.1063/1.5040067
19. Li SJ, Cao XY, Xu HX, Zhang Z, Zhou YL, Han JF, et al. Ultra-Wideband RCS reduction of metasurface antenna based on spoof surface plasmon polariton and transmission. *Radio engineering*. (2018) **27**:386–93. doi: 10.13164/re.2018.0386
20. Meng Y, Ma H, Wang J, Li Y, Li Z, Qu S. BroadBand spoof surface plasmon polaritons coupler based on dispersion engineering of metamaterials. *Appl Phys Lett*. (2017) **111**:1–6. doi: 10.1063/1.4995505
21. Zhu J, Ma Z, Sun W, Ding F, He Q, Zhou L, et al. Ultra-broadband terahertz metamaterial absorber. *Appl Phys Lett*. (2014) **105**:4890521. doi: 10.1063/1.4890521
22. Li L, Xi R, Liu H, Lv Z. Broadband polarization-independent and low-profile optically transparent metamaterial absorber. *Appl Phys Express*. (2018) **11**:052001. doi: 10.7567/APEX.11.052001
23. Cui Y, Fung KH, Xu J, Ma H, Jin Y, He S, et al. Ultrabroadband light absorption by a sawtooth anisotropic metamaterial slab. *Nano Lett*. (2012) **12**:1443–7. doi: 10.1021/nl204118h

24. Fu JH, Wu Q, Zhang SQ, Zhang K, Meng FY. Design of multi-layers absorbers for low frequency applications. In: *2010 Asia-Pacific International Symposium on Electromagnetic Compatibility*, Beijing (2010) 1660–1663. doi: 10.1109/APEMC.2010.5475478
25. Shen Y, Zhang J, Wang J, Pang Y, Ma H, Qu S. Multistage dispersion engineering in a three-dimensional plasmonic structure for outstanding broadband absorption. *Opt Mater Express*. (2019) **9**:1539. doi: 10.1364/ome.9.001539
26. Wu C, Neuner B, Shvets G, John J, Milder A, Zollars B, et al. Large-area wide-angle spectrally selective plasmonic absorber. *Phys Rev B Condens Matter Mater Phys*. (2011) **84**:1–7. doi: 10.1103/PhysRevB.84.075102
27. Cheng YZ, Gong RZ, Nie Y, Wang X. A wideband metamaterial absorber based on a magnetic resonator loaded with lumped resistors. *Chinese Phys B*. (2012) **21**:127801. doi: 10.1088/1674-1056/21/12/127801
28. Shen Y, Zhang J, Wang W, Pang Y, Wang J, Ma H, et al. Overcoming the pixel-density limit in plasmonic absorbing structure for broadband absorption enhancement. *IEEE Antennas Wirel Propag Lett*. (2019) **18**:674–78. doi: 10.1109/LAWP.2019.2900846
29. Jafar-Zanjani S, Inampudi S, Mosallaei H. Adaptive Genetic Algorithm for Optical Metasurfaces Design. *Sci Rep*. (2018) **8**:1–16. doi: 10.1038/s41598-018-29275-z
30. Lalbakhsh A, Afzal MU, Esselle KP. Multiobjective particle swarm optimization to design a time-delay equalizer metasurface for an electromagnetic band-gap resonator antenna. *IEEE Antennas Wirel Propag Lett*. (2017) **16**:912–5. doi: 10.1109/LAWP.2016.2614498
31. Jiang L, Zheng G, Shi L, Li X. Broad omnidirectional reflector design for optical telecommunications band using genetic algorithm. *Japanese J Appl Physics, Part 1 Regul Pap Short Notes Rev Pap*. (2008) **47**:6333–6. doi: 10.1143/JJAP.47.6333
32. Zhang Q, Wan X, Liu S, Yin JY, Zhang L, Cui TJ. Shaping electromagnetic waves using software-automatically-designed metasurfaces. *Sci Rep*. (2017) **7**:1–11. doi: 10.1038/s41598-017-03764-z
33. Yuan Q, Ma H, Sui S, Shen Y, Wang J, Feng M, et al. A broadband wide-angle synthetical absorber designed by topology optimization of resistance surface and metal wires. *IEEE Access*. (2019) **7**:142675–81. doi: 10.1109/ACCESS.2019.2942495
34. Yang J, Wang J, Li Y, Pang Y, Meng Y, Cheng Q, Cui T, Qu S. 2D achromatic flat focusing lens based on dispersion engineering of spoof surface plasmon polaritons: broadband and profile-robust. *J Phys D Appl Phys*. (2018) **51**:045108. doi: 10.1088/1361-6463/aaa11e
35. Wang, X, Yan M, Fan Y, Fu X, Qu S, et al. Transmission-absorption integrated structure via dispersion engineering of spoof surface plasmon polariton and frequency selective surface. *J Phys D Appl Phys*. (2019). **53**:085001. doi: 10.1088/1361-6463/ab56bd
36. Donohue JT, Gardelle J. Dispersion relation for a three-dimensional lamellar grating. *Phys Rev Spec Top*. (2011) **14**:60709. doi: 10.1103/PhysRevSTAB.14.060709

Conflict of Interest: The authors declare that the research was conducted in the absence of any commercial or financial relationships that could be construed as a potential conflict of interest.

frontiers in Physics

ORIGINAL RESEARCH
published: 15 July 2020
doi: 10.3389/fphy.2020.00245

Broadband Adjustable Terahertz Absorption in Series Asymmetric Oval-Shaped Graphene Pattern

Jian-Zhong Sun[1] *and Jiu-Sheng Li*[1,2*]

[1] Centre for THz Research, China Jiliang University, Hangzhou, China, [2] Key Laboratory of Electromagnetic Wave Information Technology and Metrology of Zhejiang Province, College of Information Engineering, China Jiliang University, Hangzhou, China

We propose a broadband adjustable graphene absorber in terahertz regime. A prototype is designed to verify the terahertz absorption characteristics by a periodic array layer of series asymmetric oval-shaped graphene patterns on polyimide and bottom layer of metal plate. The absorber with 92% absorption and the bandwidth ranging from 3.39 to 5.96 THz is achieved. By changing the Fermi level of graphene, the bandwidth and absorption can be flexibly adjusted. The absorption is more than 92% in the range of 0∼40° incident angle. Using these characteristics, the simple absorber has broad application prospects in the fields of filter and switch in terahertz region.

Keywords: terahertz absorption, asymmetric oval-shaped graphene, wide-incident-angle, graphene, broadband

OPEN ACCESS

Edited by:
Haiyong Gan,
National Institute of Metrology, China

Reviewed by:
Weien Lai,
Hefei University of Technology, China
Furi Ling,
Huazhong University of Science and Technology, China
Shuyun Teng,
Shandong Normal University, China

****Correspondence:***
Jiu-Sheng Li
jshli@126.com

Specialty section:
This article was submitted to Optics and Photonics, a section of the journal Frontiers in Physics

Received: *02 May 2020*
Accepted: *03 June 2020*
Published: *15 July 2020*

Citation:
Sun J-Z and Li J-S (2020) Broadband Adjustable Terahertz Absorption in Series Asymmetric Oval-Shaped Graphene Pattern. Front. Phys. 8:245. doi: 10.3389/fphy.2020.00245

INTRODUCTION

With the rapid development of terahertz technology in the potential application prospects fields of imaging, security inspection, wireless communication, and sensing [1, 2], high efficient and convenient terahertz devices becomes more urgent to meet these demands. As one of the key devices of terahertz system, terahertz absorber attracts the attention of many researchers [3–9]. However, the narrow bandwidth of terahertz wave absorber seriously limits its practicality. Different schemes have been proposed to achieve the broadband response such as complex metallic shape [10] or a multilayer structure [11, 12]. These cases face constraints such as complex structure, difficult fabrication, angle dependence, and so on [13–15]. So, a broadband tunable terahertz absorber with actively control bandwidth is the goal pursued by many researchers and is practically useful. Fortunately, we know that a structure width gradient change is conducive to broadening the absorption band. In this work, a terahertz wave absorber consisting of a series asymmetric oval-shaped graphene patterns array layer, polymer layer and metal bottom plate is proposed. The structure parameters and graphene Fermi level E_f having influence on the absorption performance such as working bandwidth and absorbance, was numerically investigated. The magnetic dipole oscillation in the graphene pattern array enhances the absorbance of the proposed structure. The absorption performance was optimized by adjusting the size of the asymmetric oval-shaped graphene pattern and the Fermi level of graphene. The simulation results show the absorber provides above 92% absorption with broadband absorption bandwidth from 3.39 to 5.96 THz.

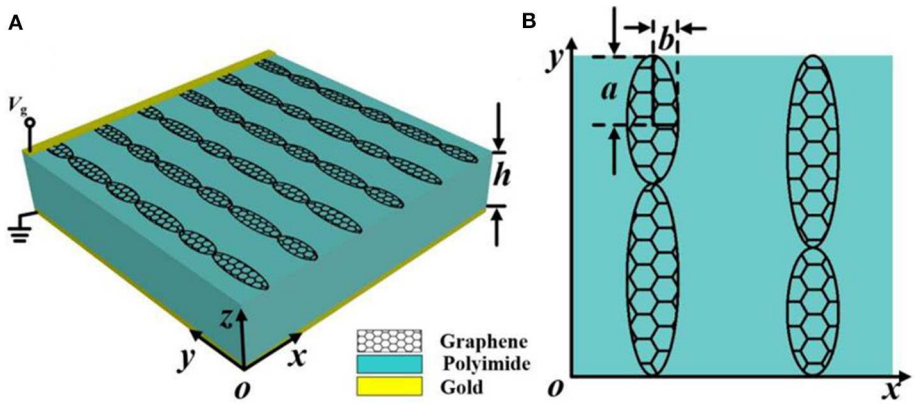

FIGURE 1 | (A) Three-dimensional schematic diagram of the proposed absorber, **(B)** Top view and geometry of the unit-cell.

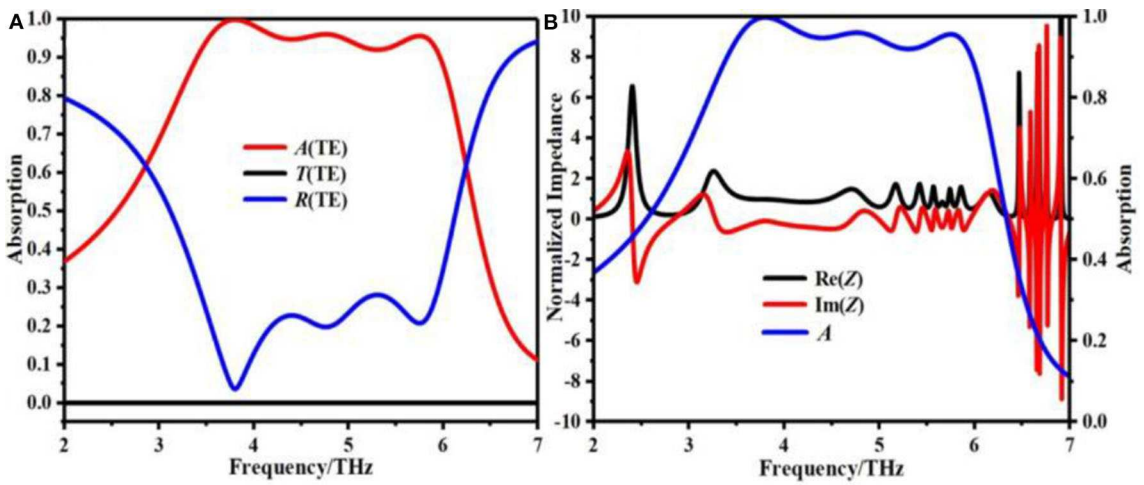

FIGURE 2 | (A) Absorption (*A*), transmittance (*T*), and reflectance (*R*) of the proposed terahertz absorber, **(B)** real and imaginary parts of the normalized input impedance.

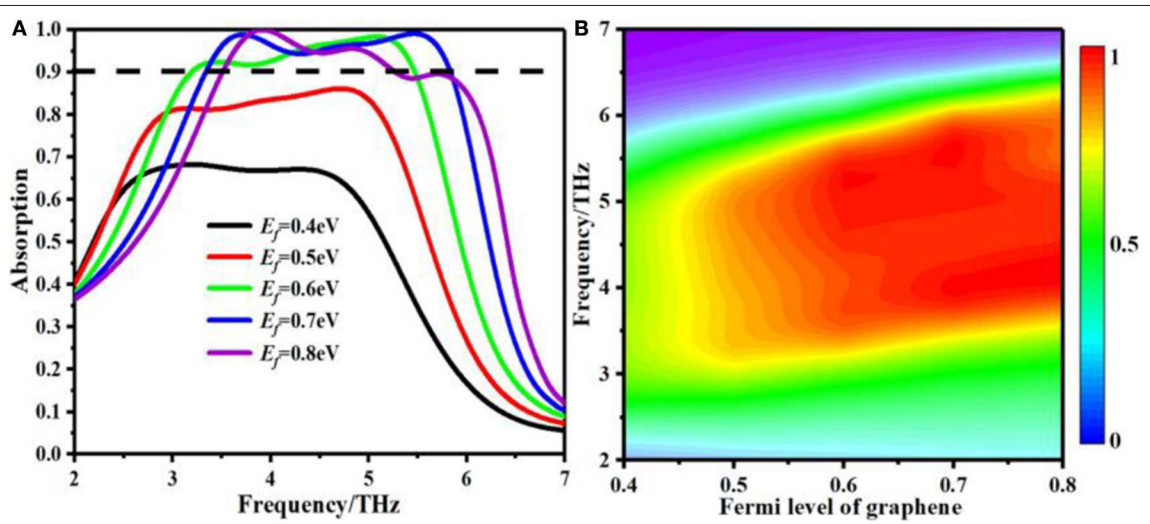

FIGURE 3 | Absorption performance of the absorber with different Fermi levels. **(A)** Absorption performance of the absorber with different Fermi levels. **(B)** Absorption spectrum with various Fermi levels.

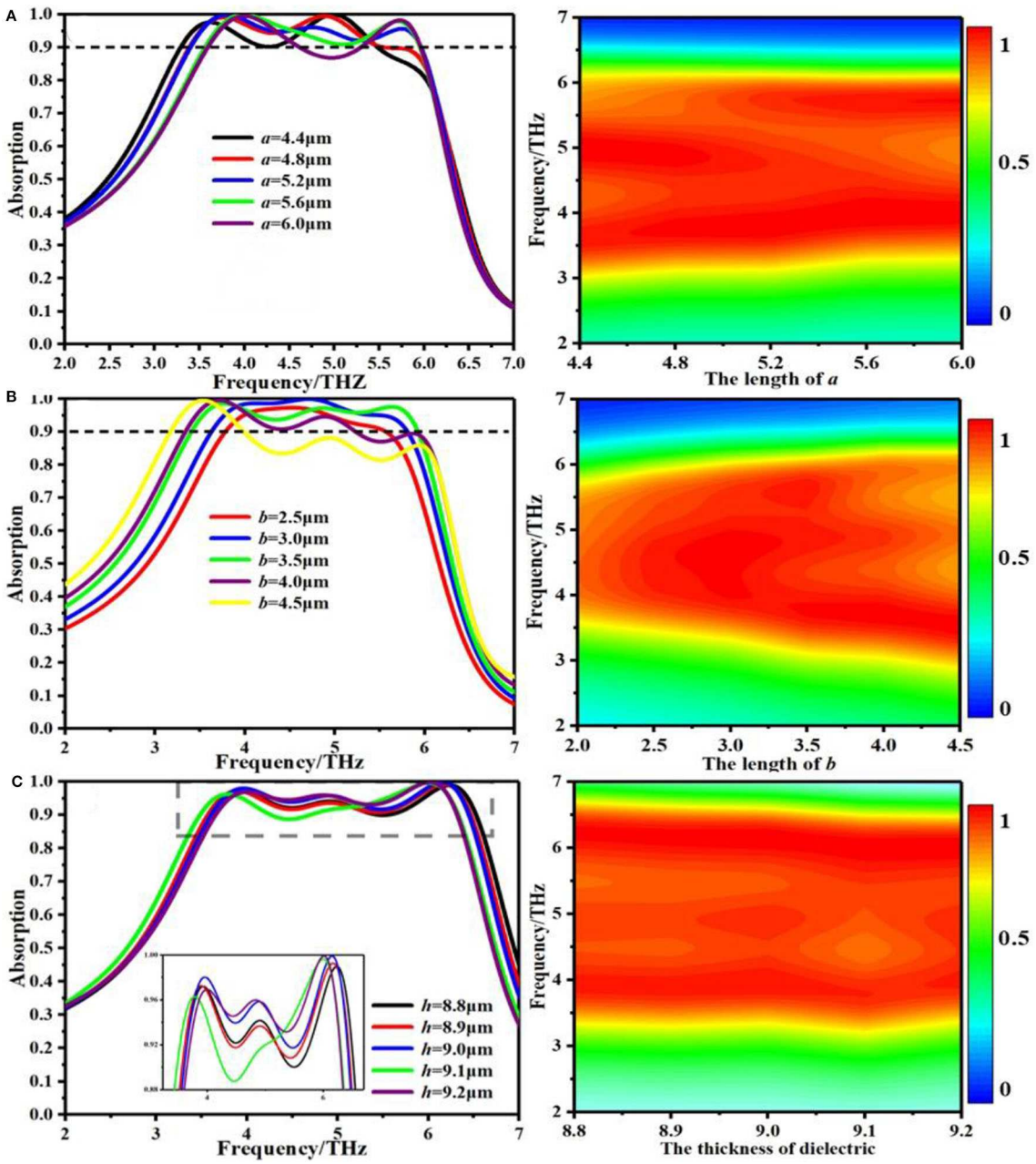

FIGURE 4 | Absorption performance of the absorber with **(A)** different semi-major axis **(B)** different semi-minor axis **(C)** different dielectric layer thicknesses.

DEVICE STRUCTURE

The schematic of the designed broadband adjustable terahertz absorber is shown in **Figure 1**. The proposed absorber is composed of series asymmetric oval-shaped graphene structure and metal plate substrate, separated by a polyimide layer. The graphene pattern is formed by the series two asymmetric oval-shaped graphene patterns, and the dielectric layer is polyimide with a dielectric constant $\varepsilon = 3.5$. Gold is used as the bottom metal plate with a conductivity of $\sigma_{\text{gold}} = 4.56 \times 10^7$ S/m. The geometrical parameters of the proposed absorber are designed as $a = 5.2\,\mu\text{m}$, $b = 3.5\,\mu\text{m}$ in the *x*-*y* plane and the thickness of the graphene sheet is set to 1 nm for easy simulation. The graphene can be fabricated by large-scale transfer techniques, and then the electron beam lithography can be employed to produce oval-shaped graphene patterns. To investigate the performance of the designed terahertz wave absorber, CST software is used to calculate the absorption responses. Floquet periodic boundary conditions are used in *x*-*y* plane and TE-polarization mode normal incident is from the top.

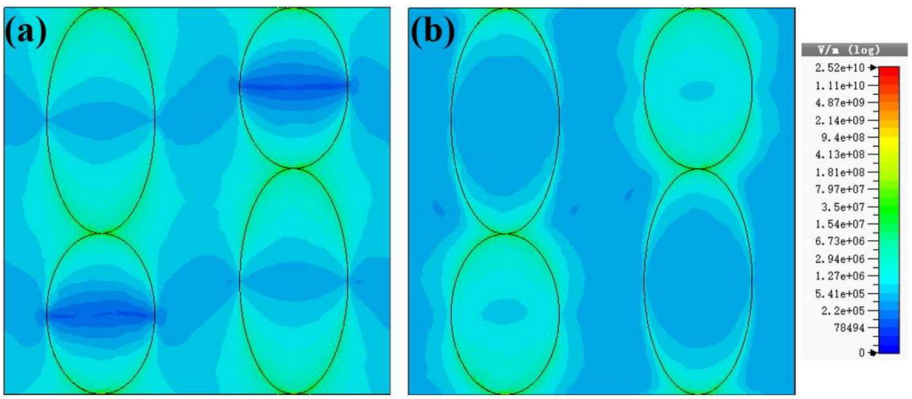

FIGURE 5 | Electric field distribution at **(a)** $f = 4$ THz **(b)** $f = 6$ THz.

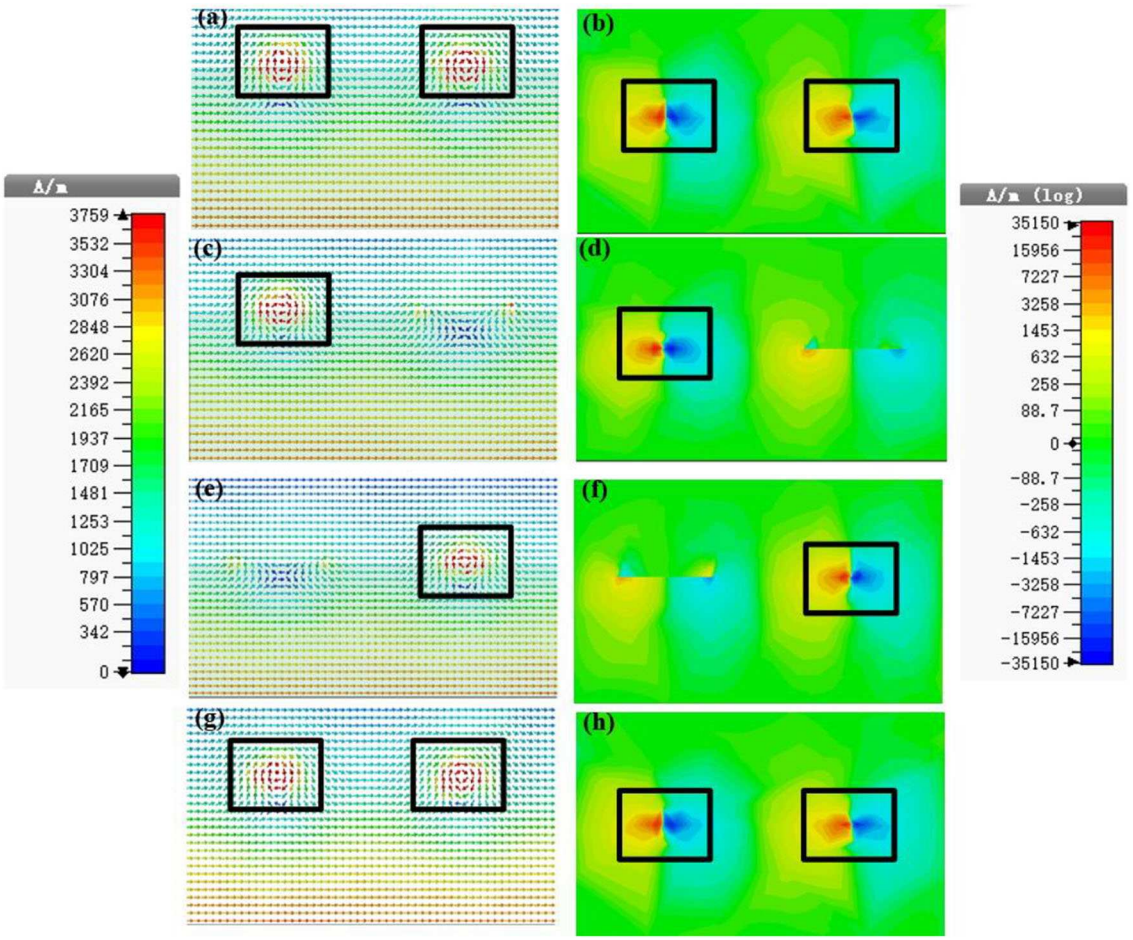

FIGURE 6 | *x-z* plane and 4 THz, **(a,b)** are magnetic induction lines and magnetic field diagrams at $y = 0\,\mu$m, **(c,d)** are magnetic induction lines and magnetic field diagrams at $y = 10.4\,\mu$m, **(e,f)** are magnetic induction lines and magnetic fields at $y = 14.6\,\mu$m, **(g,h)** are magnetic induction lines and magnetic fields at $y = 25\,\mu$m, respectively.

NUMERICAL CALCULATION AND ANALYSIS

Figure 2A shows the absorption, transmittance, reflectance spectra in TE-polarized mode under normal incidence. Absorptance can be calculated according to the equation of $A = 1\text{-}T\text{-}R$, where T is transmittance $T = |S_{21}|^2$ and R is reflectance $R = |S_{11}|^2$, which can be obtained from simulated S-parameters. From the figure, one can see that the over 90% absorption is from 3.39 to 5.96 THz. **Figure 3B** displays the real and imaginary parts

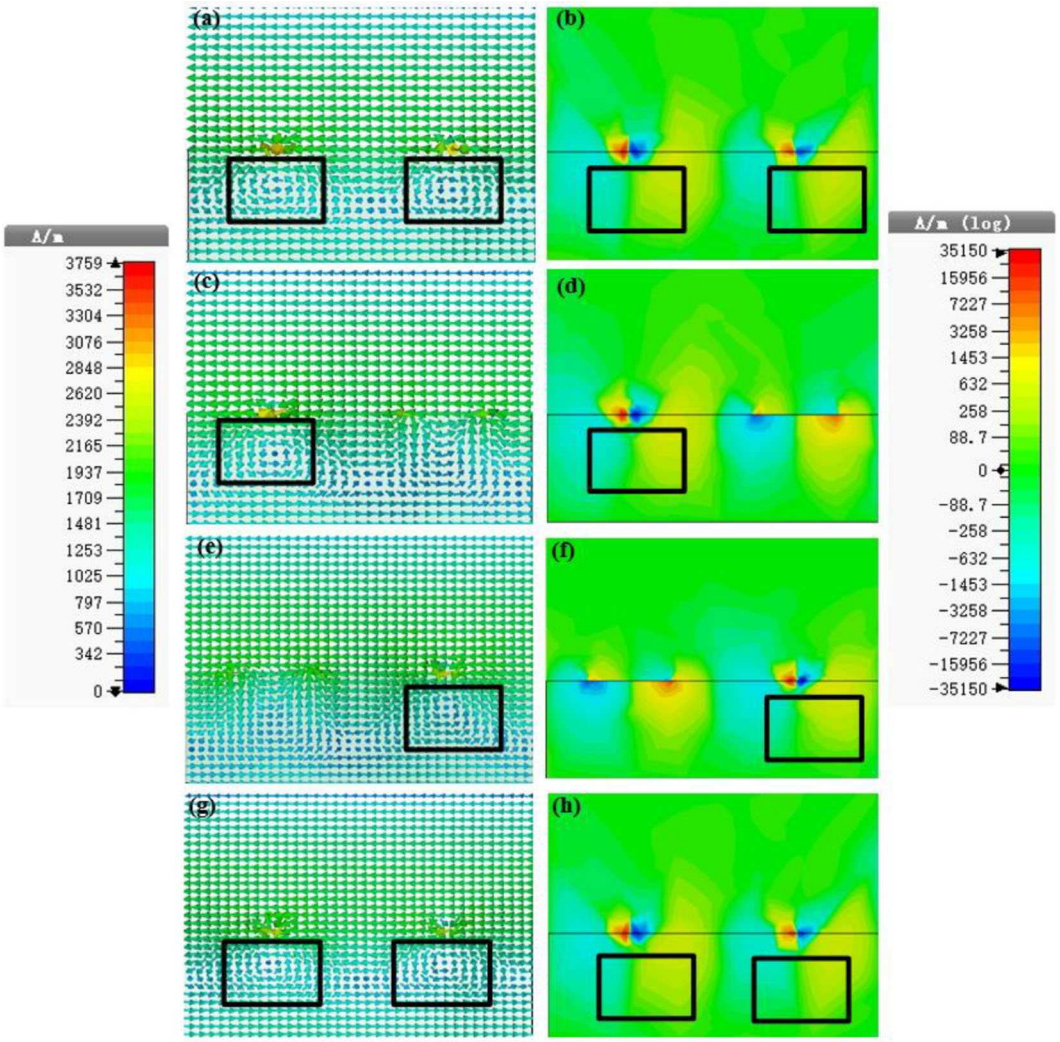

FIGURE 7 | *x-z* plane and $f = 6$ THz, **(a,b)** are magnetic induction lines and magnetic field diagrams at y = 0 μm, **(c,d)** are magnetic induction line and magnetic field diagrams at $y = 14.6$ μm, respectively, **(e,f)** are magnetic induction lines and magnetic field diagrams at $y = 10.4$ μm, **(g,h)** are magnetic induction lines and magnetic field diagrams at $y = 25$ μm, respectively.

of the normalized input impedance of the proposed absorber. When the imaginary part of the normalized input impedance of the proposed absorber is zero, the maximum absorption of the absorber can be obtained. At this time, the effective impedance of the absorber matches with the free space impedance (That is to say, the absorber is under impedance matching condition). The effective impedance Z (The impedance is normalized to free space impedance) of the absorber is obtained through the reflection and transmission coefficients and their corresponding phase relationships. The black solid and red solid lines represent the real part and imaginary part of the normalized impedance, respectively. From **Figure 2B**, one can observed that the real part of the normalized impedance Re(Z) is near 1 and the imaginary part of the normalized impedance Im(Z) is near 0 from 3.39 to 5.96 THz. It indicates that the effective impedance Z of the absorber basically matches the impedance of free space within the bandwidth. The proposed absorber reaches above 92% absorption between 3.39 and 5.96 THz.

Figure 3 shows the absorption spectra under different graphene Fermi level E_f. When Fermi level E_f is lower than 0.5 eV, the maximum absorption of the proposed structure is <85%. The average absorption gradually increases when the Fermi level increases to 0.7 eV because of the change of the conductivity. The average absorption performance increases until $E_f = 0.7$ eV, and it reaches the maximum value of above 95.0%. When Fermi level E_f exceeds 0.7 eV, the absorption effect begins to weaken and average absorption moves downwards. In addition, the bandwidth of the proposed absorber can be tunable by the chemical potentials correspondingly. To study the influence of the structural parameters changes on absorption performance, we systematically change structural parameters (including a, b, and h) to calculate the absorption spectra of the

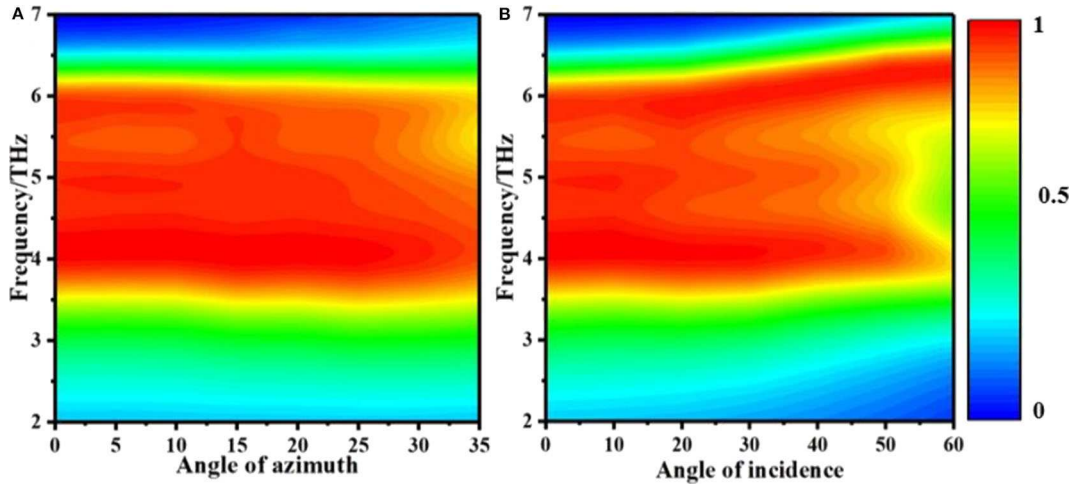

FIGURE 8 | Absorption spectra with different **(A)** azimuth angles **(B)** incidence angles.

TABLE 1 | Performance comparison of the proposed absorber with some reported absorber.

References	Bandwidth >90%	Graphene type	Polarization
Biabanifard et al. [8]	2.2 THz	Multilayer graphene disks and ribbons	Sensitive
Deng et al. [16]	8.7 THz	Graphene pattern and gold pattern	Insensitive
Our results	2.57 THz	Oval-shaped graphene	Sensitive

proposed absorber shown in **Figure 4**. As shown in **Figure 4A**, with the increase of the semi-major axis a, the absorption peak at 5.0 THz gradually decreases to 88%. When the semi-major axis a equals 5.2 μm, the absorption is above 92% at the frequency range from 3.39 to 5.96 THz. As can be seen from **Figure 4B**, when the parameter b varies from 2.5 to 4.5 μm, the average absorption has a significant weakening trend. In order to obtain a perfect absorber with above 92% absorption and broad bandwidth from 3.39 to 5.96 THz, we chose the parameter of the semi-minor axis $b = 3.5$ μm. As depicted in **Figure 4C**, it is found that as the dielectric layer thickness (h) increases from 8.8 to 9.2 μm, the absorption bandwidth exhibits slightly redshift and average absorption has a slightly weakening trend. When $h = 9.0$ μm, the absorptance is infinitely close to 100% at $f = 6$ THz.

Figures 5a,b illustrate the electric field distribution of the absorber under normal incidence of TE-polarization mode terahertz wave at the resonance frequencies of $f = 4$ THz and $f = 6$ THz, respectively. It can be observed that the electric field energy is concentrated on both ends of the long axis of the oval-shaped graphene pattern, which means surface plasmon resonances are strongly bounded to both ends of the long axis of the patterned graphene. **Figures 6a–h** show the magnetic induction lines and magnetic fields of the proposed absorber at $f = 4$ THz in x-z plane at $y = 0$ μm, $y = 10.4$ μm, $y = 14.6$ μm, and $y = 25$ μm, respectively. From **Figures 6a,g**, $y = 0$ μm and $y = 25$ μm, one can find that the magnetic induction lines of the graphene layer are symmetrical. Corresponding magnetic field strength diagrams of $y = 0$ and $y = 25$ μm are shown in **Figures 6b,h**. It indicates that the oval-shaped graphene layer generates magnetic resonance and forms two magnetic dipoles, which promotes the terahertz wave absorption. **Figures 6c,e** depicts the magnetic induction lines of $y = 10.4$ and $y = 14.6$ μm, respectively. The corresponding magnetic field diagrams are illustrated in **Figures 6d,f**, respectively. At $y = 10.4$ and $y = 14.6$ μm, the oval-shaped graphene layer forms a single magnetic dipole and promotes the terahertz wave absorption. The magnetic resonance occurs at the long axis of the oval-shaped graphene pattern, and the energy is basically concentrated on the long axis of the oval-shaped graphene pattern.

The magnetic induction lines and magnetic field diagrams of the absorber in x-z plane at $y = 0$, $y = 10.4$, $y = 14.6$, and $y = 25$ μm at a frequency of $f = 6$ THz are shown in **Figure 7**. It can be observed that, compared with the **Figure 6** ($f = 4$ THz), the magnetic field strength and magnetic loop position are different. At $f = 6$ THz, the top graphene pattern has a magnetic resonance but a corresponding magnetic loop is formed in the dielectric layer. Furthermore, the magnetic field strength is weaker than that of $f = 4$ THz. The absorption spectra of TE polarization mode, operating frequency and incidence angle are plotted in **Figures 8A,B**. One can see that the absorber has a relatively stable absorptivity (above 92%) with absorption bandwidth from 3.39 to 5.96 THz in the incident angle range of 0–40°. **Table 1** shows the performances of our absorber and some reported absorber.

CONCLUSION

To sum up, we have numerically studied a broadband tunable absorber based on series asymmetric oval-shaped graphene array. The simulated results indicate that the proposed structure provides a broadband absorption (3.39∼5.96 THz) with absorbance higher than 92%. Furthermore, one sees that both the absorption bandwidth and the absorbance of the proposed absorber can be dynamically controlled by changing the Fermi level of the series asymmetric oval-shaped graphene array. The proposed absorber may have potential applications such as filter and switch in terahertz range.

DATA AVAILABILITY STATEMENT

The raw data supporting the conclusions of this article will be made available by the authors, without undue reservation.

AUTHOR CONTRIBUTIONS

J-ZS performed the calculations. J-SL concerned the devices structure and developed the theoretical model. All authors discussed the results and co-wrote the manuscript.

FUNDING

This work was sponsored by Natural Science Foundation of Zhejiang Province (LY18F010016), National Natural Science Foundation of China (Grant Nos. 61871355 and 61831012) and Zhejiang Lab (No. 2019LC0AB03).

ACKNOWLEDGMENTS

We would like to thank X. Chen for his help and support.

REFERENCES

1. Kuznetsov S, Paulish A, Gelfand A, Lazorskiy P, Fedorinin V. Bolometric THz-to-IR converter for terahertz imaging. *Appl Phys Lett.* (2011) **99**:710. doi: 10.1063/1.3607474
2. Liu N, Mesch M, Weiss T, Hentschel M, Giessen H. Infrared perfect absorber and its application as plasmonic sensor. *Nano Lett.* (2010) **10**:2342–8. doi: 10.1021/nl9041033
3. He G, Stiens J. Enhanced terahertz absorption of graphene composite integrated with double circular metal ring array. *Plasmonics.* (2017) **9**:1–6. doi: 10.1007/s11468-017-0682-2
4. Xu Y, Li E, Wei X, Yi D. A novel tunable absorber based on vertical graphene strips. *IEEE Microw Wireless Compon Lett.* (2016) **26**:10–2. doi: 10.1109/LMWC.2015.2505610
5. Fu P, Liu F, Ren G, Fei S, Dong L, Jian Y. A broadband metamaterial absorber based on multi-layer graphene in the terahertz region. *Opt Commun.* (2018) **417**:62–6. doi: 10.1016/j.optcom.2018.02.034
6. Zhu Z, Guo C, Zhang J, Liu K, Yun X, Qin S. Broadband single-layered graphene absorber using periodic arrays of graphene ribbons with gradient width. *Appl Phys Express.* (2015) **8**:015102. doi: 10.7567/APEX.8.015102
7. Andryieuski, Lavrinenko A. Graphene metamaterials based tunable terahertz absorber: effective surface conductivity approach. *Opt Express.* (2013) **21**:9144–55. doi: 10.1364/OE.21.009144
8. Sadegh, Mohammad B, Somayyeh A, Shahrouz A, Mustapha Y. Tunable ultra-wideband terahertz absorber based on graphene disks and ribbons. *Opt Commun.* (2018) **427**:418–25. doi: 10.1016/j.optcom.2018.07.008
9. Lei L, Lou F, Tao K, Huang H, Cheng X, Xu P. Tunable and scalable broadband metamaterial absorber involving VO2-based phase transition. *Photon Res.* (2019) **7**:734–41. doi: 10.1364/PRJ.7.000734
10. Kenney M, Grant J, Shah Y, Carranza I, Humphreys M, Cumming D. Octave-spanning broadband absorption of terahertz light using metasurface fractal-cross absorbers. *ACS Photonics.* (2017) **4**:2604–12. doi: 10.1021/acsphotonics.7b00906
11. Grant J, Ma Y, Saha S, Khalid A, Cumming D. Polarization insensitive broadband terahertz metamaterial absorber. *Opt Lett.* (2011) **36**:3476–8. doi: 10.1364/OL.36.003476
12. Wang B, Wang L, Wang G, Huang W, Li X, Zhai X. Metamaterial based low-conductivity alloy perfect absorber. *J Lightwave Technol.* (2014) **32**:2293–8. doi: 10.1109/JLT.2014.2322860
13. Pu M, Wang M, Hu C, Huang C, Zhao Z, Wang Y, et al. Engineering heavily doped silicon for broadband absorber in the terahertz regime. *Opt Express.* (2012) **20**:25513–9. doi: 10.1364/OE.20.025513
14. Cheng YZ, Withayachumnankul W, Upadhyay A, Headland D, Nie Y, Gong R, et al. Ultrabroadband plasmonic absorber for terahertz waves. *Adv Opt Mater.* (2015) **3**:376–80. doi: 10.1002/adom.201400368
15. Rahmanzadeh M, Rajabalipanah H, Abdolali A. Multilayer graphene-based metasurfaces: robust design method for extremely broadband, wide-angle, and polarization-insensitive terahertz absorbers. *Appl Opt.* (2018) **57**:959. doi: 10.1364/AO.57.000959
16. Deng Y, Peng L, Liao X, Jiang X. An ultra-broadband terahertz absorber based on coplanar graphene and gold hybridized metasurface. *Plasmonics.* (2019) **14**:1057–61. doi: 10.1007/s11468-018-0893-1

Conflict of Interest: The authors declare that the research was conducted in the absence of any commercial or financial relationships that could be construed as a potential conflict of interest.

frontiers in Physics

ORIGINAL RESEARCH
published: 17 July 2020
doi: 10.3389/fphy.2020.00256

Double Fano Resonances in S-Shaped Plasmonic Metasurfaces in Terahertz Region

Weihang Xu[1], *Lingling Chen*[1], *Fangming Zhu*[2], *Jianjun Liu*[1], *Chuanshuai Sui*[1] and *Zhi Hong*[1]*

[1] Centre for THz Research, China Jiliang University, Hangzhou, China, [2] School of Information Science and Engineering, Hangzhou Normal University, Hangzhou, China

We numerically and experimentally demonstrated double Fano resonances in a simple S-shaped plasmonic metasurface in the terahertz frequency range. Apart from the electric-LC resonance and electric dipole (ED) resonance, two trapped modes are excited in two different types of asymmetric S-shaped structures in the frequency range 0.2–1.4 THz, which are mainly attributed to a magnetic dipole (MD) and an electric quadrupole (EQ). Thereafter, double Fano resonances [one Fano and one electromagnetically induced transparency (EIT) resonance] are achieved via the coupling of the two dark trapped modes and a broad bright ED at normal incidence of the metasurfaces. Furthermore, under oblique incidence, strong Fano responses can be observed; they are considerably enhanced in asymmetric structures, and even in a symmetric structure. The proposed S-shaped plasmonic metasurfaces are easy to fabricate and have potential applications in multi-wavelength optical switches, filters, and sensors.

Keywords: Fano resonance, metasurface, plasmonic, trapped mode, terahertz

OPEN ACCESS

Edited by:
Olivier J. F. Martin, École Polytechnique Fédérale de Lausanne, Switzerland

Reviewed by:
Ranjan Singh, Nanyang Technological University, Singapore
Yugui Peng, CUNY Advanced Science Research Center, United States
Maria Kafesaki, University of Crete, Greece

***Correspondence:**
Zhi Hong
hongzhi@cjlu.edu.cn

Specialty section:
This article was submitted to Optics and Photonics, a section of the journal Frontiers in Physics

Received: *13 April 2020*
Accepted: *09 June 2020*
Published: *17 July 2020*

Citation:
Xu W, Chen L, Zhu F, Liu J, Sui C and Hong Z (2020) Double Fano Resonances in S-Shaped Plasmonic Metasurfaces in Terahertz Region. Front. Phys. 8:256. doi: 10.3389/fphy.2020.00256

INTRODUCTION

In the last decade, metamaterials (MMs) have been extensively studied because of their peculiar electromagnetic properties, such as negative index media, cloaking, and subwavelength resolution imaging [1–5], which cannot be obtained from naturally occurring materials. The fundamental characteristic of an MM is its electromagnetic resonance responses, one of which is the interesting trapped mode, which results from the anti-phased dipole resonance in an asymmetric plasmonic MM [6–10]. The trapped mode has a high *Q* factor because of its small radiation loss, so it can be used in sensor and modulator [11–15]. Researchers have focused on MMs containing a single trapped mode observed in simple one-meta-atom MMs for a long time, and in recent years, multiple trapped modes, usually excited in a complicated multi-meta-atom called metamolecule MMs, have attracted extensive attention due to their superior performance in terms of modifying resonant waveforms at multiple spectral locations simultaneously [16–20]. For example, two or more trapped modes are demonstrated in MMs with a double-chain meander wire array or two different lattices of metamolecules [19, 20]. On the other hand, trapped mode, as a dark resonance, can be coupled with a low-Q bright mode to generate Fano resonance or an EIT response [21–28]. Furthermore, multiple Fano resonances can be excited via multiple trapped modes in multi-meta-atom MMs [29–33], which could be useful in multi-wavelength optical switches, filters,

and sensors. For example, only one Fano resonance is observed in a Z-shaped one-meta-atom plasmonic metasurface [26], but three Fano resonances have been observed in two different-sized asymmetric double-bar structures, where two Fano resonances are attributed to two individual meta-atoms, and one to their combinations or metamolecule MM [33]. However, the metamolecule structure will increase the size of the devices, which may not be conducive to practical applications.

In this work, we propose and experimentally demonstrate a metasurface with double trapped modes consisting of only one S-shaped plasmonic structure in the terahertz region. Furthermore, double Fano resonances were also observed in this type of one-meta-atom metasurface. This planar plasmonic metasurface is easy to fabricate and has potential applications in biochemical sensing, optical switching, and slow-light devices.

DESIGN AND SIMULATION RESULTS

S-shaped Symmetric and Asymmetric Plasmonic Metasurfaces

The unit cell of the symmetric S-shaped plasmonic metasurface is similar to Refs. [34–36] and shown in **Figure 1A**, where the S-shaped aluminum structure (electric conductivity $\sigma = 3.56 \times 10^7$ S/m) with a thickness of 200 nm is deposited on a 12-μm-thickness polyethylene terephthalate film (PET, permittivity $\varepsilon = 3.2$). The atom S exhibits inversion symmetry, and its geometrical dimensions are $l_1 = 100\,\mu$m, $l_2 = 80\,\mu$m, and $w = 10\,\mu$m. The unit cells are periodically arranged in the x and y planes with identical lattice constants $Px = Py = 200\,\mu$m. In addition, two different types of asymmetric S-shaped structures are considered, as shown in **Figures 1B,C**, respectively. In Case I, the symmetry of the *S* is broken by changing the lengths of the horizontal metal arms, and the degree of asymmetry is determined by *d*. In Case II, the lengths of the vertical arms are changed, and the degree of asymmetry is determined by *g*. To investigate the resonant properties of the metasurface, numerical simulations are carried out with commercial CST software. In our simulations, we utilize periodic boundary conditions in both x and y directions, and open boundary conditions are applied in the wave propagating direction z. In the simulation, a lossless substrate is assumed for PET.

Double Trapped Modes in Asymmetric Metasurfaces

At first, the metasurfaces are illuminated by a normally incident plane wave with the electric field along the y-axis. **Figure 2** shows the simulated transmissions of three symmetric and asymmetric S-shaped plasmonic metasurfaces in the frequency range 0.2–1.4 THz. It is evident in **Figure 2A** that two strong resonances are located around 0.3 and 1.3 THz in the centrally symmetric S-shaped metasurface. From the surface current distributions (not shown here) at these two frequencies, we know that they are typical electric-LC and electrical dipole (ED) resonances, respectively. For an asymmetric S-shaped metasurface as in Case I, however, in addition to the two resonances at 0.3 and 1.3 THz, two new weak and narrow resonances can be clearly seen at 0.6 and 1.0 THz in **Figure 2B**, which are dependent on the related asymmetric value of *d*. As theoretical analysis has shown, the origin of the narrow spectral response in an asymmetry structure can be attributed to the so-called "trapped mode," which is weakly coupled to free space [6, 23], and a larger asymmetric value of the structure corresponds to a stronger trapped resonance with a wider bandwidth [25–29, 33]. Similarly, two strong trapped modes at the same frequencies of 0.6 and 1.0 THz in **Figure 2C** can be observed in another asymmetric structure in Case II. The same dependence of the trapped modes on the asymmetry value *g* is also shown in **Figure 2C**. As *g* decreases from 30 to 10 μm, the *Q*-values of the trapped modes at 0.6 and 1.0 THz increase from 78 to 149, and from 72 to 203, respectively. And the *Q* factor of the trapped mode at 1.0 THz will reach up to 270 when $g = 5\,\mu$m, but very sensitive to the loss of the substrate. Compared to Case I, the trapped modes in Case II are much stronger, which is related to their different excitation nature and discussed in the following.

To explain the excitation nature of these two trapped modes, the structure *S* can be regarded as the splicing of double U-shaped sub-structures. Because of the anti-phase symmetry, the dipolar moments in them are in opposite directions, and perfectly canceled in the symmetric S-shaped metasurface, indicating that the modes are not excited and remain dark at 0.6 and 1.0 THz. However, the trapped modes can be excited when the symmetry of *S* is broken. The instantaneous current distributions at 0.6 and 1.0 THz are plotted in **Figures 3A–D**. **Figures 3A,B** show the surface current distributions at 0.6 THz in Case I and Case II, respectively. Due to the different size of the double U-shaped structures, the dipole momentums can't be completely canceled, meaning the balance of the anti-phase currents is destroyed, and thus the two clockwise circulating currents enhance the magnetic dipole (MD) and suppress the toroidal dipole (TD), which means this resonance is an MD resonance. On the other hand, the surface current distributions at 1.0 THz in Case I and Case II are given in **Figures 3C,D**, respectively. Strong currents can be observed in the top and bottom arms, as well as in the arms on both sides. Obviously, this is reminiscent of the electric quadrupole form (EQ).

To further understand the nature of these two resonances, decomposed scattered powers for multipole moments are calculated based on the density of the induced current inside the metamolecules by using a Cartesian coordinate system [37–40]. **Figures 3E,F** plot the five strongest scattering powers of multipoles around the resonant frequencies of Case I and Case II, which include the ED *P*, MD *M*, TD *T*, EQ *Qe*, and magnetic quadrupole (MQ) *Qm*. For multipole moments of Case I around the resonant frequency of 0.6 THz, the magnetic dipole *M* increases greatly and dominates the other multipoles in far-field scattering power, which confirms that the resonant mode is an MD. The TD *T* appears weaker than the other multipoles, as previously analyzed from surface currents. At the frequency of 1.0 THz, it is evident that the electric quadrupole *Qe* occupies the dominant position, while the ED *P* is in the second position, which means this resonance is an EQ. Similar to Case I, the MD

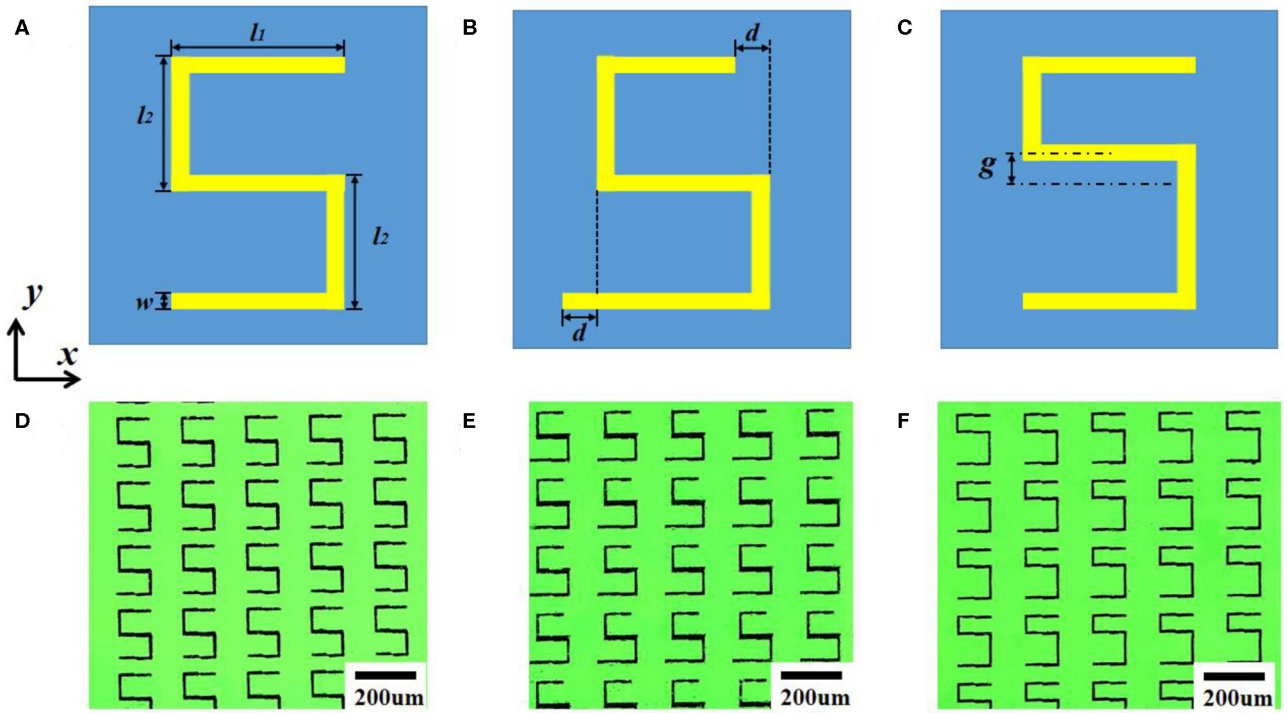

FIGURE 1 | Unit cells of three S-shaped plasmonic metasurfaces and the corresponding fabricated samples. **(A)** Inversion symmetry, **(B)** Case I: Broken symmetry produced by changing the length of the horizontal arms, **(C)** Case II: Broken symmetry produced by changing the length of the vertical arms, **(D–F)** Microscopic images of the corresponding three fabricated metasurfaces, where $d = 20\,\mu m$ in **(E)** and $g = 20\,\mu m$ in **(F)**.

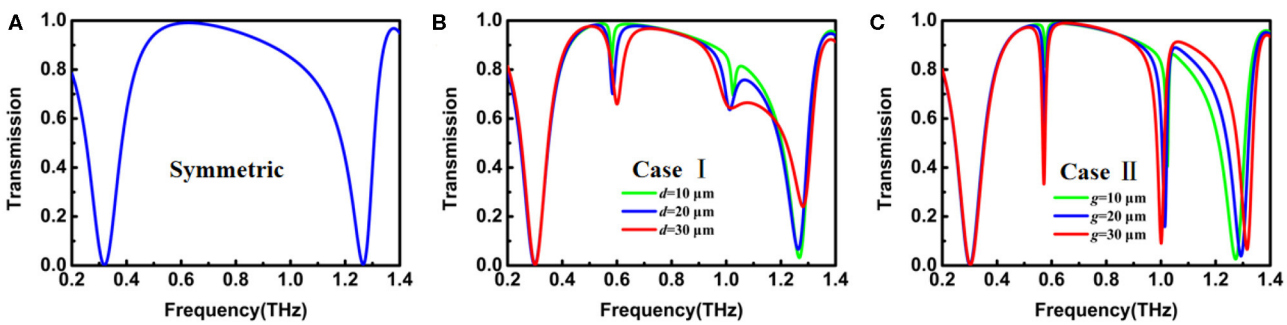

FIGURE 2 | Simulated transmission spectra for **(A)** symmetric metasurface; **(B)** Case I with different values of d; **(C)** Case II with different values of g. The E-field of incident wave is polarized along the y-axis.

M and EQ *Qe* for Case II occupy the dominant positions at 0.6 and 1.0 THz, respectively, which indicates that the two trapped modes in Case I and Case II are identical.

Double Fano Resonances in Asymmetric Metasurfaces

For an incident wave polarized along the x-axis instead of the y-axis, the transmission spectra of three S-shaped metasurfaces are calculated and shown in **Figure 4**. The transmission of symmetric metasurface shown in **Figure 4A** displays a clear, broad resonance dip around 1.0 THz, which is a typical ED resonance from the surface current distribution (not shown here). However, once the symmetry of the S structure is broken as in Case I, we interestingly observe a distinct EIT-like resonance (shown in **Figure 4B**) in the vicinity of 1.0 THz. The EIT-like transparency peak coincidentally appears at the dip of the broad ED resonance shown in **Figure 4A**, and is consistent with the trapped EQ given in **Figure 2B** as well. Consequently, this EIT-like resonance can be interpreted as a destructive interference between the bright ED and the trapped

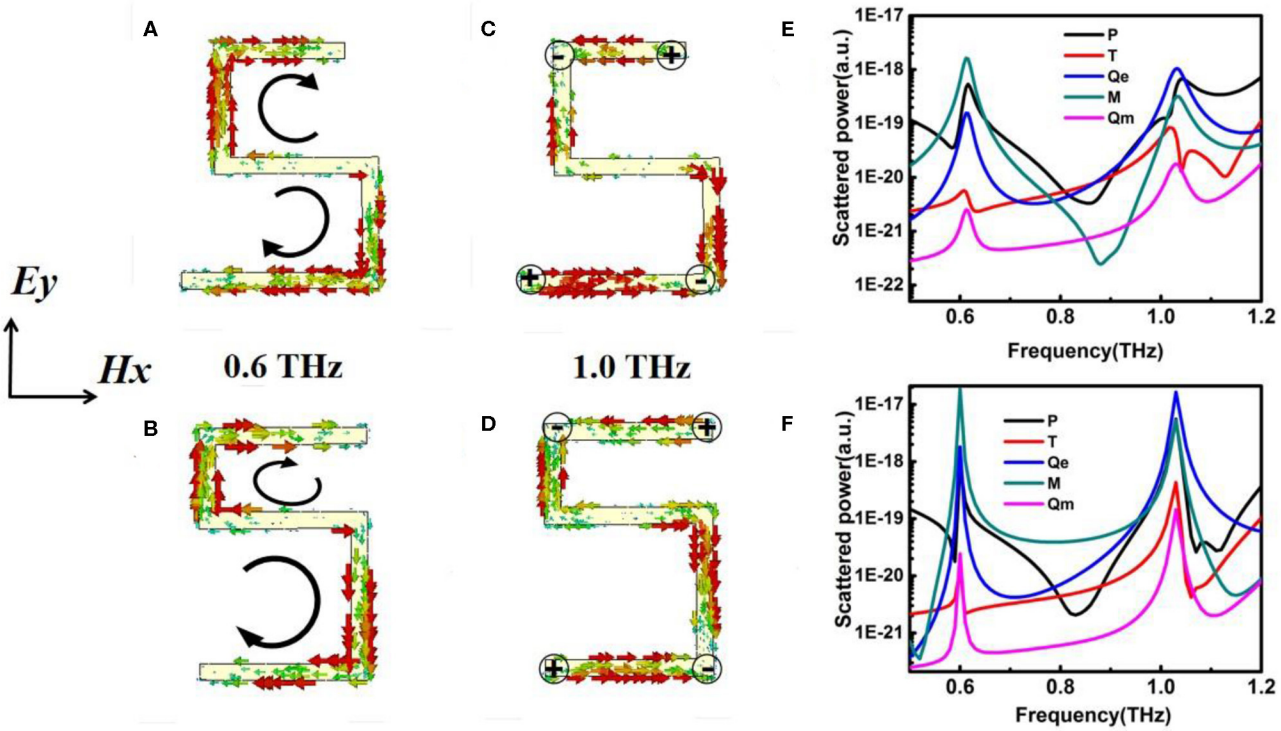

FIGURE 3 | Simulated current distributions at resonant frequencies of **(A)** 0.6 THz in Case I, **(B)** 0.6 THz in Case II, **(C)** 1.0 THz in Case I, **(D)** 1.0 THz in Case II. Multipole decomposition results of the scattering spectrum by using the Cartesian coordinate system for **(E)** Case I when $d = 20\,\mu$m and **(F)** Case II when $g = 20\,\mu$m, where P, M, T, Qe, and Qm represent the ED, MD, TD, EQ, and magnetic quadrupole (MQ), respectively.

EQ. Moreover, besides the EIT-like transparency window, a sharp Fano resonance appears at 0.6 THz that lies in the range of the broad ED resonance (**Figure 4A**) and coincides with the trapped MD resonance given in **Figure 2B** as well, which indicates that this Fano resonance is excited by optical coupling between the dark trapped MD and the bright ED mode. It is noteworthy that the large detuning between the bright ED (1.0 THz) and the trapped MD (0.6 THz) results in a Fano response rather than an EIT resonance; here, EIT is a special form of Fano resonance when the detuning between the two coupling bright and dark trapped modes is very small [20]. Furthermore, considering that Fano responses are related to the asymmetry of the structures, the transmission curves of the metasurface with different values of d are also calculated and shown in **Figure 4B**. As d decreases from 30 to 10 μm, the Q-values of the Fano resonance at 0.6 THz and EIT at 1.0 THz increase from 22 to 95, and from 12 to 54, respectively, but their central frequencies remain unchanged.

However, the results for the other asymmetric metasurface of Case II shown in **Figure 4C** are quite different from those for Case I. The broad ED resonance with its dip at 1.0 THz is clearly observed, but two much weaker Fano resonances respectively appeared at 0.6 and 1.0 THz for the large asymmetric value $g = 30\,\mu$m, and they can almost be neglected when $g = 10\,\mu$m. Considering that two much stronger trapped modes are excited in Case II compared to Case I (shown in **Figure 2**), we can conclude that the coupling path between the bright and dark trapped modes, which is related to the asymmetric structure, plays an important role in the excitation of the Fano resonances.

Moreover, the frequencies of the two Fano resonances of the proposed metasurface can be easily designed and tuned by enlarging or reducing the size of the S-shaped structure. For example, when doubling the size of the structure, the two resonance frequencies will reduce to be half of the original.

Fano Resonances Under Oblique Incidence

We also explore the characteristics of the two trapped modes and two Fano resonances under off-normal incidence in the symmetric and asymmetric Case I ($d = 20\,\mu$m) and Case II ($g = 20\,\mu$m) S-shaped metasurfaces. Two different types of incident field polarizations are considered as shown in **Figures 5A,B**, and for each case, there are two oblique incidences in both the E-plane (the plane containing vectors E and k) and the H-plane (the plane containing vectors H and k); here, E, H, and k stand for the electric field, magnetic field, and wave vector, respectively. The calculated transmissions of three different metasurfaces under the field polarization of **Figure 5A** at 15° incidence are presented in **Figures 5C,E**. We can see that two trapped modes are excited around 0.6 and 1.0 THz in all three metasurfaces in both E-plane and H-plane oblique incidences. Unlike the normal incidence, the excitation of the two dark trapped modes

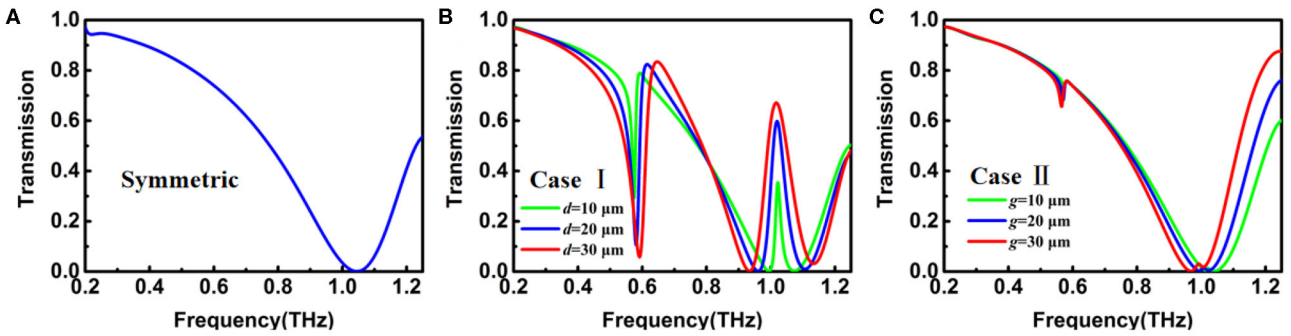

FIGURE 4 | Simulated transmission spectra for **(A)** symmetric S-shaped metasurface, **(B)** Case I with different values of *d*, **(C)** Case II with different values of *g*. The *E*-field of incident wave is polarized along the *x*-axis.

in the symmetric structure becomes possible under off-normal incidence, which can be simply explained by the structure being geometrically symmetric but optically asymmetric under oblique incidence. When the field polarization of **Figure 5B** is used, we find that the responses under *E*-plane oblique incidence shown in **Figure 5D** are close to transmissions at normal incidence (shown in **Figure 4**) (i.e., two strong Fano resonances appear at 0.6 and 1.0 THz, respectively, in Case I, but much weakened in Case II, and disappear in the symmetric structure).

However, under *H*-plane oblique incidence, **Figure 5F** shows that both strong Fano and EIT resonances can be excited in all three symmetric and asymmetric S-shaped metasurfaces, and the strengths of the resonances in Case I are the largest, the symmetric structure being second, and Case II third. Therefore, oblique incidence can not only make the excitation of the trapped mode possible even in symmetric metasurfaces, but can also enhance the coupling of the bright and trapped modes significantly as well.

EXPERIMENTAL RESULTS

In the fabrication of our metasurface, we used the purchased composite of a PET-aluminum film as the raw material. This type of commercial aluminum foil is very cheap and often used in common food packaging. Positive photoresist was spin-coated on the film and baked on a hot plate. After cooling to room temperature, the samples were exposed by laser direct writing with a spatial light modulator (DMD, Digital Micromirror Device). Finally, wet etching was carried out in a mixed acidic solution. **Figures 1D–F** are the microscope images of the three fabricated symmetric and asymmetric Case I ($d = 20\,\mu$m) and Case II ($g = 20\,\mu$m) S-shaped metasurfaces. The size of the samples is 1×1 cm. The transmission spectra of the samples at normal incidence were measured using a terahertz time-domain spectroscopy (THz-TDS) system under both *x*- and *y*-polarized incidences, a Gaussian focused beam was used as the THz source, and the spectral resolution is 10 GHz. The measured transmissions for the three samples are shown as black curves in **Figure 6**, and simulations are also shown as red curves for lossy PET (loss tangent = 0.05). From **Figures 6A–C**, the measured electric-LC resonance at ∼0.3 THz and ED resonance at ∼1.3 THz at the *y*-polarized incidence are clearly seen for all three samples and are in good agreement with the simulations. The measured two trapped modes are located at 0.6 and 1.0 THz for asymmetric samples (Case I and Case II) as the simulations predicted, the Q factor of the trapped mode at 0.6 THz (shown in **Figure 6C**) reaches up to over 50, but they are much weaker than those for lossless substrates as shown in **Figure 2**. Other reason for the differences between measured and simulated results is the limited sample size or effective unit cells of the structure in the measurements, in contrast to the infinite unit cells in the simulations, which impacts the high-Q resonance more than the low-Q resonance. In addition, the imperfect fabrication geometry will produce a small difference as well. As the metasurfaces are illuminated by the *x*-polarized wave, the measured transmissions in **Figure 6E** show a clear Fano resonance at 0.6 THz and an EIT at 1.0 THz in the asymmetric sample in Case I, but Case II (**Figure 6F**) shows a very weak Fano and no EIT, which are basically consistent with the simulation results. Thus, the two trapped modes and two Fano resonances in the asymmetric S-shaped metasurfaces have been verified experimentally.

CONCLUSION

In summary, we numerically and experimentally demonstrated double Fano resonances in simple S-shaped plasmonic metasurfaces in the terahertz spectral region. Transmissions of two types of asymmetric S-shaped structures were investigated under both normal and oblique incidences in the frequency range 0.2–1.4 THz. At normal incidence, apart from the electric-LC resonance at 0.3 THz and ED at 1.3 THz, two trapped modes at 0.6 and 1.0 THz are simultaneously excited in both the asymmetric structures, which are mainly attributed to the MD and the EQ, respectively. Furthermore, strong Fano and EIT resonances are achieved by coupling the two dark trapped modes with a broad ED in one asymmetric structure, but very weak resonances are observed for the other asymmetric structure. This indicates that the asymmetric structure plays an important role in the excitation of Fano resonances. Moreover,

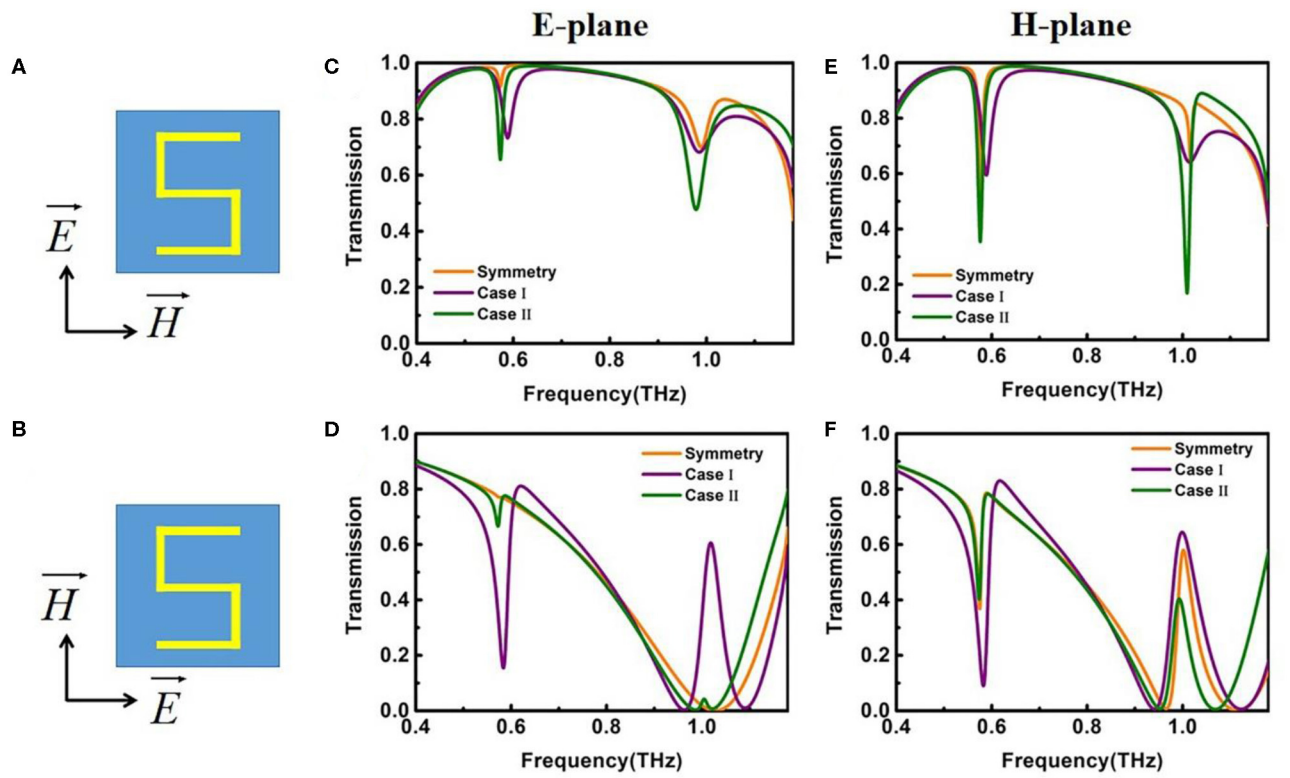

FIGURE 5 | (A,B) Incident field polarizations for three S-shaped metasurfaces. **(C–F)** Computed transmission spectra at oblique incidence of 15° in *E*-plane and *H*-plane, respectively. Here, $d = 20\,\mu$m, $g = 20\,\mu$m for Case I and Case II, respectively.

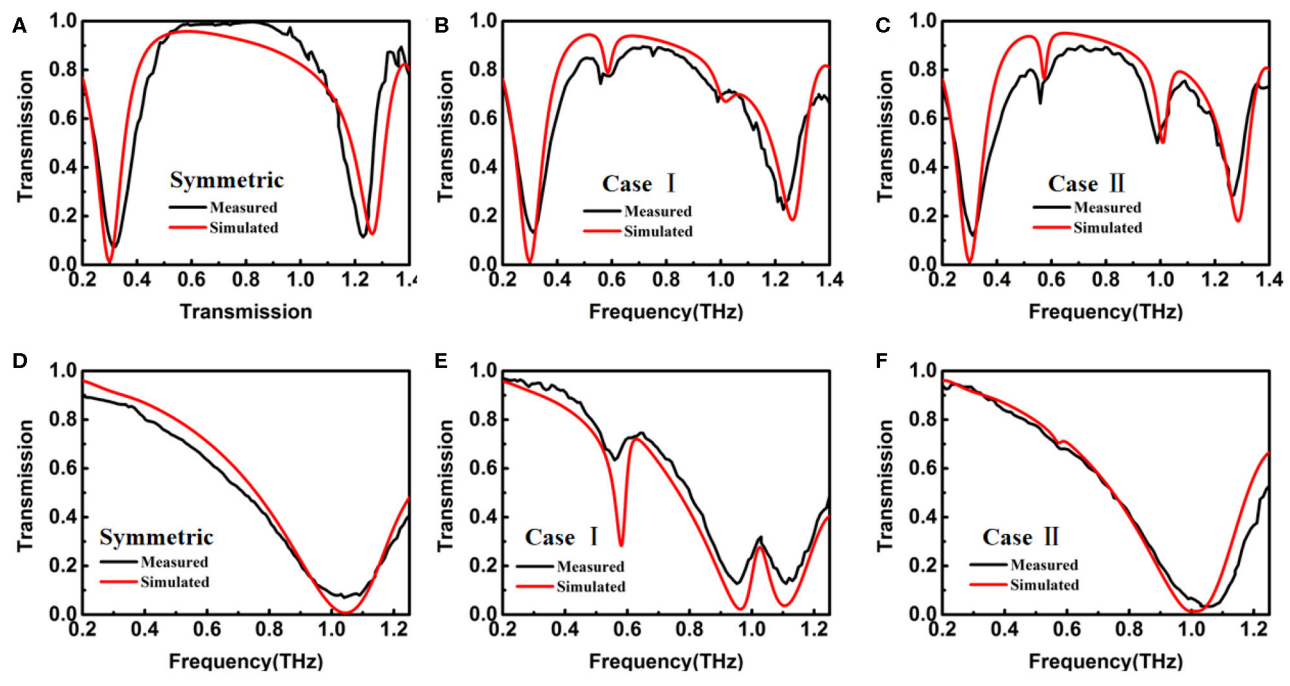

FIGURE 6 | Measured transmission spectra (black line) for **(A,D)**: symmetric metasurface; **(B,E)**: Case I; **(C,F)**: Case II. The *E*-field of the incident wave is polarized along **(A–C)**: the *y*-axis; **(D–F)**: the *x*-axis. Simulated curves (red line) are also given for the lossy substrate (loss tangent = 0.05).

at oblique incidence, strong Fano responses can be observed and greatly enhanced in both the asymmetric metasurfaces, and even for inversion symmetry, which is impossible at normal incidence. The results measured by THz-TDS for the fabricated symmetric and asymmetric structures are in good agreement with calculations. The proposed S-shaped plasmonic metasurfaces have wide applications in biochemical sensing, optical switching, and slow-light devices.

DATA AVAILABILITY STATEMENT

The original contributions presented in the study are included in the article/supplementary material, further inquiries can be directed to the corresponding author/s.

AUTHOR CONTRIBUTIONS

ZH was the leader of the work. ZH and WX wrote the manuscript. WX, CS, and JL were responsible for experiment setting. LC and FZ were mainly engaged in picture editing and related data processing. All authors have made positive contributions to the work.

ACKNOWLEDGMENTS

Natural Science Foundation of China (NSFC) (61875179) and Zhejiang Province (LY17F010010 and LGG19F050004); Primary Research and Development Plan of Zhejiang Province (2019C03114).

REFERENCES

1. Shelby RA, Smith DR, Schultz S. Experimental verification of a negative index of refraction. *Science.* (2001) **292**:77–9. doi: 10.1126/science.1058847
2. Valentine J, Zhang S, Zentgraf T, Ulin-Avila E, Genov DA, Bartal G, et al. Three-dimensional optical metamaterial with a negative refractive index. *Nature.* (2008) **455**:376–9. doi: 10.1038/nature07247
3. Schurig D, Mock JJ, Justice BJ, Cummer SA, Pendry JB, Starr AF, et al. Metamaterial electromagnetic cloak at microwave frequencies. *Science.* (2006) **314**:977–80. doi: 10.1126/science.1133628
4. Khorasaninejad M, Chen WT, Devlin RC, Oh J, Zhu AY, Capasso F. Metalenses at visible wavelengths: diffraction-limited focusing and subwavelength resolution imaging. *Science.* (2016) **352**:1190–4. doi: 10.1126/science.aaf6644
5. Yang S, Tang C, Liu Z, Wang B, Wang C, Li J, et al. Simultaneous excitation of extremely high-Q-factor trapped and octupolar modes in terahertz metamaterials. *Opt Express.* (2017) **25**:15938–46. doi: 10.1364/OE.25.015938
6. Fedotov VA, Rose M, Prosvirnin SL, Papasimakis N, Zheludev NI. Sharp trapped-mode resonances in planar metamaterials with a broken structural symmetry. *Phys Rev Lett.* (2007) **99**:147401. doi: 10.1103/PhysRevLett.99.147401
7. Singh R, Al-Naib IAI, Koch M, Zhang W. Asymmetric planar terahertz metamaterials. *Opt Express.* (2010) **18**:13044–50. doi: 10.1364/OE.18.013044
8. Abdeddaim R, Ourir A, Rosny J. Realizing a negative index metamaterial by controlling hybridization of trapped modes. *Phys Rev B.* (2011) **83**:033101. doi: 10.1103/PhysRevB.83.033101
9. Kabantsev AA, Driscoll CF, Hilsabeck TJ, O'Neil TM, Yu JH. Trapped-particle asymmetry modes in single-species plasmas. *Phys Rev Lett.* (2001) **87**:225002. doi: 10.1103/PhysRevLett.87.225002
10. Yang S, Liu Z, Xia X, E Y, Tang C, Wang Y, et al. Excitation of ultrasharptrapped-mode resonances in mirror-symmetric metamaterials. *Phys Rev B.* (2016) **93**:235407. doi: 10.1103/PhysRevB.93.235407
11. Mousavi SH, Kholmanov I, Alici KB, Purtseladze D, Arju N, Tatar K, et al. Inductive tuning of Fano-resonant metasurfaces using plasmonic response of graphene in the mid-infrared. *Nano Lett.* (2013) **13**:1111–7. doi: 10.1021/nl304476b
12. Wu C, Khanikaev AB, Adato R, Arju N, Yanik AA, Altug H, et al. Fano-resonant asymmetric metamaterials for ultrasensitive spectroscopy and identification of molecular monolayers. *Nat Mater.* (2011) **11**:69–75. doi: 10.1038/nmat3161
13. Chen CY, Un IW, Tai NH, Yen TJ. Asymmetric coupling between subradiant and superradiant plasmonic resonances and its enhanced sensing performance. *Opt Express.* (2009) **17**:5372–80. doi: 10.1364/OE.17.015372
14. Fedotov VA, Tsiatmas A, Shi JH, Buckingham R, Groot PD, Chen Y, et al. Temperature control of Fano resonances and transmission in superconducting metamaterials. *Opt Express.* (2010) **18**:9015–9. doi: 10.1364/OE.18.009015
15. Zhao W, Ju D, Jiang Y, Zhan Q. Dipole and quadrupole trapped modes within bi-periodic Silicon particle array realizing three-channel refractive sensing. *Opt Express.* (2014) **22**:31277–85. doi: 10.1364/OE.22.031277
16. Zhao T, Xiao H, Li Y, Yang J, Jia H, Ren G, et al. Independently tunable double Fano resonances based on waveguide-coupled cavities. *Opt Express.* (2019) **44**:3154–7. doi: 10.1364/OL.44.003154
17. Tuz VR, Novitsky DV, Mladyonov PL, Prosvirnin SL, Novitsky AV. Non-linear interaction of two trapped-mode resonances in a bilayer fish-scale metamaterial. *J Opt Soc Am B.* (2014) **31**:2095–103. doi: 10.1364/JOSAB.31.002095
18. Zheng X, Zhao Z, Peng W, Zhang J, Zhao H, Shi W. Tuning the terahertz trapped modes of conductively coupled Fano-resonators in reflectional and rotational symmetry. *Opt Mater Express.* (2018) **8**:105–18. doi: 10.1364/OME.8.000105
19. Tang X, Liu J, Zhang X, Zhu Y. Double trapped modes due to the hybridization effect in a composite meander wire array. *J Phys D Appl Phys.* (2014) **47**:265304. doi: 10.1088/0022-3727/47/26/265304
20. Born N, Al-Naib I, Jansen C, Ozaki T, Morandotti R, Koch M. Excitation of multiple trapped-eigenmodes in terahertz metamolecule lattices. *Appl Phys Lett.* (2014) **104**:101107. doi: 10.1063/1.4868420
21. Luk'yanchuk B, Zheludev NI, Maier SA, Halas NJ, Nordlander P, Giessen H, et al. The Fano resonance in plasmonic nanostructures and metamaterials. *Nat Mater.* (2010) **9**:707–15. doi: 10.1038/nmat2810
22. Papasimakis N, Fu YH, Fedotov VA, Prosvirnin SL, Tsai DP, Zheludev NI. Metamaterial with polarization and direction insensitive resonant transmission response mimicking electromagnetically induced transparency. *Appl Phys Lett.* (2009) **94**:211902. doi: 10.1063/1.3138868
23. Diao J, Han B, Yin J, Li X, Lang T, Hong Z. Analogue of electromagnetically induced transparency in an S-shaped all-dielectric metasurface. *Photon J IEEE.* (2019) **11**:4601110. doi: 10.1109/JPHOT.2019.2920433
24. Zhao W, Leng X, Jiang Y. Fano resonance in all-dielectric binary nanodisk array realizing optical filter with efficient linewidth tuning. *Opt Express.* (2015) **23**:6858–66. doi: 10.1364/OE.23.006858
25. Cao W, Singh R, Al-Naib IAI, He M, Taylor AJ, Zhang W. Low-loss ultra-high-Q dark mode plasmonic Fano metamaterials. *Opt Lett.* (2012) **37**:3366–68. doi: 10.1364/OL.37.003366
26. Dhouibi A, Nawaz Burokur S, Lupu A, Lustrac AD, Priou A. Excitation of trapped modes from a metasurface composed of only *Z*-shaped meta-atoms. *Appl Phys Lett.* (2013) **103**:184103. doi: 10.1063/1.4827880
27. Liu N, Weiss T, Mesch M, Langguth L, Eigenthaler U, Hirscher M, et al. Planar metamaterial analogue of electromagnetically induced transparency for plasmonic sensing. *Nano Lett.* (2010) **10**:1103–7. doi: 10.1021/nl902621d
28. Cong L, Manjappa M, Xu N, Al-Naib I, Zhang W, Singh R. Fano resonances in terahertz metasurfaces: a figure of merit optimization. *Adv Opt Mater.* (2015) **3**:1537–43. doi: 10.1002/adom.201500207
29. Wang J, Fan C, He J, Ding P, Liang E, Xue Q. Double Fano resonances due to interplay of electric and magnetic plasmon modes in planar plasmonic

structure with high sensing sensitivity. *Opt Express.* (2013) **21**:2236–44. doi: 10.1364/OE.21.002236
30. Zhang Q, Wen X, Li G, Ruan Q, Wang J, Xiong Q. Multiple magnetic mode-based fano resonance in split-ring resonator/disk nanocavities. *ACS Nano.* (2013) **7**:11071–8. doi: 10.1021/nn4047716
31. Yan Z, Wen X, Gu P, Zhong H, Zhan P, Chen Z, et al. Double Fano resonances in individual metallic nanostructure for high sensing sensitivity. *Nanotechnology.* (2017) **28**:475203. doi: 10.1088/1361-6528/aa8229
32. Le KQ, Alù A, Bai J. Multiple Fano interferences in a plasmonic metamolecule consisting of asymmetric metallic nanodimers. *J Appl Phys.* (2015) **117**:023118. doi: 10.1063/1.4905619
33. Moritake Y, Kanamori Y, Hane K. Demonstration of sharp multiple Fano resonances in optical metamaterials. *Opt Express.* (2016) **24**:9332–9. doi: 10.1364/OE.24.009332
34. Jung H, In C, Choi H, Lee H. Anisotropy modeling of terahertz metamaterials: polarization dependent resonance manipulation by meta-atom cluster. *Sci Rep.* (2014) **4**:5214. doi: 10.1038/srep05217
35. Chen H, Ran L, Huang J, Zhang X, Chen K. Left-handed materials composed of only S-shaped resonators. *Phys Rev E.* (2004) **70**:057605. doi: 10.1103/PhysRevE.70.057605
36. Nesimoglu T, Karaali M, Sabah C. Tuning the electric resonance of a metamaterial based single-sided S-Shaped resonator. In: *20th International Conference on Microwaves, Radar, and Wireless Communications*. Gdansk, Poland (2014). doi: 10.1109/MIKON.2014.6899923
37. Basharin AA, Kafesaki M, Economou EN. Dielectric metamaterials with toroidal dipolar response. *Phys Rev X.* (2015) **5**:011036. doi: 10.1103/PhysRevX.5.011036
38. Radescu EE, Vaman G. Exact calculation of the angular momentum loss, recoil force, and radiation intensity for an arbitrary source in terms of electric, magnetic, and toroid multipoles. *Phys Rev E.* (2002) **65**:046609. doi: 10.1103/PhysRevE.65.046609
39. Han B, Li X, Sui C, Diao J, Jing X, Hong Z. Analog of electromagnetically induced transparency in an E-shaped all-dielectric metasurface based on toroidal dipolar response. *Opt Mater Express.* (2018) **8**:2197–207. doi: 10.1364/OME.8.002197
40. Savinov V, Fedotov VA, Zheludev NI. Toroidal dipolar excitation and macroscopic electromagnetic properties of metamaterials. *Phys Rev B.* (2014) **89**:205112. doi: 10.1103/PhysRevB.89.205112

Conflict of Interest: The authors declare that the research was conducted in the absence of any commercial or financial relationships that could be construed as a potential conflict of interest.

frontiers in Physics

ORIGINAL RESEARCH
published: 12 August 2020
doi: 10.3389/fphy.2020.00306

Graphene-Assisted Narrow Bandwidth Dual-Band Tunable Terahertz Metamaterial Absorber

Dexian Yan [1,2,3], Miao Meng [1,2], Jiusheng Li [1,2] and Xiangjun Li [1,2]*

[1] Key Laboratory of Electromagnetic Wave Information Technology and Metrology of Zhejiang Province, College of Information Engineering, China Jiliang University, Hangzhou, China, [2] Centre for THz Research, China Jiliang University, Hangzhou, China, [3] State Key Laboratory of Crystal Materials, Shandong University, Jinan, China

A tunable graphene terahertz metamaterial absorber is designed by treating a monolayer continuous dumbbell-shaped structure graphene layer, which can simultaneously realize the narrow bandwidth and dual-band absorption with transverse magnetic (TM) polarization and wide incident angle operation. Two pronounced absorption peaks are caused by the novel toroidal dipole phenomenon and magnetic plasmon polariton. By optimizing the geometry parameters, the relative narrow bandwidths of the two absorption peaks are 26.4 and 23.5 GHz at frequencies of 0.2242 THz and 0.5302 THz, respectively, with the absorption rate above 99.6%. Since the continuous dumbbell-shaped graphene structure is treated in the absorber, a more convenient way to realize the tuning ability by treating a bias voltage compared to the absorbers with discrete graphene structures. The designed device can work at a wide incident angles (up to 80°) under TM polarization with the absorption above 88% at low frequency. The simulation results are basically in good agreement with the results of the equivalent circuit model. This work offers huge potential applications in terahertz imaging, detecting and sensing, especially in the 6G communication systems.

Keywords: terahertz absorber, narrow bandwidth, toroidal dipole, graphene, terahertz communication

OPEN ACCESS

Edited by:
Haiyong Gan,
National Institute of Metrology, China

Reviewed by:
Somak Bhattacharyya,
Indian Institute of Technology (BHU), India
Guangsheng Deng,
Hefei University of Technology, China
Li-an Bian,
Changsha University of Science and Technology, China

****Correspondence:***
Dexian Yan
yandexian1991@cjlu.edu.cn

Specialty section:
This article was submitted to Optics and Photonics, a section of the journal Frontiers in Physics

Received: *26 April 2020*
Accepted: *03 July 2020*
Published: *12 August 2020*

Citation:
Yan D, Meng M, Li J and Li X (2020) Graphene-Assisted Narrow Bandwidth Dual-Band Tunable Terahertz Metamaterial Absorber. Front. Phys. 8:306. doi: 10.3389/fphy.2020.00306

INTRODUCTION

The standardization of fifth generation (5G) communications has been finished, and the 5G network will be built into commercial applications in 2020. Based on the above fact, the outlook and development plan of 6G communications has been put on the agenda, laying a foundation for the new generation of communication systems for future needs of the 2030s [1]. The terahertz band ranged from 0.1 to 10 THz is referred to as a gap region located between the microwave and optical spectra. Because of its huge application potential in communication, biomedical imaging, security, and so on, terahertz technology has caught increasing attention in recent years.

The pivotal problem influencing the actual application in hybrid terahertz/free-space-optical systems expected to be implemented in 6G frequency band is the shortage of functional devices with outstanding characteristics. This is mainly caused by the shortage of the materials in nature that can directly interact with terahertz waves. To overcome this problem, an artificial composite material containing periodically arranged structural units named metamaterial is proposed and investigated. Different from nature materials, by designing the resonant unit structure, the metamaterial can provide some abnormal electromagnetic characteristics, including negative refractive index [2], invisibility [3], perfect absorption [4] and electromagnetic induced transparency [5]. Based on

their unique electromagnetic characteristics, metamaterial has been applied in terahertz function devices, including sensors [6, 7], modulators [8], filters [9], and switches [10].

Metamaterial absorbers showcase huge application value in communication, security, detection and other fields, and have increasingly become one of the study hotspots in terahertz region [11–20]. Landy et al. reported a metamaterial absorber with perfect absorption characteristics for the first time [21]. Since then, various metamaterial absorbers operating in various frequency regions were achieved, from microwave to infrared range [22–24]. In terahertz region, Tao et al. demonstrated the first narrowband absorber [25]. Therefore, dual-band and multi-band terahertz absorbers were put forward continuously. For the proposed absorbers, the characteristics have been realized on the basis of the geometry structures, which restrict their practical applications. There is an urgent need to actively modulate and control the metamaterial absorbers by applying heat, electric field, magnetic field and optical field.

In recent years, researchers have treated some functional material to design tunable terahertz metamaterial absorbers. Yin et al. showed a terahertz tunable dual-band metamaterial absorber by employing the liquid crystal material [26]. Liu et al. proposed a thermally tunable broadband terahertz metamaterial absorber on the basis of the mixed VO_2 [27]. Caused by the excellent transition characteristics of VO_2 material, the maximum tuning range of the designed device can be changed from 5 to 100% by treating an external thermal field. Zhang et al. designed a tunable metamaterial terahertz absorber treating 3D Dirac semimetal films (DSF) [28]. The operating characteristics of the DSF absorber can be dynamically tuned by changing the Fermi level instead of structure geometry parameters. Recently, they also reported a tunable broadband metamaterial sandwich-structured terahertz absorber containing black phosphorous and vanadium dioxide [29]. The dynamical tuning operation of the broadband absorption is resulted from the variation of the electron doping of black phosphorous and conductivity of

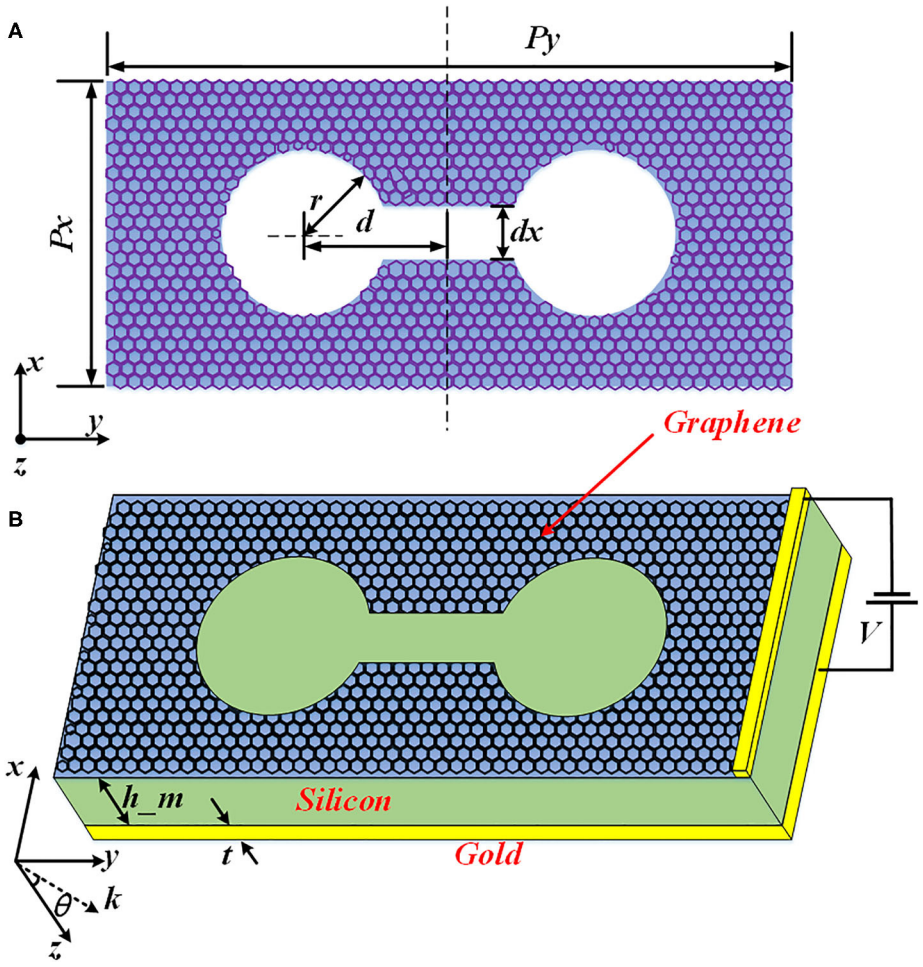

FIGURE 1 | (A) Structure of the dumbbell-shaped graphene layer; **(B)** Schematic of the designed terahertz perfect absorber, including a top layer of continuous graphene metasurface, a middle layer of the silicon dielectric layer, and a metal gold plate. Geometry parameters here: $Px = 200\,\mu m$, $Py = 450\,\mu m$, $r = 55\,\mu m$, $d = 95\,\mu m$, $dx = 35\,\mu m$, $h\_m = 50\,\mu m$, and $t = 0.2\,\mu m$.

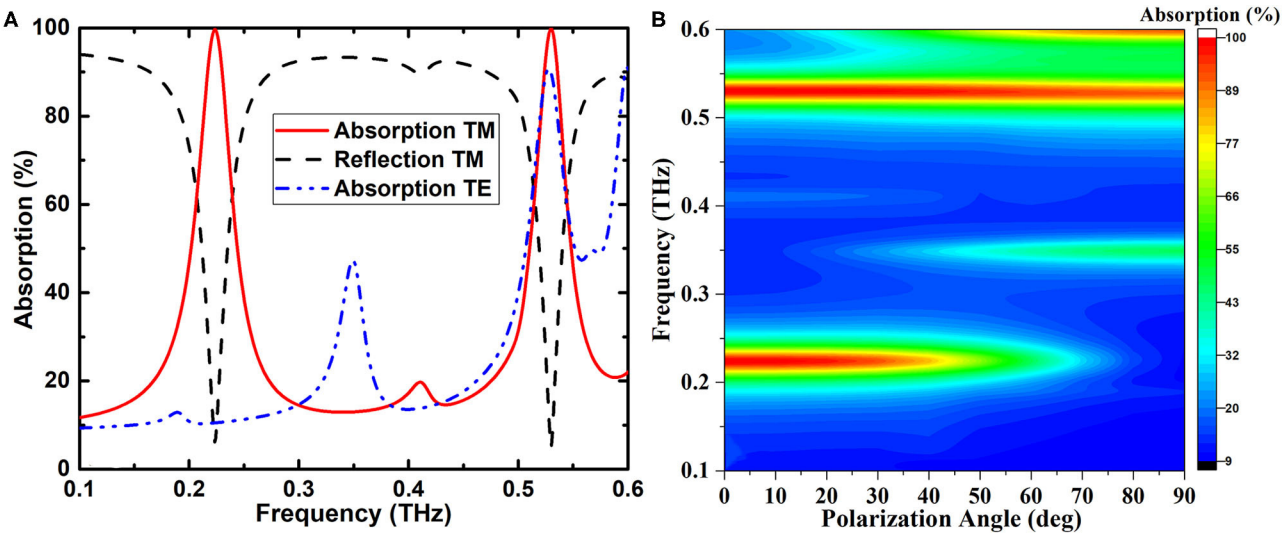

FIGURE 2 | (A) Absorption and reflection of the dual-band absorber. **(B)** Relationship between the absorption and the terahertz frequency with different polarization angles φ changing from 0° to 90°.

VO_2. Huang et al. designed a metamaterial absorber based on temperature variation that contains a periodic array of metal circle resonators with strontium titanate [30]. Gu et al. designed and fabricated a new kind of Salisbury screen absorber formed by DAST crystalline films [31]. The terahertz response of the absorber can be adjusted by changing the thickness of the DAST film and the spacer. On the other hand, graphene-assisted switchable liquid crystal terahertz metamaterial absorber was reported by Wang et al. [32]. However, the limitation of the tuning range of the material constitutive parameters will restrict the realization of the narrow band absorption performance.

How to obtain tunable narrow-bandwidth dual-band absorption is a hot research topic in graphene-based metamaterial absorber. One way to realize the multiband absorbers is to use multi-resonator structures in one unit cell [33, 34]. Another way is to superimpose the multi-layered graphene structures with different geometric sizes [35]. Although the characteristics of the tunable dual-band absorption are ideal, however, the bandwidths of the absorption peaks are wide and cannot satisfy the narrow-bandwidth requirements in 6G or terahertz communication systems. It is a very difficult task to combine the two properties of dual-band and narrow bandwidth with simple manufacturing process.

Motivated by the previous studies, in this work, a dual-band tunable metamaterial absorber with narrow bandwidth in the terahertz region is designed by using a simple sandwich structure. The absorber is formed by a dumbbell-shaped monolayer graphene metasurface layer and a gold ground plane, and the two layers are separated by a silicon layer. The theoretical and numerical investigation on the internal mechanism of narrow-bandwidth dual-band tunable absorber are performed based on CST Microwave Studio and equivalent circuit model. The absorption characteristics of the designed metamaterial absorber are analyzed by optimizing different parameters of graphene geometry, substrate thickness, and incident angle of terahertz wave. The results demonstrate that the absorption can reach 99.62 and 99.76% at 0.2242 and 0.5302 THz with the extreme narrow bandwidths as low as 26.4 and 23.5 GHz, respectively. The designed absorber offers dual-band absorption, high absorptivity, polarization-sensitivity and wide incident angles. In addition, the tenability of the terahertz absorptivity and the absorption peaks can be achieved conveniently by changing the bias voltages.

STRUCTURAL DESIGN AND RESEARCH TECHNIQUES

The unit cell of the dumbbell-shaped graphene structure metamaterial absorber is depicted in **Figure 1**. The metamaterial structure used in this paper is formed by a planar array of continuous graphene structure suspended in a rectangular dielectric silicon layer and a metal ground plane. The structure of the graphene layer is a dumbbell shape and aligned with *y*-axis (see **Figure 1**). The detailed geometric parameters are defined in the caption of **Figure 1A**. As shown in **Figure 1B**, the graphical graphene periodic array is fabricated on top of silicon layer. The voltage V between the gold plate and the metal electrode is used to change the chemical potential of graphene. The excitation signal is a linear polarized plane wave with transverse magnetic (TM) polarization transmitting along the *z* direction. At resonance, the normal incident plane wave radiation, polarized along *x*-axis, will cause dipole effects along *x*-axis, as depicted in **Figure 1**. These excitations will couple with the free-space radiation and result in the absorption characteristics of the metamaterial structure [36]. The dielectric material used in this paper is lossless silicon with relative permittivity $\varepsilon_r = 11.9$ [37, 38]. Gold is treated as the ground plane with conductivity $\sigma_{gold} = 4.561 \times 10^7$ S/m [38]. The thickness of the graphene layer can be set as $h\_g = 1$ nm. Other parameters

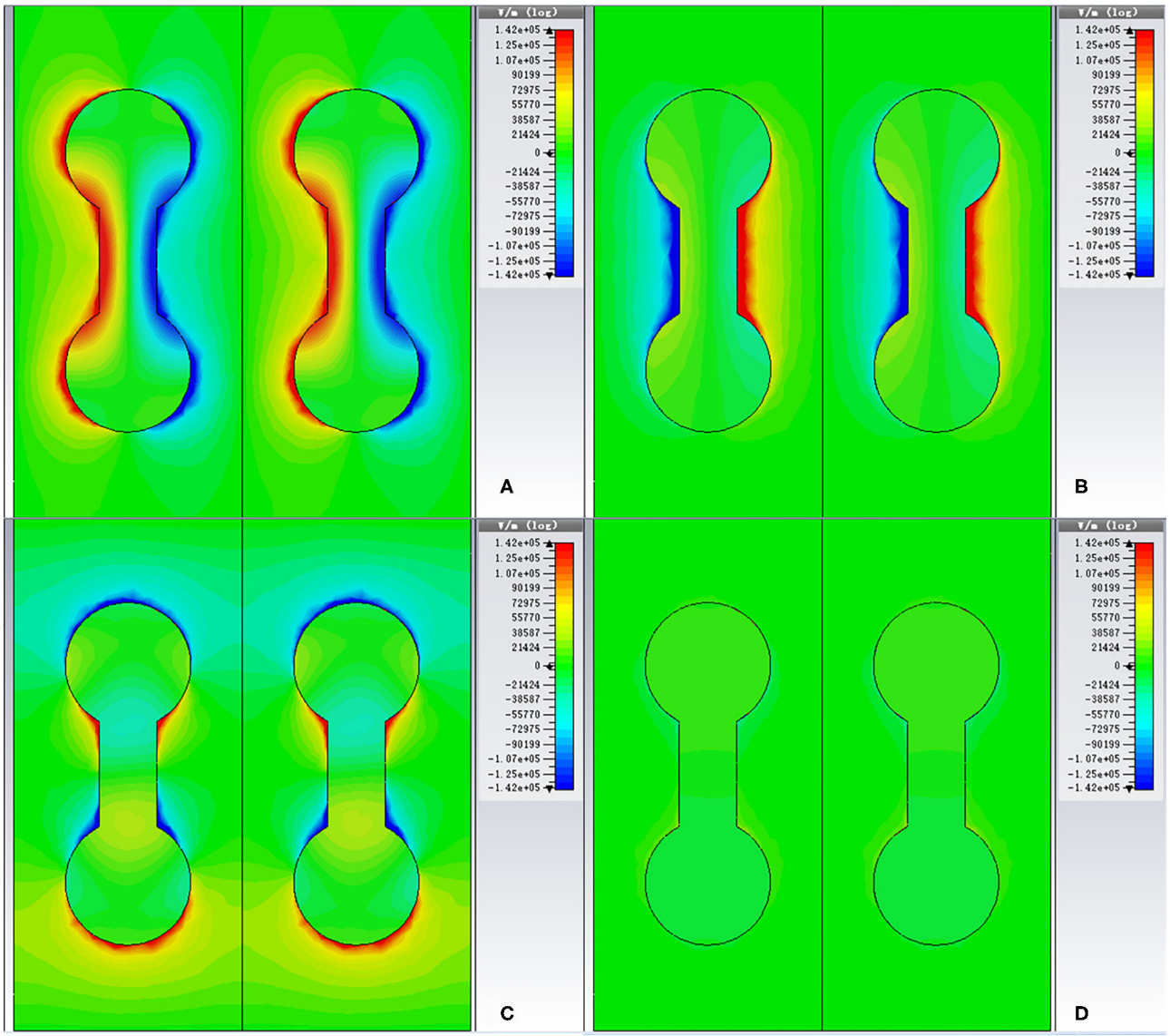

FIGURE 3 | Induced electric field distributions of the dumbbell-shaped graphene absorber for different modes: **(A)** TM for 0.5302 THz; **(B)** TM for 0.2242 THz; **(C)** TE for 0.5302 THz; **(D)** TE for 0.2242 THz.

are listed as follow: $r = 55\,\mu\text{m}$, $d = 95\,\mu\text{m}$, $dx = 35\,\mu\text{m}$, $h\_m = 50\,\mu\text{m}$, $t = 0.2\,\mu\text{m}$, $Px = 200\,\mu\text{m}$ and $Py = 450\,\mu\text{m}$.

The permittivity of the graphene can be expressed as [39]:

$$\varepsilon = 1 + j\frac{\sigma(\omega)}{\varepsilon_0 \omega t_g} \tag{1}$$

where ω defines the terahertz frequency, t_g represents the thickness of the graphene layer, ε_0 denotes the permittivity of vacuum. Surface conductivity of graphene $\sigma(\omega) = \sigma_{\text{intra}}(\omega) + \sigma_{\text{inter}}(\omega)$ can be obtained on the basis of the Kubo formula [5], containing the interband and intraband transition contributions. In terahertz frequencies, the interband transitions can be neglected caused by the Paili Exclusion Principle, and at room temperature ($T = 300\,\text{K}$), the Kubo formula can be expressed by a Drude-like expression [40, 41]:

$$\sigma(\omega) = \frac{e^2 \mu_c}{\pi \hbar^2} \cdot \frac{j}{\omega + j\tau^{-1}} \tag{2}$$

where e is the electron charge, and $\hbar$ represents the reduced Planck constant. μ_c denotes the chemical potential. The carrier relaxation time $\tau = \mu\mu_c/(ev2\,\text{f})$ [42], where v_f denotes the Fermi velocity (the value is 10^6 m/s here). μ represents the carrier mobility., which relies mainly on the fabrication method. Higher carrier mobility higher than 10,000 $\text{cm}^2/(\text{Vs})$ was achieved for graphene grown by chemical vapor deposition (CVD) [43]. Also, the mobility in excess of 200,000 $\text{cm}^2/(\text{Vs})$

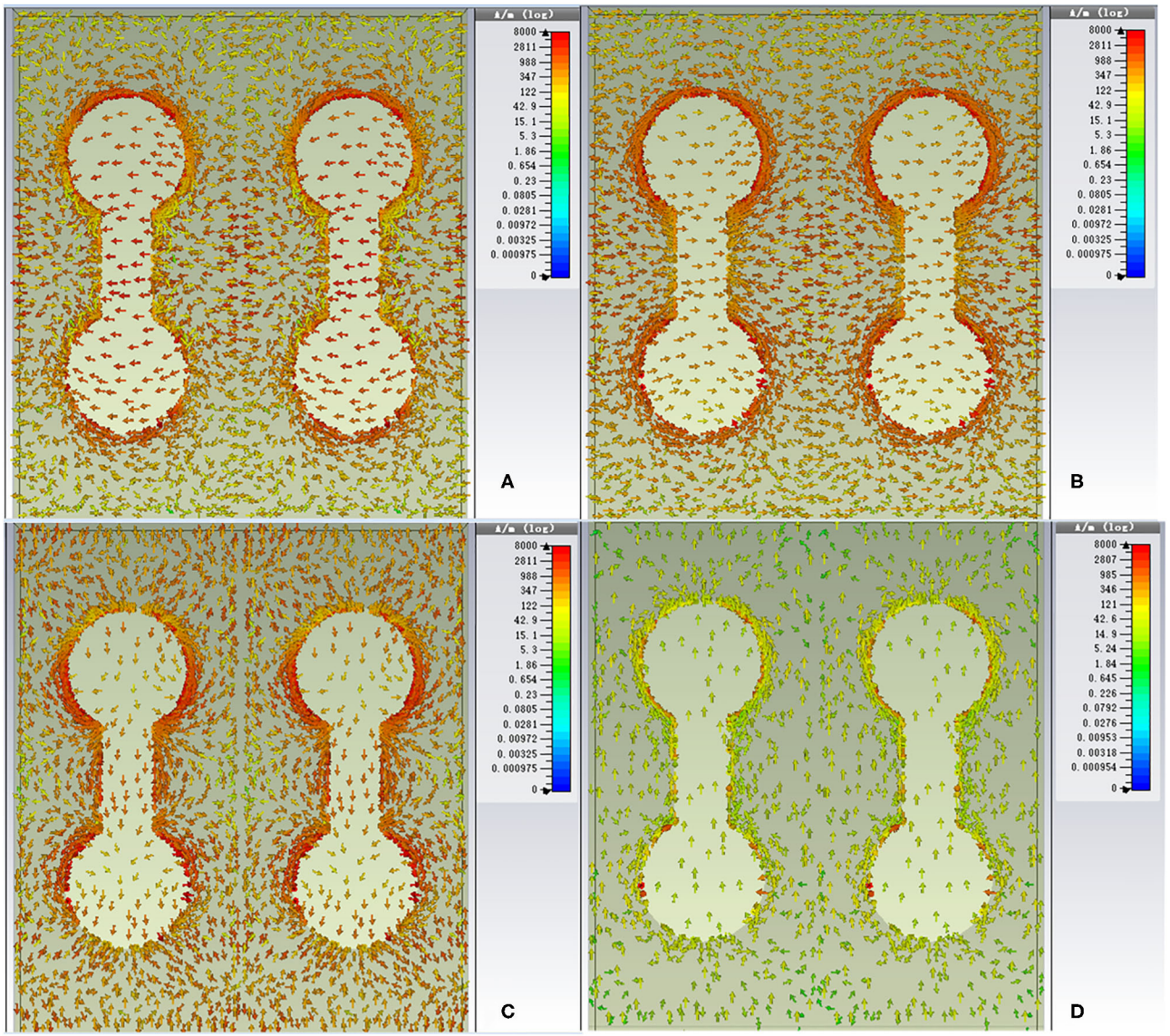

FIGURE 4 | Induced surface current distributions of the dumbbell-shaped graphene absorber for different modes: **(A)** TM for 0.5302 THz; **(B)** TM for 0.2242 THz; **(C)** TE for 0.5302 THz; **(D)** TE for 0.2242 THz.

was obtained experimentally based on suspended monolayer graphene [44]. In view of the feasibility of practical applications, an appropriate mobility of 10,000 $cm^2/(Vs)$ could be assumed in our design. Recently, by fabricating the graphene layer on hexagonal Boron nitride (h-BN) substrate, the high mobility of 50,000 $cm^2/(Vs)$ was realized at room temperature based on CVD method, and the carrier mobility increased to 300,000 $cm^2/(Vs)$ at ultralow temperature [45]. h-BN has no dangling bonds and its atomic structure is flat. Also, h-BN can provide a much less amount of charge traps than silicon dioxide [46]. In addition, it shows a minor lattice mismatch with graphene. Thus, a monolayer graphene manufactured on h-BN demonstrates the tendency to provide a much higher mobility.

Numerical simulations are investigated based on the commercial software CST Microwave Studio [47]. The frequency domain solver is treated in simulation to calculate the reflection coefficient $|S_{11}|$ and the transmission coefficient $|S_{21}|$. Open boundary condition is set in the z direction and unit cell boundary conditions are used in the x and y directions. Adaptive tetrahedral mesh refinement is adopted to improve the simulation accuracy. The absorption of the metamaterial structure can be calculated by the expression $A = 1-|S_{21}|^2-|S_{11}|^2$, where the transmission $|S_{21}|^2$ can be neglected since the gold plate prevents the terahertz wave from going through the absorber. In the simulation, the electric field of terahertz wave paralleled to the x axis is defined the TM polarization while the electric field paralleled to the y axis is TE polarization.

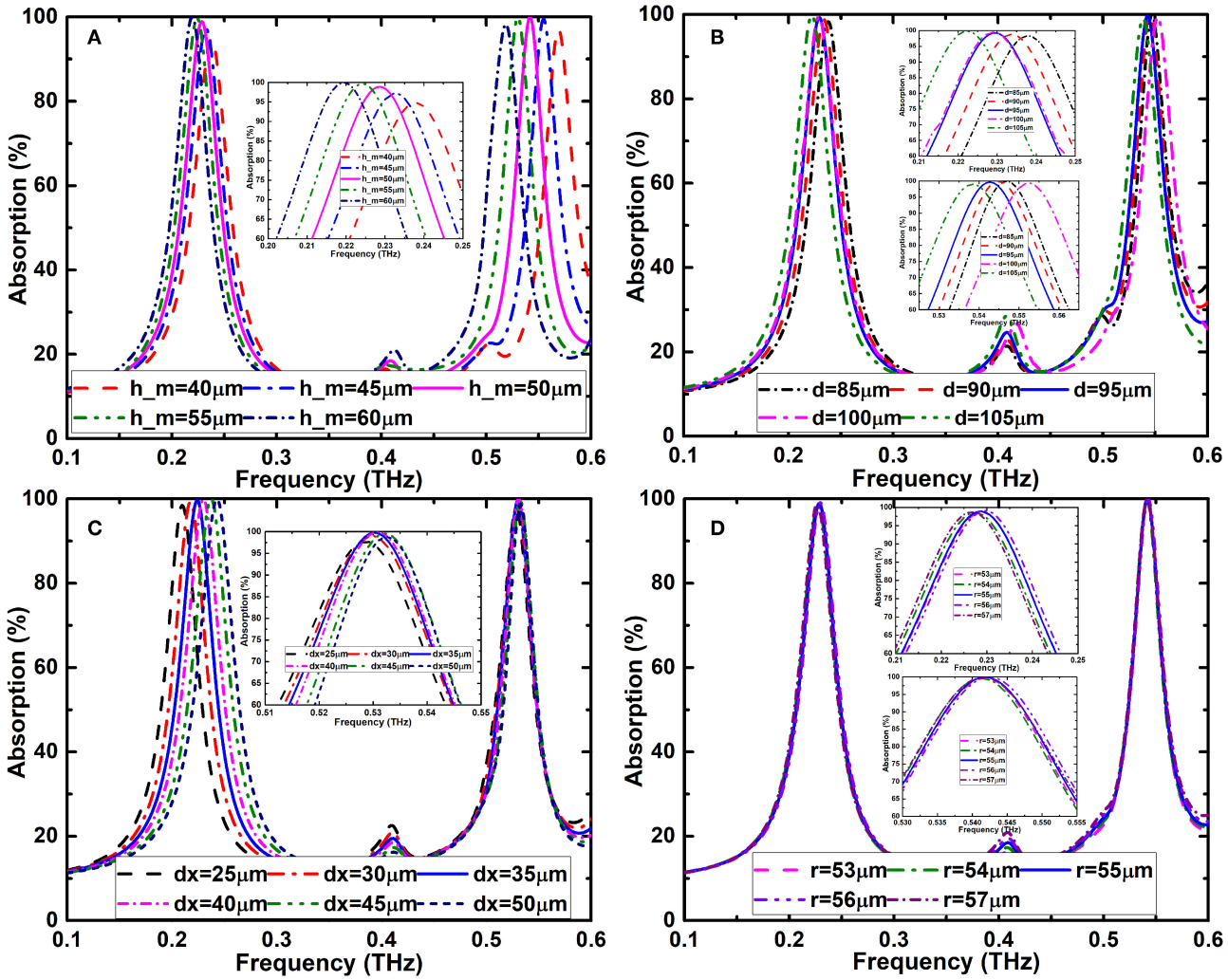

FIGURE 5 | Absorption spectra under **(A)** different dielectric layer thickness *h_m* when $d = 95\,\mu m$, $dx = 35\,\mu m$, $r = 55\,\mu m$; **(B)** different distance *d* when $h\_m = 50\,\mu m$, $dx = 35\,\mu m$, $r = 55\,\mu m$; **(C)** different width *dx* when $h\_m = 50\,\mu m$, $d = 95\,\mu m$, $r = 55\,\mu m$; **(D)** different radius *r* when $h\_m = 50\,\mu m$, $d = 95\,\mu m$, $dx = 35\,\mu m$.

RESULTS AND DISCUSSION

The absorption characteristics of the designed dumbbell-shaped dual-band metamaterial absorber at normal incidence for TM polarization illustrate in **Figure 2A**. The red and black curves indicate the absorption and reflection of the TM polarization, respectively. Because the continuous gold plate is placed on the bottom of the absorber, the transmittance of the absorber is zero. The blue line denotes the absorption of TE polarization. For the two absorption peaks of TM polarization, the maximum absorptions are 99.62 and 99.76% at frequencies of 0.2242 and 0.5302 THz with the excellent narrow bandwidths as low as 26.4 and 23.5 GHz, respectively. The color map shown in **Figure 2B** reveals the relationship between the absorption and the terahertz frequency with different polarization angles φ changing from 0° to 90° with a step of 5°. The characteristic of the two absorption peaks is changed over the interested frequency as the polarization angle φ changing. This result reveals the polarization-dependent characteristic of the absorption at normal incidence.

In order to furtherly figure out the physical origin of dual-band absorption characteristic, the electric field at absorption peaks of 0.2242 THz and 0.5302 THz with TM- and TE-polarizations are given in **Figure 3**. The physical mechanism of the dual-band perfect absorber designed in this paper has relation to the electric dipole resonance in dumbbell-shaped structure array, which is attributed to the local surface plasmon resonance and magnetic dipolar resonance between the graphene microstructure and the gold plate [34]. For TM polarization, as depicted in **Figures 3A,B**, the physical mechanism of the two absorption peaks is different. In **Figure 3A**, when the resonant frequency is 0.5302 THz, the induced electric fields concentrate mostly around the edges of the graphene dumbbell-shaped metasurfaces. In this case, charges with opposite polarity will store up at the left and right halves of each graphene

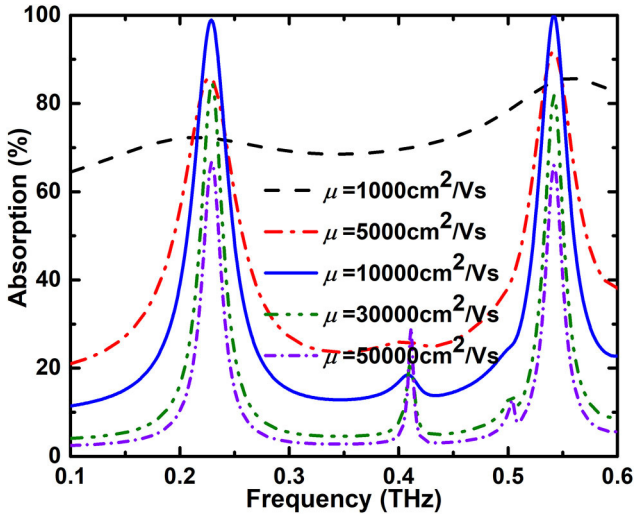

FIGURE 6 | Absorption spectra of the dual-band absorber with different values of μ from 1,000 to 50,000 cm^2/(Vs) with $\mu_c = 1$ eV.

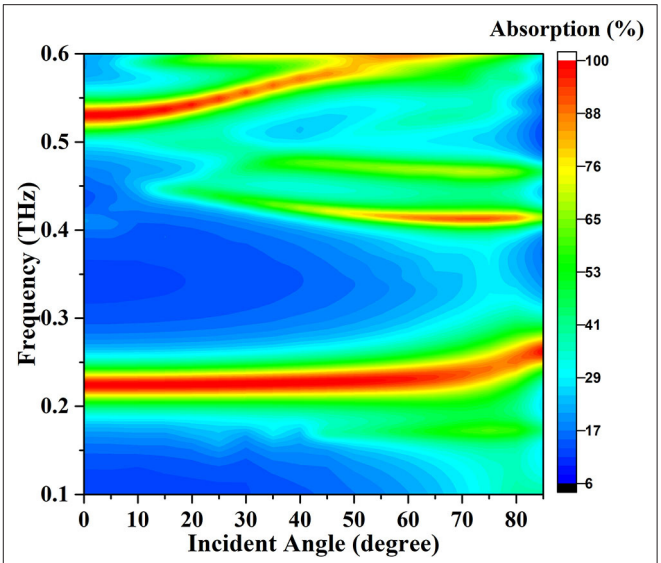

FIGURE 8 | Absorption spectra for the designed perfect absorber with different frequencies and incident angles for TM polarization.

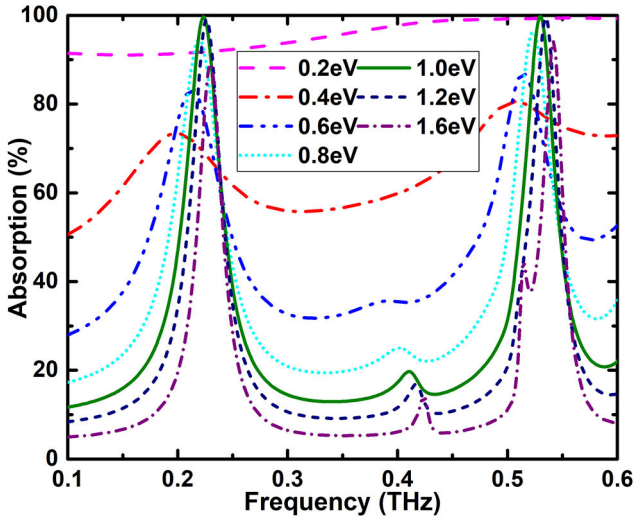

FIGURE 7 | Relationship between the absorptivity and frequency with different chemical potentials from 0.2 to 1.6 eV.

microstructure along the *x* direction, resulting in the capacitive properties [38]. The surface current distributions of the absorber at the resonant frequencies are also given in **Figure 4** to explain the resonance type. At the resonant frequency of 0.5302 THz (given in **Figure 4A**), the direction of surface currents of the dumbbell-shaped graphene layer is opposite to the surface currents direction of the gold ground plane. The resonance type at absorption peak of 0.5302 THz can be deemed to the magnetic plasmon excitation. When the frequency is 0.2242 THz, as depicted in **Figure 3B**, the excited electric fields mainly concentrate at the edges of the middle part of the dumbbell-shaped graphene layer. As depicted in **Figure 4B**, when the resonant frequency is 0.2242 THz for TM polarization, the opposite circular displacement currents surround the two ends of the dumbbell-shaped structure simultaneously. Two magnetic fields with different directions along the *z* direction will be excited by the two ring currents. The excited magnetic fields show low radiation characteristics and will generate a circular magnetic moment perpendicular to the graphene layer. Thus, the head-to-tail connection magnetic moment results in the toroidal dipole moment in the *x* direction [36, 48]. With the above discussion, the absorption peak at the resonant frequency of 0.2242 THz is caused by the toroidal dipole phenomenon in the dumbbell-shaped graphene layer. The detail investigation about the toroidal dipole will be reported in our future work. For the terahertz wave with TE polarization, since no resonant mode is excited at the frequency around 0.2 THz, there is no absorption peak appears around 0.2 THz in the absorption spectrum shown in **Figure 2**.

The impact of various geometry parameters of the absorber on the absorption performances are investigated. The absorption spectra of the designed dumbbell-shaped narrow bandwidth metamaterial absorber with different silicon substrate thickness *h_m*, distance *d*, width *dx* and radius *r* in frequency band of 0.1–0.6 THz, are shown in **Figure 5**. **Figure 5A** demonstrates that the thickness variation of the silicon layer will slightly influence the absorption rate and the shift of the resonant peak simultaneously. When the thickness of the silicon layer (*h_m*) increases from 45 to 60 μm, the two absorption peaks depicts red-shift. Also, the absorption around peak frequency of 0.22 THz increases gradually and the absorption around peak of 0.53 THz increases first and then decreases. As given in **Figure 5B**, the change of the distance *d* between the two circles demonstrates a slight impact on the absorption rete and shift of the two absorption peaks. When *d* increases from 85 to 105 μm, the two absorption peaks exhibit red-shift. However, the absorption

TABLE 1 | Comparisons between the designed absorber and the reported results.

References	Operation frequency	Absorption	Bandwidth (Fraction)	Graphene structure
Tao et al. [25]	4.95 & 9.2 THz	99 &99%	–	Graphene sheet separated by SiO_2 layers and graphene ribbon
Wang et al. [28]	0.512 & 1.467 THz	98 & 98%	>100 GHz (19.5%)	Graphene metasurface
Wang et al. [29]	0.94 & 2.69 THz	80 & 80%	934 & 839 GHz (99.4 & 31.2%)	Nonstructural graphene
Qi et al. [39]	0.69 & 2.21 THz	90 & 90%	300 & 160 GHz (43.5 & 7.2%)	A cross-elliptical graphene pattern
Wang et al. [50]	7.1 & 10.4 THz	99 & 99%	>100 GHz (1.4%)	Five separated graphene circles
Zhang et al. [51]	1.12 & 1.24 THz	95 & 90%	100 GHz (8.9%)	Graphene patch array
He et al. [52]	1.512 & 1.537 THz	99 & 99%	60 GHz (4%)	Two graphene circle elements
Deng et al. [53]	6.42 & 8.37 THz	98.5 & 99.1%		Gold resonator-Graphene-SiO_2-Gold
Here	0.2242 & 0.5302 THz	99.62 & 99.76%	26.4 & 23.5 GHz (11.8 & 4.4%)	Dumbbell-shaped continuous structure

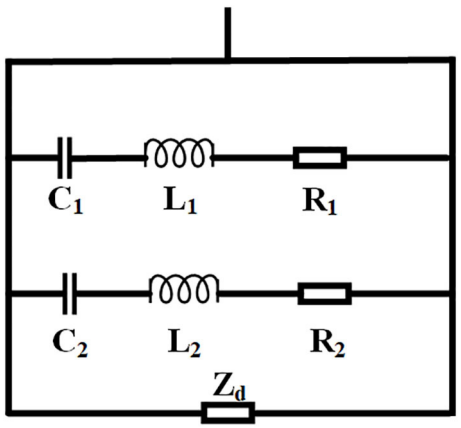

FIGURE 9 | Equivalent circuit model of designed dumbbell-shaped dual-band graphene absorber.

peak around 0.53 THz with $d = 100\,\mu m$ doesn't satisfy the red-shift rule. **Figure 5C** depicts that as the width dx increasing from 25 to 50 μm, the resonant peak around 0.22 THz shows blue-shift, while the resonant peak around 0.53 THz is almost unchanged. As depicted in **Figure 5D**, when the radius r of the circles changes, the two absorption peaks are almost unchanged. Based on the above parameters analysis, the optimal geometrical parameters are concluded as follows: $d = 95\,\mu m$, $dx = 35\,\mu m$, $r = 55\,\mu m$ and $h\_m = 50\,\mu m$.

The influence of carrier mobility μ of graphene on the operation performance of the designed dual-band metamaterial absorber is demonstrated. Based on the discussion given in section Methods, when the chemical potential is fixed at $\mu_c = 1$ eV, the absorption spectra of the absorber with different values of μ changing from 1,000 $cm^2/(Vs)$ to 50,000 $cm^2/(Vs)$are discussed and given in **Figure 6**. The change of μ doesn't affect the location of the absorption peak. When the carrier mobility μ is higher, the absorption decreases caused by the higher loss. On the contrary, the absorption peaks become more non-significant with the increase of μ, and the absorption of the two absorption peaks decreases.

For the graphene-based terahertz devices, one of the major merits is the dynamic tenability that the traditional devices cannot provide. The optical characteristics of the designed graphene absorber can be manipulated by changing the chemical potential μ_c of graphene instead of reconstructing the physical structure. In this paper, the electric tuning can be obtained by applying a bias voltage since the dumbbell-shaped graphene structure of the design absorber is continuous. The continuous graphene structure has the advantage of being easy to manufacture. The variation of the graphene chemical potential can be realized based on the adjustment of the voltage between the electrode and the ground plane. **Figure 7** depicts the absorption spectra of the dual-band absorber with different μ_c from 1.6 to 0.2 eV. When $\mu_c = 1.6$ eV, the two resonant peaks locate at 0.2296 and 0.5419 THz with the absorption of 89.17 and 94.05%, respectively. And the corresponding narrow bandwidths are 27.87 and 24.82 GHz, respectively. When the chemical potential μ_c decreases from 1.6 to 0.2 eV, the two absorption peaks slightly red shifted. Meanwhile, the spectral bandwidth of the two absorption peaks become smaller first and then become larger. When the chemical potential is $\mu_c = 1$ eV, the absorption of the two peaks of 0.2242 THz and 0.5302 THz are 99.62 and 99.76% with the bandwidth of 26.4 and 23.5 GHz, respectively. When the chemical potential furtherly decreases, the absorption peaks disappeared, and only a wide absorption band with the absorption above 91% in the interested frequency range is achieved. Here, the excited absorption peaks realize a maximum absorption change from 99.62 to 73.40% around 0.2 THz and 99.76 to 80.56% around 0.5 THz, which located in the 6G-communication frequency band.

The performance of the designed absorber under arbitrary incidence with TM polarization is investigated and illustrated in **Figure 8**. **Figure 8** shows that the frequency of the lower absorption peak slightly increases with the increase of the incident angle of TM polarization, resulting in the absorption peak being divided into two. This phenomenon may be caused by the parasitic resonances in the structure at a large incident angle [49]. Meanwhile, the higher absorption peak moves to high frequencies. This result can be explained that the variation of the electrical length will influence the magnetic resonance frequency. However, the absorption of the lower frequency absorption peak can still keep above 88% under 80° incidence.

TABLE 2 | Optimum circuit parameters based on the equivalent circuit model.

Components	$R_1(\Omega)$	L_1(pH)	C_1(fH)	$R_2(\Omega)$	L_2(pH)	C_2(fH)	L_d(pH)	C_d(pF)
Values-TM	0.78	10.98	116.99	1.79	5.04	38.58	5.45	11.78
Values-TE	0.71	17.83	8.00	0.83	4.65	12.07	5.43	918.79

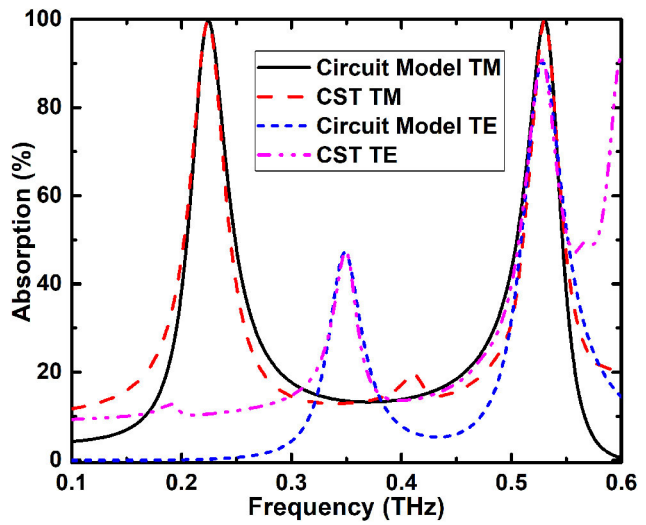

FIGURE 10 | Comparison of simulation results and equivalent circuit calculated results of the tunable dual-band absorber with TE and TM polarizations.

In order to prove the superiority of the designed absorber, result comparison with reported terahertz graphene absorbers is listed in **Table 1**. The results illustrate that the dual-band absorber designed here can provide the excellent narrow absorbing bandwidths with two tunable absorption peaks, which can be widely used in the 6G-communication systems. Furthermore, since only one monolayer continuous graphene layer is treated in the design, the metamaterial absorber is easy to fabricate and tune.

RLC CIRCUIT MODEL

The equivalent circuit model can be used to qualitatively forecast the behavior of the structures and the characteristics of the designed absorber. Furthermore, the impact of the geometry and periodic structure on the performance of absorber can also be estimated. Thus, the equivalent circuit model is beneficial for designing the new applications and providing physical mechanism of absorbers.

Based on the equivalent circuit model, the dual-band metamaterial absorber can be equivalently modeled as an equivalent circuit containing parallel-connected two series RLC circuits illustrated in **Figure 9**. Hence, the interaction between the terahertz wave and the absorbers can be investigated based on the transmission line theory.

By investigating the numerical simulation results, the value of the reflection coefficient S_{11} corresponding to the resonance point can be used to approximate the lumped parameter values of R, L, and C in the equivalent circuit [54–56].

Z_R is the surface impedance of microstructure which can be expressed as:

$$Z_R = \sqrt{\frac{(1+S_{11})^2 - S_{21}^2}{(1-S_{11})^2 - S_{21}^2}} \tag{3}$$

The value R can be obtained by:

$$R = \mathrm{Re}(Z_R(\omega)) \tag{4}$$

By taking two points ω_1 and ω_2 near the low-frequency resonant peak around 0.2 THz, the values of the capacitor C_1 and inductor L_1 in the equivalent circuit can be obtained by:

$$C_1 = \frac{\omega_2/\omega_1 - \omega_1/\omega_2}{\mathrm{Im}(Z_R(\omega_2)) \times \omega_1 - \mathrm{Im}(Z_R(\omega_1)) \times \omega_2} \tag{5}$$

$$L_1 = \frac{\mathrm{Im}(Z_R(\omega_2)) + 1/(\omega_2 \times C_1)}{\omega_2} \tag{6}$$

Similarly, by taking two points ω_3 and ω_4 near the high-frequency resonant peak around 0.53 THz, the values of the capacitor C_2 and the inductor L_2 in the equivalent circuit can be achieved.

The silicon layer and gold ground plane can be regarded as a shot-circuited transmission line with the length of d, and the impedance can be expressed as:

$$Z_d(\omega) = jZ_m^{TE,TM} \tan(\beta d) \tag{7}$$

where $\beta = \frac{\omega}{c}\sqrt{\varepsilon_r \mu_r - (\sin\theta)^2}$, c represents the wave speed in vacuum, θ defines the angle of incidence terahertz wave. $Z_m^{TM} = \beta/(\omega\varepsilon_r\varepsilon_0)$ is the intrinsic impedance with TM polarization, $Z_m^{TE} = (\omega\mu_r\mu_0)/\beta$ is the intrinsic impedance with TE polarization.

Z_d can be equivalent by the series connection of inductor L_d and capacitor C_d. The C_d and L_d can be calculated by using two frequency points ω_5 and ω_6 around the high-resonant frequency:

$$C_d = \frac{\omega_6/\omega_5 - \omega_5/\omega_6}{\mathrm{Im}(Z_d(\omega_6)) \times \omega_5 - \mathrm{Im}(Z_d(\omega_5)) \times \omega_6} \tag{8}$$

$$L_d = \frac{\mathrm{Im}(Z_d(\omega_6)) + 1/(\omega_6 \times C_d)}{\omega_d} \tag{9}$$

Table 2 summarizes the parameters of the equivalent circuit calculated by optimizing the *RLC* parameters based on the above equations.

Figure 10 illustrates the absorption of the absorber based on the calculation from equivalent circuit model and full wave

simulation, respectively. The results obtained from equivalent circuit agree well with the full-wave simulation results.

Finally, the working speed of the designed absorber depends on the *RC* value, where the capacitor C is mainly caused by the stray capacitance between the graphene layer and the dielectric substratum [40]. The capacitance can be expressed as $C = \varepsilon_0\varepsilon_d S_g/d$, where ε_0 represents the permittivity of vacuum, ε_d represents the relative permittivity of silicon, $d = 55\,\mu m$ defines the thickness of silicon, and S_g is the total effective area of graphene. In this work, the absorber is assumed to be a 100×100 array, and the S_g is about 6.7 mm^2. Thus, the capacitance of the absorber is about ∼12.83 pF. Considering that the resistance of the silicon substratum is relative low, the resistance *R* is mainly caused by the graphene layer. According to previously reported work, the resistance of graphene is usually several hundred ohms [57, 58]. When the highly doped graphene material is treated, the resistance of the absorber can be extremely decreased [40]. Therefore, when the resistance is set to ∼200 Ω, the working speed is up to ∼67.3 MHz calculated from $1/2\pi RC$.

CONCLUSIONS

A tunable dumbbell-shaped narrow-bandwidth dual-band terahertz perfect absorber based on a monolayer continuous graphene meta-surface is designed and investigated in this paper. By optimizing the geometry structure parameters of the absorber, the absorption of the two peaks are 99.62% at 0.2242 THz and 99.76% at 0.5302 THz. The corresponding excellent narrow bandwidths of the absorption peaks are 26.4 and 23.5 GHz, respectively. The electric field and surface current distributions are discussed to interpret the physical origin of the absorption characteristics. In addition, the operating characteristics can be easily tuned by changing the graphene chemical potentials owing to the merits of the monolayer continuous graphene layer. The CST simulated results of the absorber are in good agreement with the theoretically calculated results based on the equivalent circuit model. The equivalent circuit model can effectually and rationally interpret the physical origin of the device. This graphene-based absorber demonstrates a great potential in 6G-communication systems.

DATA AVAILABILITY STATEMENT

The original contributions presented in the study are included in the article/Supplementary Material, further inquiries can be directed to the corresponding authors.

AUTHOR CONTRIBUTIONS

DY carried out the whole simulation and wrote part of the paper. MM analyzed the data and wrote part of the paper. JL provided the project support. XL polished the manuscript. All authors discussed the results and contributed to the paper.

FUNDING

This study was supported by the National Natural Science Foundation of China under Grant Nos. 61871355 and 61831012, Zhejiang Province Natural Science Fund under Grant Nos. LQ20F010009 and LY18F010016, and State Key Laboratory of Crystal Materials Shandong University (No. KF1909).

REFERENCES

1. Dang SP, Amin O, Shihada B, Alouini MS. What should 6G be? *Nat Electron.* (2020) **3**:20–9. doi: 10.1038/s41928-019-0355-6
2. Ling F, Zhong Z, Huang R, Zhang B. A broadband tunable terahertz negative refractive index metamaterial. *Sci Rep.* (2018) **8**:9843. doi: 10.1038/s41598-018-28221-3
3. Liu D, Hong YL, Fan RH, Jing H, Peng RW, Lai Y, et al. Bendable disordered metamaterials for broadband terahertz invisibility. *Opt Express.* (2020) **28**:3552–60. doi: 10.1364/OE.384764
4. Lu Y, Li J, Zhang S, Sun J, Yao JQ. Polarization-insensitive broadband terahertz metamaterial absorber based on hybrid structures. *Appl Opt.* (2018) **57**:6269–75. doi: 10.1364/AO.57.006269
5. Zhao XL, Yuan C, Lv WH, Xu SL, Yao JQ. Plasmon-induced transparency in metamaterial based on graphene and split-ring resonators. *IEEE Photon Technol Lett.* (2015) **27**:1321–4. doi: 10.1109/LPT.2015.2421302
6. Li J, Shah CM, Withayachumnankul W, Ung BS, Mitchell A, Sriram S, et al. Flexible terahertz metamaterials for dual-axis strain sensing. *Opt Lett.* (2013) **38**:2104–6. doi: 10.1364/OL.38.002104
7. Li JN, Shah CM, Withayachumnankul W, Ung BSY, Mitchell A, Sriram S, et al. Mechanically tunable terahertz metamaterials. *Appl Phys Lett.* (2013) **102**:121101. doi: 10.1063/1.4773238
8. Xiao SY, Wang T, Liu TT, Yan XC, Li Z, Xu C. Active modulation of electromagnetically induced transparency analogue in terahertz hybrid metal-graphene metamaterials. *Carbon.* (2018) **126**:271–8. doi: 10.1016/j.carbon.2017.10.035
9. Yang Y, Li J, Li JN, Huang J, Zhang YT, Liang LJ, et al. Plasmon-induced reflection metasurface with dual-mode modulation for multi-functional THz devices. *Opt Laser Eng.* (2020) **127**:105969. doi: 10.1016/j.optlaseng.2019.105969
10. Gupta M, Srivastava YK, Singh R. A toroidal metamaterial switch. *Adv Mater.* (2018) **30**:1704845. doi: 10.1002/adma.201704845
11. Huang ML, Cheng YZ, Cheng ZZ, Chen HR, Mao XS, Gong RZ. Based on graphene tunable dual-band terahertz metamaterial absorber with wide-angle. *Opt Commun.* (2018) **415**:194–201. doi: 10.1016/j.optcom.2018.01.051
12. Luo H, Cheng YZ. Dual-band terahertz perfect metasurface absorber based on bi-layered all dielectric resonator structure. *Opt Mater.* (2019) **96**:109279. doi: 10.1016/j.optmat.2019.109279
13. Li W, Cheng Y. Dual-band tunable terahertz perfect metamaterial absorber based on strontium titanate (STO) resonator structure. *Opt Commun.* (2020) **462**:125265. doi: 10.1016/j.optcom.2020.125265
14. Luo H, Cheng Y. Thermally tunable terahertz metasurface absorber based on all dielectric indium antimonide resonator structure. *Opt Mater.* (2020) **102**:109801. doi: 10.1016/j.optmat.2020.109801
15. Huang ML, Cheng YZ, Cheng ZZ, Chen HR, Mao XS, Gong RZ. Design of a broadband tunable terahertz metamaterial absorber based on complementary structural grapheme. *Materials.* (2018) **11**:540. doi: 10.3390/ma11040540
16. Chen F, Cheng Y, Luo H. A broadband tunable terahertz metamaterial absorber based on single-layer complementary gammadion-shaped grapheme. *Materials.* (2020) **13**:860. doi: 10.3390/ma13040860
17. Ghosh SK, Yadav VS, Das S, Bhattacharyya S. Tunable graphene based metasurface for polarization-independent broadband absorption in lower mid infrared (MIR) range. *IEEE T Electromagn C.* (2020) **62**:346–54. doi: 10.1109/TEMC.2019.2900757
18. Huang H, Xia H, Xie W, Guo Z, Li H, Xie D. Design of broadband graphene metamaterial absorbers for permittivity sensing at mid-infrared regions. *Sci Rep.* (2018) **8**:4183. doi: 10.1038/s41598-018-22536-x

19. Jiang Y, Zhang HD, Wang J, Gao CN, Wang J, Cao YP. Design and performance of a terahertz absorber based on patterned graphene. *Opt Lett.* (2018) **43**:4296–9. doi: 10.1364/OL.43.004296
20. Schneider LE, Sun ET, Garland DJ, Taghert PH. Enhanced spatial terahertz modulation based on graphene metamaterial *Chin Opt Lett.* (2017) **15**:051603. doi: 10.3788/COL201715.051603
21. Landy NI, Sajuyigbe S, Mock JJ, Smith DR, Padilla WJ. Perfect metamaterial absorber. *Phys Rev Lett.* (2008) **100**:207402. doi: 10.1103/PhysRevLett.100.207402
22. Bhattacharyya S, Ghosh S, Chaurasiya D, Srivastava KV. Wide-angle broadband microwave metamaterial absorber with octave bandwidth. *IET Microw Antennas Propag.* (2015) **9**:1160–6. doi: 10.1049/iet-map.2014.0632
23. Yan DX, Li JS. Tunable all-graphene-dielectric single-band terahertz wave absorber. *J Phys D Appl Phys.* (2019) **52**:275102. doi: 10.1088/1361-6463/ab1892
24. Mason JA, Allen G, Podolskiy VA, Wasserman D. Strong coupling of molecular and mid-infrared perfect absorber resonances. *IEEE Photon Technol Lett.* (2012) **24**:31–3. doi: 10.1109/LPT.2011.2171942
25. Tao H, Landy NI, Bingham CM, Zhang X, Averitt RD, Padilla WJ. A metamaterial absorber for the terahertz regime: design, fabrication and characterization. *Opt. Express.* (2008) **16**:7181–88. doi: 10.1364/OE.16.007181
26. Yin ZP, Lu YJ, Xia TY, Lai WE, Yang J, Lu HB, et al. Electrically tunable terahertz dual-band metamaterial absorber based on a liquid crystal. *RSC Adv.* (2018) **8**:4197–203. doi: 10.1039/C7RA13047C
27. Liu H, Wang ZH, Li L, Fan YX, Tao ZY. Vanadium dioxide-assisted broadband tunable terahertz metamaterial absorber. *Sci Rep.* (2019) **9**:5751. doi: 10.1038/s41598-019-42293-9
28. Wang T, Cao M, Zhang H, Zhang Y. Tunable terahertz metamaterial absorber based on Dirac semimetal films. *Appl Opt.* (2018) **57**:9555–61. doi: 10.1364/AO.57.009555
29. Wang TL, Qu LZ, Qu LF, Zhang YP, Zhang HY, Cao MY. Tunable broadband terahertz metamaterial absorber using multi-layer black phosphorus and vanadium dioxide. *J Phys D Appl Phys.* (2020) **53**:ab6af4. doi: 10.1088/1361-6463/ab6af4
30. Huang X, He W, Yang F, Ran J, Yang Q, Xie SY. Thermally tunable metamaterial absorber based on strontium titanate in the terahertz regime. *Opt Mater Express.* (2019) **9**:1377–85. doi: 10.1364/OME.9.001377
31. Gu Y, Xu X, Wang F, Zhang M, Cheng X, Jiang Y, et al. Salisbury screen terahertz absorber formed with an insulator: 4-N, N-Dimethylamino-4′-N′-methyl-stilbazolium Tosylate (DAST). *ACS Omega.* (2019) **4**:9204–10. doi: 10.1021/acsomega.9b00013
32. Wang L, Ge SJ, Hu W, Nakajima M, Lu YQ. Graphene-assisted high-efficiency liquid crystal tunable terahertz metamaterial absorber. *Opt Express.* (2017) **25**:23873–9. doi: 10.1364/OE.25.023873
33. Yan DX, Li JS. Tuning control of dual-band terahertz perfect absorber based on graphene single layer. *Laser Phys.* (2019) **29**:046203. doi: 10.1088/1555-6611/ab05bd
34. Yao G, Ling FR, Yue J, Luo CY, Ji J, Yao JQ. Dual-band tunable perfect metamaterial absorber in the THz range. *Opt Exp.* (2016) **24**:1518–27. doi: 10.1364/OE.24.001518
35. Xing R, Jian SS. A dual-band THz absorber based on graphene sheet and ribbons. *Optic Laser Technol.* (2018) **100**:129–32. doi: 10.1016/j.optlastec.2017.10.003
36. Wu PC, Liao CY, Savinov V, Chung TL, Chen WT, Huang YW, et al. Optical anapole metamaterial. *ACS Nano.* (2018) **12**:1920-7. doi: 10.1021/acsnano.7b08828
37. Gao RM, Xu ZC, Ding CF, Wu L, Yao JQ. Graphene metamaterial for multiband and broadband terahertz absorber. *Opt Commun.* (2015) **356**:400–4. doi: 10.1016/j.optcom.2015.08.023
38. Zhou Q, Liu P, Liu C, Zhou Y, Zha S. Flexible dual-band all-graphene-dielectric terahertz absorber. *Opt Mater Exp.* (2019) **9**:2067–75. doi: 10.1364/OME.9.002067
39. Qi LM, Liu C, Shah SMA. A broad dual-band switchable graphene-based terahertz metamaterial absorber. *Carbon.* (2019) **153**:179–88. doi: 10.1016/j.carbon.2019.07.011
40. Zhao X, Yuan C, Zhu L, Yao J. Graphene-based tunable terahertz plasmon-induced transparency metamaterial. *Nanoscale.* (2016) **8**:15273–80. doi: 10.1039/C5NR07114C
41. Cai Y, Xu KD. Tunable broadband terahertz absorber based on multilayer graphene-sandwiched plasmonic structure. *Opt Express.* (2018) **26**:31693–705. doi: 10.1364/OE.26.031693
42. Lin X, Xu Y, Zhang BL, Hao R, Chen HS, Li EP. Unidirectional surface plasmons in nonreciprocal graphene. *N J Phys.* (2013) **15**:113003. doi: 10.1088/1367-2630/15/11/113003
43. Zhang EL, Zhou Q, Shen J. Resistive switching device based on high-mobility graphene and its switching mechanism. *J Phys Conf Seri.* (2019) **1168**:022074. doi: 10.1088/1742-6596/1168/2/022074
44. Bolotin KI, Sikes KJ, Jiang Z, Klima M, Fudenberge G, Hone J, et al. Ultrahigh electron mobility in suspended graphene. *Solid State Commun.* (2008) **146**:351–5. doi: 10.1016/j.ssc.2008.02.024
45. Banszerus L, Schmitz M, Engels S, Dauber J, Oellers M, Haupt F, et al. Ultrahigh-mobility graphene devices from chemical vapor deposition on reusable copper. *Sci Adv.* (2015) **1**:e1500222. doi: 10.1126/sciadv.1500222
46. Polini M, Koppens FHL. Plasmons in moiré superlattices. *Nat Mater.* (2015) **14**:1187–8. doi: 10.1038/nmat4496
47. *CST Studio Suite—User's Manual,* Darmstadt, Germany (2016).
48. Li XJ, Yin J, Liu ZH, Wang Y, Hong Z. Tailoring the excitation of two kinds of toroidal dipoles in all-dielectric metasurfaces. *Optik.* (2020) **201**:163502. doi: 10.1016/j.ijleo.2019.163502
49. Zhang X, Wu W, Li C, Wang C, Ma Y, Yang Z, et al. A dual-band terahertz absorber with two passbands based on periodic patterned graphene. *Materials.* (2019) **12**:3016. doi: 10.3390/ma12183016
50. Wang FL, Huang S, Li L, Chen WD, Xie ZW. Dual-band tunable perfect metamaterial absorber based on graphene. *Appl Optics.* (2018) **57**:6916–22. doi: 10.1364/AO.57.006916
51. Zhang LH, Hu FR, Xu XL, Wang YE, Guo EZ. Design of separately tunable terahertz two-peak absorber based on graphene. *Opt Commun.* (2016) **369**:65–71. doi: 10.1016/j.optcom.2016.02.036
52. He XJ, Yao Y, Zhu ZH, Chen MH, Zhu L, Yang WL, et al. Active graphene metamaterial absorber for terahertz absorption bandwidth, intensity and frequency control. *Opt Mater Express.* (2018) **8**:1031–42. doi: 10.1364/OME.8.001031
53. Deng G, Chen P, Yang J, Yin Z, Qiu L. Graphene-based tunable polarization sensitive terahertz metamaterial absorber. *Opt Commun.* (2016) **380**:101–7. doi: 10.1016/j.optcom.2016.05.075
54. Costa F, Genovesi S, Monorchio A, Manara G. A circuit-based model for the interpretation of perfect metamaterial absorbers. *IEEE Trans Antennas Propag.* (2013) **61**:1201–9. doi: 10.1109/TAP.2012.2227923
55. Liu XB, Qin WP. Wideband E-shaped element of THz metamaterial absorber and equivalent-circuit analysis 2015. In *Asia-Pacific Microwave Conference* (IEEE) (2015). p. 3:1–3. doi: 10.1109/APMC.2015.7413381
56. Liu XB. *Design and research on broadband element structure of metamaterial teraherz absorber*. Nanjing, Nanjing University of Posts and Telecommunications, MS thesis (2016).
57. Sensale-Rodriguez B, Yan R, Kelly MM, Fang T, Tahy K, Hwang WS, et al. Broadband graphene terahertz modulators enabled by intraband transitions. *Nat Commun.* (2013) **3**:780. doi: 10.1038/ncomms1787
58. Rahmanzadeh M, Rajabalipanah H, Abdolali A. Multilayer graphene-based metasurfaces: robust design method for extremely broadband, wide-angle, and polarization-insensitive terahertz absorbers. *Appl Optics.* (2018) **57**:959–68. doi: 10.1364/AO.57.000959

Conflict of Interest: The authors declare that the research was conducted in the absence of any commercial or financial relationships that could be construed as a potential conflict of interest.

frontiers in Physics

ORIGINAL RESEARCH
published: 13 August 2020
doi: 10.3389/fphy.2020.00308

Multiple-Band Terahertz Metamaterial Absorber Using Multiple Separated Sections of Metallic Rectangular Patch

Ben-Xin Wang[1], Yuanhao He[1], Pengcheng Lou[1], Nianxi Xu[2], Xiaoyi Wang[2], Yanchao Wang[2] and Jianjun Cao[1]*

[1] School of Science, Jiangnan University, Wuxi, China, [2] Key Laboratory of Optical System Advanced Manufacturing Technology, Changchun Institute of Optics, Fine Mechanics and Physics, Chinese Academy of Sciences, Changchun, China

Multiple-band metamaterial absorbers have been widely reported using the co-planar or layered design methods. However, these obtained absorption devices are of complex structure, large unit size, heavy weight, and time-consuming construction steps. Herein, an alternative design strategy is suggested to realize the multiple-band absorption at terahertz frequency. By introducing air gaps into the rectangular metallic patch, the original rectangular resonator can be divided into multiple sub-structures (or separated sections), and the combined effect of the localized resonance response of these sub-structures (or separated sections) gives rise to the multiple-band absorption. More importantly, the size, position and number of air gaps play the important roles in controlling the resonance performance of the absorption peaks and even in regulating the amount of the absorption peaks. Compared with the existing multiple-band absorption design strategies, the proposed approach does not increase the unit size, nor need to stack multiple layers, which provides important guidance for the design of multiple-band terahertz metamaterial absorbers with simple, compact, and easy to fabricate for full details.

Keywords: metamaterial, terahertz, perfect absorber, multiple-band absorption, rectangular patch resonator

OPEN ACCESS

Edited by:
Zhi Hong,
China Jiliang University, China

Reviewed by:
Guangsheng Deng,
Hefei University of Technology, China
Liang Wu,
Tianjin University, China

****Correspondence:***
Ben-Xin Wang
wangbenxin@jiangnan.edu.cn

Specialty section:
This article was submitted to Optics and Photonics, a section of the journal Frontiers in Physics

Received: *21 May 2020*
Accepted: *06 July 2020*
Published: *13 August 2020*

Citation:
Wang B-X, He Y, Lou P, Xu N, Wang X, Wang Y and Cao J (2020) Multiple-Band Terahertz Metamaterial Absorber Using Multiple Separated Sections of Metallic Rectangular Patch. Front. Phys. 8:308. doi: 10.3389/fphy.2020.00308

INTRODUCTION

Metamaterial absorbers, as an important branch of metamaterial-based resonant devices, have attracted wide attention because of their near-perfect absorption to the incident beam, ultra-thin dielectric layer thickness, and adjustable operating performance [1–3]. In view of these excellent properties, metamaterial absorbers can be extensively used in selective thermal emitter, solar energy harvesting, surface enhanced Raman scattering, refractive index sensing, and so on [2, 3]. Metamaterial absorbers are usually consisted of three functional layers that are, respectively, the top patterned metallic structure and the bottom metallic mirror separated by the middle insulating dielectric layer. The three functional layers have different roles in realizing the perfect absorption. Please refer to Review works in [2] and [3] for details. Under their guidance, various of top metallic structures for the perfect absorption has been wide-ranging investigated [4–8], such as metallic cross, electric-ring resonator, loop frames, rectangular patch, etc. However, metamaterial absorbers designed by these structures have similar disadvantages of single absorption band or

single-band absorption. It is foreseeable that the single-band absorption device will inevitably have some limitations in applications. In order to avoid these potential limitations, the design of the multiple-band metamaterial absorbers is urgently needed [2, 3].

Multiple-band metamaterial absorbers mean that they enable perfect absorption at several discrete frequency points. According to the number of frequency points [9–28], the multiple-band absorption devices can be divided into dual-band absorption, triple-band absorption, quad-band absorption, and even more. In terms of design ideas, the principles of these multiple-band metamaterial absorbers are similar that they are resulted from the combined effect of the single resonance response of each metallic resonator. As a result, the multiple-band metamaterial absorbers require metallic resonators with not less than the number of their own absorption peaks. In terms of implementation modes, the realization of the multiple-band metamaterial absorbers usually has two methods. One of which is the co-planar design method for placing multiple sub-resonators [9–21]. However, this type of design is at the expense of increasing the interaction of the sub-arrays (resulting in weak absorption strength) and expanding the unit size (resulting in large and non-compact structure size). The another strategy is the layered design method formed by several metallic sub-resonators with different sizes [22–28]. However, the layered design has the complex structure and thick structure size, which leads to the heavy weight of the device and the time-consuming construction processes. Either the co-planar design or the layered design is not an ideal way to realize the multiple-band perfect absorption. The fascinating method should be combined with the advantages of being as small size or compact as possible, ultra-thin, light weight, and easy to fabricate. However, such multiple-band metamaterial absorbers are rarely reported at this stage.

In this paper, an alternative design method for multiple-band perfect absorption is proposed. By introducing air gaps into the rectangular metallic patch, the introduction of the air gaps can split the original rectangular patch resonator into several separated parts or sections. The superposition effect of the localized resonance responses of the several separated sections exhibits the ability to gain the multiple-band absorption at terahertz frequency. The performance of the multiple-band absorption shows a significant dependence on the gap sizes, number, as well as the gap position in the rectangular patch. Compared with the existing design technologies of realizing multiple-band absorption [9–28], the multiple-band absorption device has some superior features, especially it does not increase the transverse and longitudinal dimensions of the basic cell, so it can effectively avoid the coupling effect of the sub-structures in the large-sized co-planar design method and can avoid the time-consuming fabrication steps and complex structure faced in the layered design approach. Therefore, the multiple-band terahertz metamaterial absorber should have a wide range of application prospects in the terahertz technology related fields, including terahertz imaging, terahertz detection, terahertz sensing, etc.

The framework of this manuscript is as follows: In "Design of single-band absorption" section, we first use a rectangular patch to obtain the single-band absorption at terahertz frequency. The physical origin of the single-band absorption is investigated. Its mechanism is mainly derived from the three-order resonance response of rectangular patch. We also evaluate the influence of the rectangular patch sizes on the single-band absorption. In "Design of dual-band absorption" section, an air gap is introduced into the rectangular patch, and its introduction can divide the rectangular patch into two separated sections. The combination effect of the localized resonance response of the two separated sections can gain the dual-band absorption. The near-field patterns of the dual-band absorption as well as the dependence of the dual-band absorption on the changes in the gap position and sizes are also demonstrated to further explain its formation mechanism. In "Design of triple-band absorption" section, a more air gap is introduced into the rectangular patch, three separated sections are obtained due to the introduction of the two air gaps. Results show that each separated section has the single localized resonance mode, and the combination of these resonance modes in the three separated sections leads to the triple-band absorption. The relevant dimensions of air gaps have a considerable influence on the resonance performance of the triple-band absorption. In "Conclusion" section, we summarize the results of each section and conclude the whole manuscript.

DESIGN OF SINGLE-BAND ABSORPTION

Side-view and top-view of the basic cell of the single-band metamaterial absorber are, respectively, shown in **Figures 1A,B**. Three layers of top metallic resonator, ultra-thin middle insulating medium layer having thickness of $t = 4.1\,\mu$m and dielectric constant of $3(1+i0.06)$, and bottom metallic board with thickness larger than the skin depth of incident beam are utilized to realize the single-band absorption. The top metallic resonator is actually a rectangular patch, it has the length of $l = 94\,\mu$m and width of $w = 44\,\mu$m. The basic cell of the single-band absorption has periodic dimensions of $a = 100\,\mu$m along the x-axis and $b = 70\,\mu$m along the y-axis.

We use commercial simulation software FDTD Solutions, which is based on the finite difference time domain method, to analyze and study the resonance performance, and near-field patterns of the designed absorption devices, including the single-band absorption, dual-band, and triple-band absorption in the following sections. During the analysis, periodic boundary conditions along the x and y directions are applied to reveal the periodic arrangement of absorption device, while the perfectly matched layers are employed in the z direction to absorb the unnecessary scattering. A plane light source with x-axis polarization propagating along the z direction radiates into the absorption device from top metallic resonator to bottom metallic board. The absorption AA is obtained from the $AA = 1—TT—RR$, of which the TT and RR are, respectively, the transmission and reflection of the metamaterial. Since the thickness of the bottom metallic board is greater than the skin depth of the incident beam, the $TT = 0$. Then the AA could be expressed by $AA = 1—RR$.

But the need to pay attention to is that the sizes of rectangular patch, the thickness and dielectric constant of middle

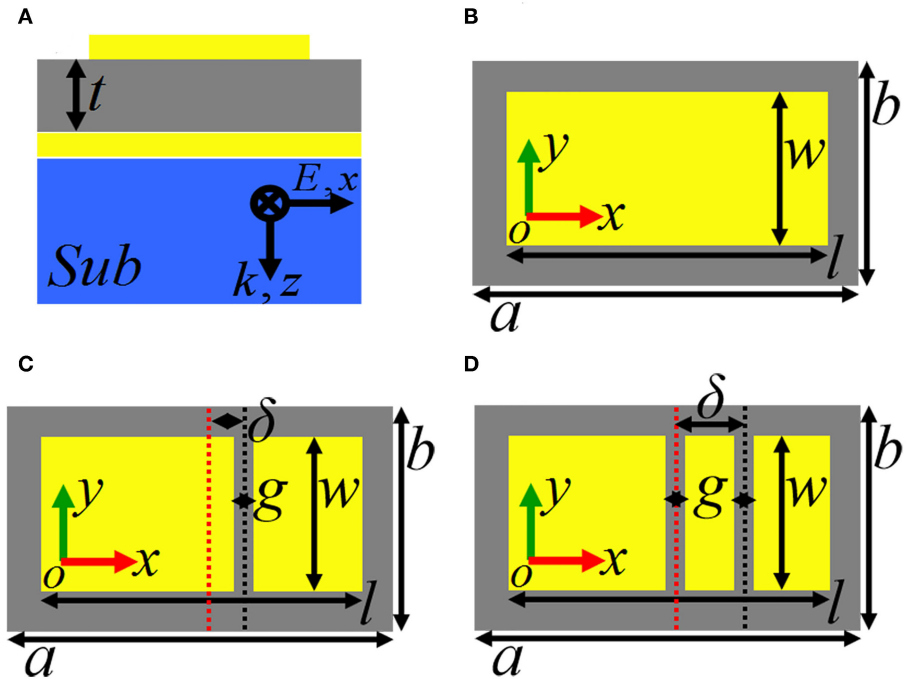

FIGURE 1 | (A) Side view of the metamaterial absorber having the single-band, dual-band, and triple-band absorption; **(B)** Top view of the single-band metamaterial absorber; **(C)** Top view of the dual-band metamaterial absorber; **(D)** Top view of the triple-band metamaterial absorber.

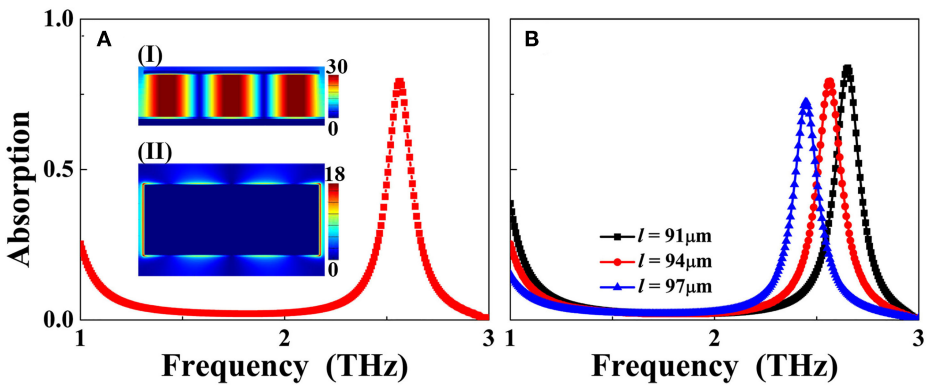

FIGURE 2 | (A) Absorption response of the single-band metamaterial absorber, of which the insets (I) and (II) are, respectively, the electric and magnetic field patterns of the maximum absorption peak at 2.57 THz; **(B)** Dependence of the absorption response on the length (*l*) change of the rectangular patch resonator.

insulating medium layer, the periodic dimensions of basic cell, the calculation model and its boundary conditions are unchanged in the whole manuscript unless otherwise specified. In other words, except for the introduction of air gaps into the rectangular patch, there is no other parameter changes for the dual-band and triple-band absorption in the following sections. Therefore, the advantage of this method (by introducing air gaps into the rectangular patch) in this manuscript is that the multiple-band absorption can be obtained without increasing the cell sizes horizontally and vertically, which is totally different from the previous design strategies.

Under the preset parameters and appropriate calculation model, the absorption response of the metallic rectangular patch resonator is shown in **Figure 2A**. Single resonance absorption peak with the frequency of 2.57 THz is obtained. To insight into the physical mechanism of the single-band absorption, near-field distributions of this absorption peak at 2.57 THz are given in Insets (I) and (II) of **Figure 1A**. It is observed that its electric field in Inset (II) is mostly concentrated on the edges of the rectangular resonator, and its magnetic field in Inset (I) presents strong aggregation effect in the middle insulating medium layer under the rectangular

patch resonator. These near-field patterns reveal that this absorption peak is mainly caused by the localized resonance response of the rectangular patch resonator. We further observed that the magnetic-field patterns of the absorption peak have three obvious aggregation areas (or nodes), which is confirmed that this absorption peak at 2.57 THz is due to the third-order localized resonance of the rectangular patch [29, 30].

Because the absorption peak originates from the third-order (localized) resonance response of the rectangular patch resonator, the change in rectangular patch sizes should strongly affect the frequency of the absorption peak. As revealed in **Figure 2B**, the single-band absorption peak frequency exhibits blue-shift with the increase of the rectangular patch length (l). This resonance feature gives us the opportunity to design multiple-band metamaterial absorber by introducing air gaps into the rectangular patch so that the rectangular patch resonator can be divided into several separated sections with different lengths. The combined effect of the localized resonance response of each separated section should provide the possibility of realizing the multiple-band absorption. This advantage of this method is that it does not increase the structure size of the absorption device and or need to stack multiple metallic resonators, so this strategy has a lot of merits over traditional design methods of co-planar or layered, such as small size or compact structure design, ultra-thin, light weight and easy to fabricate. The following two sections will discuss in details how to use this method of introducing air gaps into the basis of the original rectangular patch resonator to design multiple-band absorption.

DESIGN OF DUAL-BAND ABSORPTION

In this section, we mainly investigate and study the realization of the dual-band absorption. In the process of realization, an (or single) air gap needs to be introduced into the original rectangular patch resonator. The top-view of the dual-band absorption is demonstrated in **Figure 3A** or **Figure 1C**. The introduced air gap has the gap (g) of $g = 6\,\mu$m, and width (w) of $w = 44\,\mu$m. The distance between the introduced air gap and the rectangular patch center is represented by δ, here we set $\delta = 10\,\mu$m. Because δ is not equal to 0, the introduced air gap can split the original rectangular patch into two separated metallic sections having different lengths. As observed in **Figure 3A**, the length of the left separated metallic section is larger than that of the right separated metallic section. As observed in **Figure 3B**, two discrete resonance absorption peaks with near 100% absorbance are gained, in which the absorption peak with the lower frequency at 1.50 THz is labeled as mode A, while the absorption peak with the higher frequency at 2.25 THz is labeled as mode B. In fact, the below **Figure 5B** shows that the value of δ (i.e., the position of air gap into the rectangular patch) plays an important role in regulating the resonance performance of dual-band absorption.

In order to analyze and investigate the formation mechanism of the two absorption peaks A and B, the near-field patterns of them are given, as demonstrated in **Figure 4**, of which the **Figures 4A,C** are, respectively, the electric field patterns of the absorption peaks A and B in the center plane of the top metallic array, while the magnetic field patterns of the absorption peaks A and B in the middle insulating dielectric layer under the metallic array are presented in **Figures 4B,D**, respectively. We first study the physical mechanism of absorption peak A, it is found that its electric field in **Figure 4A** is mainly localized at both edges (or sides) of the left separated metallic section. In the meantime, its magnetic field in **Figure 4C** is mostly concentrated on the middle insulating dielectric layer under the left separated metallic section. The electric and magnetic field patterns of the absorption peak A indicate that the localized resonance response of the left separated metallic section is the operating mechanism of the absorption mode. We further found in **Figure 4C** that there is only one strong magnetic field aggregation area (or node) for absorption peak A, which shows that this absorption is caused by the first-order localized resonance response of the left separated metallic section [29, 30]. Unlike the case of the absorption peak A that its electric and magnetic fields are mainly related to the left separated metallic section, the near-field patterns of the absorption peak B are primarily associated with the right separated metallic section. In detail, the electric field of the absorption peak B in **Figure 4B** shows the strong enhancement effect at both sides of the right separated metallic section, and its magnetic field with one strong aggregation area (or node) is mostly distributed at the middle insulating dielectric layer under the right separated metallic section, see **Figure 4D**. These near-field distributions reveal that the formation of the absorption peak B is chiefly due to the first-order localized resonance response of the right separated metallic section [29, 30]. From these analyses, it can be seen that the superposition effect of the first-order localized resonance response of the two (or left and right) separated sections leads to the dual-band absorption.

Because the absorption peaks A and B are associated with the left and right separated metallic sections, respectively, the size changes in the specific section will affect its corresponding resonance performance. As shown in **Figure 5A**, the gap (g) of the air gap into the rectangular patch play an important role in controlling the resonance frequencies of the absorption peaks A and B. The frequencies of them exhibit the similar moving trend, that is, with the increase of the gap (g), they are both gradually increasing. This is a known fact that the resonance (or absorption) frequency of the localized resonance response is inversely proportional to the metallic resonator length. The larger the metallic resonator length, the smaller the absorption frequency. As the rectangular patch length (l) remains unchanged in whole manuscript, the larger the gap (g), the smaller the separated metallic section length, corresponding to the larger absorption frequency.

The resonance frequencies of the absorption peaks A and B can also be adjusted by varying the position (δ) of the air gap into the rectangular patch as well as the length of the rectangular patch itself. As revealed in **Figure 5B**, the resonance frequency of the absorption peak A gradually decrease with the increase of the air gap position (δ), while the frequency of the absorption peak B is increasing gradually. With the increase of the air gap position (δ), the length of the left separated metallic section becomes larger,

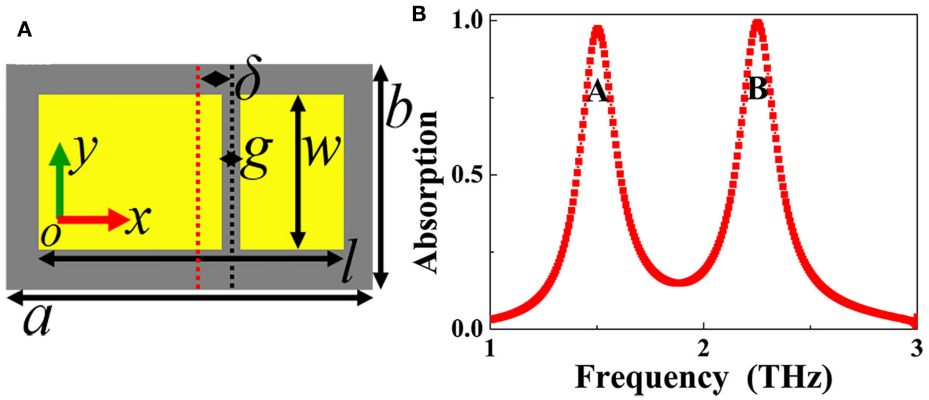

FIGURE 3 | (A) Top view of the dual-band metamaterial absorber; **(B)** Absorption response of the dual-band metamaterial absorber.

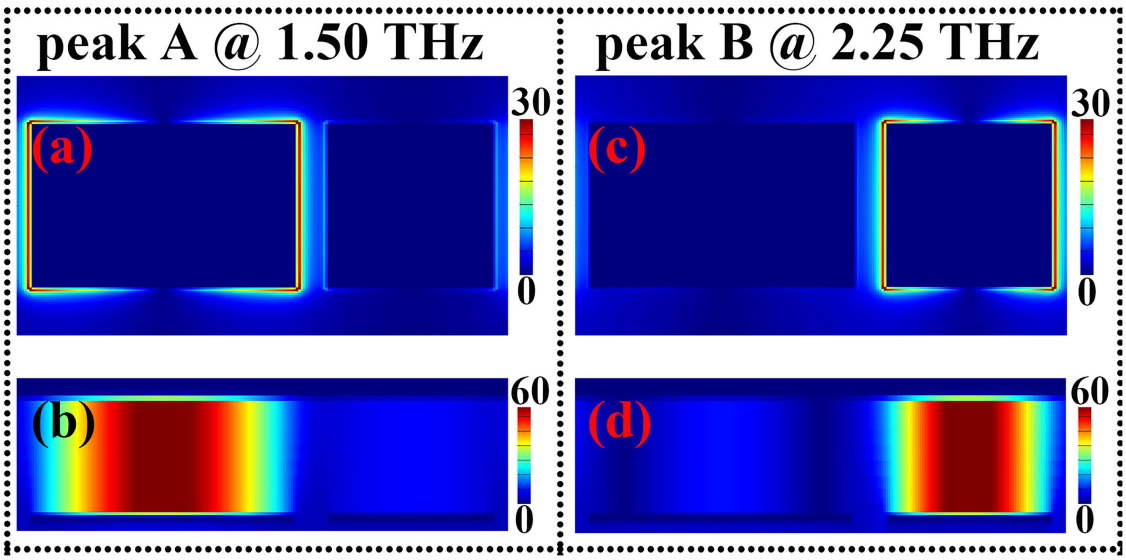

FIGURE 4 | Panels **(A,B)** are respectively the electric and magnetic field patterns of the absorption peak A at 1.50 THz; **(C,D)** are respectively the electric and magnetic field patterns of the absorption peak B at 2.25 THz.

while the length of the right separated metallic section decreases, resulting in the opposite movement trend of their respective absorption frequencies. Obviously, when the air gap position (δ) is equal to zero, the left separated metallic section length is the same as that of the right, thus only one absorption peak should be realized. As given in the black curve of the **Figure 5B**, it is true that only one absorption peak labeled as mode C. According to the near-field patterns of the mode C in **Figures 5D,E**, the formation mechanism of this mode is mainly derived from the first-order localized resonance response of the two (or left and right) separated metallic sections with identical sizes. In addition, when the length (l) of the rectangular patch itself is increasing, it will increase the lengths of the left and right separated metallic sections at the same time, resulting in the simultaneous decrease of the absorption peaks A and B, as shown in **Figure 5C**.

DESIGN OF TRIPLE-BAND ABSORPTION

The introduction of more air gaps into the rectangular patch has the ability to achieve the perfect absorption at more frequency bands. As a typical example, this section presents the realization of the triple-band metamaterial absorber using two air gaps with the identical sizes into the rectangular patch. The top-view of the triple-band absorption device is illustrated in **Figure 6A** (or **Figure 1D**). The two air gaps have the same gap (g) of $g = 6\,\mu$m and width (w) of $w = 44\,\mu$m. The center of the left (or first) air gap coincides with the rectangular patch center, while the distance between the right (or second) air gap and the rectangular patch center is $\delta = 20\,\mu$m. Because of the different positions of the two air gaps into the rectangular patch, the original rectangular patch resonator can be divided into three separated

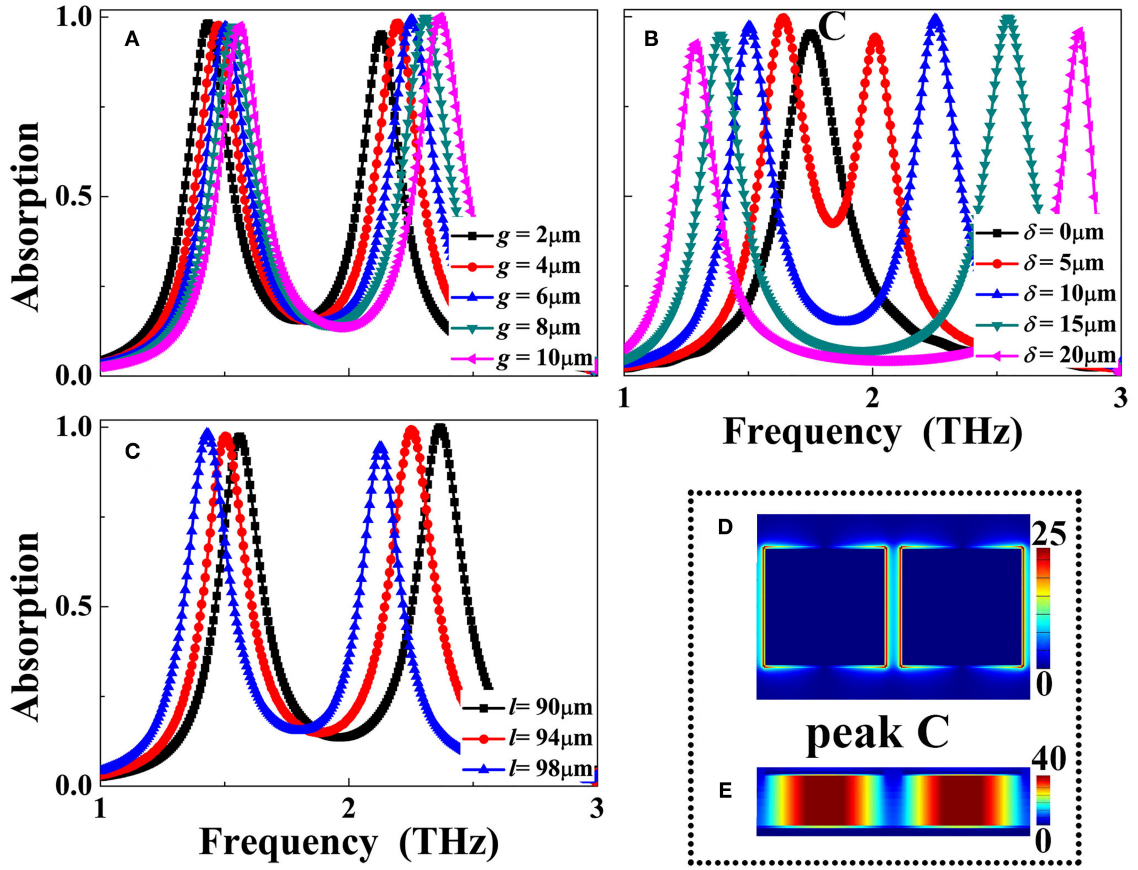

FIGURE 5 | Dependence of the absorption response of the dual-band metamaterial absorber on the size changes of the gap (*g*) in **(A)**, position (*δ*) in **(B)**, and rectangular patch length (*l*) in **(C)**; **(D,E)** are, respectively, the electric and magnetic field patterns of the absorption peak C at 1.75 THz.

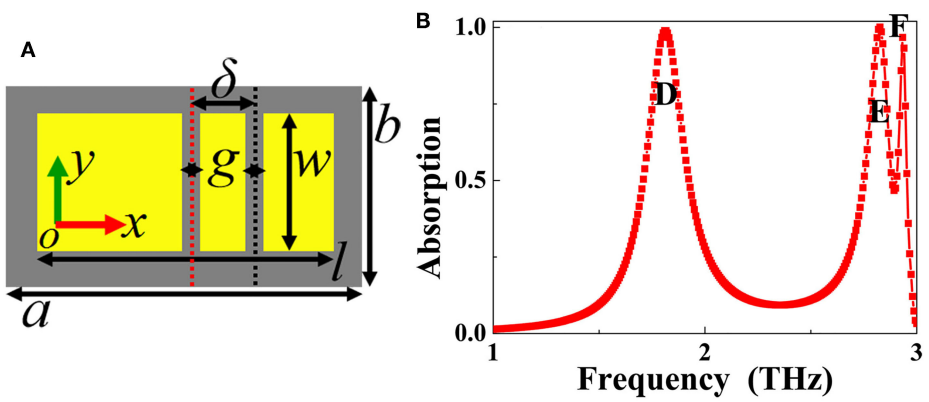

FIGURE 6 | (A) Top view of triple-band metamaterial absorber; **(B)** Absorption response of the triple-band metamaterial absorber.

metallic sections, of which the left section has the longest length, the right section is the second, and the middle section is the smallest. As shown in the absorption spectral of **Figure 6B**, three distinct absorption peaks with near perfect absorbance are realized. The first absorption peak with the resonance frequency of 1.82 THz is labeled as the mode D, and the last two absorption peaks localized at the frequencies of 2.83 THz and 2.93 THz are, respectively, marked as modes E and F.

To insight into the physical origin of the triple-band absorption, near-field patterns of the three absorption peaks

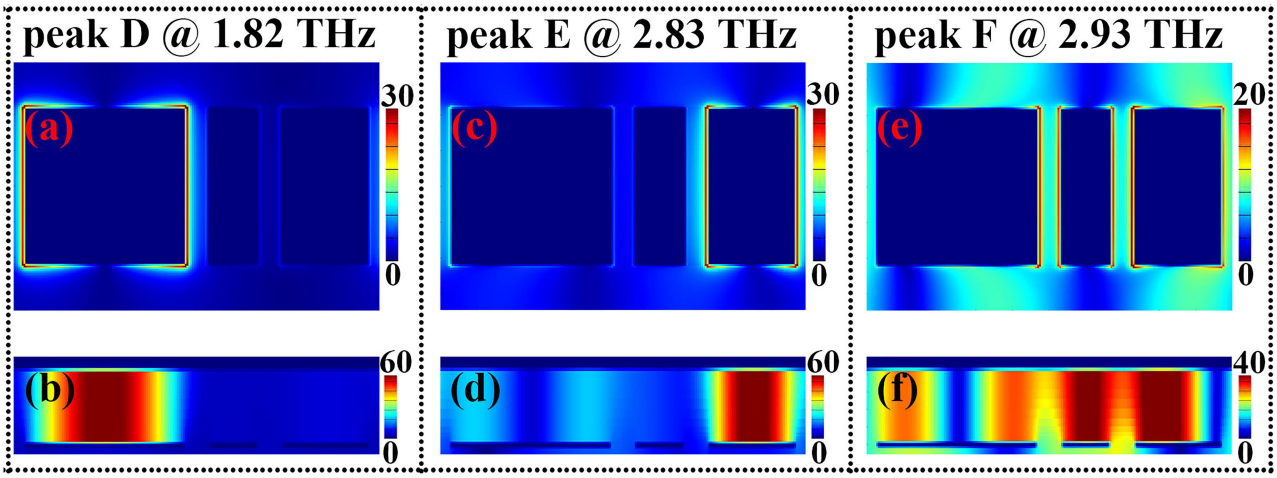

FIGURE 7 | Panels **(A,B)** are respectively the electric and magnetic field patterns of the absorption peak D at 1.82 THz; **(C,D)** are respectively the electric and magnetic field patterns of the absorption peak E at 2.83 THz; **(E,F)** are respectively the electric and magnetic field patterns of the absorption peak F at 2.93 THz.

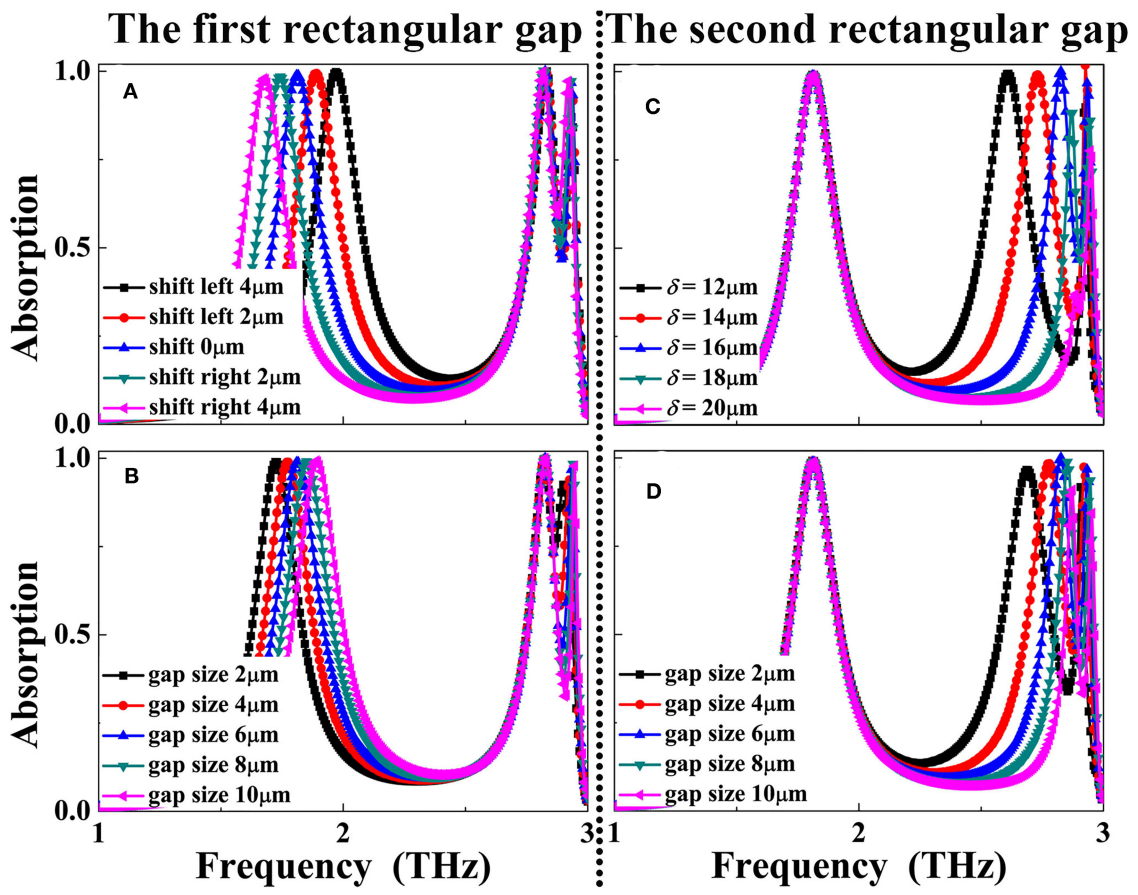

FIGURE 8 | Dependence of the absorption response of the triple-band metamaterial absorber on the size changes of the left (or first) air gap position (δ) in **(A)**, gap (g) in **(B)**; Dependence of the absorption response of the triple-band metamaterial absorber on the size changes of the right (or second) air gap position (δ) in **(C)**, gap (g) in **(D)**.

D, E, and F are presented, as given in **Figure 7**, of which the **Figures 7A,B** are, respectively, the electric and magnetic field patterns of the absorption peak D in the center plane of the top metallic array and the middle insulating dielectric layer under the top metallic array, the electric and magnetic field patterns of the absorption peak E (or F) in the center plane of the top metallic array and the middle dielectric layer under the top metallic array are, respectively, demonstrated in **Figures 7C,D** (or **Figures 7E,F**). In detail, for absorption peak D, its electric field in **Figure 7A** is chiefly focused on both edges (or sides) of the left separated metallic section along the electric field direction of the incident beam, and the magnetic field of the absorption peak with one strong aggregation area (or node) is mostly concentrated on the insulating dielectric layer under the left separated metallic section, see **Figure 7B**. These field patterns prove that the absorption peak D is resulted from the first-order localized resonance response of the left separated metallic section. Considering the distribution characteristics of the electric and magnetic fields in **Figures 7C,D**, the physical mechanism of the absorption peak E should be come from the first-order localized resonance response of the right separated metallic section.

Different from the resonance mechanism of the absorption peaks D and E, the formation of the absorption peak F is not due to the localized resonance response of the single separated metallic section (or a specific separated section), but to the superposition effect of the separated metallic sections. The enhanced electric field patterns are not only distributed on both edges of the middle separated metallic section, but also on the edges of the left and right separated metallic sections, see **Figure 7E**. The enhanced magnetic fields also have the similar distribution characteristics that they are not only focused on the insulating dielectric layer under the middle separated metallic section, but also on the insulating dielectric layer under the left and right separated metallic sections, see **Figure 7F**. It should be noted that the proportion of electric field distributions in the left separated metallic section is significantly lower than that of the other separated metallic sections, and the magnetic field patterns in the insulating dielectric layer under the top separated metallic sections have also the similar features that the proportion of the magnetic fields in the left insulating dielectric layer is obviously smaller than that of the other two parts. It is revealed that the formation of the absorption peak F is mostly attributed to the hybrid effect of the first-order resonance response of the middle and right separated metallic sections.

The geometric parameters of the introduced air gaps, including the gap (g) and the position (δ), play the rather important role in controlling the performance of the triple-band absorption device. It can be seen from **Figure 8A** that resonance frequency of the absorption peak D is strongly affected by the position shift of the left (or first) air gap, while the last two absorption peaks E and F show the slight frequency movements. The resonance frequency of the absorption peak D can also be controlled by varying the gap (g) of the left (or first) air gap, see **Figure 8B**. Different from the case of the parameter changes of the left (or first) air gap that mainly regulate the resonance frequency of the absorption peak D, the size changes of the right (or second) air gap chiefly affect the absorption peaks E and F, while the frequency movement of the absorption peak D is nearly unchanged, see **Figures 8C,D**. These results indicate that triple-band absorption with specific resonance frequencies (or application demands) can be realized by independently adjusting the parameters of the air gap.

CONCLUSION

In conclusion, this manuscript presents the design of multiple-band terahertz metamaterial absorber by introducing air gaps into the rectangular patch resonator. The introduction of the air gaps can split the original rectangular patch into several separated metallic sections having different lengths. The superposition effect of the first-order localized resonance response of each separated metallic section results in the multiple-band absorption. The near-field patterns of each absorption frequency point are given to investigate the physical origin of the multiple-band absorption. Results further prove that the parameters of the air gaps, including their gap and position into the rectangular patch, possess large ability in tuning the absorption frequencies of the multiple-band metamaterial absorber. The strategy proposed here, which is different from the existing one, could provide important guidance for the design of the next generation of the multiple-band metamaterial absorbers.

DATA AVAILABILITY STATEMENT

The original contributions presented in the study are included in the article/supplementary material, further inquiries can be directed to the corresponding author/s.

AUTHOR CONTRIBUTIONS

B-XW conceived the research, conducted simulations and analysis, and wrote the manuscript. YH and PL conducted simulations and analysis. NX, XW, and YW conducted analysis. JC wrote the manuscript. All authors contributed to the article and approved the submitted version.

FUNDING

This research was funded by National Natural Science Foundation of China (11647143), Natural Science Foundation of Jiangsu (BK20160189), China Postdoctoral Science Foundation (2019M651692), Jiangsu Postdoctoral Science Foundation (2018K113C), Fundamental Research Funds for Central Universities (JUSRP51721B), Open Fund of Key Laboratory of Optical System Advanced Manufacturing Technology, and Chinese Academy of Sciences (KLOMT190103).

REFERENCES

1. Landy NI, Sajuyigbe S, Mock JJ, Smith DR, Padilla WJ. Perfect metamaterial absorber. *Phys Rev Lett.* (2008) **100**:207402. doi: 10.1103/PhysRevLett.100.207402
2. Watts CM, Liu X, Padilla WJ. Metamaterial electromagnetic wave absorbers. *Adv Mater.* (2012) **24**:OP98–120. doi: 10.1002/adma.201200674
3. Cui Y, He Y, Jin Y, Ding F, Yang L, Ye Y, et al. Plasmonic and metamaterial structures as electromagnetic absorbers. *Laser Photon Rev.* (2014) **8**:495–520. doi: 10.1002/lpor.201400026
4. Chen HT. Interference theory of metamaterial perfect absorbers. *Opt Express.* (2012) **20**:7165–72. doi: 10.1364/OE.20.007165
5. Liu X, Starr T, Starr AF, Padilla WJ. Infrared spatial and frequency selective metamaterial with near-unity absorbance. *Phys Rev Lett.* (2010) **104**:207403. doi: 10.1103/PhysRevLett.104.207403
6. Li Z, Butun S, Aydin K. Ultranarrow band absorbers based on surface lattice resonances in nanostructured metal surfaces. *ACS Nano.* (2014) **8**:8242–48. doi: 10.1021/nn502617t
7. Wang BX, Wang GZ. Temperature tunable metamaterial absorber at THz frequencies. *J Mater Sci.* (2017) **28**:8487–93. doi: 10.1007/s10854-017-6570-x
8. Hu X, Xu G, Wen L, Wang H, Zhao Y, Zhang Y, et al. Metamaterial absorber integrated microfluidic terahertz sensors. *Laser Photon Rev.* (2016) **10**:962–9. doi: 10.1002/lpor.201600064
9. Song J, Wang L, Li M, Dong J. A dual-band metamaterial absorber with adjacent absorption peaks. *J Phys D.* (2018) **51**:385105. doi: 10.1088/1361-6463/aad7e1
10. Yuan S, Yang R, Xu J, Wang J, Tian J. Photoexcited switchable single-/dual-band terahertz metamaterial absorber. *Mater Res Express.* (2019) **6**:075807. doi: 10.1088/2053-1591/ab1962
11. Agarwal M, Meshram MK. Metamaterial-based dual-band microwave absorber with polarization insensitive and wide-angle performance. *AIP Adv.* (2018) **8**:095016. doi: 10.1063/1.5020702
12. Kim J, Han K, Hahn JW. Selective dual-band metamaterial perfect absorber for infrared stealth technology. *Sci Rep.* (2017) **7**:6740. doi: 10.1038/s41598-017-06749-0
13. Yao G, Ling F, Yue J, Luo C, Ji J, Yao J. Dual-band tunable perfect metamaterial absorber in the THz range. *Opt Express.* (2016) **24**:1518–27. doi: 10.1364/OE.24.001518
14. Khuyen BX, Tung BS, Kim YJ, Hwang JS, Kim KW, Rhee JY, et al. Ultra-subwavelength thickness for dual/triple-band metamaterial absorber at very low frequency. *Sci Rep.* (2018) **8**:11632. doi: 10.1038/s41598-018-29896-4
15. Mishra N, Choudhary DK, Chowdhury R, Kumari K, Chaudhary RK. An investigation on compact ultra-thin triple band polarization independent metamaterial absorber for microwave frequency applications. *IEEE Access.* (2017) **5**:4370–6. doi: 10.1109/ACCESS.2017.2675439
16. Chaurasuya D, Ghosh S, Bhattacharyya S, Srivastava KV. An ultrathin quad-band polarization-insensitive wide-angle metamaterial absorber. *Micro Opt Technol Lett.* (2015) **57**:697–702. doi: 10.1002/mop.28928
17. Jafari FS, Naderi M, Hatami A, Zarrabi FB. Microwave Jerusalem cross absorber by metamaterial split ring resonator load to obtain polarization independence with triple band application. *AEU-Inter J Electron Commun.* (2019) **101**:138–44. doi: 10.1016/j.aeue.2019.02.002
18. Agarwal M, Behera AK, Meshram MK. Wide-angle quad-band polarisation-insensitive metamaterial absorber. *Electron Lett.* (2016) **52**:340–2. doi: 10.1049/el.2015.4134
19. Singh HS. Super compact ultrathin quad-band with wide angle stability polarization independent metamaterial absorber. *Micro Opt Technol Lett.* (2020) **62**:718–25. doi: 10.1002/mop.32054
20. Stephen L, Yogesh N, Subramanian V. Realization of bidirectional, bandwidth-enhanced metamaterial absorber for microwave applications. *Sci Rep.* (2019) **9**:10058. doi: 10.1038/s41598-019-46464-6
21. Kalraiya S, Chaudhary RK, Gangwar RK, Abdalla AM. Compact quad-band polarization independent metamaterial absorber using circular/square metallic ring resonator. *Mater Res Express.* (2019) **6**:055812. doi: 10.1088/2053-1591/ab0623
22. Hokmabadi MP, Wilbert DS, Kung P, Kim SM. Polarization-dependent, frequency-selective THz stereometamaterial perfect absorber. *Phys Rev Appl.* (2014) **1**:044003. doi: 10.1103/PhysRevApplied.1.044003
23. Su Z, Yin J, Zhao X. Terahertz dual-band metamaterial absorber based on graphene/MgF2 multilayer structures. *Opt Express.* (2015) **23**:1679–90. doi: 10.1364/OE.23.001679
24. Bhattacharyya S, Ghosh S, Chaurasiya D, Srivastava KV. Bandwidth-enhanced dual-band dual-layer polarization-independent ultra-thin metamaterial absorber. *Appl Phys A.* (2015) **118**:207–15. doi: 10.1007/s00339-014-8908-z
25. Wang BX, Tang C, Niu Q, He Y, Chen T. Design of narrow discrete distances of dual-/triple-band terahertz metamaterial absorbers. *Nanoscale Res Lett.* (2019) **14**:64. doi: 10.1186/s11671-019-2876-3
26. Liu S, Zhuge J, Ma S, Chen H, Bao D, He Q, et al. A bi-layered quad-band metamaterial absorber at terahertz frequencies. *J Appl Phys.* (2015) **118**:245304. doi: 10.1063/1.4938110
27. Kajtar G, Kafesaki M, Economou EN, Soukoulis CM. Theoretical model of homogeneous metal-insulator-metal perfect multi-band absorbers for the visible spectrum. *J Phys D.* (2016) **49**:055104. doi: 10.1088/0022-3727/49/5/055104
28. Astorino MD, Frezza F, Tedeschi N. Ultra-thin narrow-band, complementary narrow-band, and dual-band metamaterial absorbers for applications in the THz regime. *J Appl Phys.* (2017) **121**:063103. doi: 10.1063/1.4975687
29. Dayal G, Ramakrishna SA. Multipolar localized resonances for multi-band metamaterial perfect absorbers. *J Opt.* (2014) **16**:094016. doi: 10.1088/2040-8978/16/9/094016
30. Dayal G, Ramakrishna SA. Flexible metamaterial absorbers with multi-band infrared response. *J Phys D.* (2015) **48**:035105. doi: 10.1088/0022-3727/48/3/035105

Conflict of Interest: The authors declare that the research was conducted in the absence of any commercial or financial relationships that could be construed as a potential conflict of interest.

frontiers in Physics

ORIGINAL RESEARCH
published: 28 August 2020
doi: 10.3389/fphy.2020.00267

Ultra-Precision Replication Technology for Fabricating Spiral-Structure Metamaterial

Weiguo Zhang[1,2], *Guodong Zhu*[2], *Xiaoqiang Zhu*[2] *and Chunlei Du*[1,2]*

[1] School of Optoelectronic Engineering, Chongqing University, Chongqing, China, [2] Chongqing Institute of Green and Intelligent Technology, Chinese Academy of Sciences, Chongqing, China

Spiral-structure metamaterial (SSM) is of great importance, however, there are fewer methods to fabricate SSM due to limitations of material particularity and working accuracy. In this paper, a systematic scheme for fabricating SSM is proposed by employing the metal mold making with diamond-based ultra-precision turning technique and then molding replication method. By studying the path planning algorithm of the turning, molding error law, and a technique of how to compensate for the error, a solution for SSM is consequently formed. Our experimental results show a satisfying SSM with a surface roughness under 5 nm and a surface shape error under 0.63% of the designed wavelength (30 um). Moreover, this SMM element is processed within 10 min, with low cost materials and processes. Based on these advantages, our SSM processing scheme shows a remarkable potential in precise fabricating phase plates and industrialized application of terahertz metamaterial in the future.

Keywords: micron/nano-fabrication, spiral-structure matamaterial, optics, terahertz optics elements, microoptics, ultra-precision fabrication

OPEN ACCESS

Edited by:
Xufeng Jing,
China Jiliang University, China

Reviewed by:
Venu Gopal Achanta,
Tata Institute of Fundamental Research, India
Meina Zhang,
Qilu University of Technology, China

***Correspondence:**
Chunlei Du
cldu@cigit.ac.cn

Specialty section:
This article was submitted to Optics and Photonics, a section of the journal Frontiers in Physics

Received: *26 April 2020*
Accepted: *15 June 2020*
Published: *28 August 2020*

Citation:
Zhang W, Zhu G, Zhu X and Du C (2020) Ultra-Precision Replication Technology for Fabricating Spiral-Structure Metamaterial. Front. Phys. 8:267. doi: 10.3389/fphy.2020.00267

INTRODUCTION

Spiral-structure metamaterial (SSM) can modulate the beam of an electromagnetic plane wave into a spiral wave by controlling the spiral state of the electromagnetic wave. In this paper, we propose a method to fabricate the SSM in a wavelength range in 30 um ∼1 mm, which has an important application in many fields, such as quantum optics, communication, and sensing detection [1–4]. The relevant characteristic parameters require the fabrication between micro-machining and traditional machining. It is therefore difficult to use an existing fabrication technique to make the SSM with high precision and efficiency.

It was expected that the fabrication of SSM would need to involve the microlithography method and ultra-precision machining technique. For the microlithography technique, the available materials in the terahertz region mainly include quartz and silicon [5–9]. This technique has high machining precision with a quartz-based etching depth under 10 um and a silicon-based etching depth under 50 um. However, at such etching depths, the application requirement of the terahertz waveband is difficult to meet. Additionally, there are some other shortcomings when using the etching technique, such as tedious processing steps, long processing period, and a high cost. As for the ultra-precision machining technique, by employing the diamond cutter equipment which can be controlled with nanometer precision, both the processing area and adjustable precision will be greatly improved [10–13]. In fact, the diamond cutter is not suitable for terahertz materials such as polymethylpentene, polyethylene (PE), polypropylene, and polytetrafluoroethylene, while this cutter shows an excellent machinability in some other materials, for instance, metals and crystals

[14, 15]. The high-polymer-based terahertz material may cause obvious wear to the diamond cutter and may, consequently, influence the forming quality of SMM.

Combining the ultra-precision machining technique with the thermoplasticity of high-polymer -based materials, we present an ultra-precision replication method for fabricating the SSM. By applying the single-point diamond turning mold and using the error compensation technique, the error between device and design parameters can be reduced, and the SSM can be fabricated with high efficiency, high precision, and at a low cost.

PRINCIPLE OF THE ULTRA-PRECISION REPLICATION TECHNOLOGY FOR SSM

The Principle of the ultra-precision replication technology is shown in **Figure 1**. The whole fabrication process contains the fabrication of a diamond turning mold, replication of a high polymer device, demolding, and shape modification. Herein, the metal mold for turning was 7,075 aluminum material. The turning process is composed of substrate leveling, rough turning, and fine turning. It is therefore possible to improve the process efficiency of the mold and to reduce the wear of the cutter, while the homogeneity, surface form precision, and surface roughness of the mold are well controlled. Molding replication is accomplished through the tooling design, preheating, molding, heat preservation, and annealing. To realize the precise printing of the polymer material surface graphics, it is necessary to clarify the rule of distortion between the printing device and mold, which can provide a basis for mold error compensation technology.

DIAMOND ULTRA-PRECISION TURNING TECHNOLOGY FOR THE SSM MOLD

In the fabrication of the SSM mold, some parameters, such as surface roughness, surface shape precision, and machining efficiency, will have an influence. The key factor is the planning algorithm of the cutting tool path. In this paper, we propose two processing methods, i.e., the radial feeding method and the angular feeding method. A comparative analysis of the characteristics of these two methods is conducted.

Radial Feeding Method

For the radial feeding method, with every machining process of the cutter, the sample position remains unchanged, and the depth is equal in the same radius direction. With every cutting, the sample is rotated with a fixed angle by C axis, as shown in **Figure 2**. The relationship between the depth and angle is given by Equation (1):

$$h_\theta = \frac{\lambda\theta}{360n} \tag{1}$$

Where h_θ is the depth corresponding to a rotation angle θ, which starts from the highest point, λ is the terahertz wavelength, and n is refractive index of the high polymer material with respect to terahertz wave.

Angular Feeding Method

The principle of the angular feeding method is shown in **Figure 3**. During the machining process of the cutter, the work piece always remains rotational. By using the slow tool servo mode, the cuter is then processed with a fixed length in the direction from the external diameter to the center of the SSM over a period of a 360° rotation. After rotating the sample by an angle θ_m, the relation between the cutting depth of the cutter and rotational angle is shown as in Equation (2):

$$h_{\theta_\mathrm{m}} = \frac{\lambda(\theta_m - 360m)}{360n} \tag{2}$$

Here $h_{\theta m}$ is the depth corresponding to a rotation angle θ_m, which starts from the highest point (zero), λ is the terahertz wavelength, n is the refractive index of the high polymer material with respect to the terahertz wave, and m is the number of turns of the work piece.

Comparison of the Cutting Methods

In the SSM process, some key parameters are presented, such as low surface roughness, tiny surface profile error, and high processing efficiency. As for the surface profile error, both the radial feeding method and angular feeding method are restricted by the positioning precision of the equipment and the radius of curvature of the tool's nose. In the context of using similar equipment and a fixed cutter, there is a negligible difference between them. And for the surface roughness of the mold, it mainly relies on the radius of curvature of the cutter nose, the linear velocity in cutting, and the feeding velocity of the cutter.

For the radial feeding method, the linear velocity of the cutter is equal to the planning velocity of Y axis in a diamond lathe. Moreover, the liner velocity in cutting at a point is equal to each other. The feeding velocity of the cutter is the arc length from the center to edge of the work piece for each rotation. The feeding velocity in each point is proportional to a distance from the point to the center. In other words, with the increase of feeding velocity of the work piece, the roughness in processing is also increased.

For the axial spiral cutting method, the cutter is used for discrete cutting. Once the phase plate is rotated, the orthogonal coordinates are then transformed into the polar coordinates. The system obtains discrete points in terms of radian and traces the processing depth at each point. After finishing a period of processing, the cutter is propelled with some distance from the edge to the center of the work piece. When using discrete cutting, the influence of the linear velocity to surface roughness of the work piece can be considered with little focus due to the fast-tracking velocity. In contrast, the feeding velocity acts as the key factor influencing surface roughness, containing two velocity components in the axial and radial directions. The feeding velocity in the axial direction mainly relies on the revolving speed of the work piece and the point density. With the decrease in revolving speed and the increase of point density, the velocity is then decreased, resulting in low surface roughness on the work piece. Here the point density is related to the distance between a point and the center of a circle, and to the density in dividing angles. A large point density is obtained by reducing this distance

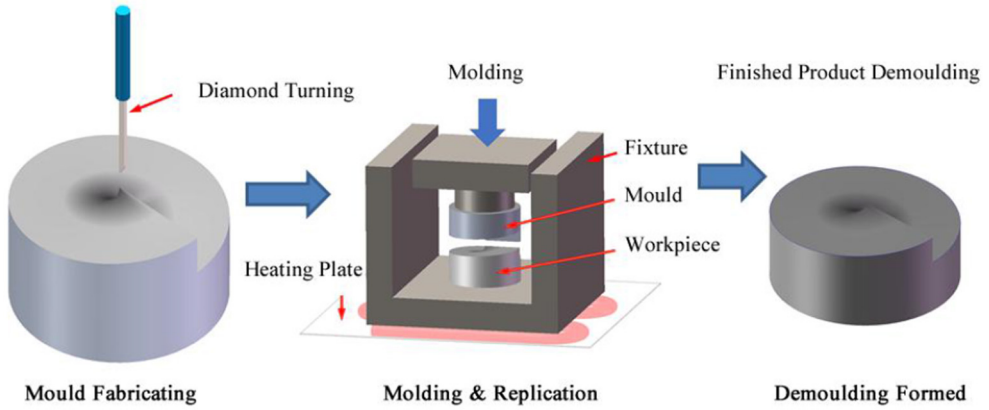

FIGURE 1 | Principle diagram of the SSM processing technique.

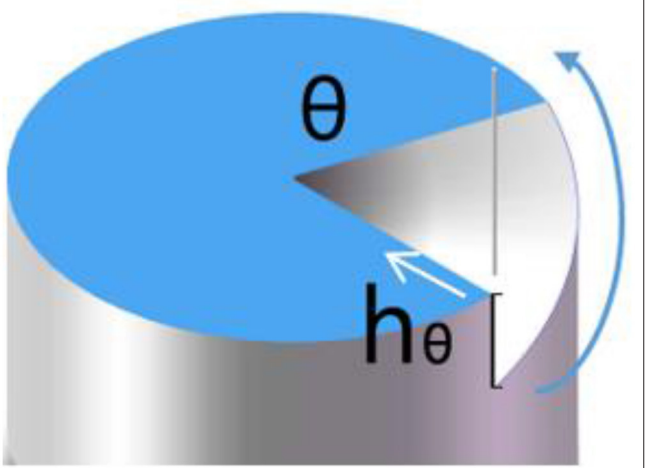

FIGURE 2 | Diagram of the radial feeding process. White arrows represent the cutting direction of the cutter, while the blue curved arrows represent the marching direction of the work piece. The work piece is rotated by a tiny angle increment $d\theta$ after cutting with a radius length by the planning cutter.

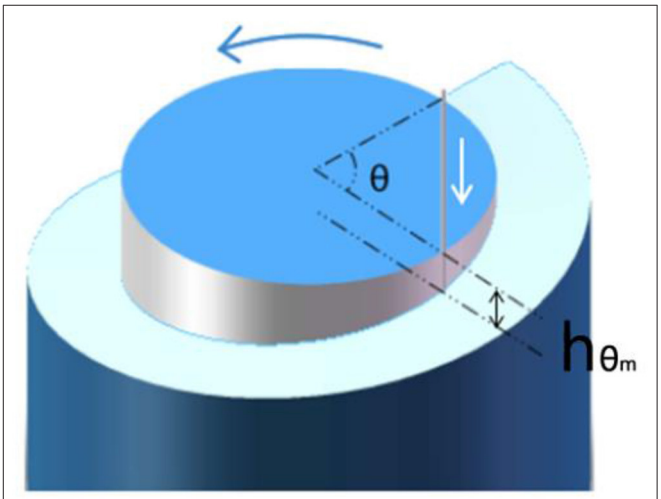

FIGURE 3 | Diagram of the angular feeding process. Blue curved arrows represent the cutting direction of the cutter, while the white arrows represent the motion track of the cutter along the cutting-in direction. Here the feed direction of sample is determined as the radial direction. After a rotation period, the sample is moved by a tiny distance ds along a plane perpendicular to the cutter away from the original point.

and increasing the angle density. As for the feeding velocity in the radial direction, it mainly relies on the marching velocity of the cutter in radial direction. In principle, a large velocity leads to large surface roughness.

In the case of reaching the precision limit of the equipment and process, it is possible to fabricate the SSM with low surface roughness and form error *via* the radial feeding method or the angular feeding method. However, from the point of processing efficiency, there is an obvious difference between the two methods. To attain similar surface roughness, the discrete precision in two methods was chosen as the rotational resolution of 1 arc s. For the angular feeding method, the processing time is calculated as:

$$T_1 = 2\pi \times 3600 \times \frac{r}{v} \times 2 = \frac{14400\pi r}{v} \tag{3}$$

Here r is the radius of spiral phase plate, and v is the linear velocity of Y axis that is ≤1,000 mm/min in general, which satisfies $T_1 \geq 14.4\pi r$. When working on the same samples, it is possible to form a same surface roughness through the angular feeding method. Based on this technology, the radial feeding is calculated at the edge for a period of a rotation. Hence, the radial feeding process time is given by:

$$T_2 = r \div \frac{2\pi r}{3600} \times \frac{3600}{f \times 60} = \frac{108000}{f\pi} \tag{4}$$

Where f is the servo tracking frequency of the cutter that is <1,000 Hz in general, therefore $T_2 \geq 108/\pi$. If T1 ≤ T2 (i.e., $14.4\pi r \leq 108/\pi$), which corresponds to a conversion result $r \leq$

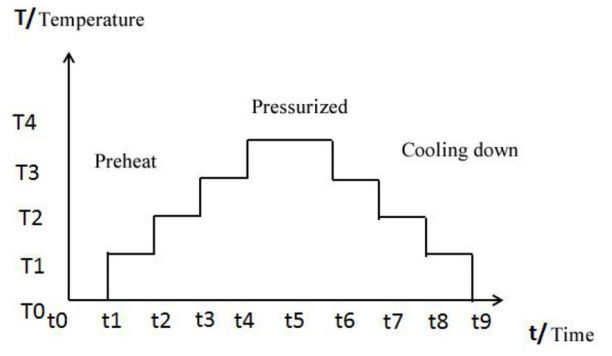

FIGURE 4 | Molding process diagram.

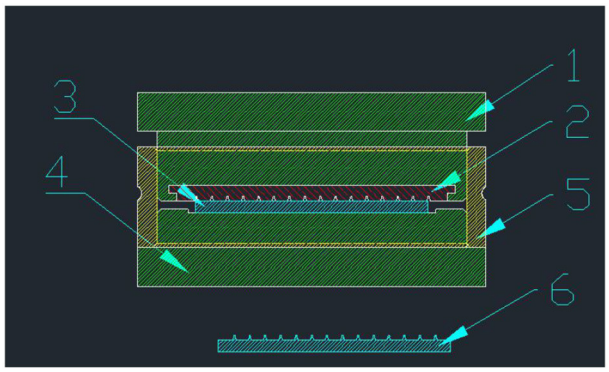

FIGURE 5 | Diagram of the fixture, 1 is the mold fixed plate, 2 is the mold, 3 is the PE substrate, 4 is the substrate fixed plate, 5 is the limited-position sleeve, and 6 is the fabricated SSM.

$7.5/\pi$, so it is more efficient to use the radial feeding method. In contrast, if $r \geq 7.5/\pi^2$, it is more suitable to use the angular feeding method.

COMPRESSION MOLDING OF POLYETHYLENE SSM

Polyethylene (PE) is kind of material with a good chemical and physical property in the terahertz region, such as high transmission, good dielectric properties, corrosion resistance, and radiation resistance. The refractive index is 1.54 in a broad spectral range. In this paper, PE material is utilized to illustrate how to fabricate the terahertz SSM. In order to achieve the SSM fabrication in batches, we have used the SSM mold to replicate a PE terahertz element.

Temperature Control Processing

The molding process diagram is shown in **Figure 4**. We first designed and made a work fixture and assembled the metal spiral phase plate and the PE substrate, as shown in **Figure 4**, followed by a heating and pressure treatment in the molding apparatus. Hence, a conformal deformation on the PE substrate is induced in terms of the surface morphology of the metal mold. Ultimately, the spiral structure on the surface of the PE substrate is cooled and solidified after the pressure treatment. We consequently disassembled the fixture and took out the PE SSM.

The main factors affecting the terahertz molding precision includes heating speed, temperature, heat preservation time, pressure size, and cooling speed, etc.

Fixture Design

When molding the SSM, we needed to keep the mold and PE substrate fixed, to avoid the relative displacement. Because the displacement will cause SSM deformation, a special fixture needed to be designed. The requirements for the fixture include the following: (1) The material of the mold should be resistant to high temperature; (2) the substrate and the mold need to be fixed, so that there is no lateral sliding between them when the pressure is forced, and (3) an exhaust mechanism is needed in the fixture. The pressure process gas will not be closed in the micro-structure of the sample, which will affect the die pressure accuracy of the micro-structure. (4) The pressure of the die press device can be transmitted vertically to the mold and substrate, to maintain the uniformity of the force.

In accordance with the above requirements, the fixture scheme that was designed is shown in **Figure 5**. The fixture consists of a substrate fixed plate, a mold fixed plate, and a limited-position sleeve. Both the PE substrate and the mold have a base plate fixed slot. The depth of the slot is slightly less than the thickness of the substrate and the mold. The height of the sleeve limits the final sample processing height, and the diameter of the limiting sleeve controls the slip between the substrate and the mold. In order to make an exhaust mechanism, a vent hole on the limiting sleeve should be opened.

Demolding of the SSM

In order to ensure that there is no adhesion between the mold and the substrate surface during the demolding process, we needed to make an anti-adhesion layer on the mold surface. Because some Fluorinated polymer materials have excellent characters such as high temperature tolerance and no adhesion with other material, we coated the polymer which contains fluorine element to make an anti-adhesion layer on the aluminum mold. The anti-adhesion layer should be as thin as possible, so that the polymer layer does not affect the structure on the mold. We used the steam plating coating method to make the thin layer.

In order to reduce the mechanical damage of molds and SSM components while demolding, we first make the PE substrate structure, the fixture and the mold are cooled to room temperature, thus all the elements are stable. Second, we used the mechanical devices to ensure that the demolding force direction was perpendicular to the surface of the PE substrate and mold, and the mold and the SSM were separated vertically, which can reduce the mechanical damage caused by the lateral sliding in the demolding process.

PROCESSING EXPERIMENT OF SSM

In order to present a systematic processing method, the following parameters were used: the topological charge number is 1, the diameter is 50 mm, and the depth difference between two sides of the total step is approximated as 55.56 um, which corresponds to a wavelength of 30 um.

Experiment of the Cutting Tool Wear in Metal and PE Cutting

The cutting properties of metals and PE materials were studied through an experiment. The cutting speed was set as 10 mm/s, the cutting depth is 50 um, the cutting length is 50 mm per round, and the diamond tools with curvature radius is 0.4 mm. After a total of 10 rounds of cutting, the tool wear was observed under a microscope, as shown in **Figure 6**. **Figure 6a** is the picture of the tool after the aluminum has been cut, the results show that the tool has little wear. **Figure 6b** shows the tool after the PE has been cut, and the tool wears significantly and a gap phenomenon appears, which shows that the diamond turning methods cannot be used in PE materials processing. Therefore, the molding method is necessary in PE SMM fabrication.

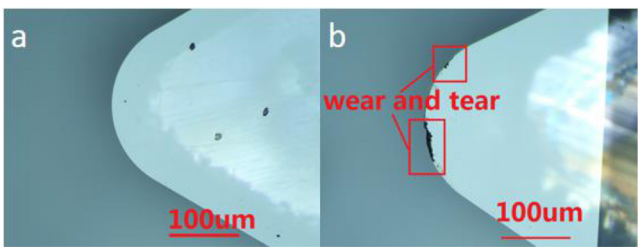

FIGURE 6 | (a) Is the picture of tool's wear after cutting aluminum; **(b)** is the picture of tool's wear after cutting PE material.

Experiment of the Radial Feed Method and Angular Feed Method

Taking the SSM with 50 mm diameter and 55.56 um total depth as an example, this paper adopted the 7,075 Aluminum Material as the substrate and carried out the diamond ultra-precision cutting of the mold. We employed the diamond lathe from Moore company in US (Nanotech350FG) and made the mold turning experiment. After processing, the surface profile data of SSM were measured by the white-light interferometer, and then the obtained data were processed and analyzed by MATLAB software. Due to the limitation of the FOV of measurement equipment and data volume of the analysis, we measured the area of 5 × 4 mm in the middle of the SSM. In theory, the pattern distribution outside 5 mm is the same as that along radial direction. The periodicity error caused by tool marks is

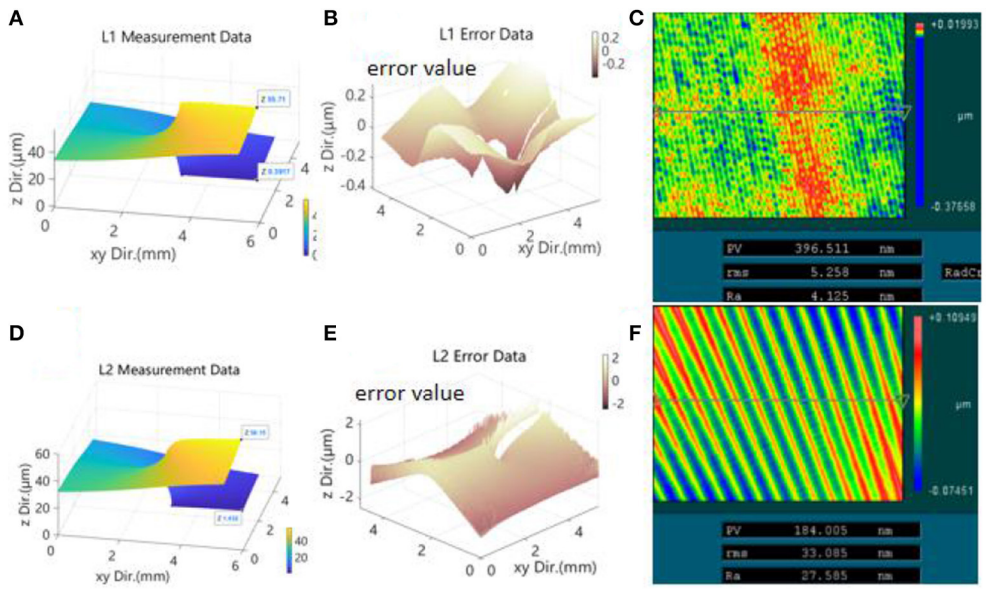

FIGURE 7 | Graph **(A)** is the measurement data of SSM which is processed by the method of angular feeding, it can clearly be seen that the SSM is a spiral structure; Graph **(B)** is the error analysis data between graph **(A)** and the theoretical data, horizontal coordinate represents the measurement data location on the plane of SSM, and vertical coordinate represents the error data value, the PV value of the error data is about 0.7 um; Graph **(C)** is the roughness data of the SSM that was fabricated by angular feeding, this figure was taken by white light interferometer under 10× objective, and the figure size is about 0.4 × 0.3 mm. The color bar represents the roughness value of the SSM, and the PV, rms, and Ra values which were shown in the table was calculated by the instrument's own software. From the table we can see that the Ra value of roughness is about 4.1 nm. Graph **(D)** is the measurement data of SSM which is processed by the method of radial feeding, it can clearly be seen that the SSM is a spiral structure; Graph **(E)** is the error analysis data between graph **(D)** and the theoretical data, it is the same format as figure. **(B)**, the PV value of the error data is about 4.1 um; Graph **(F)** is the roughness data of the SSM that is fabricated by the radial feeding method, it is the same format as figure. **(C)**, and the Ra value of roughness is about 27.5 nm.

proportional to the radius. The results of the processing are shown in **Figure 7**. **Figure 7A** is a three-dimensional profile produced by the angular feeding method. The scheme of one-step roughing, one-step semi-finishing, and one-step finishing were adopted. The cutting depth was 40, 10, and 5 um, respectively, and the feed speed was 10, 5, and 2 mm/min, and the turning speed of the lathe was 20 rpm. The overall mold processing time was 20 min, and the precision of the pattern surface error PV value was 700 nm, as shown in **Figure 7B**, and the surface roughness Ra value was about 4.1 nm, as shown in **Figure 7C**. **Figure 7D** is a three-dimensional contour map produced by the radial feeding method. The scheme of one-step roughing, one-step semi-finishing, and one-step finishing was adopted. Each cutting depth was 40, 10, and 5 um, respectively, and each step was 0.5, 0.2, and 0.1°. The cutting speed was 600 mm/min. After each line had been cut, the tool must return to the center before the next line can be cut, and the total processing time was 15 h. The three-dimensional profile of SMM is shown in **Figure 7D**, and the surface accuracy error PV value was about 4.78 um, which is shown in **Figure 7E**. Finally, the surface roughness Ra value was about 27.5 nm, as shown in **Figure 7F**. The experimental results are in good agreement with the theoretical results in Chapter 2. In the process of making SMM, the machining method of rotating around the axis had obvious advantages in machining efficiency and accuracy.

Experiment of PE SSM Molding Processing

After the mold of SSM was fabricated, we fabricated the PE material SSM using the precision molding method. First, we assembled these elements and then used the sleeve to fix them. Afterwards, the assembled work piece was placed into MYLMR-3300 molding equipment, and we improved the temperature from the indoor temperature. Note that a temperature of 20°C should be maintained for 1 min for each improvement. When the temperature reached 130°C, we imposed a pressure of 0.22 MPa on the work piece for 5 min. With this pressure, we refrigerated the work piece to a temperature <40°C, with a cooling rate of 20°C/min. Ultimately, by repealing the pressure treatment and disassembling these elements, the molded SSM was taken out. The graph of the mold and PE SSM is shown in **Figure 8**. The picture of the SSM mold is shown in **Figure 8a**, and the step height of the mold is shown in **Figure 8c**, which is about 55.41 um. **Figure 8b** is the picture of the molded PE SSM, and the molded PE SSM step height is shown in **Figure 8d**, which is about 55.37 um. From these data we could see that the step height error between the mold and PE SSM was only about 40 nm, which was about 0.1% in the total step height. The step height error between PE SSM and the theoretical value was about 0.19 um, here this error accounts for 0.34% of the total depth, which is 0.63% of the designed wavelength. The roughness was 3.1 nm, which accounts for only about 0.01% of the wavelength, resulting in a negligible influence on the terahertz optical property.

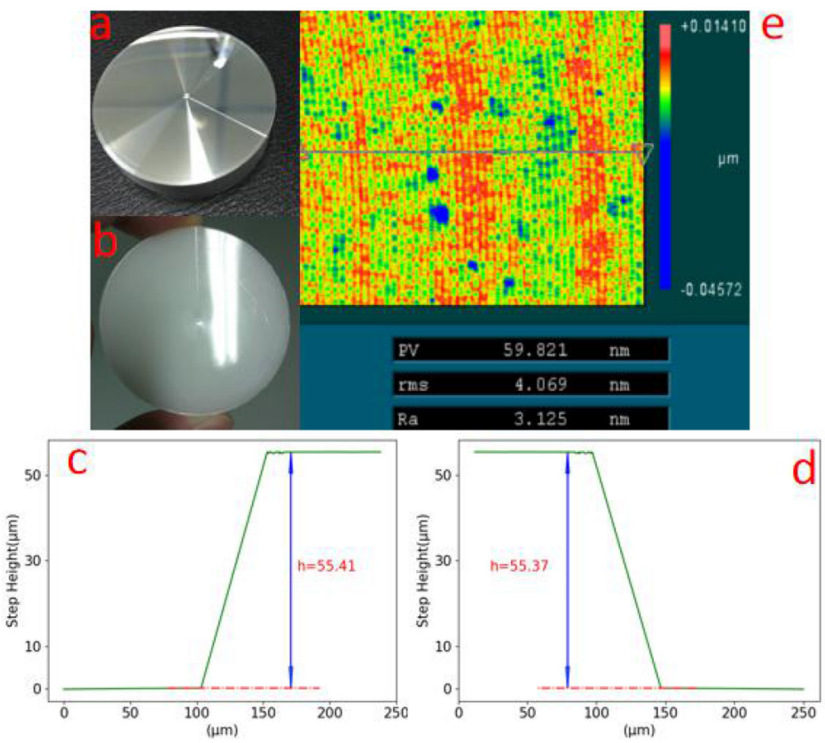

FIGURE 8 | Graph **(a)** is the picture of the Metal SSM mold; graph **(b)** is the picture of PE SSM product; graph **(c)** is the measurement data of step height of the SSM mold, that is about 55.41 um; graph **(d)** is the measurement data of the step height of the PE SSM, which is about 55.37 um; **(e)** is the measurement data of the roughness of the PE SSM, which is about 3.1 nm.

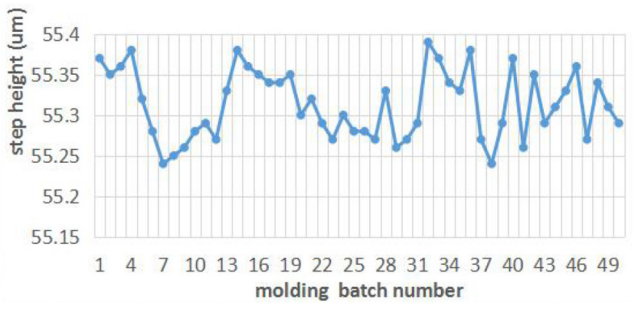

FIGURE 9 | Measurement data of step height repeatability experiment.

Experiment of the Molding Repeatability Test

In order to study the repeatability of the molding process of PE SSM, we used the same molding process parameters and carried out molding experiments. According to the analysis of the difference between the surface step height value between each batch number of molding, the repeatability of this method is estimated, to judge the feasibility of mass production. Due to the limitation of the cost of material and time, 50 molding experiments were carried out. The results in **Figure 9** show that the step height of PE SSM is between 55.24 and 55.38 um, the repeatability can reach about 0.25%, and the step height error between PE SSM and the designed value is about 0.58%. We then checked the mold surface after the molding, and there was no significant change before the molding.

CONCLUSION

By developing a process method for the diamond turning and molding technology, we have accomplished a precision process of SSM, which provides an effective means for the bulk-production of SSM. In fact, our experimental results show that there no limit in application to what this technique can achieve. Our process method may be suitable for some other applications, such as a terahertz lens, terahertz beam splitter prism, and a terahertz plane mirror. Moreover, through error compensation of the mold and by optimizing our molding process, the processing precision of PE SSM has potential to be even further improved.

DATA AVAILABILITY STATEMENT

The raw data supporting the conclusions of this article will be made available by the authors, without undue reservation.

AUTHOR CONTRIBUTIONS

All authors listed have made a substantial, direct and intellectual contribution to the work, and approved it for publication.

FUNDING

This work was supported by the Natural Science Foundation of China (61775213) and Natural Science Foundation of Chongqing, China (cstc2019jcyj-msxmX0352).

REFERENCES

1. Fan RH, Zhou Y, Ren XP, Peng RW, Jiang SC, Xu DH, et al. Freely tunable broadband polarization rotator for terahertz waves. *Adv Mater.* (2015) **27**:1201–6. doi: 10.1002/adma.201404981
2. Liu C, Wei X, Niu L, Wang K, Yang Z, Liu J. Discrimination of orbital angular momentum modes of the terahertz vortex beam using a diffractive mode transformer. *Opt Express.* (2016) **24**:12534–41. doi: 10.1364/OE.24.012534
3. Sabah C, Roskos HG. Design of a terahertz polarization rotator based on a periodic sequence of chiral-metamaterial and dielectric slabs. *Prog Electromagn Res.* (2012) **124**:301–14. doi: 10.2528/PIER11112605
4. Lu B, Wang H, Shen J, Yang J, Mao H, Xia L, et al. A high extinction ratio THz polarizer fabricated by double-bilayer wire grid structure. *AIP Adv.* (2016) **6**:025215. doi: 10.1063/1.4942515
5. Ma T, Shen YB, Yang GG. Improving diffraction efficiency of DOE in wide waveband application by multilayer micro-structure. *Infared Laser Eng.* (2008) **37**:119–23. doi: 10.3969/j.issn.1007-2276.2008.01.027
6. Kong X, Fu Y, Xia L, Zhang W, Zhang Z, Dong L, et al. Analysis of Ag nanoparticle resist in fabrication of transmission-enhanced subwavelength structures. *J Nanophotonics.* (2016) **10**:046017. doi: 10.1117/1.JNP.10.046017
7. Wang Y, Zhang W, Yang Z, Xiong X, Xia L, Gao M, et al. Fabrication of large area diffractive optical elements by laser direct writing. In: *2016 IEEE International Conference on Manipulation, Manufacturing and Measurement on the Nanoscale (3M-NANO).* Chongqing: IEEE (2016).
8. Liu M, Xie C. *Microfabrication Technology*. Beijing: Chemistry industry press (2004). 11–2 p.
9. Herzig HP. *Micro–Optical Elements, System and Application*. Beijing: National Defense Industry Press (2002). 156–8 p.
10. To S, Wang H, Jelenković EV. Enhancement of the machinability of silicon by hydrogen ion implantation for ultra-precision micro-cutting. *Int J Mach Tools Manu.* (2013) **74**:50–5. doi: 10.1016/j.ijmachtools.2013.07.005
11. Ji C, Zhu G, Zhang C, Nam S, Li Q, Xia L. Lenticular-lens-based colored antiglare dashboard surfaces. *Adv Mater Technol.* (2016) 2:1600177. doi: 10.1002/admt.201600177
12. Zhang SJ, To S, Wang SJ, Zhu ZW. A review of surface roughness generation in ultra-precision machining. *Int J Mach Tools Manu.* (2015) **91**:76–95. doi: 10.1016/j.ijmachtools.2016.01.001
13. Nishio Y, Fujimura K, Ogihara S, Okano M, Kitagawa S. Random micro-lens array illumination device manufactured by ultra-precision machining. *SPIE.* (2015) **8794**:271–350. doi: 10.1117/12.2037486
14. Hao W, Lianhe D, Guodong Z, Dong Z, Weiguo Z. Fabrication of quartz microlens array by using ultra-precision turning mask. *Opto-Electron Eng.* (2018) **45**:170671. doi: 10.12086/oee.2018.170671
15. Zhang W, Liu F, Zhu G, Wang D, Xiong X, Du C. Fabricating fresnel mirrors imaged in visible light region by ultra precision manufacturing technology. In: *IEEE International Conference on Manipulation*. Chongqing: IEEE (2016). doi: 10.1109/3M-NANO.2016.7824966

Conflict of Interest: The authors declare that the research was conducted in the absence of any commercial or financial relationships that could be construed as a potential conflict of interest.

frontiers in Physics

ORIGINAL RESEARCH
published: 04 September 2020
doi: 10.3389/fphy.2020.00279

Dual-Band Microstrip Antenna Based on Polarization Conversion Metasurface Structure

Huiming Yao[1†], *Xinyi Liu*[1†], *Hongbo Zhu*[1], *Haihong Li*[1], *Guoyan Dong*[2*] *and Ke Bi*[1,3*]

[1] School of Science, Beijing University of Posts and Telecommunications, Beijing, China, [2] College of Opto-Electronic Technology, University of Chinese Academy of Sciences, Beijing, China, [3] Beijing University of Posts and Telecommunications Research Institute, Shenzhen, China

A dual-band microstrip patch antenna (MPA) based on a polarization conversion metasurface structure was designed. By etching the complementary split ring resonator (CSRR) on the ground plane, a new resonance frequency is generated. The proposed antenna is obtained through optimizing the structural parameters of CSRR. Compared with the antenna without CSRR, the return loss of the proposed antenna increases by ∼40% at the original resonance frequency. The measured results are similar to the simulated results, verifying the reliability of the antenna. This work introduces a new way of designing multi-band antenna.

Keywords: microstrip antenna, dual-band, polarization conversion, metasurface structure, complementary split ring resonator

OPEN ACCESS

Edited by:
Xufeng Jing,
China Jiliang University, China

Reviewed by:
Xiaojian Fu,
Southeast University, China
Shobhit K. Patel,
Marwadi University, India
Fenglong Wang,
Shandong University, China

***Correspondence:**
Guoyan Dong
gydong@ucas.ac.cn
Ke Bi
bike@bupt.edu.cn

[†]*These authors have contributed equally to this work*

Specialty section:
This article was submitted to Optics and Photonics, a section of the journal Frontiers in Physics

Received: *14 May 2020*
Accepted: *22 June 2020*
Published: *04 September 2020*

Citation:
Yao H, Liu X, Zhu H, Li H, Dong G and Bi K (2020) Dual-Band Microstrip Antenna Based on Polarization Conversion Metasurface Structure. Front. Phys. 8:279. doi: 10.3389/fphy.2020.00279

INTRODUCTION

An antenna plays an important role in modern wireless communication systems. In recent years, the miniaturization and multi-functionalization of communication devices require that the internal antenna has strong integration capabilities [1, 2]. Meanwhile, owing to the lack of wireless spectrum resources, the demand for multi-band antenna has increased [3–5]. Microstrip patch antenna (MPA) are extensively used due to their advantages of small size, simple structure, low cost, and ease of integration [6, 7]. Many methods have been studied to obtain multi-band antenna, such as coupling feed technologies [8], slot-loaded technologies [9], and reconfigurable technologies [10, 11]. Unfortunately, these methods require complex calculation, and the antenna structures are difficult to manufacture. Thus, new designs should be explored to simplify the structure and theoretical analysis.

Metasurface, due to its extraordinary electromagnetic properties, is widely used in antenna design [12–14], namely in the realization of multi-band [15, 16], ultra-wide-band [17–19], and high-gain antenna [20, 21]. In most cases, the metasurface structure is loaded on the antenna as a radiating element. The capability of a multi-band operation is not currently apparent. Many efforts have been made to solve this problem, such as etching a complementary split ring resonator (CSRR) on the ground plane. The CSRR unit cell can resonate with an electromagnetic wave, resulting in new resonance peaks. Ali et al. [22] created a triple-band antenna by etching rectangular and circular CSRRs. Zhou et al. [23] fabricated a composite right/left-handed structure as the radiating element and employed a square CSRR to get a dual-band antenna. Xu et al. [24] used a simple square split ring resonator to design an ultra-broad-band linear polarization converter, which provided a way to change the antenna polarization mode. We have recently obtained a broadband microstrip patch antenna by using a complementary rhombus resonator [25].

In this work, we designed a dual-band MPA loaded with a CSRR structure. The CSRR serves as a resonator. From the simulated results, it is found that the MPA exhibits excellent performance within the dual-band resonance in the range of 3.0–7.5 GHz. The measured results are similar to the simulated ones, which proves that the proposed antenna can be well–applied to physical devices.

ANTENNA DESIGN

C-band antenna have been widely used in satellite communication and navigation [26]. Therefore, we designed an antenna operating at 6.9 GHz. The top and back view of the antenna are, respectively, shown in **Figures 1A,B**. The upper layer of the antenna consists of a rectangular patch, and two different-width feedlines. The middle layer is an FR4 substrate with a relative dielectric constant of 2.65 and the lower layer is a metal ground plane. In order to realize the design of the dual-band antenna, the ground plane is modified. As shown in **Figure 1C**, CSRR was etched on the ground plane which is used to generating new resonance frequency. To further improve the electromagnetic performance of the antenna, a series of parameter optimization was carried out, and the ground plane of the proposed antenna is shown in **Figure 1D**.

The simulated results of the proposed antenna are shown in **Figure 2**, with a series of side length r, split width d, rotation angle θ, and distance h. It can be seen that the original resonance frequency is affected by length r, split width d, and rotation angle θ, while the new resonance frequency is mainly tuned by distance h. According to **Figure 2A**, as r increases from 15.0 to 16.5 mm, the original resonance frequency moves to the lower frequency. When $r = 16.0$ mm, the return loss at the original resonance frequency is maximum. **Figure 2B** demonstrates that, as d increases from 0 to 4.5 mm, the original resonance frequency moves to the higher frequency. When $d = 0$, which means CSRR is a closed ring, the original resonance disappears. At this time, the antenna only works in S-band. As displayed in **Figure 2C**, when θ increases from 0 to 45°, the original resonance frequency moves to the lower frequency. Moreover, when $\theta = 30°$, the return loss at the original resonance frequency reaches maximum. **Figure 2D** depicts that, as h increases from 24.0 to 25.5 mm, the new resonance frequency moves to the lower frequency. When $h = 24.5$ mm, the return loss at new resonance point is at its maximum, now the centers of CSRR and the substrate coincide. Considering the performance of antenna comprehensively, we designed the ground plane of the proposed antenna as **Figure 1D**. The parameters of the proposed antenna are listed in **Table 1**.

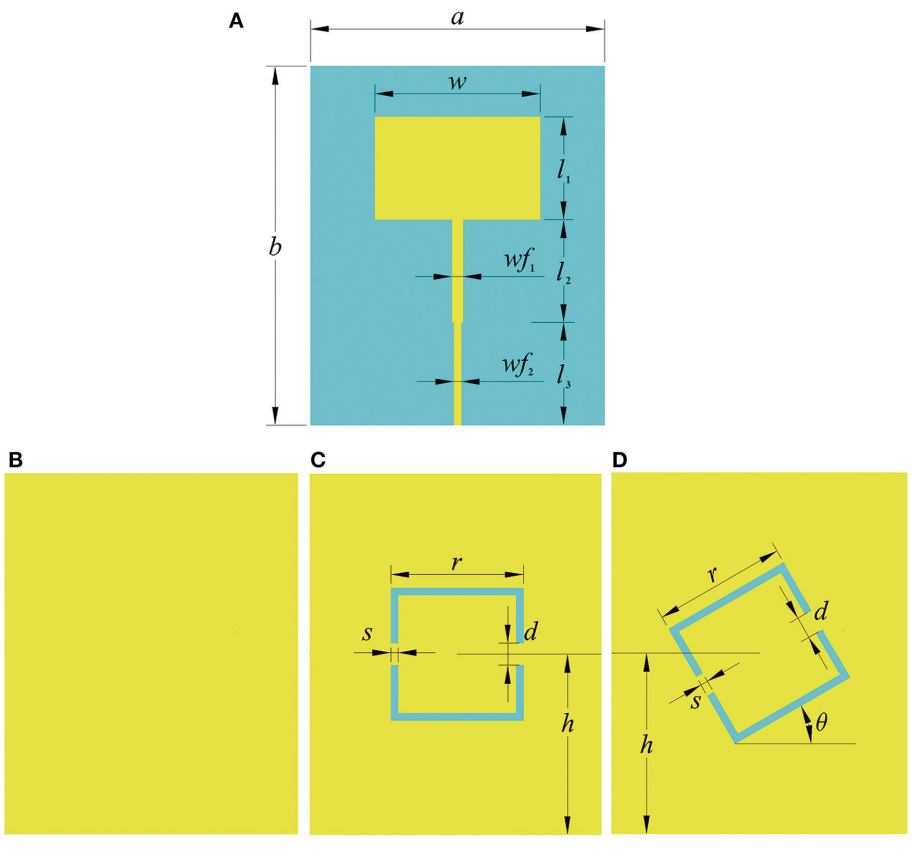

FIGURE 1 | (A) Top view and **(B–D)** design process for the ground plane of the proposed antenna.

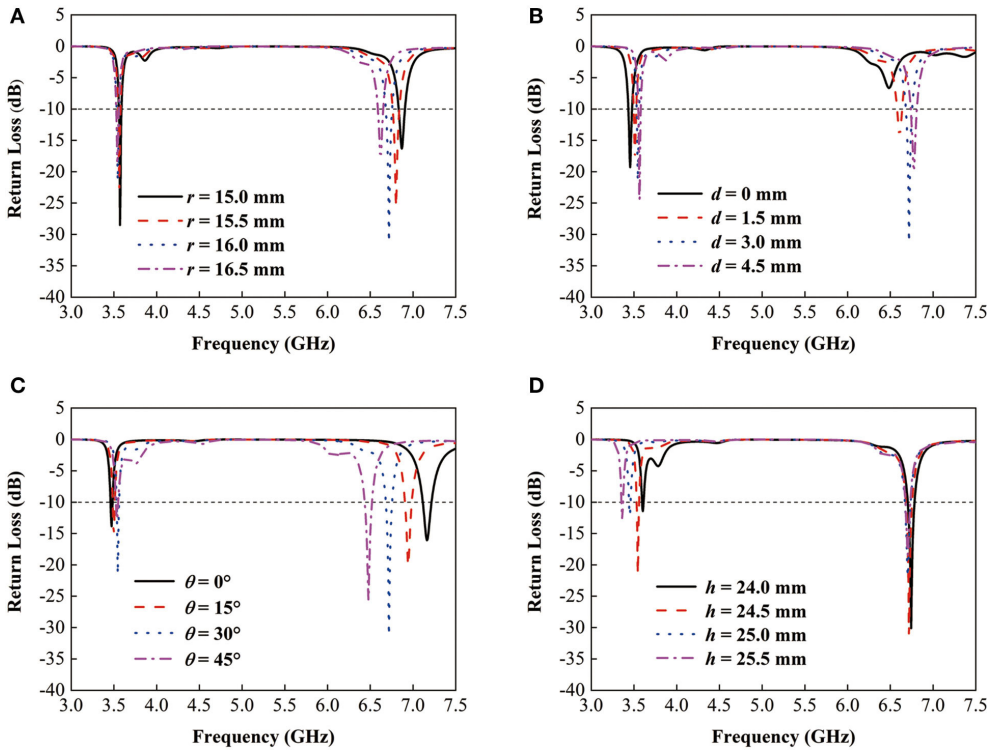

FIGURE 2 | Return loss of the proposed antenna with a series of **(A)** side length *r*; **(B)** split width *d*; **(C)** rotation angle θ; **(D)** distance *h*.

TABLE 1 | Parameters of the proposed antenna.

Parameter	Value	Parameter	Value
a	40.0 mm	*b*	49.0 mm
t	1.5 mm	*w*	22.5 mm
wf_1	1.5 mm	wf_2	1.0 mm
t_1	0.035 mm	l_1	14.0 mm
l_2	14.0 mm	l_3	14.0 mm
r	16.0 mm	*d*	3.0 mm
s	1.0 mm	*h*	24.5 mm
θ	30°		

To intuitively illustrate the effect of CSRR on the antenna frequency band, the return loss of the original antenna and the proposed antenna are compared. As shown in **Figure 3**, it can be inferred that the proposed antenna has a new resonance peak centered at 3.54 GHz with a return loss of 21.4 dB. The original resonance frequency shifts from 6.87 to 6.72 GHz, and its return loss increases from 22.1 to 31.2 dB.

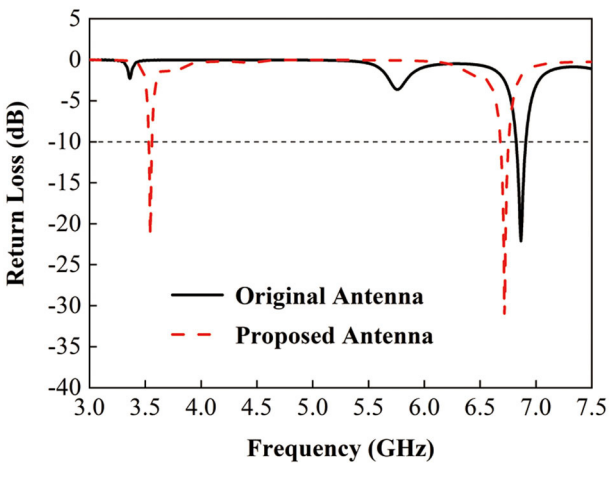

FIGURE 3 | Return loss of the original antenna and the proposed antenna.

RESULTS AND DISCUSSION

In order to explain the work principle of CSRR, the surface current distribution of the antenna is observed. **Figure 4** shows the surface current distribution of the antenna without CSRR at 6.87 and 5.00 GHz. From **Figures 4A,B**, we can see that the current density at 6.87 GHz is higher than 5.00 GHz. It can be deduced that the electromagnetic wave of a specific frequency is excited by the rectangular patch and the feedlines, resulting in resonance at 6.87 GHz.

Figure 5 shows the surface current distribution of the antenna with CSRR at two resonance frequencies. It can be observed that the current is no longer limited between the radiation patch and feedlines. It also distributes around CSRR, which demonstrates that the CSRR can act as a resonator to generate new resonance peak. Obviously, etching CSRR damages the structure of the

ground plane, so that the current distribution is changed. Moreover, the current shocks back and forth in the CSRR, radiating a specific frequency of electromagnetic wave. However, there are some differences in the surface current distribution of **Figures 5A,B**. At the frequency of 3.54 GHz, the surface current mainly distributes around the CSRR. Thus, the new generated resonance peak is mainly affected by the parameters of the CSRR. Similarly, the resonance peak centered at 6.72 GHz is modulated by the rectangle patch and CSRR.

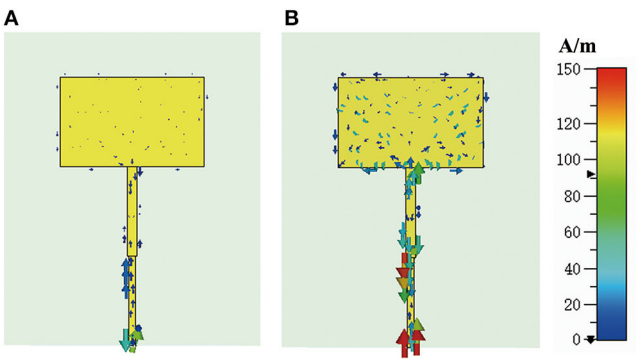

FIGURE 4 | Surface current distributions of the original antenna: **(A)** 5.00 GHz; **(B)** 6.87 GHz.

In order to figure out why CSRR can be used as a resonator, a few more details are exhibited. Comparing the results shown in **Figure 5**, it can be observed that the surface current distributes around the whole CSRR at 3.54 GHz, while only the lower half of CSRR has a current distribution at 6.72 GHz. It can be inferred that CSRR serves as a frequency-controlled switch which only opens at specific frequencies. When the switch is closed, the current in the CSRR shocks back and forth, resulting in new resonance within the antenna at 3.54 GHz. When the switch is on, the electromagnetic wave is only generated by the lower section of CSRR and it couples with the antenna radiating element, resulting in the original resonance point shifting by ∼0.15 GHz. Combining with the return loss diagram in **Figure 3**, it can be concluded that the return loss at the resonance frequency increases by ∼40%.

CSRR can not only produce resonance peaks as a resonator, but also affect the radiation characteristics of the antenna. To analyze the effect of CSRR on the polarization mode, the

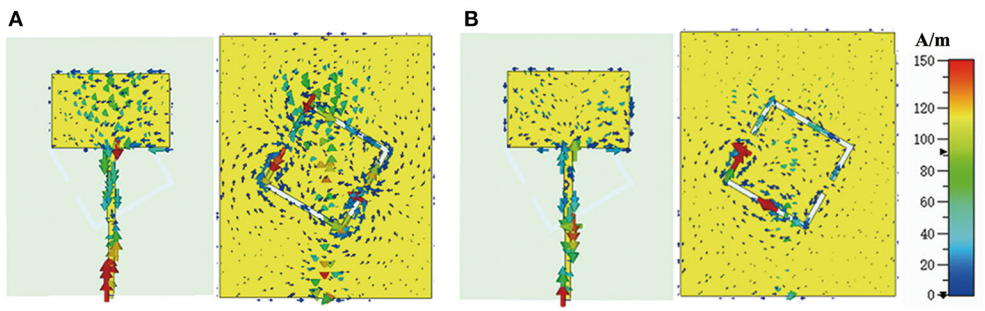

FIGURE 5 | Surface current distributions of the proposed antenna: **(A)** 3.54 GHz; **(B)** 6.72 GHz.

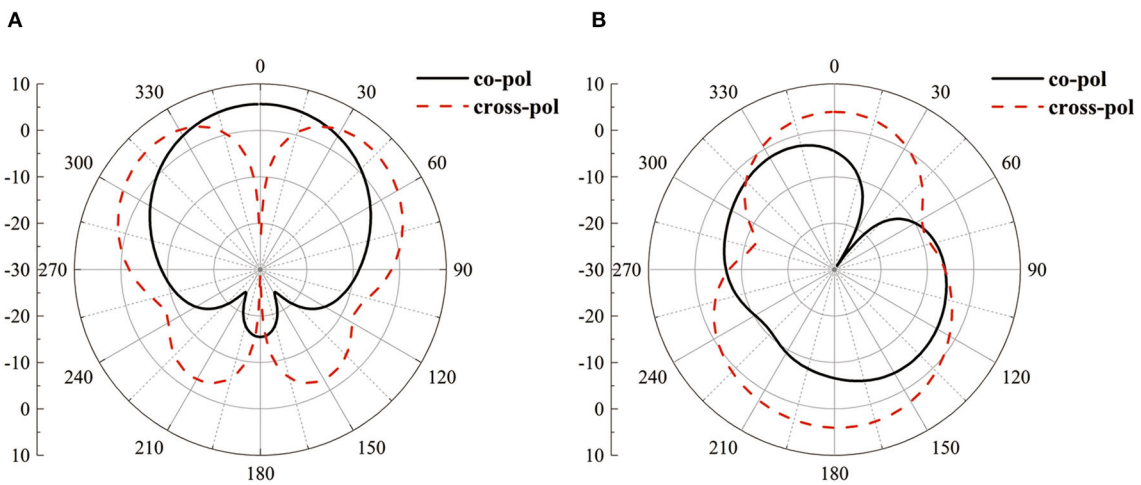

FIGURE 6 | Polarization direction of the antenna: **(A)** 6.87 GHz (the original antenna); **(B)** 6.72 GHz (the proposed antenna).

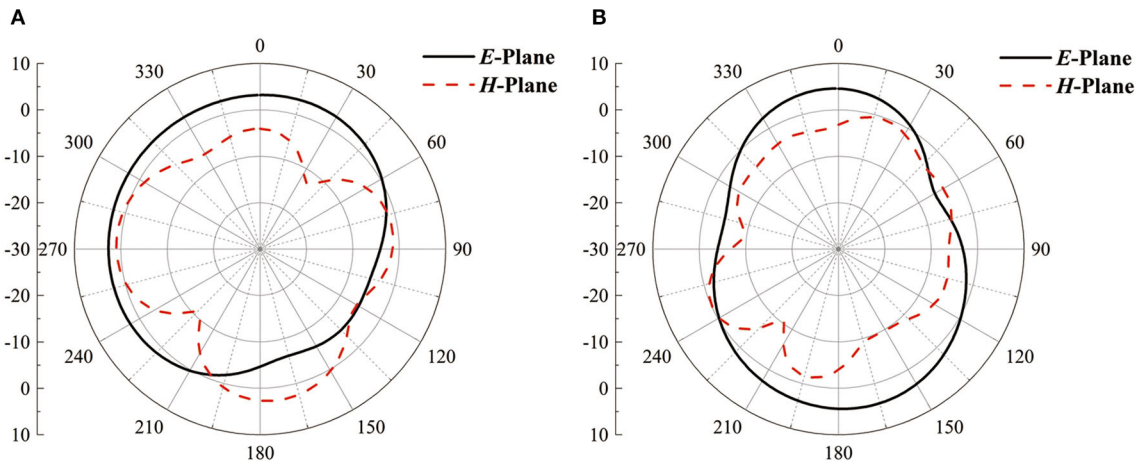

FIGURE 7 | Radiation patterns of the proposed antenna: **(A)** 3.54 GHz; **(B)** 6.72 GHz.

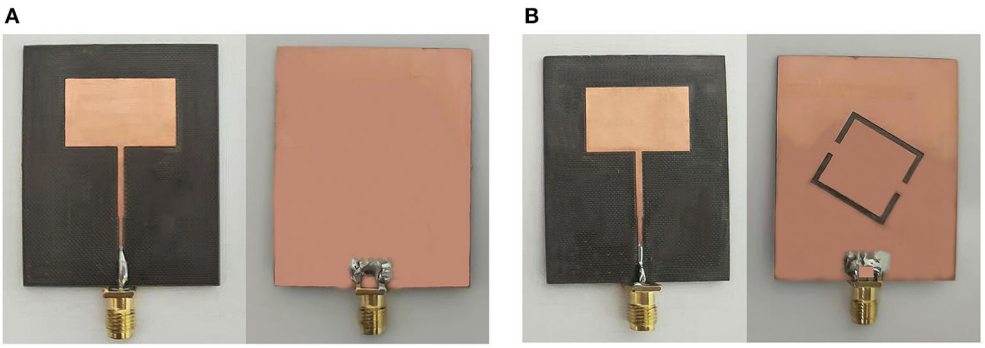

FIGURE 8 | Photographs of the fabricated antenna: **(A)** the original antenna; **(B)** the proposed antenna.

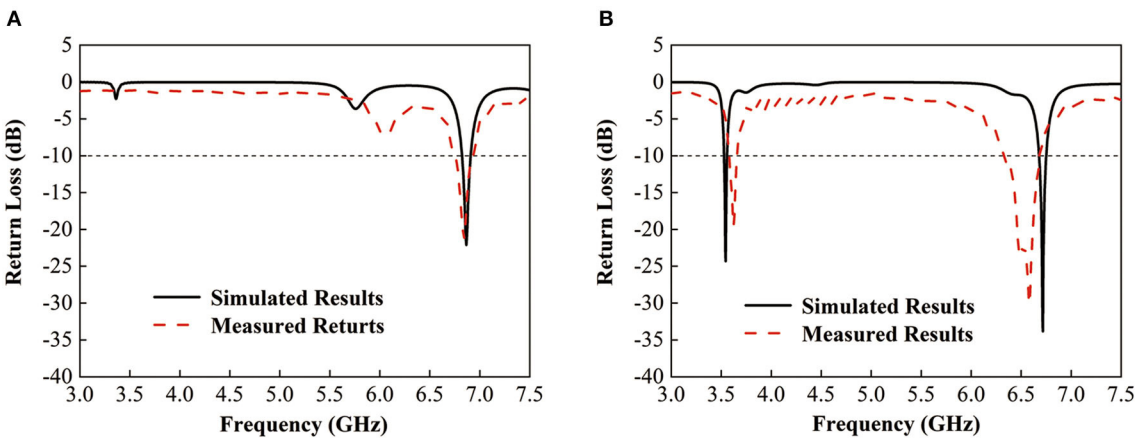

FIGURE 9 | Simulated and measured return loss of the antenna: **(A)** the original antenna; **(B)** the proposed antenna.

polarization direction of the antenna with and without CSRR are shown in **Figure 6**. **Figure 6A** shows that the polarization direction of the antenna without CSRR is symmetrical at 6.87 GHz, while **Figure 6B** indicates that the symmetry of the antenna with CSRR is broken at 6.72 GHz. It can be interpreted that the polarization mode of antenna is highly related to its

TABLE 2 | Comparison of the antenna performances of this work and the previous literatures.

References	Antenna size (mm^2)	Number of resonance peaks	Operating frequency band	Resonance frequencies (GHz)/ Peak gain (dBi)
[8]	50 × 58	4	S, C, X	2.1/1.30 3.3/1.59 5.3/2.12 7.5/3.73
[14]	5 × 5	1	C	—
[22]	60 × 60	3	S, C	2.45/1.03 3.56/5.10 5.60/5.41
This work	40 × 49	2	S, C	3.54/4.78 6.72/4.65

structure and changes within the structure. In order to better evaluate the antenna performance, the radiation patterns of the proposed antenna at resonance points are investigated as shown in **Figure 7**. It can be seen that the radiation patterns in *H*-Plane are almost omnidirectional and the radiation patterns in *E*-Plane are monopole-like. In addition, the distortion of the radiation patterns is extremely slight, which proves that the introduction of CSRR has almost no effect on the performance of the antenna.

To verify the simulated results, the original antenna and the proposed antenna are fabricated, measured, and compared. A circuit board engraving machine is used to fabricate the antenna and a vector network analyzer (VNA) is used to measure the electromagnetic properties of the antenna. The fabricated antenna are shown in **Figure 8**. The simulated and measured return loss of the original antenna and the proposed antenna are shown in **Figure 9**. From **Figure 9A**, the two curves have a nearly consistent trend and the resonance peaks almost coincide. As depicted in **Figure 9B**, the two measured resonance frequencies move from 3.54 and 6.72 GHz to 3.62 and 6.58 GHz, respectively. Compared with the simulated curves, the return loss decreases by 3–4 dB. Considering the inevitable errors in the process of antenna manufacturing, welding, and measuring, the above deviation can be ignored. Similarly, the fact that the bandwidth of measured curves is broader than the simulated curves is also due to fabrication and measurement errors. Therefore, the measured results correlate with the simulated ones, which proves the reliability of the antenna.

Based on the above analysis, it can be summarized that an antenna etched with CSRR performs excellently despite being small in size and containing a simple structure. Furthermore, we compared the dual-band antenna designed in this work with other literature [8, 14, 22] in terms of size, number of resonance peaks, operating frequency bands, and peak gain, as listed in **Table 2**. It is observed that, in other works, multi-band antenna are larger, while small size antenna operate at single-band. The design of our work realizes both miniaturization and multi-band in an antenna, which widens the possibilities for multi-band antenna design.

CONCLUSION

In conclusion, a dual-band MPA etched with CSRR was designed. The proposed antenna with high performance was obtained by optimizing the structural parameters of CSRR. Based on the simulated results of surface current distribution, it was found that the current shocks back and forth in the CSRR, generating a new resonance peak. By adjusting the rotation angle of the CSRR, an obvious resonance frequency appears. Moreover, the consistency between the simulation and the recorded measurement demonstrates the validity of the design. This work provides a new way to design multi-band antenna.

DATA AVAILABILITY STATEMENT

The raw data supporting the conclusions of this article will be made available by the authors, without undue reservation.

AUTHOR CONTRIBUTIONS

HY, KB, and XL designed the structure and fabricated the sample. HZ and HL performed the experiments. HY, HL, and KB wrote the manuscript with contribution from all the other authors. All authors participated in the discussion of the results.

FUNDING

This work was supported by the National Natural Science Foundation of China (Grant Nos. 51972033, 61774020, 51788104, 61672108, 11574311, and 61976025), Science and Technology Program of Shenzhen Science and Technology Innovation Commission (Grant Nos. JCYJ20180306173235924 and JCYJ20180305164708625).

REFERENCES

1. El-Halaoui M, Kaabal A, Asselman H, Ahyoud S, Asselman A. Multiband planar inverted-F antenna with independent operating bands control for mobile handset applications. *Int J Antennas Propag.* (2017) **2017**:8794039. doi: 10.1155/2017/8794039
2. Huang S, Guo B, Liu Y. 5G-oriented optical underlay network slicing technology and challenges. *IEEE Commun Mag.* (2020) **58**:13. doi: 10.1109/MCOM.001.1900583
3. Montalvao ESR, Montalvao ACPS, Campos ALPS, Gomes Neto A. A new model of metasurface used for linear-to-circular polarization conversion in antenna array. *Microw Opt Technol Lett.* (2016) **58**:861. doi: 10.1002/mop.29681
4. Yu Z, Yu JG, Ran XY, Zhu CH. A novel ancient coin-like fractal multiband antenna for wireless applications. *Int J Antennas Propag.* (2017) **2017**:6459286. doi: 10.1155/2017/6459286
5. Xu J, Guo Y, Yang P, Zhang R, Zhai X, Huang S, et al. Recent progress on RF orbital angular momentum antennas. *J Electromagnet Wave.* (2020) **34**:275. doi: 10.1080/09205071.2019.1708814

6. Zhang ZJ, Zhang WY, Zeadally S, Wang YA, Liu Y. Cognitive radio spectrum sensing framework based on multi-agent architecture for 5G networks. *IEEE Wirel Commun.* (2015) **22**:34–9. doi: 10.1109/MWC.2015.7368822
7. Ran XY, Yu Z, Xie TY, Li Y, Wang XX, Huang P. A novel dual-band binary branch fractal bionic antenna for mobile terminals. *Int J Antennas Propag.* (2020) **2020**:6109093. doi: 10.1155/2020/6109093
8. Kumar A, Sankhla V, Deegwal JK, Kumar A. An offset CPW-fed triple-band circularly polarized printed antenna for multiband wireless applications. *AEU-Int J Electron Commun.* (2018) **86**:133–41. doi: 10.1016/j.aeue.2018.02.002
9. Akhtar F, Naqvi SI, Arshad F, Amin Y, Tenhunen H. A flexible and compact semicircular antenna for multiple wireless communication applications. *Radioengineering.* (2018) **27**:671–8. doi: 10.13164/re.2018.0671
10. Chen Y, Ye LF, Zhuo JL, Liu YH, Zhang L, Zhang M, et al. Frequency reconfigurable circular patch antenna with an arc-shaped slot ground controlled by PIN diodes. *Int J Antennas Propag.* (2017) **2017**:7081978. doi: 10.1155/2017/7081978
11. Ullah S, Ahmad S, Khan BA, Tahir FA, Flint JA. An hp-shape hexa-band antenna for multi-standard wireless communication systems. *Wirel Netw.* (2019) **25**:1361–9. doi: 10.1007/s11276-018-1760-x
12. Zhao Y. Design of high-gain, wideband antenna using microwave hyperbolic metasurface. *AIP Adv.* (2016) **6**:055022. doi: 10.1063/1.4952752
13. Xu J, Bi K, Zhang R, Hao Y, Lan C, Mcdonald-Maier K, et al. A small-divergence-angle orbital angular momentum metasurface antenna. *Research.* (2019) **2019**:9686213. doi: 10.34133/2019/9686213
14. Almutairia AF, Islam MS, Samsuzzaman M, Islam MT, Misran N, Islam MT. A complementary split ring resonator based metamaterial with effective medium ratio for C-band microwave applications. *Results Phys.* (2019) **15**:102675. doi: 10.1016/j.rinp.2019.102675
15. Xu JC, Hao YN, Bi K, Zhang R, Huang SG, Zhou J. Microwave orbital angular momentum beam generation based on circularly polarized metasurface antenna array. *Eng Sci.* (2019) **6**:30–35. doi: 10.30919/es8d748
16. Patel SK, Kosta YP. Meandered multiband metamaterial square microstrip patch antenna design. *Wave Random Complex.* (2012) **22**:475–87. doi: 10.1080/17455030.2012.723837
17. Fu X, Cui T. Recent progress on metamaterials: From effective medium model to real-time information processing system. *Prog Quant Electron.* (2019) **67**:100223. doi: 10.1016/j.pquantelec.2019.05.001
18. Xu JC, Tao L, Zhang R, Hao YN, Huang SG, Bi K. Broadband complementary ring-resonator based terahertz antenna. *Opt Express.* (2017) **25**:17099–104. doi: 10.1364/OE.25.017099
19. Patel SK, Argyropoulos C, Kosta YP. Broadband compact microstrip patch antenna design loaded by multiple split-ring resonator superstrate and substrate. *Wave Random Complex.* (2017) **27**:92–102. doi: 10.1080/17455030.2016.1203081
20. Gupta A, Bansal B, Mishra VK, Agrawal A. Miniaturised tri-band rhombus-shaped metamaterial-inspired antenna with gain enhancement using complementary closed ring resonators. *IET Microw Antennas Propag.* (2020) **14**:185–93. doi: 10.1049/iet-map.2019.0567
21. Patchala K, Raja-Rao Y, Prasad AM. Triple band notch compact MIMO antenna with defected ground structure and split ring resonator for wideband applications. *Heliyon.* (2020) **6**:e03078. doi: 10.1016/j.heliyon.2019.e03078
22. Ali W, Hamad E, Bassiuny M, Hamdallah M. Complementary split ring resonator based triple band microstrip antenna for WLAN/WiMAX applications. *Radioengineering.* (2017) **26**:78–84. doi: 10.13164/re.2017.0078
23. Zhou C, Wang GM, Wang YW, Zong BF, Ma J. CPW-Fed dual-band linearly and circularly polarized antenna employing novel composite right/left-handed transmission-line. *IEEE Antennas Wirel Propag Lett.* (2013) **12**:1073–6. doi: 10.1109/LAWP.2013.2279689
24. Xu J, Li RQ, Jiang XP, Wang SY, Han TC. Ultra-wideband linear polarization converter based on square split ring. *Acta Phys Sin.* (2019) **68**:117801. doi: 10.7498/aps.68.20190267
25. Tao L, Xu JC, Li HH, Hao YN, Huang SG, Lei M, et al. Bandwidth enhancement of microstrip patch antenna using complementary rhombus resonator. *Wirel Commun Mob Com.* (2018) **2018**:6352181. doi: 10.1155/2018/6352181
26. Lan JX, Cao XY, Gao J, Han JF, Liu T, Cong LL, et al. Novel design of microstrip antenna array with low scattering performance. *Acta Phys Sin.* (2019) 68:034101. doi: 10.7498/aps.68.20181708

Conflict of Interest: The authors declare that the research was conducted in the absence of any commercial or financial relationships that could be construed as a potential conflict of interest.

frontiers in Physics

ORIGINAL RESEARCH
published: 25 September 2020
doi: 10.3389/fphy.2020.578295

Suppressing Edge Back-Scattering of Electromagnetic Waves Using Coding Metasurface Purfle

Xinghua Li, Mingde Feng, Jiafu Wang*, Yueyu Meng, Jiaheng Yang, Tonghao Liu, Ruichao Zhu and Shaobo Qu*

Department of Basic Sciences, Air Force Engineering University, Xi'an, China

Edge scattering is one of the main scattering sources for metal objects, especially for those with thin front edges. In this paper, based on the principle of scattering cancelation, a coding metasurface purfle is proposed and employed to suppress the edge back-scattering of electromagnetic (EM) waves. To this end, two split-ring resonators with a π phase difference between them are designed to act as the 0- and 1-element of the coding metasurface. The coding metasurface fixed on the front edge of a thin metal plate can reduce the edge back-scattering significant for EM waves polarized along the edge direction due to the anti-phase scattering of the two coding elements. Both the simulation and experiment results verify the reduced back-scattering of the flat edge. A maximal reduction of 24 dB is attained within the central frequency of about 11 GHz. This work provides a novel alternative to suppressing edge scattering and may find applications in EM compatibility, radar stealth technologies, etc.

Keywords: edge back-scattering, coding metasurface purfle, scattering cancellation, radar cross section reduction, horizontal polarization

OPEN ACCESS

Edited by:
Zhi Hong,
China Jiliang University, China

Reviewed by:
Shobhit K. Patel,
Marwadi University, India
Yongqiang Pang,
Xi'an Jiaotong University, China

****Correspondence:***
Mingde Feng
fmingde@mail.xjtu.edu.cn
Jiafu Wang
wangjiafu1981@126.com

Specialty section:
This article was submitted to Optics and Photonics, a section of the journal Frontiers in Physics

Received: *30 June 2020*
Accepted: *13 August 2020*
Published: *25 September 2020*

Citation:
Li X, Feng M, Wang J, Meng Y, Yang J, Liu T, Zhu R and Qu S (2020) Suppressing Edge Back-Scattering of Electromagnetic Waves Using Coding Metasurface Purfle. Front. Phys. 8:578295. doi: 10.3389/fphy.2020.578295

INTRODUCTION

Edge scattering, as a strong scattering phenomenon, can be interpreted as scattering from discontinuous impedance between the edges of the considered targets and their surroundings [1]. Edge scattering can be excited by plane waves impinging upon the surface of a metal object. In fact, when a metal object is illuminated by an oblique incidence, specular reflection also arises, as shown in **Figure 1A**. But considering the distance between the source and an object, plane waves often form in a grazing condition when they arrive at a detected object [2]. In this scenario, edge scattering is the main contributor to radar cross-section (RCS) at a large angle incidence. For low RCS applications, such as stealth techniques, antennae, and RCS measurement ranges, it is crucial to suppress edge scattering in order to improve the performance of the research targets [3].

Edge scattering can be suppressed by the design of the geometry and material property [4]. From the perspective of geometric design, Ufimtsev proposed a principle of using geometrical shape to minimize the back-scattering [5]. Afterwards, there have been several different geometrical shapes that were implemented [6–12]. From the perspective of material property design, the methods for edge scattering suppression include the use of edge corrugations, resistive taper loading, and edge coatings, etc., which have received considerable attention [13–24]. In addition, other related works include using inhomogeneous anisotropic impedance surfaces to guide surface waves with

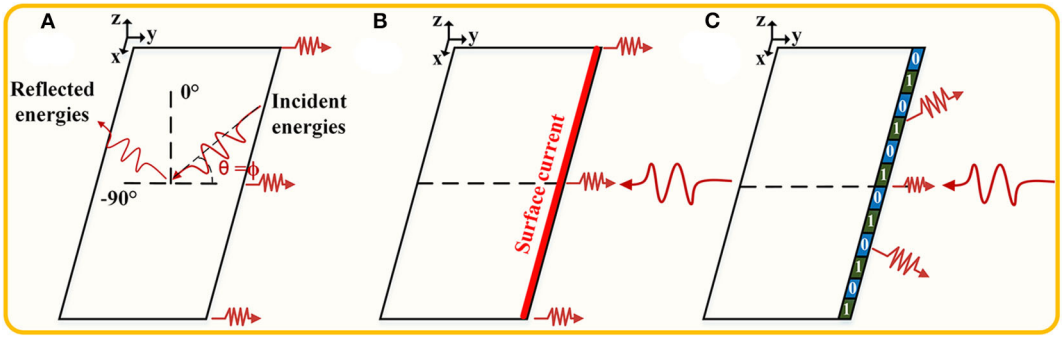

FIGURE 1 | Suppression of edge scattering. The plane waves illuminate a rectangular metal surface. **(A)** Scattering pattern at an oblique incident angle of $\theta = \phi$ ($0° < \phi < 90°$). **(B)** Edge back-scattering under horizontal polarization at the incident angle of $\theta = 90°$. **(C)** The schematic of coding metasurface purfle used to suppress edge back-scattering.

the purpose of suppressing the scattering of the hypotenuse of triangular scatterer [25] and using hard and soft anisotropic impedance surfaces to redirect the back-scattering [26]. However, many of the methods just mentioned suffer from obvious limitations when considering other engineering indicators, such as weight or aerodynamic performance [26]. So, in this paper, a coding metasurface purfle is proposed to suppress edge scattering following the principle of scattering cancelation. Compared with previously published references, this approach provides an alternative tool for suppression of edge scattering, without changing physical geometry, exhibiting excellent properties, including ease of fabrication, lightness of weight, and thinness of thickness. Coding metasurfaces have digital coding sequences, which can regulate EM waves by various combinations of different coding sequences. They are part of a class of structures, generally called metasurfaces, which include high impedance surface (HIS), electromagnetic bandgap (EBG), artificial impedance surface (AIS), and so forth. These metasurfaces are relevant to multiple applications for antennas, lenses, absorbers, imaging, and waveguides [27–34]. But, until now, using coding metasurfaces to reduce edge scattering has rarely been reported.

The basic principle of this paper is illustrated in **Figure 1**: When horizontal polarized plane waves illuminate a metal plate, the current can be induced on the front edge, due to the edge effect shown in **Figure 1B** [35], which generates the strong back-scattering. Therefore, we would expect to change the distribution of edge current in order to reduce the back-scattered energy according to the scattering cancelation principle. Following this idea, two coding elements with π phase difference are designed to realize the energy cancelation along the back-scattering direction. Then, the elements constitute the coding metasurface purfle, which are fixed on the front edge of a metal plate, as shown in **Figure 1C**. It is worth noting that two coding elements are arranged in a coding scheme similar to the grating structure. In addition, for the sake of simplicity of analysis, the incident angle of the plane wave is taken as 90°. A series of procedures of simulations and experiments have been carried out to verify the back-scattering suppression performance of our proposal. As we expected, both results indicate that this method is highly effective at the issues of suppressing edge scattering.

CODING ELEMENTS DESIGN AND SIMULATION

Edge Scattering of a Rectangular Metal Plate

There are two polarizing cases when the plane waves illuminate a rectangular metal plate at an incident angle of 90° as shown in **Figure 2A**. One is the excited electric field E_1, which is parallel to the incident plane (x–y plane), and the other, E_2, is perpendicular to the incident plane. These two exciting conditions are defined as horizontal and vertical polarization, respectively. As described commonly, the scattering of a thin metal plate under horizontal polarization is stronger than that which is under the vertical one at an incident angle of 90° due to electrons by horizontal polarization driving, which can generate the front edge current to scatter energy [5]. Theoretical research indicates that the edge scattering under horizontal polarization is independent of frequency and only varies with the square of the edge length. The mono-static RCS of edge scattering can be calculated by [6]

$$\sigma \approx \frac{l^2}{\pi}, \tag{1}$$

where σ is RCS of edge backward scattering and l is the length of front edge.

To further validate the analysis for the edge scattering of a metal plate, the CST 2018 simulation tool is used to calculate mono-static RCS of the metal plate under two different polarizations. In this case, the dimension of rectangular metal plate is 480 × 90 mm, and its thickness is 0.017 mm. As is shown in **Figure 2B**, the mono-static RCS of the metal plate under two polarizations are simulated at a frequency ranging from 10 to 12 GHz. It is obvious that the RCS under horizontal polarization (average value is −11 dB) is higher than that under vertical polarization (average value is −50 dB), which is in line with the conclusion mentioned above. So, in this investigation, edge

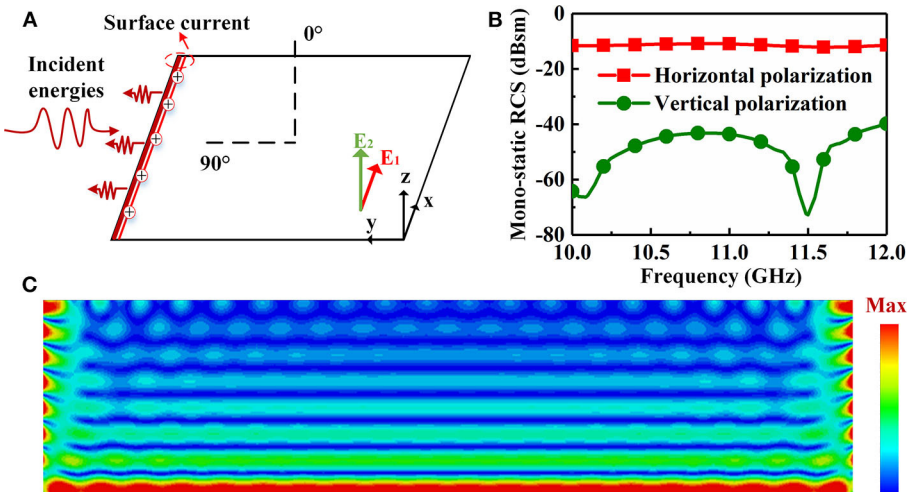

FIGURE 2 | Illustrations of edge scattering of a thin rectangular metal plate. **(A)** Edge scattering at an incident angle of 90°. **(B)** The mono-static RCS of edge scattering under horizontal and vertical polarization. **(C)** Surface current on metal plate under a horizontal polarized incidence.

scattering under horizontal polarization is the main focus of our study. According to Equation (1), the mono-static RCS under horizontal polarization can be calculated, with the result being about −11.3 dB, which also agrees with the simulated result. To intuitively understand the mechanism of edge scattering under horizontal polarized incidence, the distribution of surface current is simulated as shown in **Figure 2C**. Note that the current on the front edge is more intense than that on the other areas, which further verifies that the front edge of a metal plate is the major scattering source.

The Analysis of Coding Elements

As described above, the front-edge current scatters energy in a backward direction. In order to suppress the edge back-scattering, coding elements should be designed to change the distribution of edge current. Based on this, two coding elements numbered 0-element and 1-element have been used to divide the edge current into two different parts, following the principle of scatter cancelation. When the plane waves illuminate a metal plate, two coding elements fixed on the front edge can be considered as two different scattering sources. The wave functions of the EM waves scattered by the two sources can be written as:

$$y_0 = A_0 cos\,(\omega t + \varphi_0) \tag{2}$$

$$y_1 = A_1 cos\,(\omega t + \varphi_1) \tag{3}$$

Where ω is the angular frequency of EM waves, A_0 and A_1 are amplitudes, and φ_0 and φ_1 are initial phases. Assume that there is a point p in the normal direction of the front edge. The distance between the sources and the point is r_0 and r_1, respectively. When the EM wave y_0 and y_1 meet at this point, the superposition function at this point can be described as:

$$y = y_0 + y_1 = Acos(\omega t + \varphi) \tag{4}$$

where φ and A are the superimposed initial phase and amplitude, respectively. The superimposed amplitude meets the following expressions:

$$A = \sqrt{A_0^2 + A_1^2 + 2A_0A_1 cos\Delta\varphi} \tag{5}$$

$$\Delta\varphi = \varphi_1 - \varphi_0 - 2\pi\frac{r_1 - r_0}{\lambda} \tag{6}$$

where λ is the wavelength of free space. Based on Equations (5) and (6), the maximum reduction of scattering at the point p can be obtained under the conditions of $A_0 = A_1$ and $\Delta\varphi = (2k + 1)\pi$, $(k = 0,1,2\ldots)$. Similarly, if we want to suppress the edge back-scattering in the normal direction of the front edge, the foundation of the whole design process is also to find the two conditions just mentioned. Considering that the magnetic field of horizontal polarization is perpendicular to the front edge, a simple split-ring resonator with magnetic resonance can be employed to regulate the phase and amplitude.

The coding elements, illustrated in **Figure 3A**, consist of the split rings etched on a 3-mm thick commercial dielectric FR4 ($\varepsilon_r = 4.3$, $\tan\delta = 0.025$) with a copper ground plane on the bottom side. The split ring and copper ground plane have identical thickness of 0.017 mm. The configuration parameters after the parameter sweep by virtue of the CST are designed as follows: The period of element is $p = 5$ mm, and the length is $w = 90$ mm; the radius of split ring $r = 2$ mm, and the width is $w_r = 0.1$ mm; and the size of split is $g = 0.2$ mm. In the next step, the Frequency Domain solver function in CST 2018 is used to numerically calculate the amplitudes and phases of two coding elements. Unit cell boundaries are applied to the x axis and y axis directions, and the z planes are set as open boundaries. The height of the upper boundary to the coding element is 25 mm. The plane waves illuminate the elements along z axis. It should be emphasized that the electric field of the incident waves is always parallel to coding elements. The simulated results are shown in

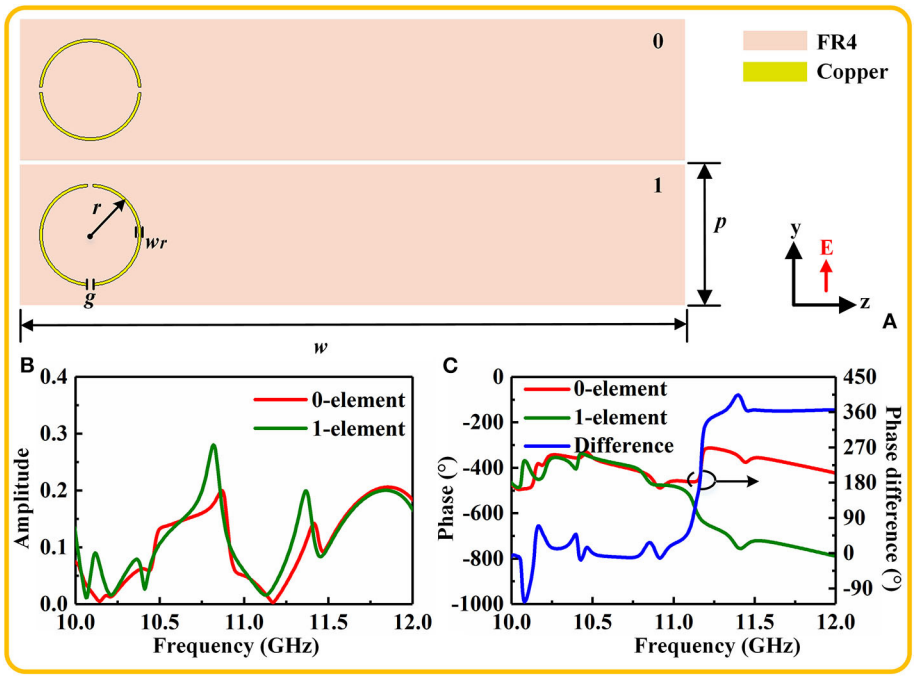

FIGURE 3 | The coding elements used to regulate the amplitude and phase. **(A)** Top view of the coding elements numbered 0-element and 1-element. **(B)** The amplitudes of reflection coefficient of two coding elements. **(C)** The phases and phase difference of two elements.

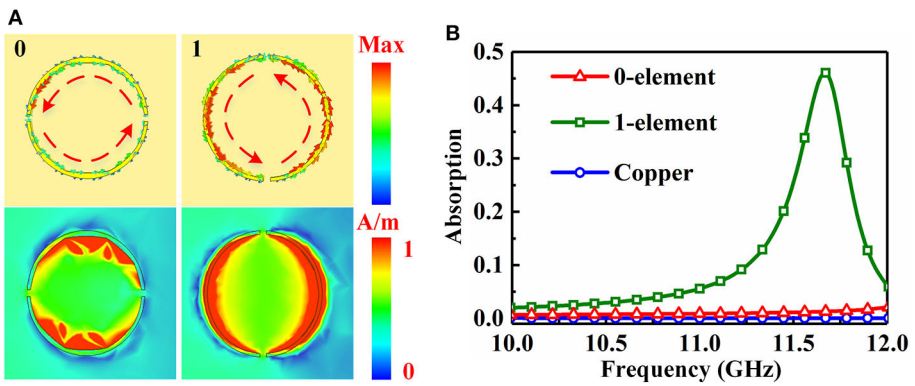

FIGURE 4 | (A) The surface current and magnetic field of two coding elements at 11.16 GHz. **(B)** The absorption of two coding elements.

Figures 3B,C. In **Figure 3C**, the condition of π phase difference is obtained at 11.16 GHz. Meanwhile, the values of amplitudes of two coding elements are small and approximately equal, which also satisfies the other condition of $A_0 = A_1$. Therefore, we can preliminarily speculate that the edge back-scattering can be suppressed at about 11.16 GHz. In order to further interpret the generation mechanism of the π phase difference, surface current and magnetic field of coding elements at 11.16 GHz are simulated and shown in **Figure 4A**. It can be seen that the surface current forms a closed loop, and a strong magnetic field is generated due to the resonance. Note that the intensity of resonance of two coding elements is different and that the intensity of 1-element is stronger than that of 0-element. Thus, the conclusion can be drawn that the π phase difference is produced by the magnetic resonance. In addition, the absorption of two coding elements is also investigated as shown in **Figure 4B**. There is little difference of absorption between the coding elements and copper plate at the operating frequency of 11.16 GHz, which implies that the coding elements cannot absorb EM waves.

SIMULATION AND MEASUREMENT OF CODING METASURFACE PURFLE

In order to verify the performance of coding elements for suppressing the edge back-scattering, two coding elements are

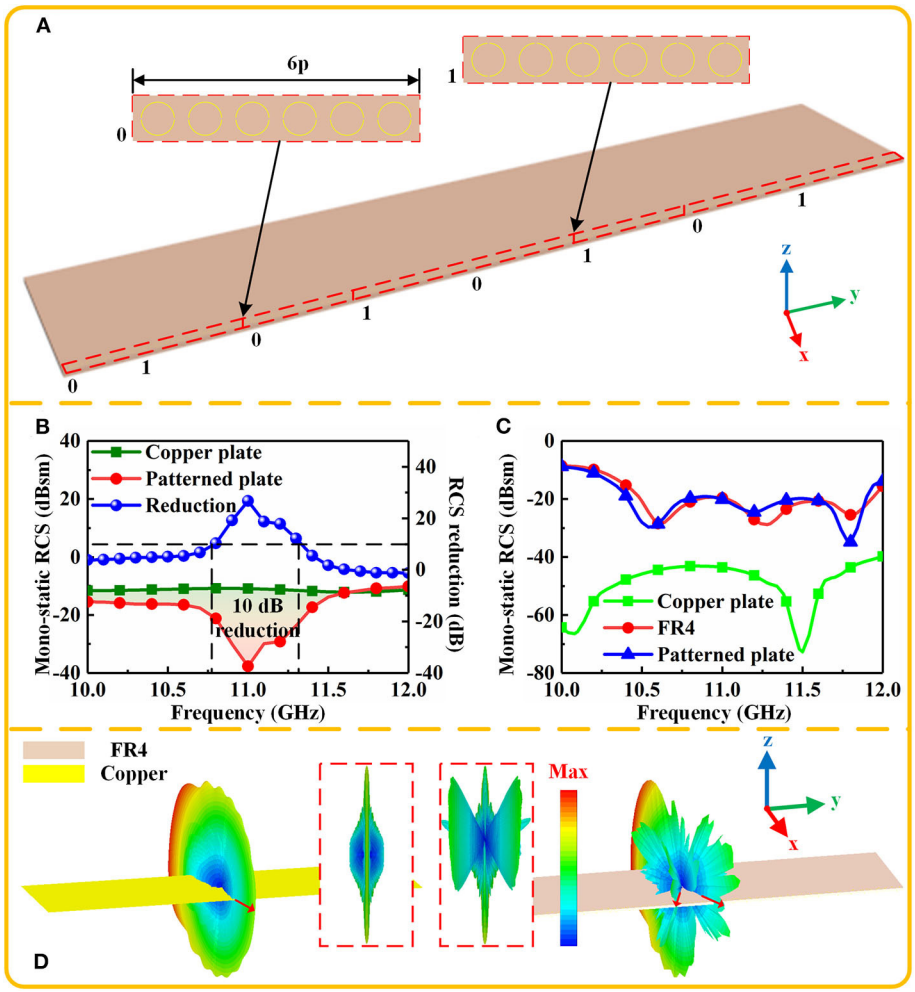

FIGURE 5 | (A) The configuration of patterned plate with coding metasurface purfle constituted by anti-phase coding elements. **(B)** The mono-static RCS of copper plate and patterned plate under horizontal polarization. **(C)** The mono-static RCS of copper plate, FR4 substrate with copper ground plane and patterned plate under vertical polarization. **(D)** The RCS plane of copper plate and patterned plate under horizontal polarization at 11 GHz.

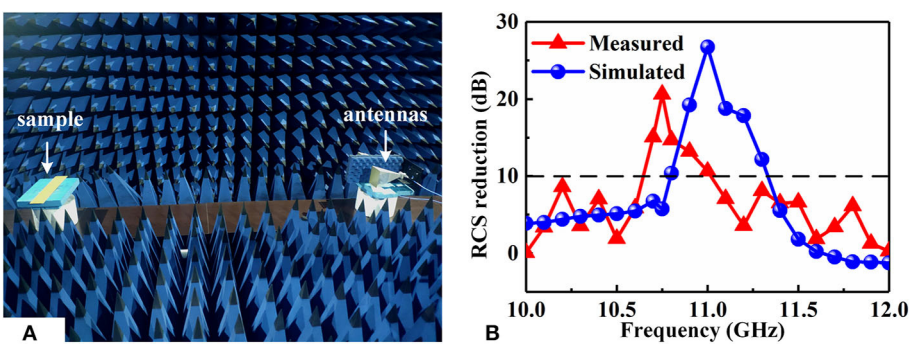

FIGURE 6 | (A) The measurement setup for RCS reduction measurement. **(B)** Comparison of simulated and measured RCS reduction.

fixed on the front edge of a rectangular copper plate to constitute a coding metasurface purfle. The spatial positions of regions 0-element and 1-elememt alternate periodically with a spatial period length of 6*p*, which is similar to the grating structure. The period length approximately corresponds to the wavelength of the operating frequency. The complete configuration is

illustrated in **Figure 5A**. The simulated mono-static RCS of the patterned plate with coding metasurface purfle is shown in **Figure 5B**. In this simulation, the boundaries are all set as open (add space). When the plane waves illuminate the patterned plate along x axis, it can be seen that the result of patterned plate demonstrates a low RCS feature, compared with the copper plate. The proposal achieves desirable reduction band over 10 dB, from 10.82 to 11.3 GHz, and the peak reduction at around 11 GHz is consistent with our reasonable analysis. **Figure 5D** illustrates the RCS plane of the two plates. The copper plate has a single main backward lobe marked by the red arrow; but, the backward lobe of coding metasurface purfle splits into two parts due to the scattering cancelation, which also implies that coding metasurface purfle can suppress the edge back-scattering under horizontal polarization. It should be noted that the coding metasurface purfle is very good for horizontal polarization, but not as efficient for vertical polarization. This is because the magnetic field of vertical polarization is parallel to the coding elements, which cannot excite magnetic resonance on the split rings. What's more, with regard to propagation of surface wave, the FR4 substrate contributes much more, compared to the metal plate, and hence can make a stronger scatter in the backward direction. The mono-static RCS curves of copper plate, FR4 substrate with copper ground plane, and the patterned plate with coding metasurface purfle are shown in **Figure 5C**. The RCS value of FR4 substrate with copper ground plane has a slight difference compared with that of the patterned plate, and both the RCS values are higher than that of copper plate at the operating frequency, which demonstrates that the coding metasurface purfle is actually not efficient for vertical polarization and hence is consistent with the analysis mentioned above.

The simulated results provide a primary verification for the coding metasurface purfle to suppress the edge back-scattering issue; now, we turn to the measurement demonstration. The patterned plate with coding metasurface purfle was fabricated using Print Circuit Board (PCB) technique, and the dimensions of fabricated sample are the same as those in the simulation. The measurement was performed in a microwave anechoic chamber, and the measurement picture is shown in **Figure 6A**. The RCS reduction for the sample is the reflection in the far field condition [36]. Here, the reflection has been performed in a low cost and simple way to represent the RCS reduction, and the measured curves of RCS reduction are presented in **Figure 6B**. The patterned plate has a reduction of 10 dB from 10.7 to 11.05 GHz with a reduction peak of 21 dB at 10.7 GHz. The measured and simulated results have good agreements with slight difference, which may be brought by the imperfection in the fabricating process. Hence, it can be concluded that the coding metasurface purfle is actually effective on suppressing the edge back-scattering.

CONCLUSION

A coding metasurface purfle is proposed in order to suppress the edge back-scattering by using the principle of scattering cancelation. Two split rings with π phase difference constitute the coding elements to implement the scattering cancelation principle. The scattering of a rectangular copper plate and the patterned plate with coding metasurface purfle were then analyzed using numerical simulations. Finally, the experimental examination has been presented to verify the suppression performance of the patterned plate with coding metasurface purfle. The measured result is line with the simulated one, which demonstrates the feasible of our proposal. In addition, the method may gear toward various applications, such as improving stealth performance, reducing coupling between the antennas, eliminating unwanted lobes and EM compatibility. Furthermore, this work is only focused on reducing horizontal polarized scattering, and the incident angle is also limited. So, in the next step, we can keep on designing a structure that is independent on the polarization and incident angle.

DATA AVAILABILITY STATEMENT

All datasets generated for this study are included in the article/supplementary material.

AUTHOR CONTRIBUTIONS

XL: software, investigation, writing - original draft. MF: project administration. JW: conceptualization, methodology. YM: formal analysis, resources. JY: data curation. TL: modification. RZ: assistance in doing experiments. SQ: supervision, funding acquisition. All authors contributed to the article and approved the submitted version.

FUNDING

The authors are grateful for the support from the National Natural Science Foundation of China under Grant Nos. 61671466, 61971435, and 61901508.

REFERENCES

1. Chen HY, Deng LJ, Zhou PH, Xie JL. Tapered impedance loading for suppression of edge scattering. *IET Microwaves Antennas Propag.* (2011) **5**:1744–9. doi: 10.1049/iet-map.2010.0623
2. Zhou Y, Cao X, Gao J, Li S, Liu X. RCS reduction for grazing incidence based on coding metasurface. *Electron Lett.* (2017) **53**:1381–3. doi: 10.1049/el.2017.2414
3. Chen HY, Zhu ZW, Lu LJ, Guan Y, Xie JL, Deng LJ. Design and implementation of the tapered resistive sheets to control edge scattering. *J Appl Phys.* (2014) **115**:164906. doi: 10.1063/1.4874162
4. Kappa J, Dang Z, Sokoluk D, Rahm M. Analysis of coding metasurfaces for incident radiation at oblique incidence angles. *OSA Continuum.* (2019) **2**:2172–80. doi: 10.1364/OSAC.2.002172
5. Ufimtsev PY. *Method of Edge Waves in the Physical Theory of Diffraction*. Foreign Technology Div Wright-Pattersonafb Oh. National Technical Information Service (1971).

6. Jenn D. *Radar and Laser Cross Section Engineering*. American Institute of Aeronautics and Astronautics, Inc. (2005).
7. Liu ZH, Huang PL, Wu Z, Gao X. Analysis of scattering from serrated edge plate on aircraft with MLFMA. *J Beij Univ Aeronaut Astronaut.* (2008) **34**:499−502. doi: 10.3969/j.issn.1003-5060.2008.12.032
8. Liu D, Huang J, Song L, Ji J. Influence of aircraft surface distribution on electromagnetic scattering characteristics. *Chin J Aeronaut.* (2017) **30**:759–65. doi: 10.1016/j.cja.2017.02.015
9. Kumar N, Vadera SR. *Stealth Materials and Technology for Airborne Systems. Aerospace Materials and Material Technologies*. Singapore: Springer (2017). p. 519–37. doi: 10.1007/978-981-10-2134-3_24
10. Ni X, Wong ZJ, Mrejen M, Wang Y, Zhang X. An ultrathin invisibility skin cloak for visible light. *Science.* (2015) **349**:1310–4. doi: 10.1126/science.aac9411
11. Pu M, Li X, Ma X, Wang Y, Zhao Z, Wang C, et al. Catenary optics for achromatic generation of perfect optical angular momentum. *Sci Adv.* (2015) **1**:e1500396. doi: 10.1126/sciadv.1500396
12. Xie X, Li X, Pu M, Ma X, Liu K, Guo Y, et al. Plasmonic metasurfaces for simultaneous thermal infrared invisibility and holographic illusion. *Adv Funct Mater.* (2018) **8**:1706673. doi: 10.1002/adfm.201706673
13. Lee WS, Lee SJ, Lee DJ, Lee WS, Yu JW. TE scattering from concaved wedges with longitudinal corrugations. *IEEE Transact Antennas Propag.* (2012) **61**:2355–9. doi: 10.1109/TAP.2012.2233703
14. Knott EF. Suppression of edge scattering with impedance strings. *IEEE Transact Antennas Propag.* (1997) **45**:1768–73. doi: 10.1109/8.650194
15. Smith FC. Edge coatings that reduce monostatic RCS. *IEE Proc Radar Sonar Navig.* (2002) **149**:310–4. doi: 10.1049/ip-rsn:20020717
16. Choi WH, Shin JH, Song TH, Kim JB, Lee WJ, Joo YS, et al. Design of thin circuit-analogue multilayer absorber and application to leading edge of wing structure. *Electron Lett.* (2013) **49**:216–7. doi: 10.1049/el.2012.3983
17. Gustafsson M. RCS reduction of integrated antenna arrays with resistive sheets. *J Electromagn Waves Appl.* (2006) **20**:27–40. doi: 10.1163/156939306775777323
18. Sjoberg D, Gustafsson M. Realization of a matching region between a radome and a ground plane. *Progr Electromagn Res.* (2010) **17**:1–10. doi: 10.2528/PIERL10071906
19. Nam Y, Choi J, Jang M, Lee WJ, Kim CG. Radar-absorbing structure with nickel-coated glass fabric and its application to a wing airfoil model. *Comp Struct.* (2017) **180**:507–12. doi: 10.1016/j.compstruct.2017.08.017
20. Choi W, Kwak B, Nam Y. Radar absorbing serrated edge for broadband radar cross-section reduction. *Microw Opt Technol Lett.* (2020) **62**:1112–6. doi: 10.1002/mop.32152
21. Huang D, Lyo SK. Suppression of impurity and interface-roughness back-scattering in double quantum wires: theory beyond the Born approximation. *J Phys Condens Matter.* (2000) **12**:3383. doi: 10.1088/0953-8984/12/14/314
22. Wang H, Liu W, Pan Z, Tao Y, Niu J, Tang J, et al. Suppression of backscattering-induced noise in a resonator optic gyro by the dual-frequency modulation method. *Opt Commun.* (2019) **459**:124766. doi: 10.1016/j.optcom.2019.124766
23. Charola S, Patel SK, Parmar J, Ladumor M, Dhasarathan V. Broadband graphene-based metasurface solar absorber. *Microw Opt Technol Lett.* (2019) **62**:1366–73. doi: 10.1002/mop.32156
24. Parmar J, Patel SK, Kartodiya D, Nguyen TK, Skibina JS, Dhasarathan V. Numerical investigation of gold metasurface based broadband near-infrared and near-visible solar absorber. *Phys B Condens Matter.* (2020) **591**:412248. doi: 10.1016/j.physb.2020.412248
25. Hou H, Long J, Wang J, Sievenpiper DF. Reduced electromagnetic edge scattering using inhomogeneous anisotropic impedance surfaces. *IEEE Transact Antennas Propag.* (2017) **65**:1193–201. doi: 10.1109/TAP.2016.2647681
26. Quarfoth R, Sievenpiper D. Alteration of electromagnetic scattering using hard and soft anisotropic impedance surfaces. *IEEE Transact Antennas Propag.* (2015) **63**:4593–9. doi: 10.1109/TAP.2015.2458330
27. Liu Y, Li K, Jia Y, Hao Y, Gong S, Guo YJ. Wideband RCS reduction of a slot array antenna using polarization conversion metasurfaces. *IEEE Transact Antennas Propag.* (2016) **64**:326–31. doi: 10.1109/TAP.2015.2497352
28. Lee GY, Hong JY, Hwang S, Moon S, Kang H, Jeon S, et al. Metasurface eyepiece for augmented reality. *Nat Commun.* (2018) **9**:4562. doi: 10.1038/s41467-018-07011-5
29. Liu T, Meng Y, Ma H, Wang J, Zhu R, Chen H, et al. Extraordinary spoof surface plasmon polaritons excitation by linear and circular polarization conversions phase gradient metasurface. *J Phys D Appl Phys.* (2020) **53**:045003. doi: 10.1088/1361-6463/ab522e
30. Sui S, Ma H, Wang J, Pang Y, Feng M, Xu Z, et al. Absorptive coding metasurface for further radar cross section reduction. *J Phys D Appl Phys.* (2018) **51**:065603. doi: 10.1088/1361-6463/aaa3be
31. Li YB, Li LL, Xu BB, Wu W, Wu RY, Wan X, et al. Transmission-type 2-bit programmable metasurface for single-sensor and single-frequency microwave imaging. *Sci Rep.* (2016) **6**:23731. doi: 10.1038/srep23731
32. Semmlinger M, Tseng ML, Yang J, Zhang M, Zhang C, Tsai WY, et al. Vacuum ultraviolet light-generating metasurface. *Nano Lett.* (2018) **18**:5738–43. doi: 10.1021/acs.nanolett.8b02346
33. Li A, Singh S, Sievenpiper DF. Metasurfaces and their applications. *Nanophotonics.* (2018) **7**:989–1011. doi: 10.1515/nanoph-2017-0120
34. Sun H, Gu C, Chen X, Li Z, Liu L, Xu B, et al. Broadband and broad-angle polarization-independent metasurface for radar cross section reduction. *Sci Rep.* (2017) **7**:40782. doi: 10.1038/srep40782
35. Wang JH, Gan YB. In-band scattering of dipole array with edge loaded rectangular reflector. *IEEE Antennas Propag Soc Int Symp Digest.* (2003) **4**:468–71. doi: 10.1109/APS.2003.1220312
36. Hou YC, Liao WJ, Tsai CC, Chen SH. Planar multilayer structure for broadband broad-angle RCS reduction. *IEEE Transact Antennas Propag.* (2016) **64**:1859–67. doi: 10.1109/TAP.2016.2535164

Conflict of Interest: The authors declare that the research was conducted in the absence of any commercial or financial relationships that could be construed as a potential conflict of interest.

frontiers in Physics

ORIGINAL RESEARCH
published: 29 September 2020
doi: 10.3389/fphy.2020.00385

Multi-Spectral Metasurface With High Optical Transparency, Low Infrared Surface Emissivity, and Wideband Microwave Absorption

Sining Huang, Qi Fan, Jiafu Wang*, Cuilian Xu, Binke Wang, Baiyu Yang, Changhui Tian and Zhen Meng*

Department of Basic Science, Air Force Engineering University, Xi'an, China

In this article, we propose the design of a multispectral metasurface (MSM), which can simultaneously achieve quite good optical transparency, low infrared (IR) emissivity, and wideband microwave absorption. To this end, optically transparent materials were used in the MSM design, including indium tin oxide, polyethylene terephthalate, and polymethyl methacrylate. The MSM is composed of three functional layers: a frequency-selective surface (FSS) on the top, a resistively absorbing layer in the middle and a complete conducting sheet at the bottom. Because of large occupation ratio of conducting area and the low-pass property of the FSS, electromagnetic waves are allowed to penetrate through it into the middle absorbing layer, simultaneously with low surface IR emissivity. A prototype was designed, fabricated, and measured. Both the simulation and experiment results show that the MSM can achieve strong absorption of $>$ 90% in 12.03–29.43 GHz and low IR emissivity of about 0.3 in 3.0–14.0 μm simultaneously. Moreover, the average optical transparency is higher than 90%. Because of the excellent multispectral compatibility, the MSM may find applications in electromagnetic protection, stealth technologies, etc.

Keywords: multi-spectral, compatible-metasurface, low infrared emissivity, microwave absorber, visible transparence

OPEN ACCESS

Edited by:
Zhi Hong,
China Jiliang University, China

Reviewed by:
Saptarshi Ghosh,
Indian Institute of Technology Indore, India
Weiren Zhu,
Shanghai Jiao Tong University, China

****Correspondence:***
Qi Fan
af-fanqi@126.com
Jiafu Wang
wangjiafu1981@126.com

Specialty section:
This article was submitted to Optics and Photonics, a section of the journal Frontiers in Physics

Received: *09 July 2020*
Accepted: *10 August 2020*
Published: *29 September 2020*

Citation:
Huang S, Fan Q, Wang J, Xu C, Wang B, Yang B, Tian C and Meng Z (2020) Multi-Spectral Metasurface With High Optical Transparency, Low Infrared Surface Emissivity, and Wideband Microwave Absorption. Front. Phys. 8:385. doi: 10.3389/fphy.2020.00385

INTRODUCTION

Metamaterials as artificial materials could actualize the propagation characteristic of manipulating electromagnetic wave [1, 2]. Plenty of metamaterial structures are designed as low-scattering materials, perfect absorbers, invisible cloak, surface wave suppressing materials, and so on [3–10]. With the rapid development of the technologies of metamaterials, the function of single-waveband materials can no longer satisfy the needs of various applications. It is the mainstream to design the multispectral metasurfaces (MSMs) to apply under a variety of environments [11–16]. According to spectroscopy, microwave band, infrared (IR) band, and visible light band are the most commonly used region. However, the mechanisms of microwave and IR counter each other in stealth technology. The mechanism of radar for microwave is to reduce echoes from the detected objects [17–20]. In contrast, IR detection requires the low-emissivity materials to be undetected. According to Kirchhoff's law, high-reflectivity materials, which are low emitters, should be needed for IR band. Therefore, this problem needs to be solved in our design thought.

Many scientists have studied the metasurfaces in multiband applications. Wang et al. [21] designed IR-radar bistealth frequency-selective surface (FSS) with IR emissivity below 0.3 and above 90% absorption in 8–18 GHz for microwave band. Zhong et al. [22] proposed a thin artificial structure with wideband absorption from 3 to 8 GHz up to incident angles of 30° and low IR emission value of 0.2. Hao et al. [23] designed a stealth-compatible structure consisting of metallic FSS and resistive FSS with reflectivity below −10 dB in whole radar X wave band and IR emissivity < 0.3 in the IR region of 8–14 μm. Pang et al. [24] fabricated an HMS with an efficient reflection reduction larger than 10 dB in the frequency band of 8.2–18 GHz and low IR emissivity < 0.27 from 3 to 14 μm. Zhang et al. [25] present a thin metasurface with broadband microwave absorptivity $>$ 8.2–16.0 GHz and low IR emissivity in the region from 8 to 14 μm.

Except for using metals, scientists also chose the visible transparent materials for studying these problems to use in more scenes, such as using indium tin oxide as main materials, polymethyl methacrylate (PMMA) as dielectric material, and so on. Xu et al. [26] proposed optically transparent metamaterial structure with a high absorptivity $>$ 90% in the region of 6.28–12.29 GHz for TE polarization, and the absorptivity in the region of 7.19–15.26 GHz is $>$ 90% for TM polarization. Its IR emissivity is about 0.30 in the IR region from 3 to 14 μm. Shuomin et al. [27] deposited four indium tin oxide films on metasurface in order to realize a low microwave reflectivity < 0.1 from 1.5 to 9 GHz and a thermal emissivity approaching 0.52.

In microwave band, radar absorbers must be the most stable application. As the absorber, the operational bandwidth is the most important parameter. In this article, we propose the design of an MSM that can simultaneously achieve quite good optical transparency, low IR emissivity, and wideband microwave absorption. To this end, optically transparent materials were used in the metasurface design, including indium tin oxide, polyethylene terephthalate (PET), and PMMA. The MSM is composed of three functional layers: an FSS on the top, a resistively absorbing layer in the middle, and a complete conducting sheet at the bottom. Because of large occupation ratio (OR) of conducting area and the low-pass property of the FSS, electromagnetic waves are allowed to penetrate through it into the middle absorbing layer, simultaneously with low surface IR emissivity. A prototype was designed, fabricated, and measured. Both the simulation and experiment results show that the MSM can achieve strong absorption $>$ 90% in 12.03–29.43 GHz and low IR emissivity about 0.3 in 3.0–14.0 μm simultaneously. Moreover, the average optical transparency is higher than 90%. To better observe our properties of our MSM, the compared results of typical compatible metamaterials are presented as **Table 1**. It can be observed clearly that our MSM has the best properties.

DESIGN AND DISCUSSION

In IR band, the most commonly used materials are metals because of their low emissivity property, such as gold, aluminum, silver, copper, etc. However, when human needs the perspective property of the naked eyes, these metals could not work anymore.

TABLE 1 | The compared results of typical compatible-metamaterials.

	The frequency band of IR-stealth	The absorption of microwave frequency band	Optical transparency	Reference
Hao T's stealth-compatible structure	8–14 μm	Radar X wave band	No	[21]
Xu's metamaterial structure	3–14 μm	6.28–12.29 GHz for TE polarization 7.19–15.26 GHz for TM polarization.	Yes	[24]
Our MSM	3–14 μm	12.03–29.43 GHz	Yes	

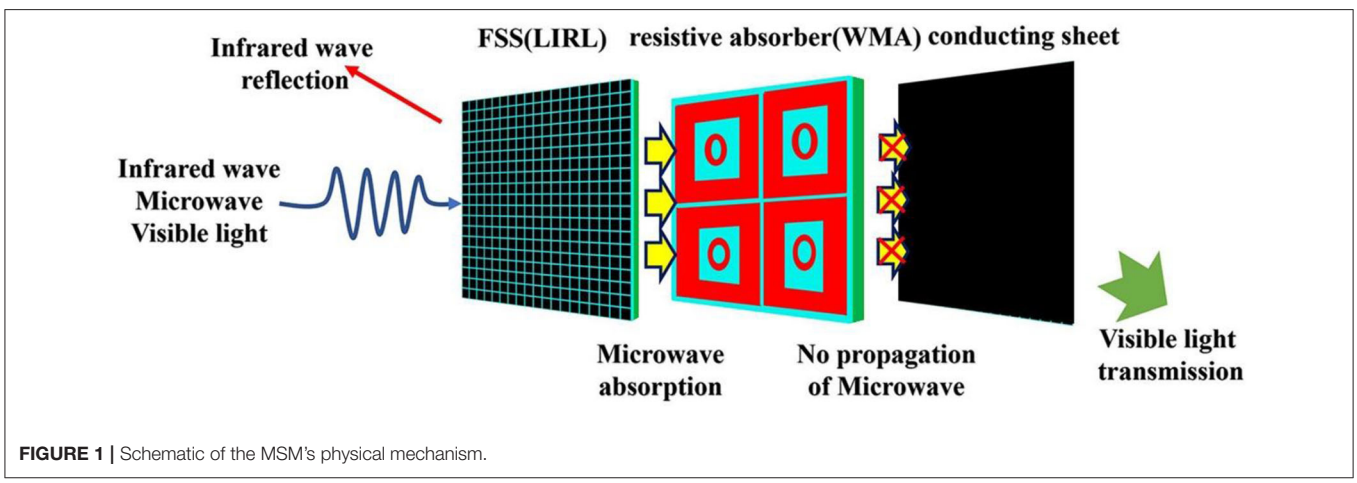

FIGURE 1 | Schematic of the MSM's physical mechanism.

Thus, in this article, a fabricated MSM chose the ITO as the main material and utilized PET and PMMA as dielectric material to achieve the feature of the visible transparency. And the ITO also has the property of metal, so it is appropriate that metals are replaced by ITO.

In the design process of the MSM, the tailored structure was divided into three functional layers: an FSS on the top, a resistively absorbing layer in the middle, and a complete conducting sheet at the bottom, as depicted in **Figure 1**. The electromagnetic waves, including IR wave, microwave, and visible, propagate in different directions after working with the MSM. Because of the existence of the top layer, which consists of the ITO patches as the low emissivity of IR layer (LIRL), it has the property of displaying low temperature. For the microwave, it must pass through the low-emissivity top layer and work at the resistively absorbing layer. Thus, it must be a loss-pass and high-resistance FSS to make the radar wave propagate to the resistively absorbing layer as the wideband microwave absorber (WMA) and be absorbed. For visible light, because of the optical transparent materials, it can achieve visible transparence.

Figure 2 depicts the unit of the MSM structure. **Figures 2A,B** exhibit LIRL and WMA, respectively. And the resistance of LIRL and WMA is different. The LIRL's resistance is 6 Ω/Sq, and that of WMA is 30 Ω/Sq. The side view is shown in **Figure 2C**. And the thicknesses of two stealth layers' PET are different. The thickness of LIRL's is 0.175 mm, and that of WMA's is 0.125 mm. The other parameters are $D = 1$ mm, d = 0.1 mm, L = 19 mm, $l_1 = 18.7$ mm, $l_2 = 11.8$ mm, $\Phi_1 = 4.8$ mm, $\Phi_2 = 3$ mm, $D_1 = 0.5$ mm, $D_2 = 1$ mm, and the ITO of LIRL OR is 81%.

Because the emissivity of ITO is low, in the IR band, the total IR emissivity ε can be calculated by the square rate in the following formula:

$$\varepsilon = \varepsilon_i f_i + \varepsilon_p f_p \tag{1}$$

where ε in Equation (1) is the emissivity of the MSM, and the ε_i and ε_p are emissivities of the ITO and PET, respectively. And the f_i is the OR of the ITO's area to that of the metasurface. The f_p is the OR of the PET's to metasurface's. For this MSM, the emissivity of the PET is high, nearly > 0.8, but filling ratio is < 0.2, so the emissivity of the MSM lower than 0.3.

In the microwave band, the simulation results were obtained by the commercial software CST Microwave Studio. The unit cell condition is set in the x–y direction, and in the z direction, the open boundary condition is chosen. The absorption can be calculated by Equation (2),

$$A = 1 - T - R = 1 - |S_{21}|^2 - |S_{11}|^2 \tag{2}$$

where $|S21|^2$ and $|S11|^2$, respectively, represent the transmissivity and reflectivity. However, the microwave could not propagate through the MSM because of the bottom a complete conducting sheet of ITO without gaps, so the average transmission is

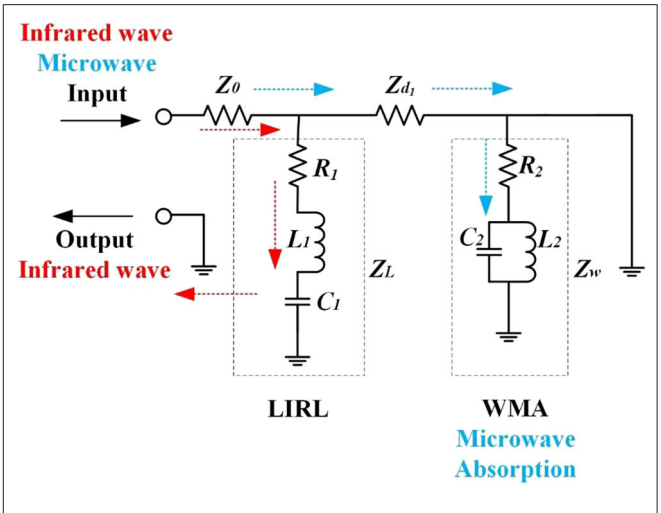

FIGURE 3 | The equivalent circuit model (ECM) of MSM.

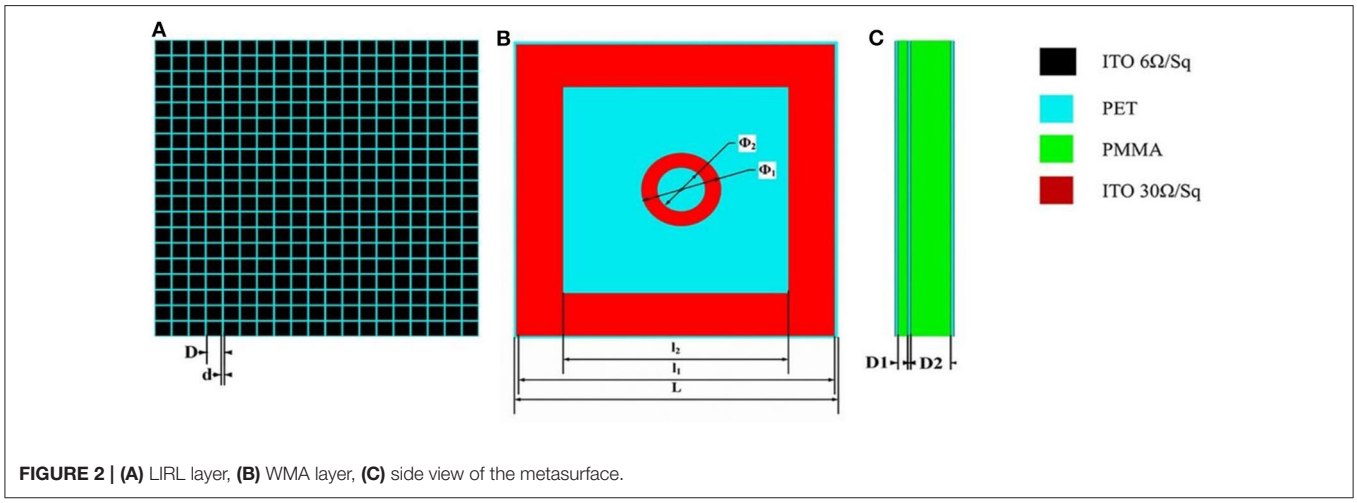

FIGURE 2 | (A) LIRL layer, **(B)** WMA layer, **(C)** side view of the metasurface.

nearly zero. For this reason, Equation (2) could be simplified as Equation (3).

$$A = 1 - R = 1 - |S_{11}|^2 \tag{3}$$

MSM could be equivalent to the circuit as shown in **Figure 3**. Z_0 is the impendence of free space, which is equal to 377 Ω. Z_L and Z_W are the equivalent impendence of the LIRL and WMA, respectively.

We can calculate the ABCD matrix as Equation (4), where $\theta = \beta t$, $\beta = 2\pi/\lambda$:

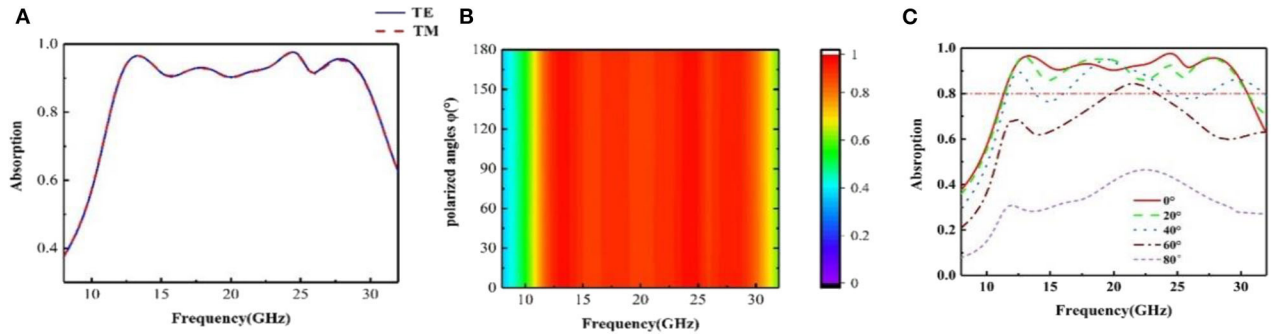

FIGURE 4 | (A) Simulated absorption at different polarization modes for TE polarized and TM polarized. **(B)** Simulated absorption at different polarization modes for full angle domain. **(C)** Simulated absorption at different incident angles.

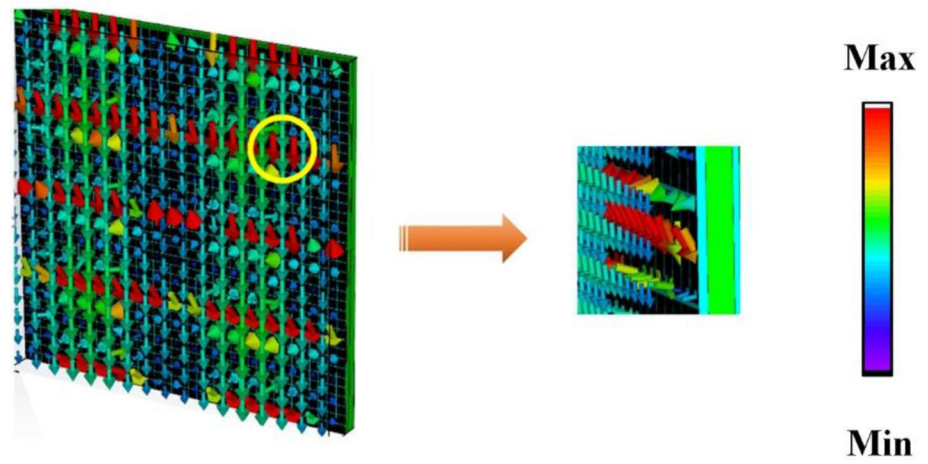

FIGURE 5 | Total surface current distribution and part surface current distribution.

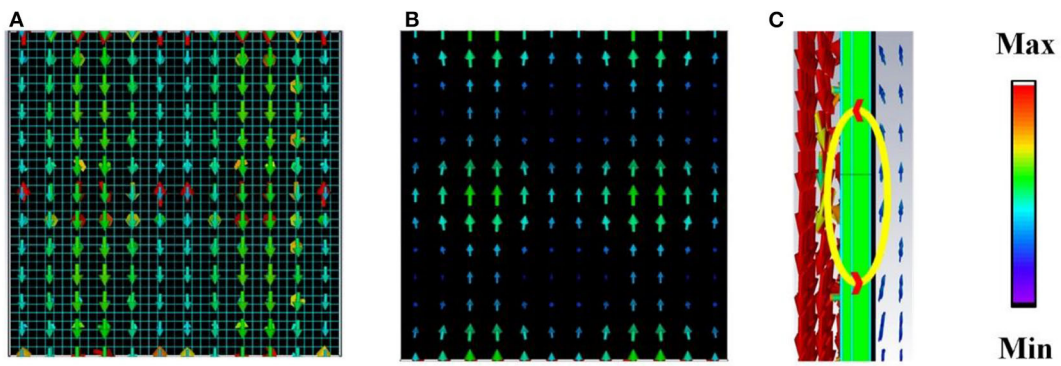

FIGURE 6 | Distribution of surface current resonance frequency $f = 13.33$ GHz: **(A)** top view, **(B)** bottom view, **(C)** side view.

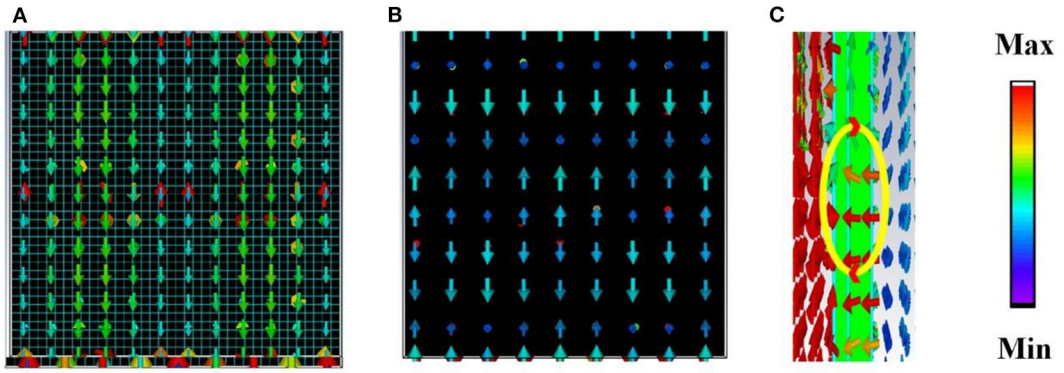

FIGURE 7 | Distribution of surface current resonance frequency $f = 24.43$ GHz: **(A)** top view, **(B)** bottom view, **(C)** side view.

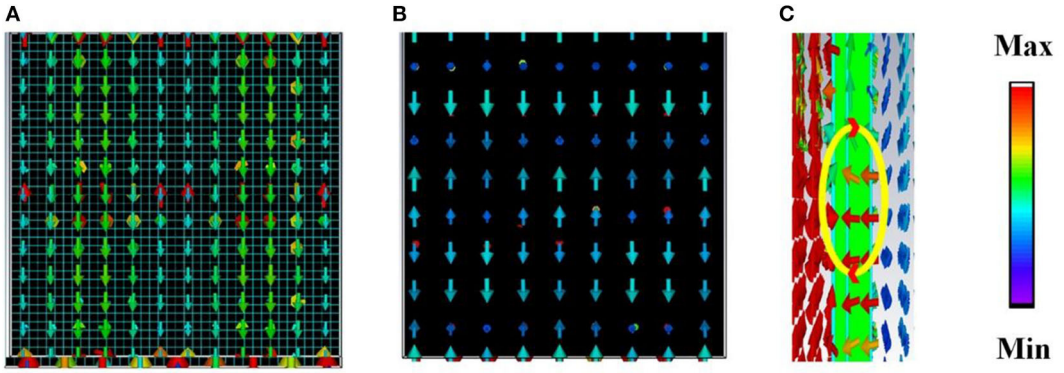

FIGURE 8 | Distribution of surface current resonance frequency $f = 27.85$ GHz: **(A)** top view, **(B)** bottom view, **(C)** side view.

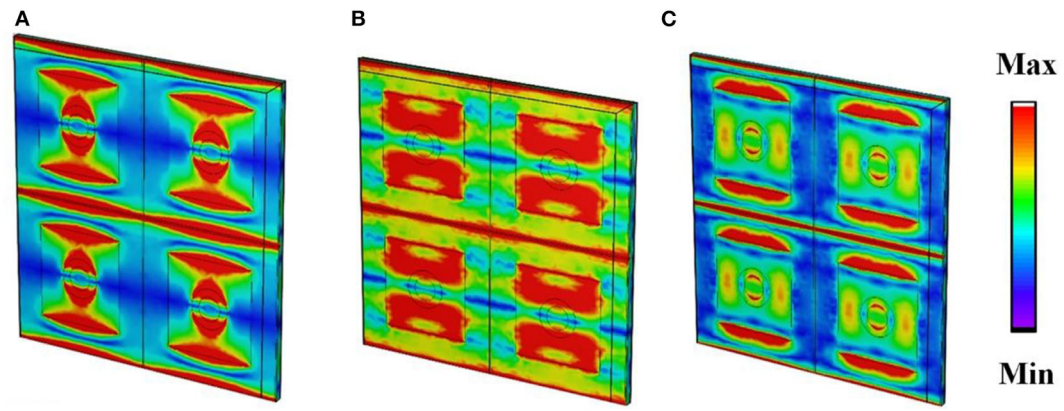

FIGURE 9 | Distribution of the electric field of WMA **(A)** $f = 13.33$ GHz, **(B)** $f = 24.43$ GHz, **(C)** $f = 27.85$ GHz.

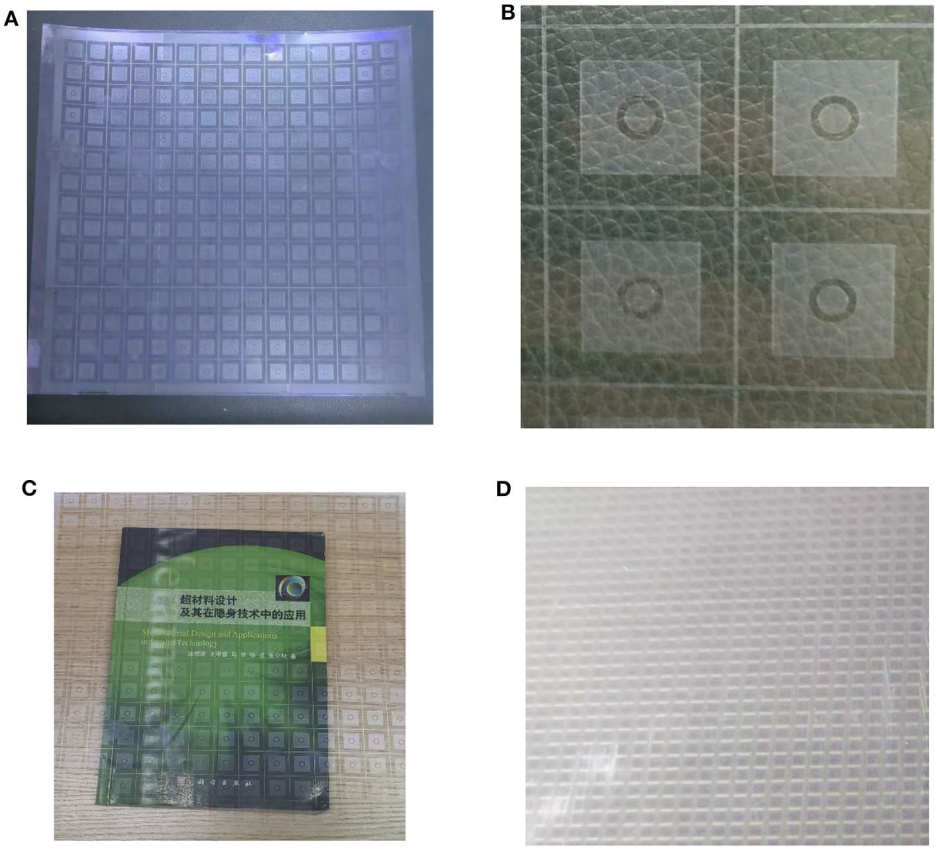

FIGURE 10 | (A) the photograph of WMA, **(B)** a large version of WMA, **(C)** visible transparent property of WMA, **(D)** a large version of LIRL.

$$\begin{bmatrix} A & B \\ C & D \end{bmatrix} = \begin{bmatrix} 1 & 0 \\ \frac{1}{Z_L} & 1 \end{bmatrix} \begin{bmatrix} cos\theta & jZ_{d_1} sin\theta \\ \frac{1}{Z_{d_1}} & cos\theta \end{bmatrix} \begin{bmatrix} 1 & 0 \\ \frac{1}{Z_w} & 1 \end{bmatrix}$$

$$= \begin{bmatrix} cos\theta + j\frac{Z_{d_1}}{Z_w} sin\theta & jZ_{d_1} sin\theta \\ \frac{Z_L+Z_w}{Z_L Z_w} cos\theta + j\left(\frac{1}{Z_{d_1}} + \frac{Z_{d_1}}{Z_L Z_w}\right) sin\theta & cos\theta + j\frac{Z_{d_1}}{Z_L} sin\theta \end{bmatrix} \quad (4)$$

The calculated absorption curves including TE and TM polarization are exhibited in **Figure 4A**. The MSM showed a strong absorptivity of $>$ 90% from 12.03 to 29.43 GHz. And the simulation results of different polarizing angles ϕ are depicted in **Figure 4B** to indicate that the tailored structure is polarization independent significantly. The calculated absorption curves at different incident angles are shown in **Figure 4C**. And it reveals that the absorption of the MSM is $>$ 80% within 40° of incident angles.

In order to uncover the physics mechanism of the microwave absorption, the surface current distributions and electric field at resonant frequencies were chosen.

On the idea of designing the LIRL, the microwave must propagate through it and work at the WMA. According to the above reasons, a loss-pass and high-resist FSS is chosen, as shown in **Figure 5**. To explain the physics mechanism of the microwave absorption behavior, based on the result of simulation, three resonant frequencies are chosen, $f = 13.33$, 24.43, and 27.85 GHz, with absorbance of 96.54, 97.65, and 95.68%, respectively.

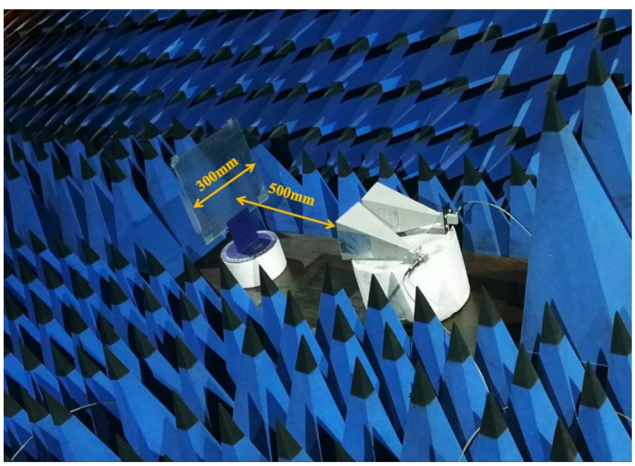

FIGURE 11 | The measure scene of microwave-absorbing.

It could be observed that an electric current loop is formed between the top and bottom layer as **Figures 6–8** depicted. It

means that a magnetic dipole is at work to obtain the absorption peak of microwave.

To understand the resonant modes of the three resonance frequencies at the WMA, the distribution of the electric field is shown in **Figure 9**. It is clear to observe that their strong interaction with the position of ITO ring is different. **Figure 9A** depicts that the resonant mode at $f = 13.33$ GHz is mostly the circular ring. By contrast, at $f = 27.85$ GHz, the resonant mode is mostly ITO square ring as **Figure 9B** shows. And as presented in **Figure 9C**, the mode at $f = 34.43$ GHz includes the circular ring and the square ring.

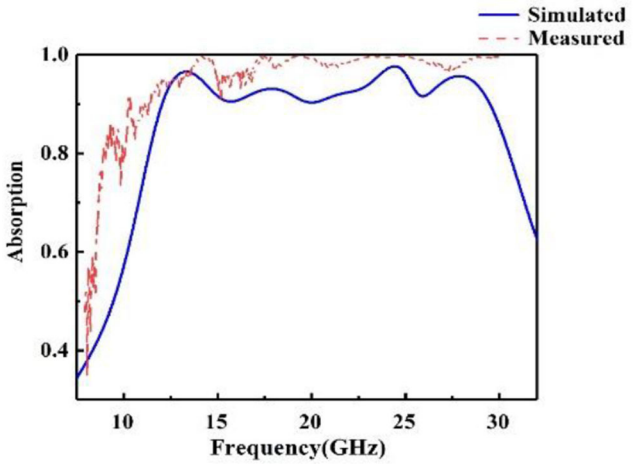

FIGURE 12 | The measurement result of microwave absorption.

EXPERIMENTAL DEMONSTRATION

A 300 × 300-mm sample was tailored by the printed circuit board technique to check the simulation result of the MSM. The PBC technique is one of the electron printing techniques. In our article, we adopted this printing technique to obtain a more accurate sample. First, ITO was deposited on the whole PET board. After depositing, the PBC technique was adopted, which uses laser to etch on the ITO film to tailor the shape of the structure we need. In the article, the shape we need is the ITO patches in LIRL, the circular ring and square ring in WMA, as shown in **Figure 10**.

For microwave-absorbing ability, an Agilent 8720ET vector network analyzer was used to measure the reflection of microwave. The detection scene is presented as shown in **Figure 11**.

The microwave was perpendicular to the sample, and the distance between structure and antennas was 500 mm. The test result is depicted in **Figure 12**. The tendency of the measured

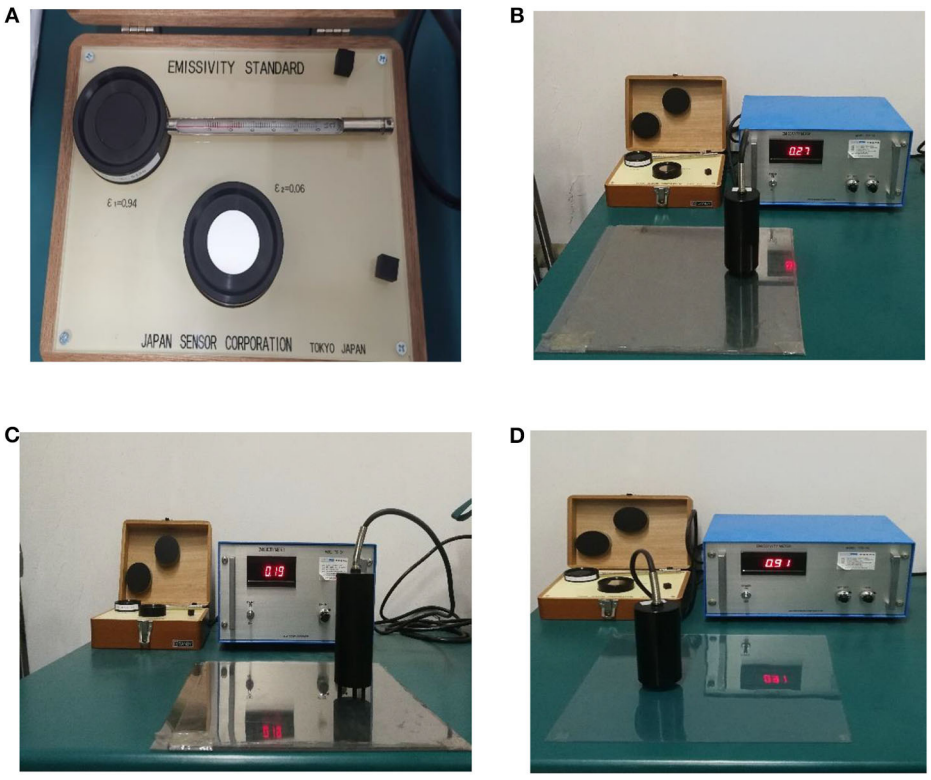

FIGURE 13 | (A) the emissivity standard of IR emissivity, **(B)** the measurement result of the sample, **(C)** the measurement result of the sample's back, **(D)** the measurement result of the reference.

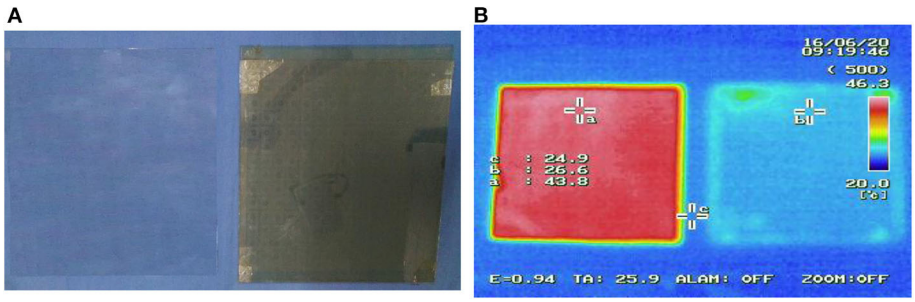

FIGURE 14 | Experimental result: **(A)** contrast test for PET and sample, **(B)** IR thermal images at 45°.

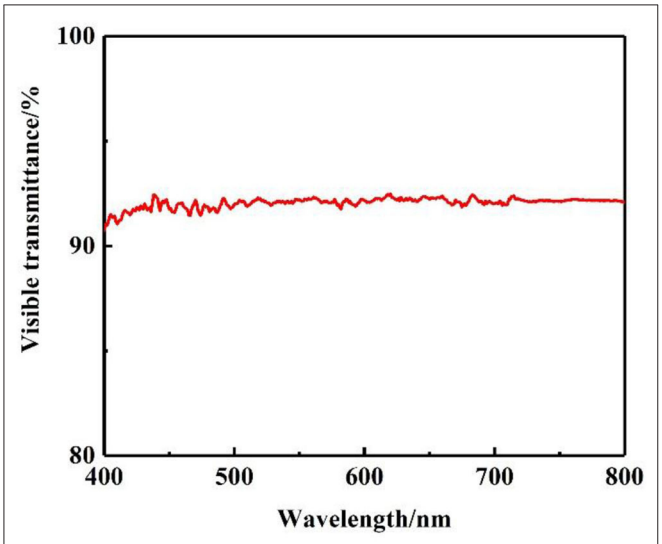

FIGURE 15 | The visible transmittance of the sample.

result and simulated result is consistent. However, the test result is better than the simulation possibly because of the thinner processed thickness of the dielectric layer.

For IR low emissivity property, TSS-5X IR emissivity and G100EX thermal camera were utilized for test. In order to get a direct analysis result, a PET board with the same size was compared with the sample. The IR emittance results were presented in **Figure 13**. Its back and the PET board were 0.27, 0.19, and 0.91, respectively, matching the intended results.

A qualitative experiment was conducted to better testify the IR-stealth property of the sample. The sample and the same size PET board were heated at the same temperature by HZ-2019A high–low temperature test chamber. And then the G100EX thermal camera was used to compare their IR thermal images.

It is direct to reveal that the IR-stealth capacity of MSM is effective as shown in **Figure 14**. Heated at the same 45° temperature, their IR thermal images show great differences. At 24.9° environment temperature (c point), the temperature of PET was 43.8° (a point), whereas the sample only showed 26.6° (b point), as displayed in **Figure 14B**.

The visible transmittances spectra of the sample are tested by ultraviolet-visible spectrophotometer in order to get accurate data of the optically transparent result. The average visible transmittance of the sample is > 90% to reveal that it has great visible light transmission property as exhibited in **Figure 15**.

CONCLUSION

In conclusion, we propose the design of an MSM that can simultaneously achieve quite good optical transparency, low IR emissivity, and wideband microwave absorption. A prototype was designed, fabricated, and measured. Both the simulation and experiment results show that the MSM can achieve strong absorption > 90% in 12.03–29.43 GHz and low IR emissivity about 0.3 in 3.0–14.0 μm simultaneously. Moreover, the average optical transparency is higher than 90%. Because of the excellent multispectral compatibility, the MSM may find applications in electromagnetic protection, stealth technologies, etc.

DATA AVAILABILITY STATEMENT

All datasets presented in this study are included in the article/supplementary material.

AUTHOR CONTRIBUTIONS

SH and JW designed the structure. SH, QF, and JW designed experiment. SH wrote the manuscript. QF and JW revised the manuscript. CX, BW, BY, CT, and ZM checked the manuscript. All authors contributed to the article and approved the submitted version.

ACKNOWLEDGMENTS

The authors are grateful to the support from the Natural Science Foundation of Shaanxi Province No. 2020JQ-471.

REFERENCES

1. Zhao J, Cheng Q, Chen J, Qi MQ, Jiang W, Cui TJ, et al. A tunable metamaterial absorber using varactor diode. *New J Phys*. (2013) 15:043049. doi: 10.1088/1367-2630/15/4/043049
2. Xiao L, Ma H, Liu J, Zhao W, Jia Y, Zhao Q, et al. Fast adaptive thermal camouflage based on flexible VO_2/Graphene/CNT Thin Films *Nano Lett*. (2015) 15:8365–70. doi: 10.1021/acs.nanolett.5b04090
3. Pu M, Hu C, Wang M, Huang C, Zhao Z, Wang C, et al. Design principles for infrared wide-angle perfect absorber based on plasmonic structure. *Opt Express*. (2011) 19:17413–20. doi: 10.1364/OE.19.017413
4. Cui Y, Fung KH, Xu J, Ma H, Jin Y, He S, et al. Ultrabroadband light absorption by a sawtooth anisotropic metamaterial slab. *Nano Lett*. (2012) 12:1443–7. doi: 10.1021/nl204118h
5. Ma J, Ma Z, Sun W, Ding F, He Q, Zhou L, et al. Ultra-broadband terahertz metamaterial absorber. *Appl Phys Lett*. (2014) 105:021102. doi: 10.1063/1.4890521
6. Liu TH, Meng YY, Ma H, Wang JF, Yuan Q, Qu SB. Extraordinary spoof surface plasmon polaritons excitation by linear and circular polarization conversions phase gradient metasurface. *J Phys*. (2020) 53:045003. doi: 10.1088/1361-6463/ab522e
7. Liu TH, Meng YY, Ma H, Wang JF, Yuan Q, Qu SB. Obtaining single mode spoof surface plasmon polaritons under circular polarized incidence. *J Phys*. (2020) 53:115003. doi: 10.1088/1361-6463/ab614b
8. Wang WJ, Wang J, Yan MB, Wang JF, Ma H, Feng MD, et al. Dual band tunable metamaterial absorber based on cuboid ferrite particles. *J Phys*. (2018) 51:315001. doi: 10.1088/1361-6463/aacf09
9. Zhang J, Wei XZ, Premaratne M, Zhu WR. Experimental demonstration of an electrically tunable broadband coherent perfect absorber based on a graphene–electrolyte–graphene sandwich structure. *Photonics Res*. (2019) 7:868–74. doi: 10.1364/PRJ.7.000868
10. Kang M, Chong YD, Wang HT, Zhu W, Premaratne M. Critical route for coherent perfect absorption in a Fano resonance plasmonic system. *Appl Phys Lett*. (2014) 105:1–5. doi: 10.1063/1.4896972
11. Jing HB, Ma Q, Bai GD, Bao L, Luo J, Cui TJ. Optically transparent coding metasurfaces based on indium tin oxide films. *J Appl Phys*. (2018) 124:023102. doi: 10.1063/1.5027589
12. Pang Y, Shen Y, Li Y, Wang J, Xu Z, Qu S. Water-based metamaterial absorbers for optical transparency and broadband microwave absorption. *J Appl*. (2018) 123:155106. doi: 10.1063/1.5023778
13. Kim J, Han K, Hahn JW. Selective dual-band metamaterial perfect absorber for infrared stealth technology. *Sci Rep*. (2017) 7:6740. doi: 10.1038/s41598-017-06749-0
14. Xu C, Wang B, Pang Y, Wang J, Yan M, Wang W, et al. Hybrid metasurfaces for infrared-multiband radar stealth-compatible materials applications. *IEEE Access*. (2019) 7:147586–95. doi: 10.1109/ACCESS.2019.2946405
15. Shen X, Cui TJ, Zhao J, Ma HF, Jiang WX, Li H. Polarization-independent wide-angle triple-band metamaterial absorber. *Opt Express*. (2011) 19:9401–7. doi: 10.1364/OE.19.009401
16. Zhang C, Cheng Q, Yang J, Zhao J, Cui JT. Broadband meta-material for optical transparency and microwave absorption. *Appl Phys Lett*. (2017) 110:143511. doi: 10.1063/1.4979543
17. Eugene Knott F, John Shaeffer F, Michael Tuley T. *Radar Cross Section*. IET Digital Library (2004). doi: 10.1049/SBRA026E
18. Immordino ML, Dosio F, Cattel L. Stealth liposomes: review of the basic science, rationale, clinical applications, existing and potential. *Int J Nanomed*. (2006) 1:297–315. Available online at: https://www.ncbi.nlm.nih.gov/pmc/articles/PMC2426795/
19. Rao GA, Mahulikar SP. Integrated review of stealth technology and its role in airpower. *Aeronaut J*. (2002) 106:629–42. Available online at: https://www.cambridge.org/core/journals/aeronautical-journal/article/integrated-review-of-stealth-technology-and-its-role-in-airpower/39A80DDAB0AA8B8112238F70F8FE3C01
20. Qi D, Wang X, Cheng Y, Gong R, Li B. Design and characteriza-tion of one-dimensional photonic crystals based on ZnS/Ge for infrared-visible compatible stealth applications. *Opt Mater*. (2016) 62:52–6. doi: 10.1016/j.optmat.2016.09.024
21. Wang Y, Cheng HF, Wang J, Zhou YJ. Infrared emissivity of capacitive frequency-selective surfaces and its application in radar and IR compatible stealth sandwich structures. *Adv Mater Res*. (2011) 382:65–9. doi: 10.4028/www.scientific.net/AMR.382.65
22. Zhong S, Jiang W, Xu P, Liu T, Huang J, Ma Y. A radar-infrared bi-stealth structure based on metasurfaces. *Appl Phys Lett*. (2017) 110:063502. doi: 10.1063/1.4975781
23. Hao T, Liu HT, Cheng HF. A thin radar-infrared stealth-compatible structure: design, fabrication, characterization. *Phys B*. (2014) 23:025201. doi: 10.1088/1674-1056/23/2/025201
24. Pang Y, Li Y, Yan M, Liu D, Wang J, Xu Z, et al. Hybrid metasurfaces for microwave reflection and infrared emission reduction. *Opt Exp*. (2018) 26:11950–58. doi: 10.1364/OE.26.011950
25. Zhang C, Yang J, Yuan W, Zhao J, Dai J, Guo T, et al. An ultralight and thin metasurface for radar-infrared bi-stealth applications. *J Phys*. (2017) 50:444002. doi: 10.1088/1361-6463/aa8ba6
26. Xu C, Wang B, Yan M, Pang Y, Wang W, Meng Y, et al. An optical-transparent metamaterial for high-efficiency microwave absorption and low infrared emission. *J Phys*. (2020) 53:135109. doi: 10.1088/1361-6463/ab651a
27. Shuomin Z, Lijie W, Taijun L, Jifu H, Wei J, Yungui M. Transparent transmission-selective radar-infrared bi-stealth structure. *Opt Exp*. (2018) 26:16466. doi: 10.1364/OE.26.016466

Conflict of Interest: The authors declare that the research was conducted in the absence of any commercial or financial relationships that could be construed as a potential conflict of interest.

frontiers in Physics

ORIGINAL RESEARCH
published: 06 October 2020
doi: 10.3389/fphy.2020.575824

Highly Efficient Bifunctional Dielectric Metasurfaces at Visible Wavelength: Beam Focusing and Anomalous Refraction in High-Order Modes

Zhenyu Xu, Zhiwei Li, Yanqing Tian, Yunbing Wei and Fei Wu*

School of Electronic and Electrical Engineering, Shanghai University of Engineering Science, Shanghai, China

Metasurface is an artificially arranged sub-wavelength micro-structure array, where each structure can be regarded as a unit cell that is controlled by electromagnetic waves. Recently, bifunctional metasurfaces have garnered increasing interest and become excellent candidates for device miniaturization and integration. In this study, we propose a highly efficient bifunctional metasurface composed of silicon nanopillars, enabling beam anomalous refraction and focusing at visible wavelength. Based on the proposed metasurface, the other two metasurfaces demonstrating high-order beam anomalous refraction and focusing are designed successfully. This work will establish a positive prospect for the development of high-performance bifunctional metasurfaces.

Keywords: metasurface, bifunctional, highly-efficient, high-order, visible band

OPEN ACCESS

Edited by:
Zhi Hong,
China Jiliang University, China

Reviewed by:
Elyas Bayati,
University of Washington, United States
Ilia L. Rasskazov,
University of Rochester, United States

****Correspondence:***
Zhiwei Li
zhiwei.li@sues.edu.cn

Specialty section:
This article was submitted to Optics and Photonics, a section of the journal Frontiers in Physics

Received: *24 June 2020*
Accepted: *07 September 2020*
Published: *06 October 2020*

Citation:
Xu Z, Li Z, Tian Y, Wei Y and Wu F (2020) Highly Efficient Bifunctional Dielectric Metasurfaces at Visible Wavelength: Beam Focusing and Anomalous Refraction in High-Order Modes. Front. Phys. 8:575824. doi: 10.3389/fphy.2020.575824

INTRODUCTION

The complete control of electromagnetic waves has always been an emerging field of research. Traditional optical equipment has a large volume, heavyweight, complex shape, and other inevitable defects, therefore, such equipment is not suitable for application in integrated photonic systems and device miniaturization. Considering the fact that the conventional optical components rely on gradual phase shifts accumulated during light propagation to shape light beams [1], a three-dimensional metamaterial, exhibits peculiar material properties that do not exist in nature, provide a more flexible way in manipulating the wavefront of electromagnetic waves, which can be used to realize negative refractive index [2], perfect lens [3], and invisibility cloaking [4]. However, three-dimensional metamaterials have many drawbacks, such as high inherent losses and manufacturing difficulties, which limit the miniaturization of the device in practice. With the development of nanotechnology, a metasurface, which is regarded as a two-dimensional metamaterial, has been proposed to cope with the drawbacks due to its ultrathin sub-wavelength structure, relatively easy to manufacture and conformal integration with systems [5, 6]. Metasurfaces typically consist of an array of sub-wavelength metallic or dielectric nanostructures, their geometric parameters, including size, shape, and direction can be adjusted to change the amplitude, phase, and polarization of light. Based on the obvious features, various metasurfaces with different functions have been extensively studied, including beam deflectors [7–10], metalenses [11–13], waveplates [14, 15], and high-resolution holograms [16, 17].

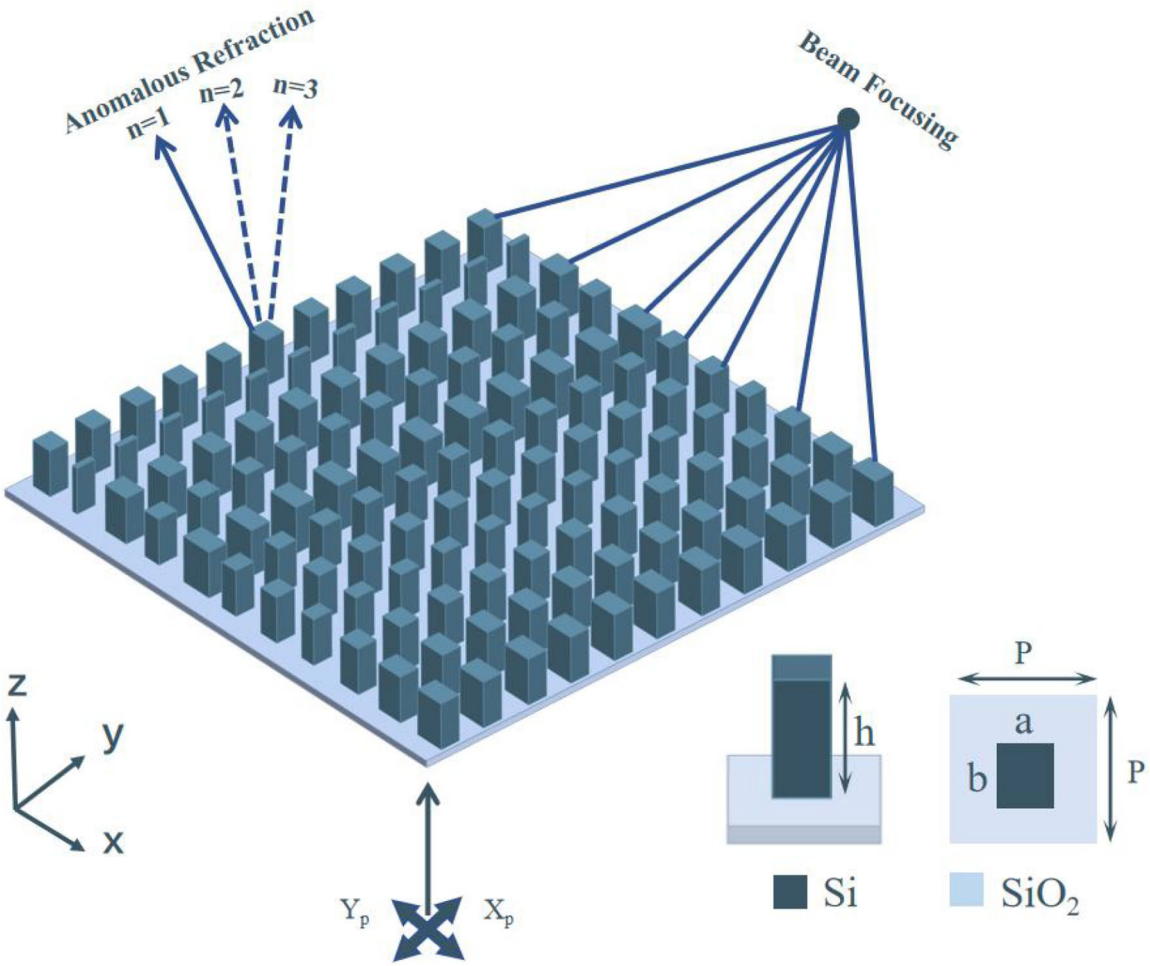

FIGURE 1 | Schematic of the proposed highly efficient bifunctional metasurface. The lower corner shows the unit cell of the metasurface.

So far, most of metasurfaces invented by people have a single function. With the increasing demand for data storage and information management, it is desirable to fabricate a device that has multiple functions. Recently, metasurfaces with multiple functions have been developed by controlling the polarization, wavelength, and incident angle [18–23]. These metasurfaces can be used in integrated systems owing to their small footprint, which has been confirmed in the microwave [24, 25] and visible bands [26, 27]. Traditional bifunctional plasmonic metasurfaces mainly depend on the Pancharatnam-Berry (PB) phase to control the wavefront of circularly polarized (CP) light. In spite of its intrinsic wavelength-independent and dispersion-free features which results in the broadband operation, the PB phase is susceptible to several restrictions. For a metasurface that depends on the PB phase, the incident CP light is known to be scattered into waves of both the same and opposite polarizations [28]. By rotating the orientation of meta-atoms, it is easy to obtain the abrupt phase shift, which is useful for wavefront shaping. However, it works only for CP light with the opposite polarization, leading to a limited polarization conversion efficiency of 25% [29]. Due to the metasurface is formed by spatial multiplexing of two metasurfaces that provide different functions, it may cause a functional crosstalk because one function tends to add background noise to the other [30].

In this paper, we propose a highly efficient bifunctional dielectric metasurface, enabling beam anomalous refraction and focusing at visible wavelength. The meta-atom constituting the metasurface unit cell is made of rectangular silicon nanopillar, enduing polarization-selective phase shifts to realize the two functions. With regard to this purpose, we first discussed the relationship between the geometric parameters of the nanopillar and the polarization-dependent phase shifts, the results show that, upon the light with the designated polarizations in normal incidence, the metasurface not only exhibits a highly efficient and ignorable functional crosstalk beam anomalous refraction, but also exhibits light focusing. Based on the metasurface proposed above, the other two metasurfaces demonstrating high-order beam anomalous refraction and focusing have been designed successfully. The reliability of the proposed method is

confirmed by the consistency between the simulation and theoretical calculation.

DESIGN AND ANALYSIS

A bifunctional metasurface is required to impart two disparate spatial phase distributions efficiently to realize distinct wavefront modulation. Moreover, the two functions will not entail crosstalk, meaning that one function is rarely affected by the other. Our bifunctional metasurface is based on the idea that a single dielectric element atom causes a flexible phase delay on incident light according to polarization. The schematic of the proposed bifunctional metasurface is shown in **Figure 1**. For the incident light of X-linear-polarized (X_p) and Y-linear-polarized (Y_p), the metasurface can realize beam anomalous refraction and focusing, respectively. The dotted lines correspond to modes 2 and 3. The unit cell is composed of a rectangular Si nanopillar on the top of a silicon dioxide (SiO_2) substrate, as shown in the illustration in the lower right corner. The illustration shows the section and top views of the unit cell. Regarding the unit cell, the Si nanopillar implies a full range of phase from 0 to 2π in the transmission of X_p and Y_p incident light, which can provide a full span of wavefront phase. To investigate the feasibility of the proposed design, we simulate the bifunctional metasurface using the finite difference time domain (FDTD) method (FDTD Solutions, Lumerical, Canada). In the simulations, the period of the unit cell is set as $P = 230$ nm, while the thickness of Si nanopillars are set as $h = 310$ nm. The operation wavelength is designed to be 660 nm for the wavelength of optical communication.

RESULTS AND DISCUSSIONS

For the proposed dielectric metasurface, it is believed that the Si nanopillar constituting the unit cell plays a role as a truncated

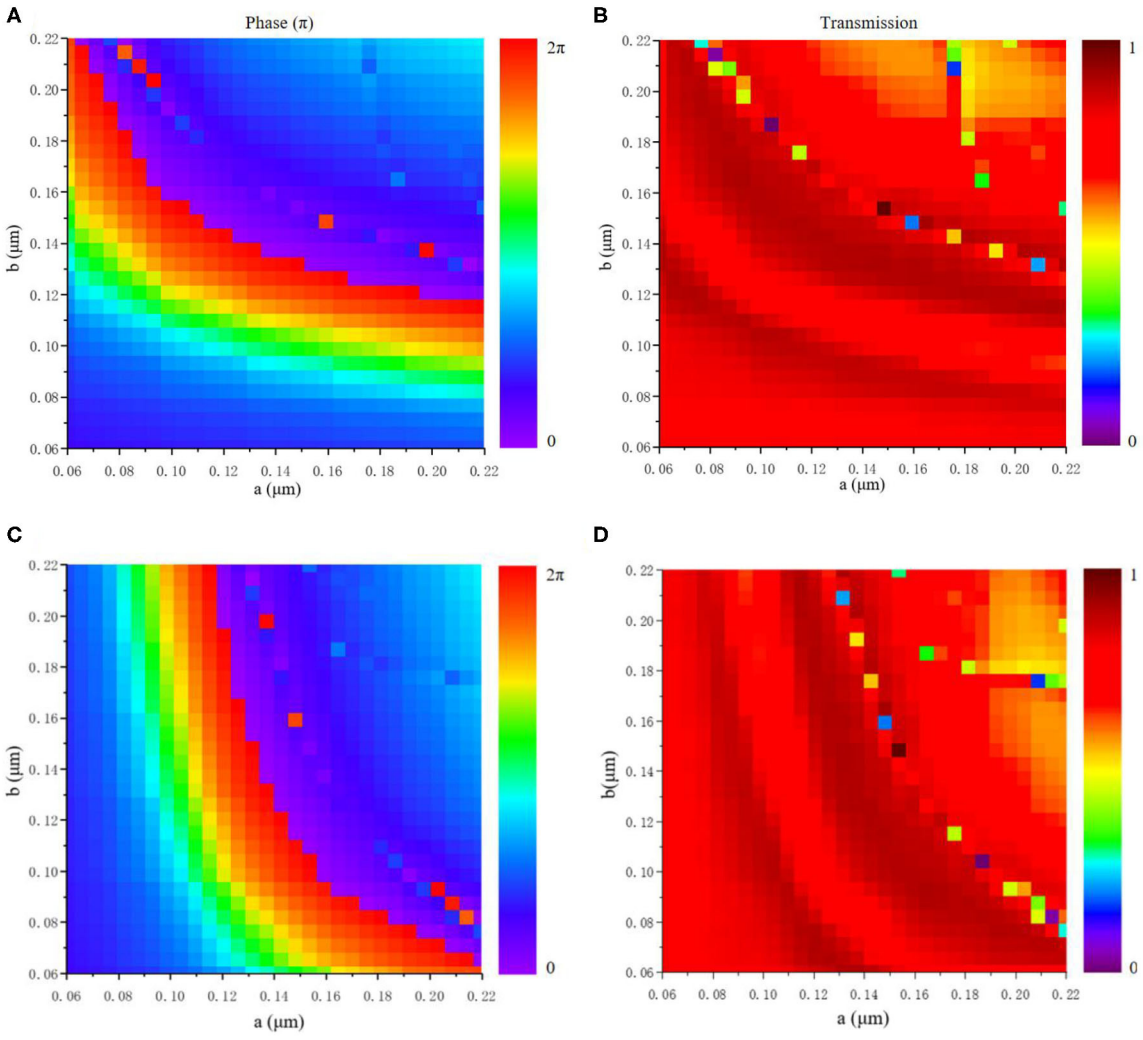

FIGURE 2 | (A,B) The phase distribution and transmission efficiency of X_p light as a function of parameters a and b. **(C,D)** The phase distribution and transmission efficiency of Y_p light as a function of parameters a and b.

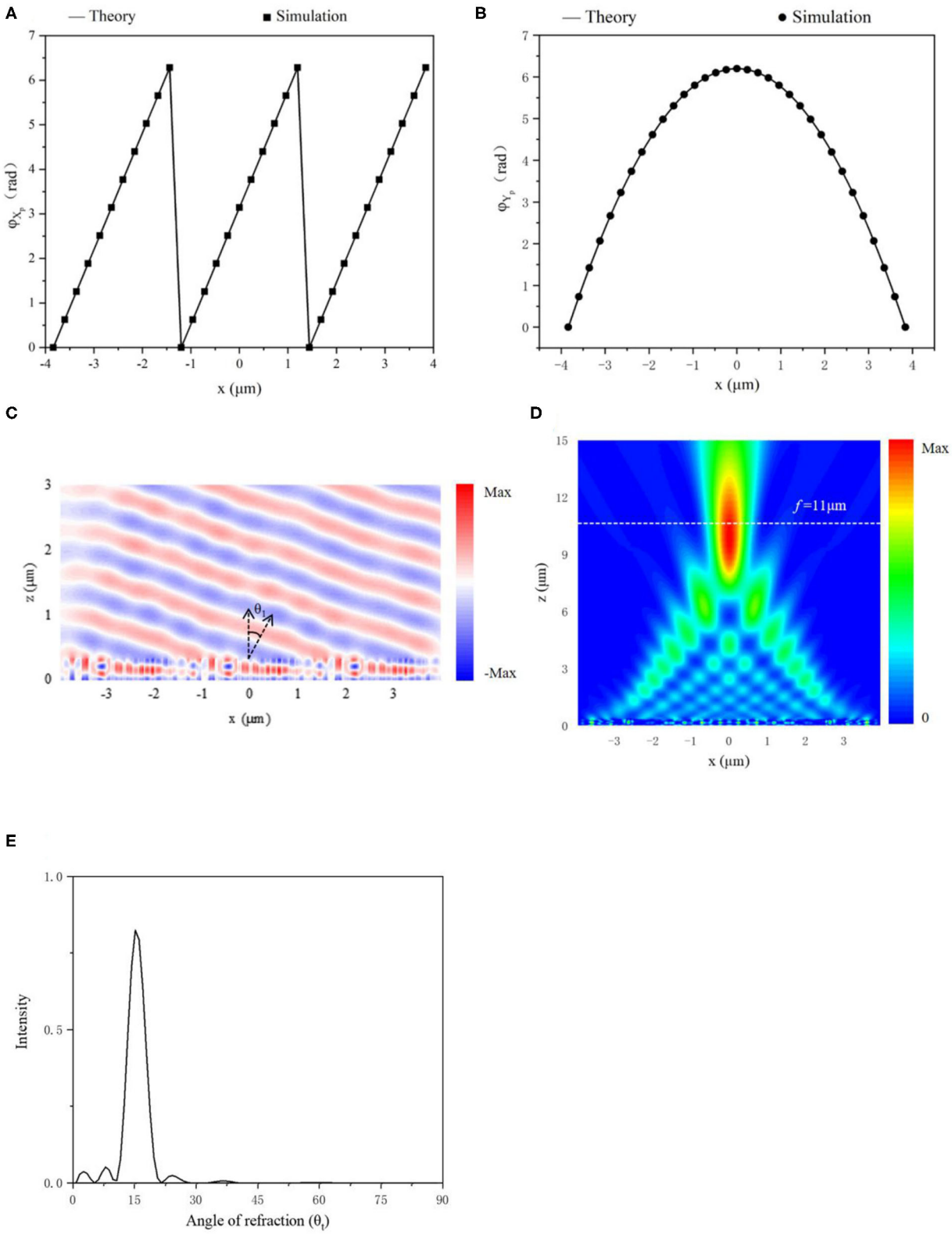

FIGURE 3 | (A,B) The theoretical and simulated phase profiles for beam anomalous refraction and focusing under normal X_p and Y_p light incidence, respectively. **(C)** The x-component of the transmitted electric field under normal X_p light incidence. **(D)** The y-component of the transmitted field intensity under normal Y_p light incidence. **(E)** Normalized far-field intensity as a function of the angle of refraction at the wavelength of $\lambda = 660$ nm under normal X_p light incidence.

waveguide and operates as a low-quality factor Fabry-Pérot resonance [20]. **Figures 2A,B** exhibit the phase variations and transmission efficiency of X_p light, respectively, as a function of the widths of the nanopillar, including a and b. Similarly, **Figures 2C,D** correspond to Y_p light, and the efficiency has reached more than 86%.

A bifunctional metasurface composed of an array of 33 × 33 meta-atoms has been proposed to realize beam anomalous refraction and focusing. In this regard, it is proved that a bifunctional metasurface that employs the proposed nanopillars can impart two different wavefront modulations. Each row of 33 nanopillars arranged along the x-axis can be considered as a supercell that imparts a hyperbolic phase distribution to the incidence of Y_p light. With regard to the anomalous refraction realized by the incidence of X_p light, the 33 nanopillars along the y-axis can be considered as three supercells, with each supercell consisting of 11 nanopillars to provide a linearly varying 2π phase shift. Both theoretical and simulated phase profiles are demonstrated in **Figures 3A,B**. For the incidence of X_p light, the anomalous refraction is depicted in **Figure 3C**, and the phase profile of the anomalous refraction is dictated by the generalized Snell's law:

$$\sin(\theta_t)n_t - \sin(\theta_i)n_i = \frac{\lambda}{2\Pi}\frac{d\Phi}{dx} \quad (1)$$

where θ_i is the incident angle, n_i and n_t are the refractive indices of the incident and transmitting media, respectively, and $d\Phi/dx$ is the gradient of phase discontinuity along the interface. For the incidence of Y_p light, the beam is focused at a focal length *f*, which is designed to be 11 μm, as shown in **Figure 3D**. Its hyperbolic phase profile is governed by the following equation:

$$\phi(x) = \frac{2\Pi}{\lambda}(f - \sqrt{(x - x_0)^2 + f^2}) \quad (2)$$

where λ is the operating wavelength, and x_0 is the central position in the middle of the supercell. The angle of refraction θ_1 is

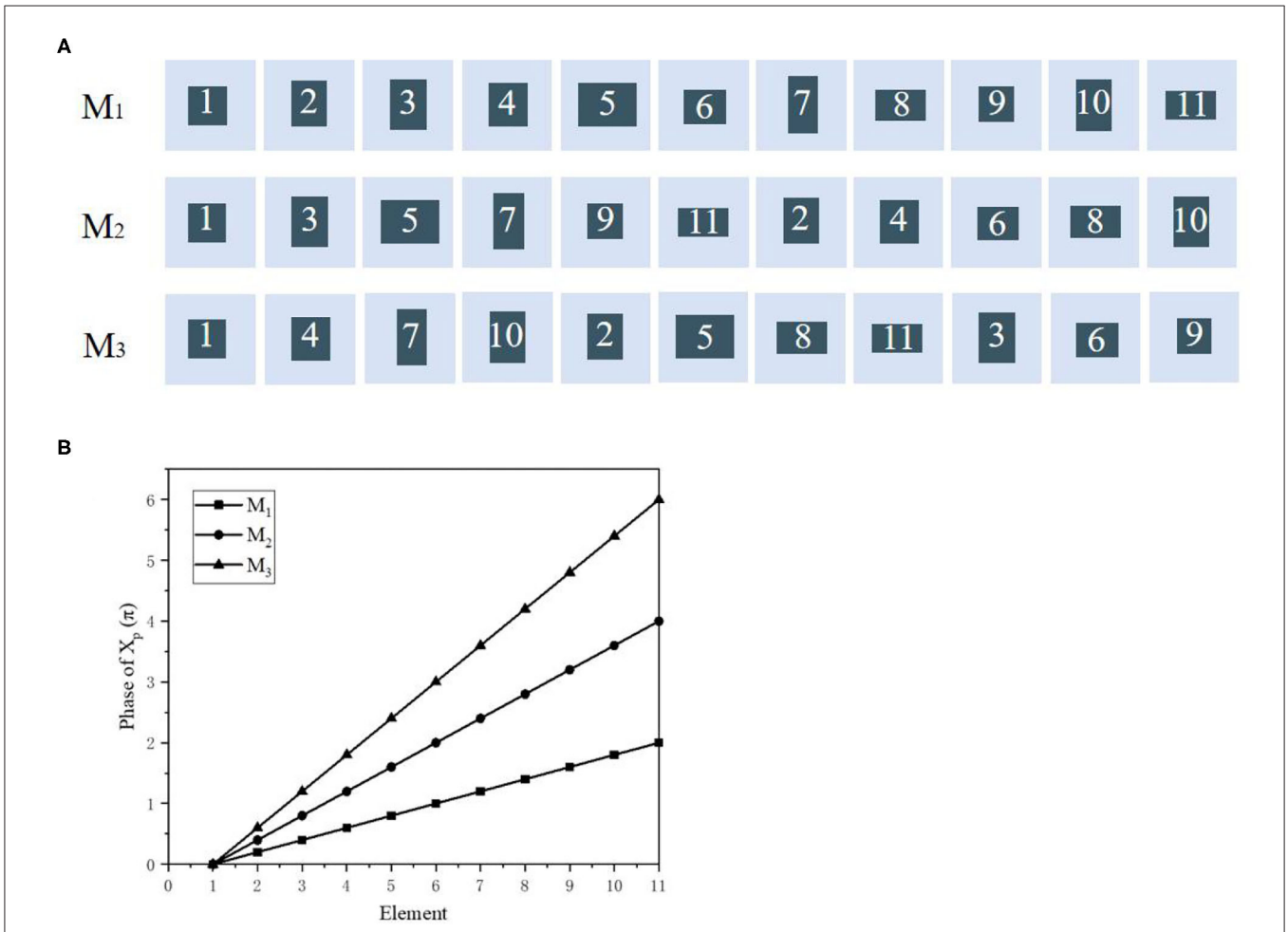

FIGURE 4 | Design of the dielectric metasurfaces with three different orders diffraction modes. **(A)** Schematics of lateral dimensions of the 11 designed nanopillars. First line M_1: a supercell with transmitted phase ranging from 0 to 2π. Second line M_2: a rearranged supercell with phase ranging from 0 to 2 × 2π. Third line M_3: a rearranged supercell with phase ranging from 0 to 3 × 2π. **(B)** The phase shift of the 11 designed nanopillars for three different modes.

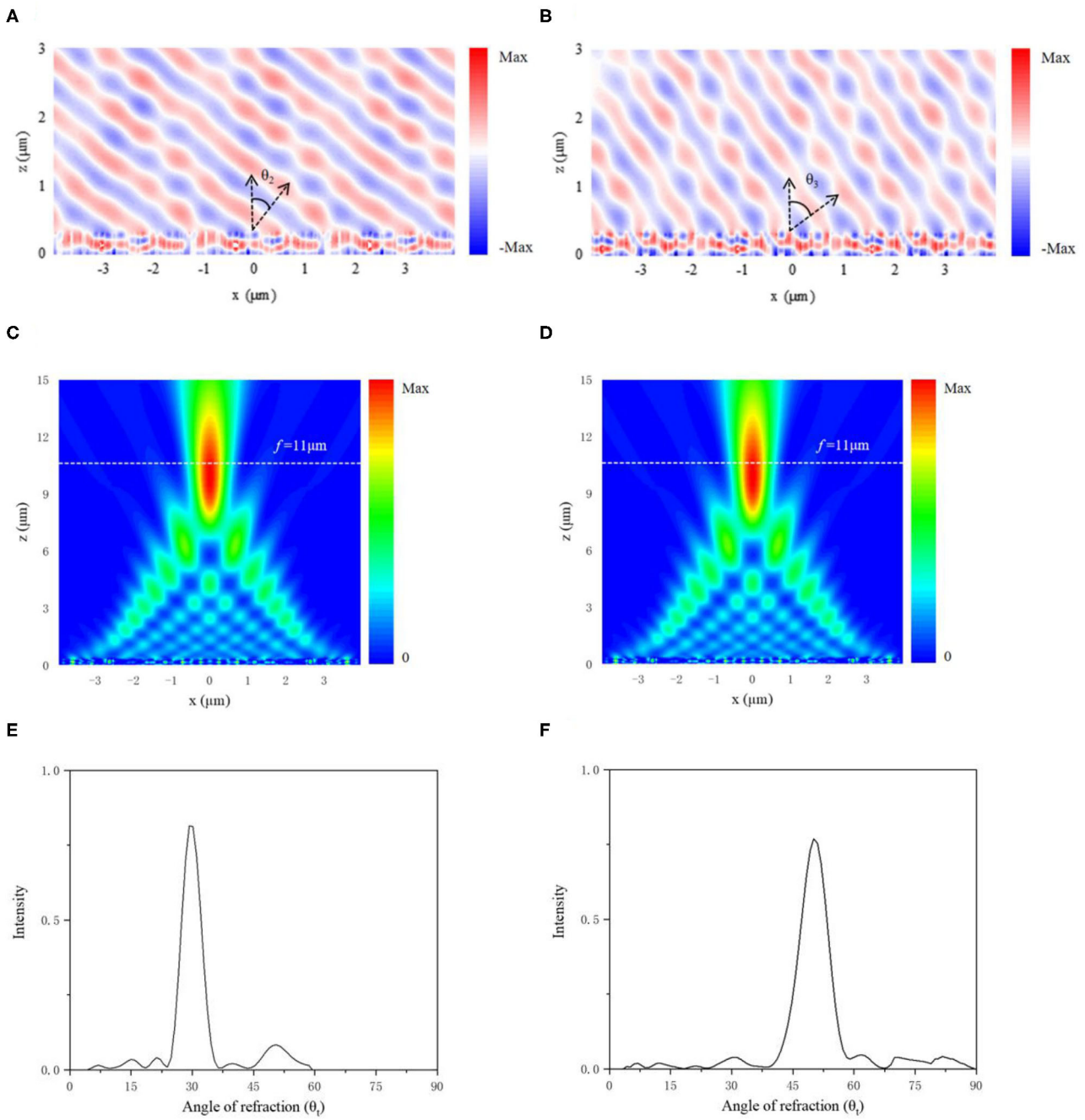

FIGURE 5 | (A,B) The x-component of the transmitted electric field under normal X_p light incidence on the metasurface working in the 2nd and 3rd orders, respectively. **(C,D)** The y-component of the transmitted field intensity under normal Y_p light incidence on the metasurface working in the 2nd and 3rd orders, respectively. **(E,F)** Normalized far-field intensity as a function of the angle of refraction at the wavelength of $\lambda = 660$ nm under normal X_p light incidence on the metasurface working in the 2nd and 3rd orders, respectively.

estimated to be 14.02° in simulation (**Figure 3E**), which closely agrees with the theoretically calculated angle of 14.48°.

Based on the designed metasurface above, two metasurfaces working in high-order diffraction modes have been designed successfully. In the design of metasurface 1 (M_1), we discrete the phase range from 0 to 2π to 0 into 11 nanopillars along the y-axis with equal step of π/5 for X_p transmitted light. The lateral dimensions of the 11 selected silicon nanopillars are numbered in ascending order, as shown in the first line of **Figure 4A**. It appears that the range of phase control could be extended to

high-order diffraction modes by appropriately selecting the unit cells in M_1 and rearranging them. For instance, if we intend to expand the diffraction mode to the Nth order, the phase coverage should be from 0 to $N\times2\pi$ with a gradient of $N\times\pi/5$ between two neighboring nanopillars for X_p transmitted light. As a result, the second line of **Figure 4A** presents the rearranged supercell for the second order diffraction mode (M_2), where the phase coverage of the unit cell is from 0 to 4π with a gradient of $2\pi/5$ between two neighboring nanopillars for X_p transmitted light. Similarly, a metasurface working in the third order diffraction mode is also constructed by a set of 11 dielectric nanopillars, whose phase coverage is from 0 to 6π with a gradient of $3\pi/5$ between two neighboring nanopillars for X_p transmitted light, as shown in the third line of **Figure 4A**. To clearly outline the concept, we plot the transmission phase of the 11 elements with three concrete arrangements for X_p transmitted light, as shown in **Figure 4B**.

For comparison, **Figure 5** demonstrates the beam anomalous refraction and focused electric field distribution of the other two rearranged metasurfaces made of newly designed supercells (M_2 and M_3) for X_p and Y_p incident light. Since the supercells of the two metasurfaces have been rearranged, the optical behavior of M_2 and M_3 are governed by the following diffraction equation:

$$\sin(\theta_t)n_t - \sin(\theta_i)n_i = m\frac{\lambda}{D} \tag{3}$$

where m is the order of diffraction spectrum, and $D = 11p$ is the periodicity of the supercell. According to Equations (1) and (3), it can be noted that the interface with the phase coverage of $2 \times 2\pi$ and $3 \times 2\pi$, correlates to $d\Phi/dx = 2\times2\pi/D$ and $d\Phi/dx = 3 \times 2\pi/D$, respectively, over a periodicity D, the resulting anomalous refraction corresponds to the second and third order diffraction. The effect of focusing will not be affected due to the phase of the supercell along the x-axis is in maintaining with the metasurface working in the first-order diffraction. **Figures 5A,C** show that the metasurface working in the second order has an anomalous refraction angle θ_2 and the beams are focused at 11 μm, **Figure 5B,D** correspond to the third order. It is clearly obtained from **Figures 5E,F** that the angles of refraction θ_2 and θ_3 are 29.58° and 48.43°, respectively, which are closely consistent with the theoretically calculated angles of 30° and 48.59°.

CONCLUSION

In conclusion, we have proposed a highly efficient transmissive bifunctional metasurface that enables the beam anomalous refraction and focusing at visible wavelength. By controlling the parameters of the Si nanopillars in each unit cell of the metasurface, a full range of phase from 0 to 2π for the transmission of incident light and a high efficiency (over 86%) are obtained. The nanopillars that comprise the bifunctional metasurface are devised accurate to impart a linear and hyperbolic phase profile to the X_p and Y_p incident lights, respectively. Based on the designed metasurface, another two metasurfaces that demonstrate the high-order beam anomalous refraction and focusing have been proposed successfully. Our work can be easily extended to the design of other optical transmitting facilities with high-efficiency, which will be useful in the fabrication of miniaturized and multifunctional metadevices.

DATA AVAILABILITY STATEMENT

The original contributions presented in the study are included in the article/supplementary material, further inquiries can be directed to the corresponding author.

AUTHOR CONTRIBUTIONS

All the authors designed research, performed research, analyzed data, and wrote the paper.

FUNDING

This work was supported by the National Natural Science Foundation of China (Grant Nos. 61705127, 11704243) and Degree construction project of Detection Technology and Automation Devices of Shanghai University of Engineering Science (No. 19XXK003).

REFERENCES

1. Yu N, Genevet P, Kats MA, Aieta F, Tetienne JP, Capasso F, et al. Light propagation with phase discontinuities: generalized laws of reflection and refraction. *Science.* (2011) **334**:333–7. doi: 10.1126/science.1210713
2. Veselago VG. The electrodynamics of substances with simultaneously negative values of and μ. *Sov Phys Usp.* (1968) **10**:509–14. doi: 10.1070/PU1968v010n04ABEH003699
3. Wang W, Guo Z, Zhou K, Sun Y, Shen F, Li Y, et al. Polarization-independent longitudinal multi-focusing metalens. *Opt Express.* (2015) **23**:29855–66. doi: 10.1364/OE.23.029855
4. Li Z, Palacios E, Butun S, Aydin K. Visible-frequency metasurfaces for broadband anomalous reflection and high-efficiency spectrum splitting. *Nano Lett.* (2015) **15**:1615–21. doi: 10.1021/nl5041572
5. Lyer PP, Butakov NA, Schuller JA. Reconfigurable semiconductor phased-array metasurfaces. *ACS Photonics.* (2015) **2**:1077–84. doi: 10.1021/acsphotonics.5b00132
6. Colburn S, Zhan A, Bayati E, Whitehead J, Ryou A, Huang L. Broadband transparent and CMOS-compatible flat optics with silicon nitride metasurfaces. *Opt Mater Express.* (2018) **8**:2330–34. doi: 10.1364/OME.8.002330
7. Shang X, Meeus L, Cuypers D. Fast switching cholesteric liquid crystal optical beam deflector with polarization independence. *Sci Rep.* (2017) **7**:6492. doi: 10.1038/s41598-017-06944-z
8. Ni X, Emani NK, Kildishev AV, Boltasseva A, Shalaev VM. Broadband light bending with plasmonic nanoantennas. *Science.* (2012) **335**:427. doi: 10.1126/science.1214686
9. Li Z, Huang L, Lu K, Sun Y, Min L. Continuous metasurface for high-performance anomalous reflection. *Appl Phy Express.* (2014) **7**:112001. doi: 10.7567/APEX.7.112001
10. Li Z, Cai X, Huang L, Xu H, Dai N. Controllable polarization rotator with broadband high transmission using all-dielectric metasurface. *Adv Theory Simul.* (2019) **2**:1900086. doi: 10.1002/adts.201900086

11. Arbabi E, Arbabi A, Kamali SM, Horie Y, Faraon A. Multiwavelength polarization-insensitive lenses based on dielectric metasurfaces with meta-molecules. *Optica*. (2016) **3**:628–33. doi: 10.1364/OPTICA.3.000628
12. Li R, Guo Z, Wang W, Zhang J, Zhou K, Liu J, et al. Arbitrary focusing lens by holographic metasurface. *Photonics Res.* (2015) **3**:252–5. doi: 10.1364/PRJ.3.000252
13. Bayati E, Zhan A, Colburn S, Zhelyeznyakov MV, Majumdar A. Role of refractive index in metalens performance. *Appl Opt.* (2019) **58**:1460–66. doi: 10.1364/AO.58.001460
14. Hao J, Yuan Y, Ran L, Jiang T, Kong JA, Chan CT, et al. Manipulating electromagnetic wave polarizations by anisotropic metamaterials. *Phys Rev Lett.* (2007) **99**:063908. doi: 10.1103/PhysRevLett.99.063908
15. Li Y, Li Z, Liu Y, Kong Y, Huang L. Broadband and highly polarization conversion in infrared region using plasmonic metasurfaces. *Opt Mater.* (2019) **98**:109420. doi: 10.1016/j.optmat.2019.109420
16. Chen W, Yang KY, Wang CM, Huang YW, Sun G, Chiang ID, et al. High-efficiency broadband meta-hologram with polarization-controlled dual images. *Nano Lett.* (2014) **14**:225–30. doi: 10.1021/nl403811d
17. Wang B, Dong F, Li QT, Yang D, Sun C, Chen J, et al. Visible-frequency dielectric metasurfaces for multiwavelength and highly dispersive holograms. *Nano Lett.* (2016) **16**:5235–40. doi: 10.1021/acs.nanolett.6b02326
18. Pors A, Albrektsen O, Radko IP, Bozhevolnyi SI. Gap plasmon-based metasurfaces for total control of reflected light. *Sci Rep.* (2013) **3**:2155. doi: 10.1038/srep02155
19. Farmahini-Farahani M, Mosallaei H, Birefringent reflectarray metasurface for beam engineering in infrared. *Opt Lett.* (2013) **38**:462–4. doi: 10.1364/OL.38.000462
20. Arbabi A, Horie Y, Bagheri M, Faraon A. Dielectric metasurfaces for complete control of phase and polarization with subwavelength spatial resolution and high transmission. *Nat Nanotechnol.* (2015) **10**:937–43. doi: 10.1038/nnano.2015.186
21. Chen Y, Yang X, Gao J. Spin-controlled wavefront shaping with plasmonic chiral geometric metasurface. *Light.* (2018) **7**:84. doi: 10.1038/s41377-018-0086-x
22. Li Z, Hao J, Huang L, Li H, Xu H, Sun Y, et al. Manipulating the wavefront of light by plasmonic metasurfaces operating in high order modes. *Opt Express.* (2016) **24**:8788–96. doi: 10.1364/OE.24.008788
23. Khan MI, Fraz Q, Tahir FA. Ultra-wideband cross polarizationconversion metasurface insensitivetoincidence angle. *J Appl Phys.* (2017) **121**:045103. doi: 10.1063/1.4974849
24. Cai T, Tang S, Wang G, Xu H, Sun S, He Q, et al. High-performance bifunctional metasurfaces in transmission and reflection geometries. *Adv Opt Mater.* (2016) **5**:1600506. doi: 10.1002/adom.201600506
25. Cai T, Wang G-M, Xu H-X, Tang S-W, Li H, Liang J-L, et al. Bifunctional pancharatnam-berry metasurface with high-efficiency helicity-dependent transmissions and reflection. Ann Phys. (2017) 530:1700321. doi: 10.1002/andp.201700321
26. Shi Z, Khorasaninejad M, Huang YW, Roques-Carmes C, Zhu AY, Chen WT, et al. Single-layer metasurface with controllable multiwavelength functions. *Nano Lett.* (2018) **18**:2420–7. doi: 10.1021/acs.nanolett.7b05458
27. Zhang C, Yue F, Wen D, Chen M, Zhang Z, Wang W, et al. Multichannel metasurface for simultaneous control of holograms and twisted light beams. *ACS Photonics.* (2017) **4**:1906–12. doi: 10.1021/acsphotonics.7b00587
28. Huang L, Chen X, Muhlenbernd H, Li G, Bai B, Tan Q, et al. Dispersionless phase discontinuities for controlling light propagation. *Nano Lett.* (2012) **12**:5750–55. doi: 10.1021/nl303031j
29. Liu C, Bai Y, Zhao Q, Yang Y, Chen H, Zhou J, et al. Fully controllable pancharatnam-berry metasurface array with high conversion efficiency and broad bandwidth. *Sci Rep.* (2016) **6**:34819. doi: 10.1038/srep34819
30. Avayu O, Almeida E, Prior Y, Ellenbogen T. Composite functional metasurfaces for multispectral achromatic optics. *Nat Commun.* (2017) **8**:14992. doi: 10.1038/ncomms14992

Conflict of Interest: The authors declare that the research was conducted in the absence of any commercial or financial relationships that could be construed as a potential conflict of interest.

frontiers in Physics

REVIEW
published: 16 November 2020
doi: 10.3389/fphy.2020.585871

Research on the Metasurface for Single-Photon Avalanche Photodiode

Linyao Chen†, Sunhao Zhang†, Yuyang Ye†, Chuang Liu†, Tianqi Zhao, Yan Shi, Ying Tian, Rui Xu and Yi Chen*

School of Optics and Electronic Technology, China Jiliang University, Hangzhou, China

As the core device of the quantum information field, the single photon avalanche photodiode (SPAD) is a solid-state single photon detector with a pico-second level time-resolution, low bias voltage, high signal-to-noise ratio, and a low cost. However, the photon detection efficiency (PDE) of SPAD is not ideal. The traditional method is to optimize the device structure, while the dark count or time resolution characteristics of the device might be sacrificed. The metasurface integrated on SPADs provides a novel approach to achieving higher PDE. As a result, the SPAD device structure could be independently designed to realize a low dark count rate and a good time resolution. In this paper, many kinds of metasurface structures that could enhance the incident photons absorption, are analyzed. Those structures compatible with CMOS or other easily mass produced processes are attractive for revolutionary changes to conventional SPAD. As a result, a metasurface integrated SPAD would greatly push its applications in the field of quantum information, single photons imaging, life medicine, and other low-level light detections.

Keywords: metasurface, single photon detection, SPAD, metamaterial, PDE

OPEN ACCESS

Edited by:
Chee Leong Tan, University of Malaya, Malaysia

Reviewed by:
Zhen-Yang Wang, Ningbo, China
Menglin Qiu, Beijing Normal University, China

****Correspondence:***
Tianqi Zhao
18a0402151@cjlu.edu.cn

†These authors contributed equally to this work.

Specialty section:
This article was submitted to Optics and Photonics, a section of the journal Frontiers in Physics

Received: *21 July 2020*
Accepted: *28 September 2020*
Published: *16 November 2020*

Citation:
Chen L, Zhang S, Ye Y, Liu C, Zhao T, Shi Y, Tian Y, Xu R and Chen Y (2020) Research on the Metasurface for Single-Photon Avalanche Photodiode. Front. Phys. 8:585871. doi: 10.3389/fphy.2020.585871

INTRODUCTION

Quantum information technology is considered to be a key technology for the future. Quantum communication, quantum computing, and quantum measurement make up its main research directions [1–3]. In recent years, quantum information technology has greeted "the second revolution of quantum" and is accelerating from being experimental to real world application. Its potential in national security, national defense, economic development, and science technology is slowly emerging [4]. Along with the push of the rapid development of quantum information technology, the single photon avalanche photodiode (SPAD) as a core device is being taken more seriously by more people.

SPAD is a solid-state single photon detector with pico-second level time-resolution. After adding reverse bias on its p-n junction, the incident light will be absorbed and produce a light current. The reason this photodiode called SPAD is the phenomenon of a Geiger avalanche generation is because the reverse bias is beyond the breakdown voltage. Compared with regular PIN type photo diodes, the SPAD has extremely high responsiveness, and could resolve single photons. Furthermore, SPAD also has advantages in high signal-to-noise ratio, operation in the room temperature, and is cost effective. Thanks to these advantages, SPAD is extensively applied in medicine [5], quantum computing and measurement [6], molecular imaging [7, 8], and other aspects, as shown in **Figure 1**.

However, the photon detection efficiency (PDE) of SPAD is not ideal. For example, the PDE of Silicon-based SPAD is not good in a near-infrared wavelength, which limits the detection performance in the application of LiDAR, etc. Recently, with the development of metasurface

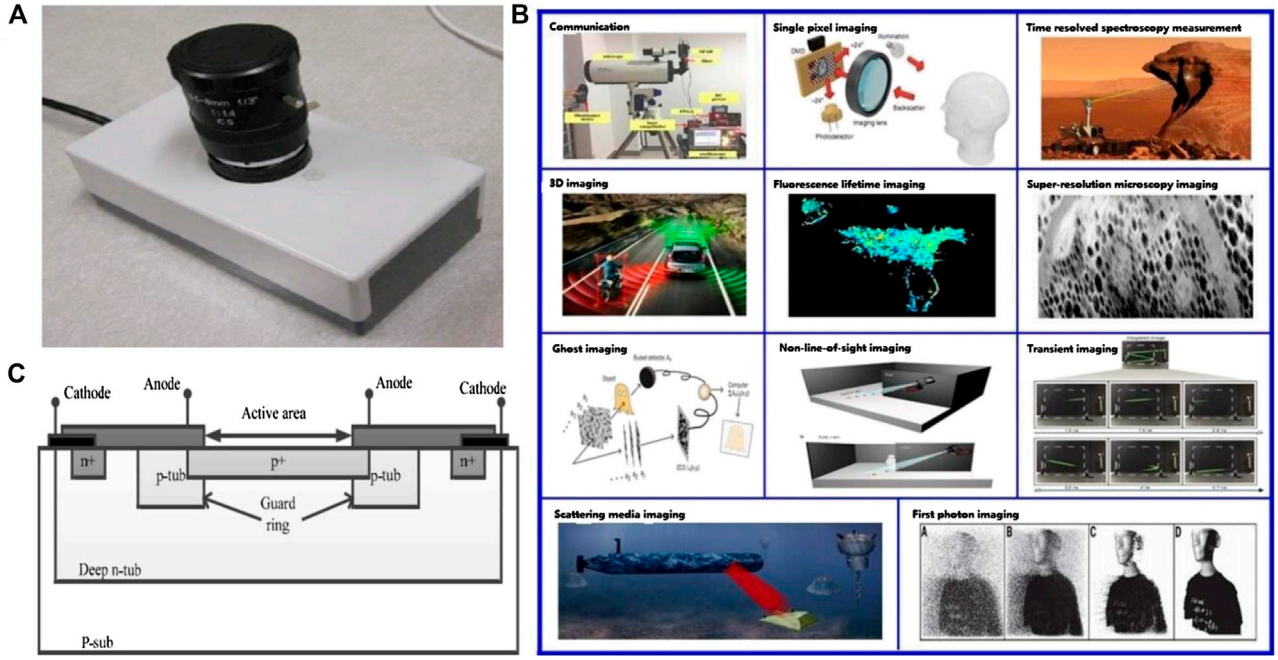

FIGURE 1 | (A) Packaged SPAD optical imager. *Source*: Reproduced from Ref. 7. **(B)** applications of SPAD. **(C)** the Silicon-based SPAD structure diagram compatible with CMOS process. *Source*: Reproduced from Ref. 15.

[9–12], the SPAD integrated with nano-structures (i.e., metasurface) was presented to overcome this drawback [13]. When this new SPAD accepted the perpendicular incidence of photons, some photons would change their direction in the nano-structure and the travel path in the absorbed layer of these photons was increased, which improves the PDE dramatically [14]. The resonant cavity to create an optical resonance in the vertical direction could also be used. Moreover, the SPAD integrated with the metasurface not only performs well in PDE, but also holds other SPAD performance metrics well, such as dark count rate, after the pulse, and time resolution [14]. The SPAD structure could be independently designed to realize a low dark count rate and a good time resolution without considering the effect of PDE on the device structure, therefore, the metasurface integration is a revolutionary technology for the development of SPAD, which would strongly push its applications in the quantum information fields.

METASURFACE STRUCTURES AND THE FABRICATION METHODS

Many types of metasurface structures and corresponding fabrication methods are discussed below. Some metasurface are directly integrated on the bottom of the SPAD device. Some, used in solar cells and other fields, can be further applied to SPAD to improve its PDE.

Nano Pyramidal or Conical Array

The light-trapping SPAD is a typical mesa-type, shallow-junction SPAD fabricated using a complementary metal oxide semiconductor (CMOS) compatible process. Si epitaxial layers with a total thickness of 2.5 μm are grown on an SOI substrate. As shown in **Figures 2A and 3**, the nano-structure is etched as an inverse pyramid, with 850 nm period in a square lattice pattern. Unlike the resonance peaks found in the responsivity of resonant-cavity-enhanced (RCE) detectors, the light-trapping SPAD has broadband responsivity enhancement. The enhancement of external quantum efficiency (EQE) mainly comes from the anti-reflection effect of the nano-structures, and the contribution from nano-structure diffraction [13]. As shown in **Figures 2 B and C**, the enhancement effect of EQE is more obvious for the longer wavelength.

Fabrication of anti-pyramid nanostructures [13]. First, a 2.5 μm Silicon layer is epitaxially grown on a SOI substrate. A reduced pressure chemical vapor deposition (CVD) is used to place 220 nm silicon on the oxide layer of 400 nm. Then, 200 nm of low temperature oxide (LTO) is deposited in a low-pressure chemical vapor deposition reactor at 400°C, a hard mask for etching nanostructures. The holes with square or hexagonal patterns were opened in the LTO mask layer by lithography and plasma using NF_3 gas etching. The entire wafer is then immersed in tetramethylammonium hydroxide to wet etch silicon at 70°C and forms a 600 nm deep etch inverse pyramid which is a nanostructure. After surface texturing, different mesa diameters were designed to be plasma etched in HBr, Cl_2, and O_2

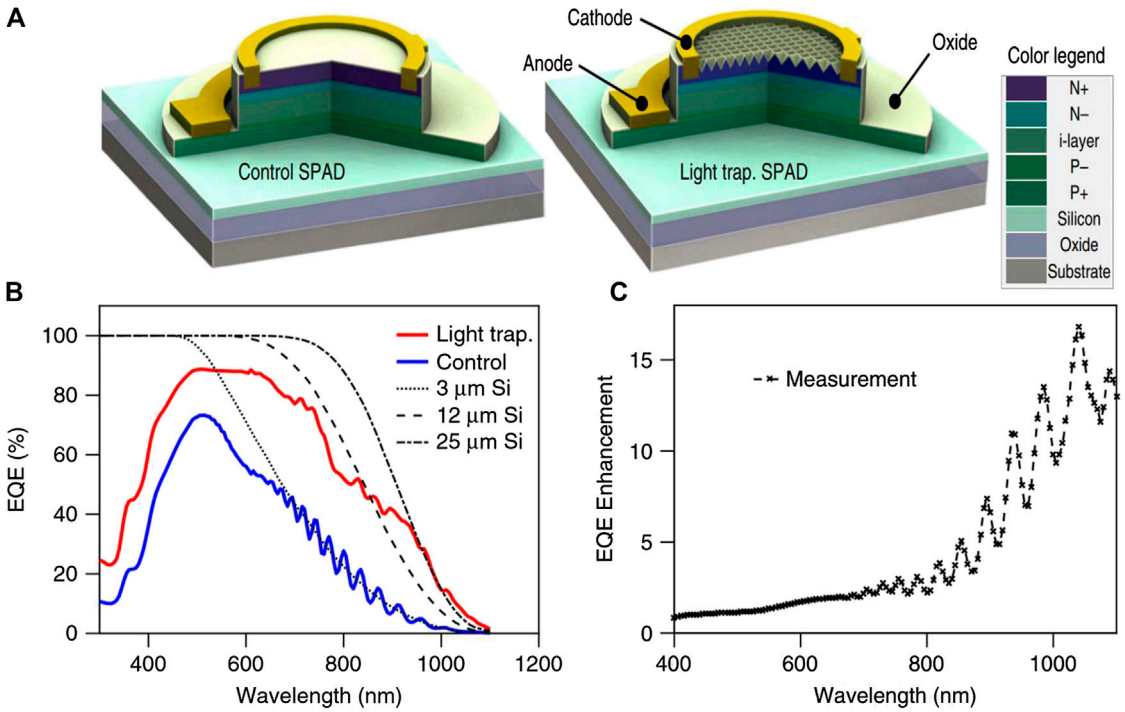

FIGURE 2 | (A) Three-dimensional (3D) cross-sectional schematics of layer configurations of control **(left)** and light-trapping SPADs **(right)**. **(B)** EQE measurements of control (blue solid) and light-trapping SPADs (red solid); dashed black lines correspond to theoretical absorption of 3, 12, and 25 μm thick Si from left to right. **(C)** EQE enhancement: ratio of light-trapping SPAD EQE compared to control SPAD. *Source*: Reproduced from Ref. 13.

FIGURE 3 | Structure of control SPAD **(A)** and light-trapping SPADs **(B)**, both with 50 μm diameter. Scale bar in both 20 μm. **(C)** SEM image **(top-down view)** of inverse pyramid nano-structure on light-trapping SPAD. Scale bar, 1 μm. *Source*: Reproduced from Ref. 13.

gas environments, then cleaned and thermal oxidation passivated at 1,000°C. After manufacturing, HF wet etching was used to open the holes, and 10 nm Ti and 200 nm Al were deposited as the readout electrode. This fabrication method has great commercial value, because it is compatible with CMOS process and obtains the potential of large-scale integration and low-cost applications.

The random vertical and inverted pyramids can increase light absorption by decreasing the broadband reflection, which scatters and captures incoming light efficiently, regardless of the angle of incidence photons [16–20]. The broadband reflection can be further reduced by using the nanotextures [21] as shown in **Figure 4**. This is because when the size of the nanostructure is smaller than the wavelength of the incident light, the optical coupling can be enhanced by the refractive index grading effect. Nanostructures are usually fabricated by wet chemical etching, dry etching, or a combination of photoetching and dry etching [22–25]. By combining the mixed micro/nano textures on the Silicon surface, the broadband reflection can be suppressed to less than 10%, even without the use of any additional anti-reflection coating on the mixed textures [26–28].

The nano cone array on the silicon as shown in **Figure 5** can be made by self-assembled nanosphere lithography technology [29]. In the fabrication of arrays, different sizes of polystyrene sphere (PS) can adjust the period, the height and basal diameter of the nano cone array can be controlled by diverse etching time of the RIE procedure, and the deposition process can decide the thickness of the Au layer.

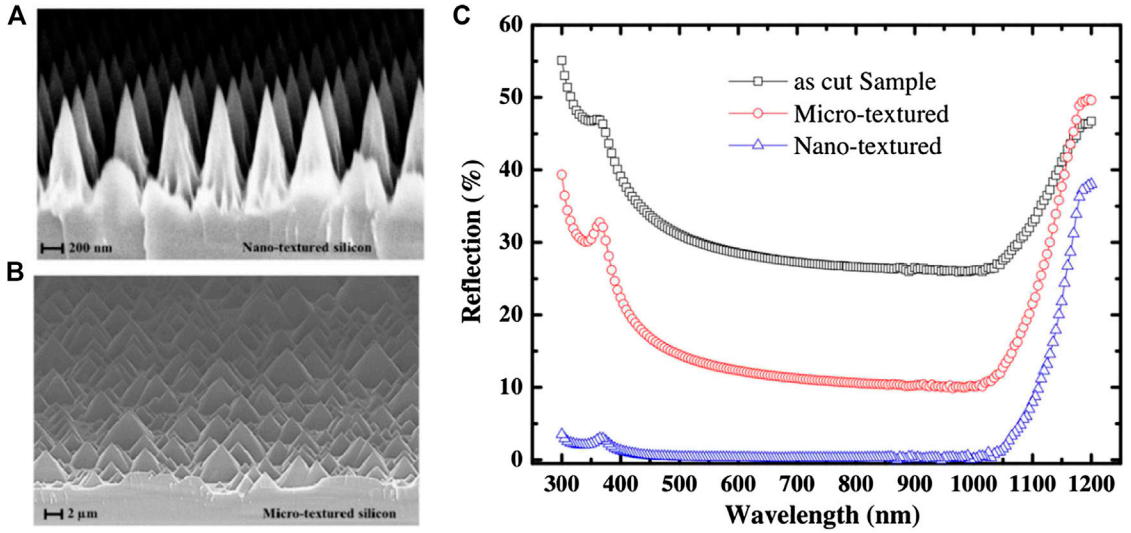

FIGURE 4 | Image of nano-textured Silicon pyramids **(A)** and micro-textured Silicon pyramids **(B)**. **(C)** Overview of hemispherical total reflectance measured on micro-, nanotextured and reference wafers. Nano-texture surface possesses excellent antireflective properties over a wide wavelength range. *Source*: Reproduced from Ref. 21.

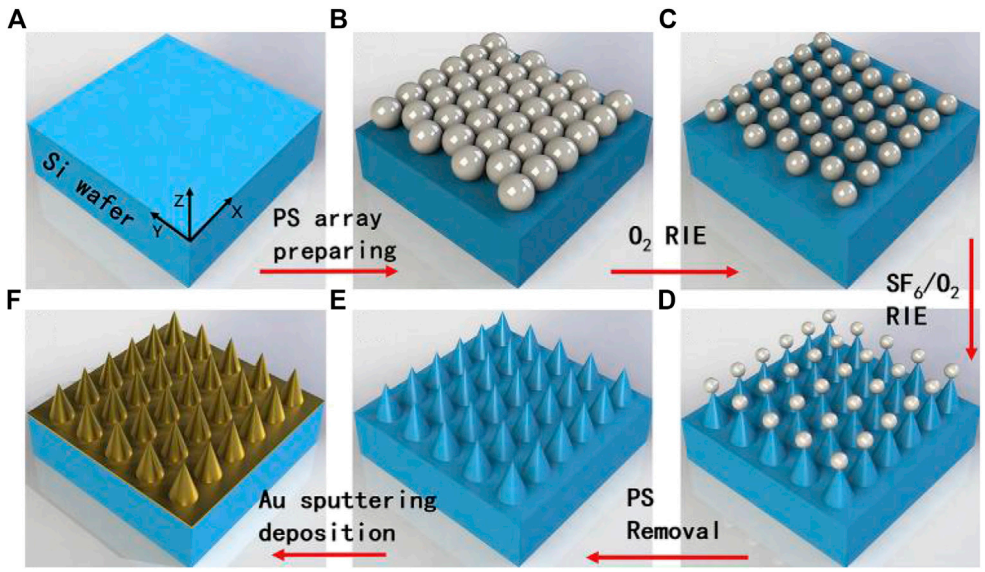

FIGURE 5 | The fabrication of nano cone array with Au layer. *Source*: Reproduced from Ref. 29.

As shown in **Figure 6A**, this nano cone array structure (**Figure 5E**) can decrease optical reflection of the Si surface and increase absorption effectively in the visible spectrum. After the Au layer deposition on the Si nano cone array structure (**Figure 5F**), the high light absorption efficiency was significantly realized within the near infrared wavelength of 1,200–2,400 nm. This is because metallic nano-structure on the Silicon substrate causes surface plasma, which can enhance absorption and overcome the limitation of a silicon band gap. Moreover, the presence of the Au film can dramatically restrain reflection and transmission, resulting in a high absorption. This novel method is suitable for mass production and provides a way for infrared photon detection by Silicon-based SPAD.

The two-dimensional periodic array of the nano pyramid was studied by Q. Han [30] as shown in **Figure 7**. The material of the pyramid is Ge. Through the nano pyramid array structure and various control methods, we would like to discuss the influence of thickness and height of the silicon substrate on absorption. As can be seen from **Figure 7C**, the average absorption rate improves with the increase of

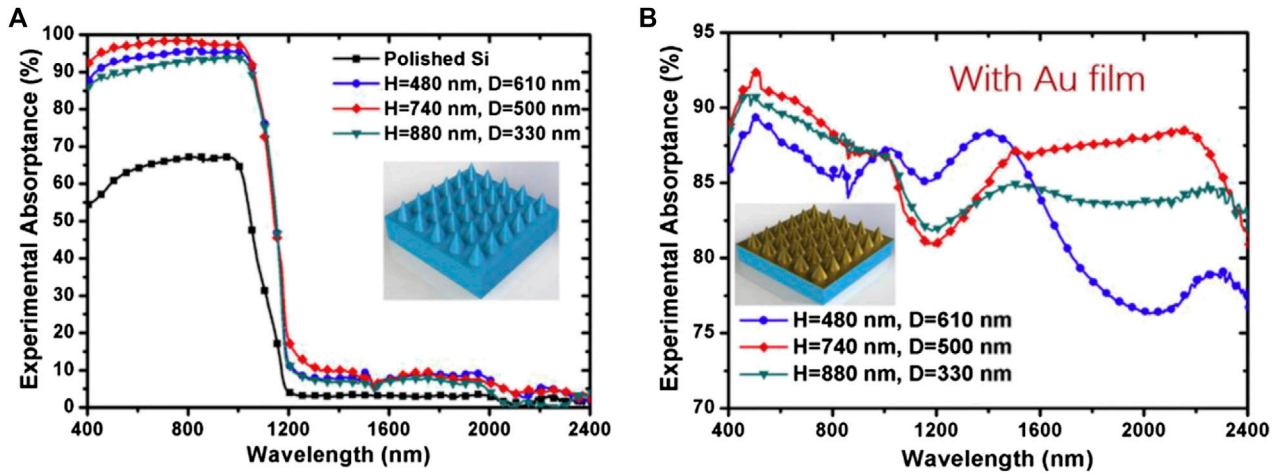

FIGURE 6 | The absorption efficiency of nano cone arrays with or without Au layer. H and D is the height and diameter of the nano cone. *Source*: Reproduced from Ref. 29.

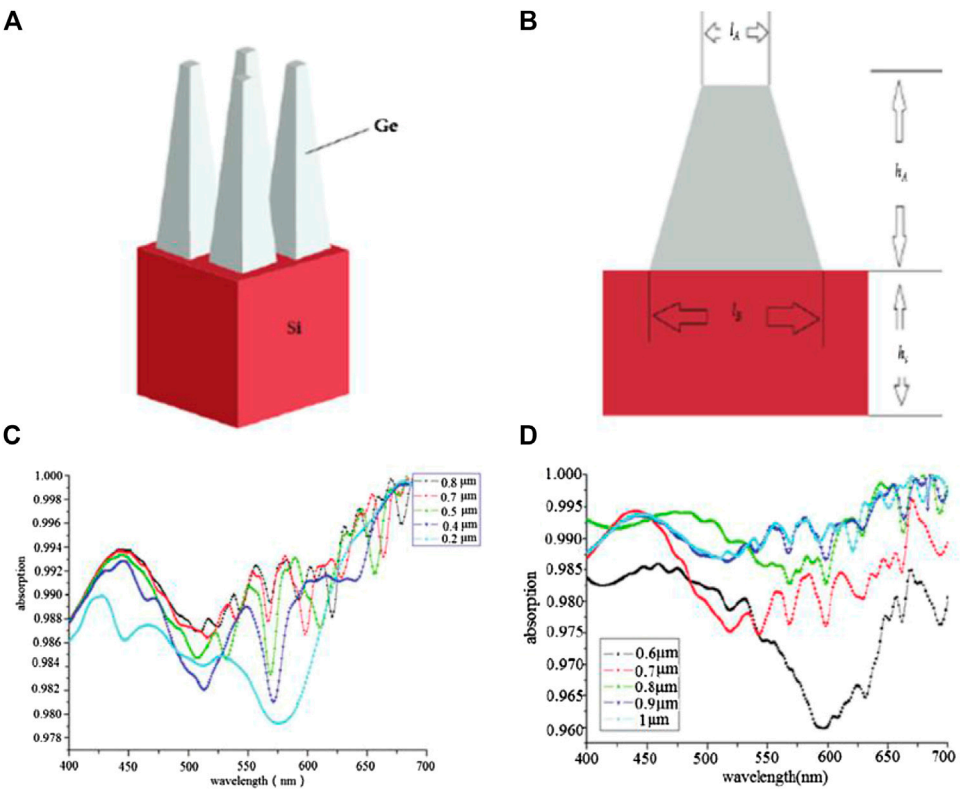

FIGURE 7 | (A) Three-dimensional structure; **(B)** side view **(C)** Curve of absorbance with underlayment thickness, **(D)** The influence of the height of the quadrangle on the absorptivity. *Source*: Reproduced from Ref. 30.

underlaying Si-layer thickness, which is compatible with SPAD with a chip thickness of several hundreds of microns. The nano pyramid array extends the optical path providing more Fabry-Perot resonances, which means that the absorption can be improved by increasing the nano pyramid height. As shown in **Figure 7D**, the efficiency of light absorption tends to be stable when the height is 0.9 μm.

Fabrication of the nano pyramid array [30]. A 1 μm thick germanium film was coated on the Silicon layer by electron beam evaporation. A focused ion beam instrument (FEI NOVA200

Nanolab) was used for the nanometer processing experiment, with a 30 KeV ion source with a tip current of 4pA–19.7 nA and an ion beam with a limiting pass-through aperture of 25 –350 μm. With the aid of a computer program, the intensity of the ion beam varies according to the milling depth. During milling, the ion beam and ion dose were 20 pA and 0.25nC/μm^2, respectively. The working distance from the sample surface to the ionic cylinder is 20 mm. The electron mode of focused ion beam milling is selected to mill germanium films. After continuous milling, the square area of the pyramid structure is completed, as shown in **Figure 8**. Most traditional focused ion beam processing is two-dimensional. This three-dimensional processing is difficult and the operator's proficiency and operational experience requirements are high.

Nanowire Arrays

Figure 9A shows the geometry of the nanowire array. The structure consists of a GaAs substrate and periodic axial p-i-n junction GaAs nanowires by gas-liquid-solid growth. As a simulation, the diameter of the nanowire (D) was set as 250 nm, the D/P determined by the minimum repetition unit period (P) and D was fixed at 0.5. The influence of height, D/P, and P on the light absorption performance of the nanowire arrays was explored [18]. As shown in **Figures 9 B and C**, when the nanowire height or D/P increases, the light absorption of the nanowire array gradually becomes stronger, the wave peak moves to the long wavelength, and the absorption spectrum is wider. From **Figure 9D**, we can see that the absorption peak moves to the long wavelength with the increase of the nanowire diameter.

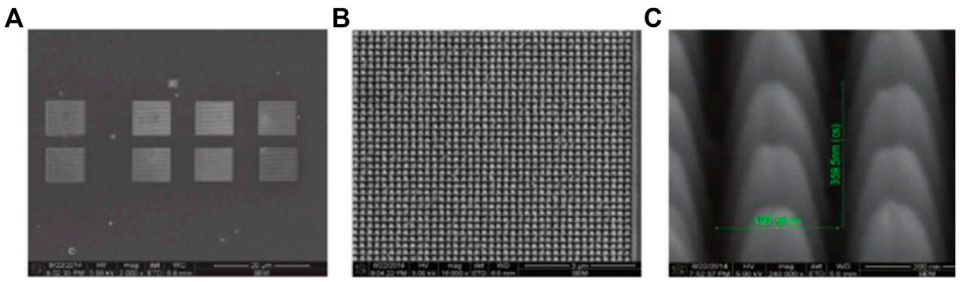

FIGURE 8 | Under different magnification, the SEM image of the processed nanometer four-pyramid array is obtained. **(A)** in a 20 μm field of view; **(B)** at 3 μm: **(C)** at 200 nm. *Source*: Reproduced from Ref. 30.

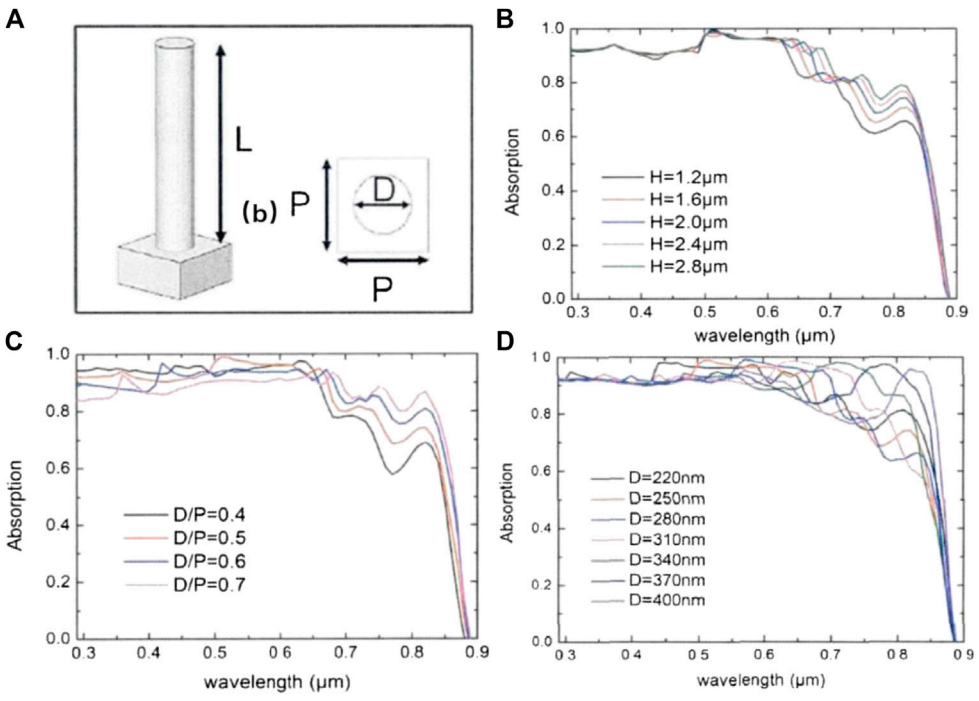

FIGURE 9 | (A) Schematic diagram of minimum repeat unit in regular nanowire array, **(B)** Opticalabsorption performance of nanowire arrays with different heights, **(C)** Optical absorptivity performance at different D/P ratios, **(D)** Optical absorptivity performance of nanowires with different diameters. *Source*: Reproduced from Ref. 31.

Nanostructures could form on the Silicon surface from the bottom to the top using the self-assembly of silicon atoms [31]. Such methods include gas-liquid-solid growth, supercritical fluid growth, and oxidation catalysis growth. The growth principle of Si nanowires by gas-liquid-solid growth is shown in **Figure 10**. The growth of gas-liquid-solid mainly takes advantage of the catalytic effect of metal and combines it with gaseous reactants to grow silicon nanowires on the silicon surface. The Au particles deposited on the Si substrate react with the Si and Au-Si alloy droplets are formed at a certain temperature. As shown in **Figure 10B**, the eutectic point of the Au-Si alloy is greatly reduced. Si atoms are deposited on the substrate after $SiCl_4$ and H_2 are mixed. The Au-Si droplets continuously absorb Si atoms from the vapor so that the droplets maintain a supersaturation state. Since the melting point of Si (1,414°C) is far higher than the melting point of eutectic, Si atoms are precipitated out of the droplets and form a cylinder, and the droplets are lifted away from the substrate to form nanowires. **Figure 10C** shows the process of Si atom absorption, diffusion, and precipitation. Compared with the traditional gas-solid growth method, the advantage of the gas-liquid-solid growth method is that the activation energy required for growth is low, the nanowires grow only in the region where the catalyst exists, and the diameter is basically determined by the size of the Au catalyst. However, the biggest problem of nanowire arrays is that the periodic structures are difficult to fabricate accurately, which limits its real application.

Nano Spherical Structure

The aspect ratio (DW) of the concave array was simulated for the assessment of surface reflectivity [32]. **Figure 11** shows the reflection curves of the structure with aspect ratios of 0, 0.2, 0.4, 0.6, 0.8, 1, and 2. The reflectivity decreases rapidly with the increase of the aspect ratio, and then tends to be smooth. Compared with the flat structure, the reflectivity of nano dimples or convex balls array structure is greatly reduced.

An example of convex balls array structure, the surface textured SPAD was proposed [33]. The schematic of epitaxial layer and surface textured SPAD and the fabricated results of SPAD and the surface nano-structure are shown in **Figures 12A–C**. The period of the convex balls array structure is 800 nm. Compared with the controlled SPAD (without convex balls array structure), the reflection measurement from the Si-air interface shows that the surface textured SPAD obtains higher light absorption efficiency (**Figure 12D**). PDE vs. the dark count rate plot in **Figure 12E** shows that there is an obvious increase of PDE for surface textured SPAD from 6.1 to 7.8%, which is a relative 28% added absorption over the control SPAD. This improvement is a contribution of the effects of anti-reflection and weak light trapping with photons scattered by the surface texturing structure.

Fabrication of Si SPADs for surface texture [33]. First, epitaxial growth of a wafer takes place on a lightly boron doped substrate in a reduced-pressure chemical vapor deposition (RPCVD) system. As shown in **Figures 12A–C**, after the 2.3 μm oxide layer is grown, a thick contact layer is formed on the top. The 800 nm cycle photoresist was etched on the light etched column. The photoresist pillars refluxed and baked into a cone. Then the nano-cone pattern is transferred from photoresist to silicon, etched in CHF_3 and O_2 environments, passivated at high temperatures to form protective rings, and finally opened and deposited metal. This fabrication method is compatible with CMOS process and has a good business prospect.

An example of dimples balls array structure, random Silver nanostructures were formed on the top of the planar surface of Silicon, and the surface deformation of the nanostructures was carried out by the etching process [34], as shown in **Figures 13A–C**. A significant reduction in reflection can be obtained from the prepared silicon sample, with a reflection of about 2% over a wide spectral range between 300 and 1,050 nm (**Figure 13D**). The etching depth can be controlled between 100 nm and 10 μm by controlling the etching time. This feature is critical because accurate etching depth control is critical for photon detection absorptivity. This work demonstrates the potential of the etching process for manufacturing high-efficiency, low-cost Si-SPAD.

Plasma resonance (SPR) as a regular technology, can be used to improve the absorption performance. Through the

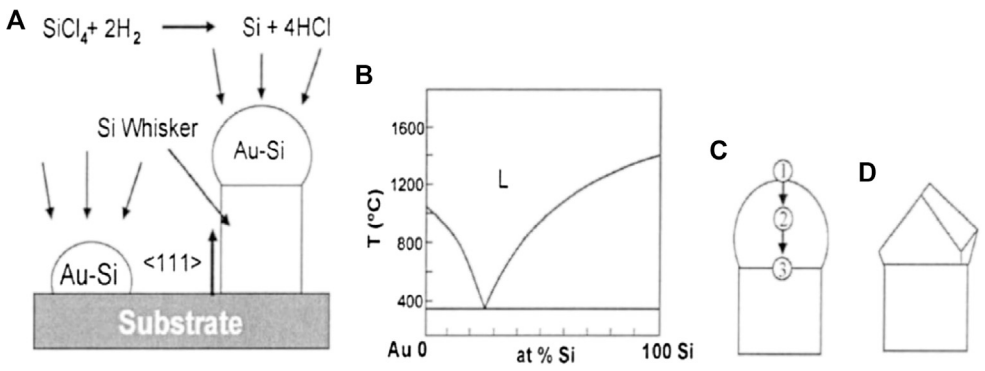

FIGURE 10 | (A) Growth of whisker catalyzed by Au-Si liquid alloy formed on Si substrate, **(B)** phase diagram of Au-Si, **(C)** diffusion path of source reactant molecule through gold droplet, **(D)** growth of whisker catalyzed by solid catalyst. *Source*: Reproduced from Ref. 31.

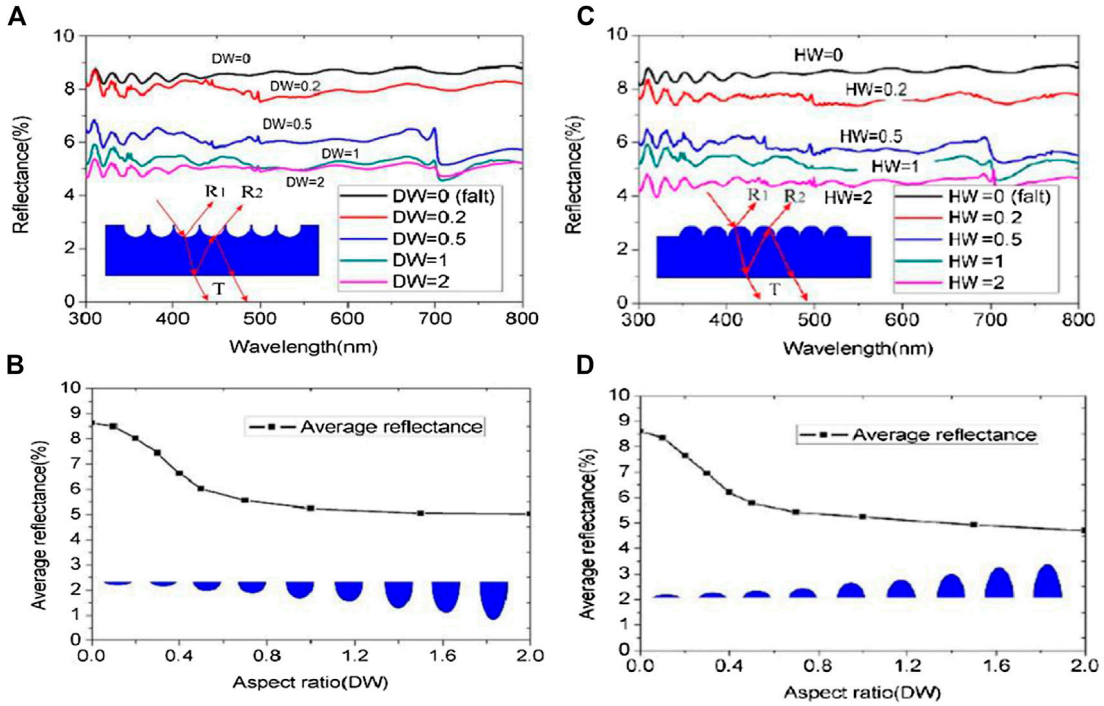

FIGURE 11 | (A) The reflectance curves of nano dimples structure with DW of 0, 0.2, 0.5, 1, and 2 respectively, and corresponding average reflectivity **(B)**. **(C)** The reflectance curves of nano convex balls structure with DW of 0, 0.2, 0.5, 1, and 2 respectively, and corresponding average reflectivity **(D)**. *Source*: Reproduced from Ref. 32.

characteristics of SPR, reflection can be reduced, and light absorption can be promoted [35]. The structure of gold coated nanospheres is shown in **Figures 14 A and B**, which is formed by coating polystyrene microsphere array in hexagonal close arrangement. The bottom layer of the simulation model is a gold film. If the nanosphere array

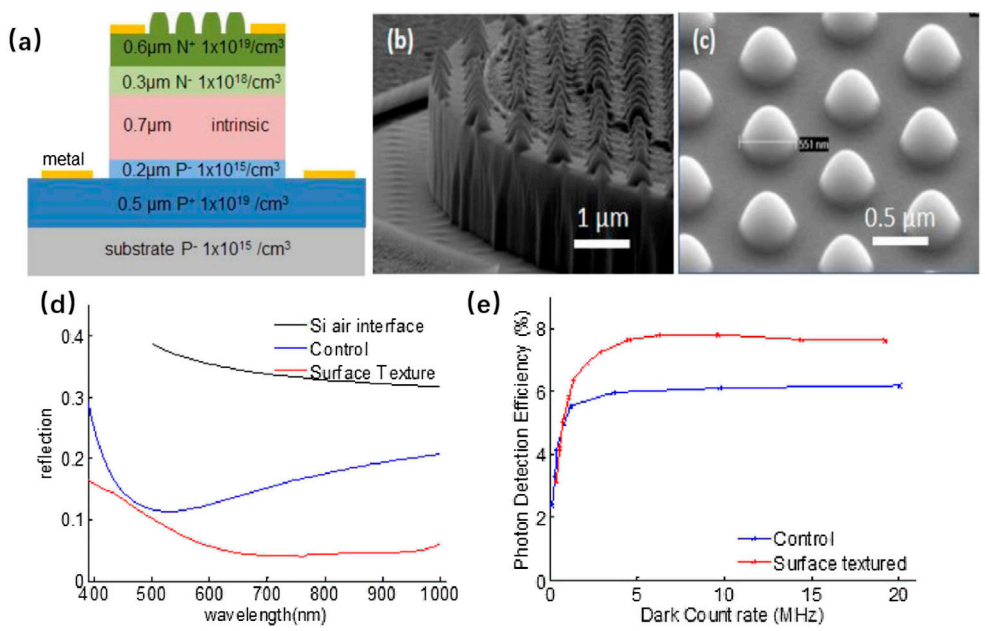

FIGURE 12 | (A) Schematic of epitaxial layer and surface textured SPAD. **(B)** Fabricated SPAD. **(C)** Surface nano-structure. **(D)** Reflection measurement from Si-air interface, control SPAD mesa top and surface textured SPAD mesa top **(E)** PDE vs. DCR for both SPADs. *Source*: Reproduced from Ref. 33.

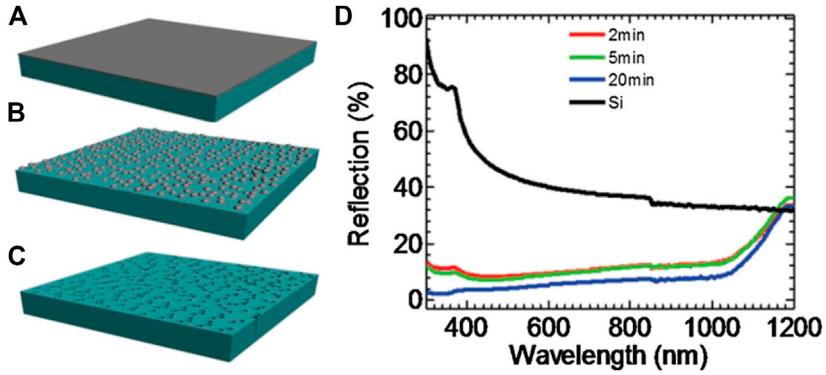

FIGURE 13 | Schematic illustration of the fabrication process of nanostructured Si: **(A)** Silver film was deposited on the Si surface; **(B)** Silver nano-particles were formed after annealing silver film in a furnace; and **(C)** Si sample after etching in the HF and H2O2 solution. **(D)** Measured reflection spectra from nano-structured Si films with 9 nm silver film and different etching times. *Source*: Reproduced from Ref. 4.

structure is coated with gold and filled with gold, the gold coated nanosphere shell array can be formed. In this model, the refractive index of the dielectric substrate is set to 1.43, i.e., The diameter of nanospheres is 630 nm. It can be seen from **Figures 14 C and D**, with the thicker coating thickness, the reflectance is lower, and the change is smaller. Under the thinner coating thickness, although there is a lower reflection trough, the wave the band width is too narrow. Therefore, the dependence of reflectance on different wavelengths gradually stabilizes, which is beneficial to a real fabrication process. For the detection of photons at specific wavelengths, the SPR nanosphere shell structure is a particluarly good choice.

The technological process of the fabrication of a nano-spherical shell structure [35]. As shown in **Figure 15**, a bottom layer of gold film is first evaporated on the substrate, then a single layer of hexagonal close-row microsphere film is

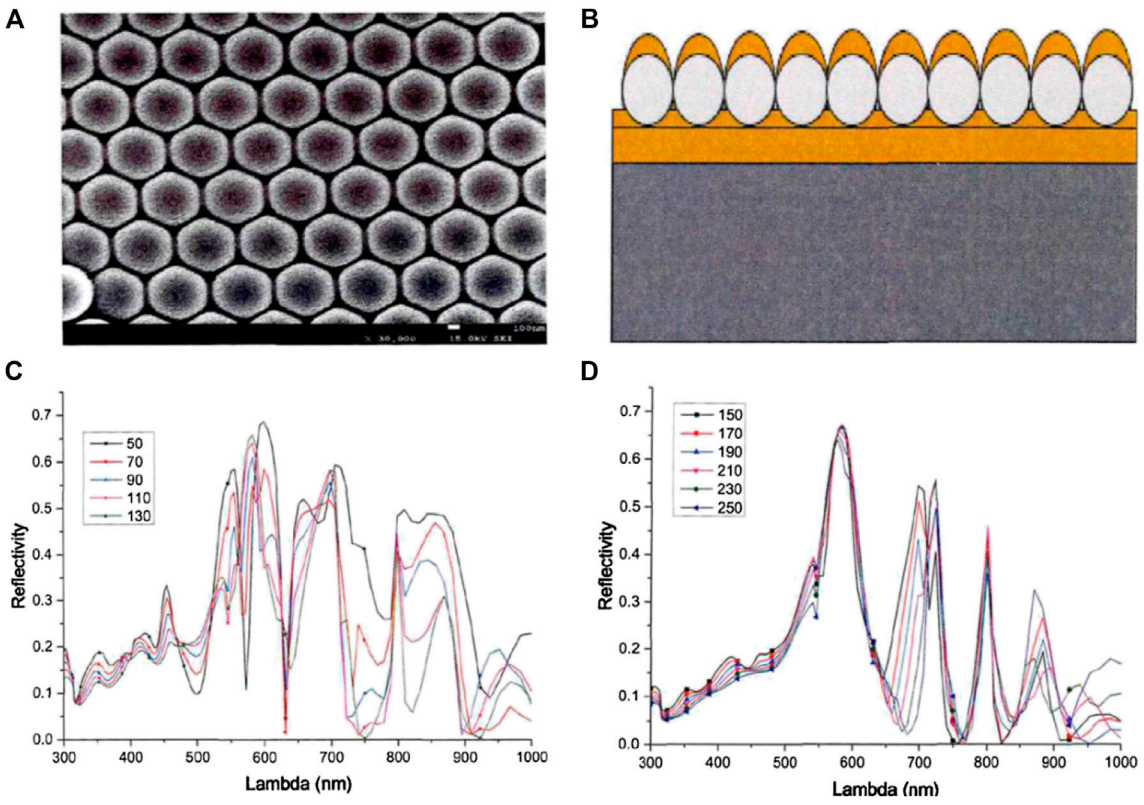

FIGURE 14 | (A) It is the SEM picture of the nano spherical. **(B)** Schematic diagram of nanospheres. **(C, D)** The dependence of reflectivity on wavelength with different coating thickness. *Source*: Reproduced from Ref. 35.

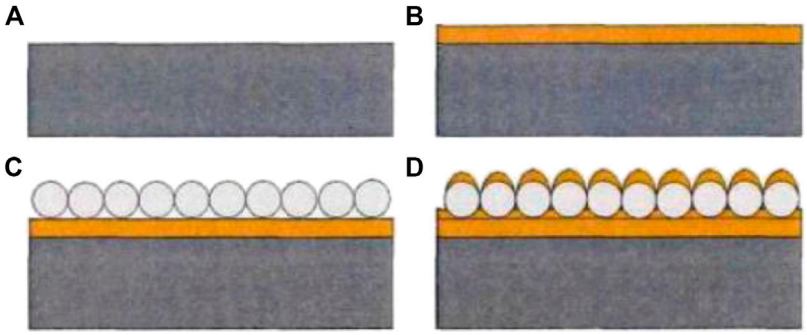

FIGURE 15 | The technological process of fabrication of nano-spherical shell structure. *Source*: Reproduced from Ref. 35.

formed on a silicon wafer through microsphere self-assembly technology, and the monolayer is transferred to the gold-plated substrate. Finally, the resistance evaporation film is applied again to form the structure of gold coated nanospheres.

Deep-Trench Microstructures

The Silicon with a wide band gap of 1.12 eV is the key to the development of Silicon-based near infrared photodetectors. This results show that the microstructure can excite SPPs with wide frequency band and standing wave resonance of the plasma resonant cavity formed in the deep trench, thus producing a high frequency band and a high near infrared absorption in the range of 1,000–1,500 nm, as shown in **Figure 16** [36]. It breaks through the absorption limit of Silicon and greatly expands its near-infrared absorption to 1,500 nm. When the groove becomes deeper, the absorption bandwidth and intensity of near-infrared absorption increases sharply. The microstructure makes it possible to achieve wide band and bloom response in the near infrared range from 1,000 to 1,500 nm.

The optical properties of the SMART texture of crystalline Silicon was researched and optimized [37]. First, a pronounced

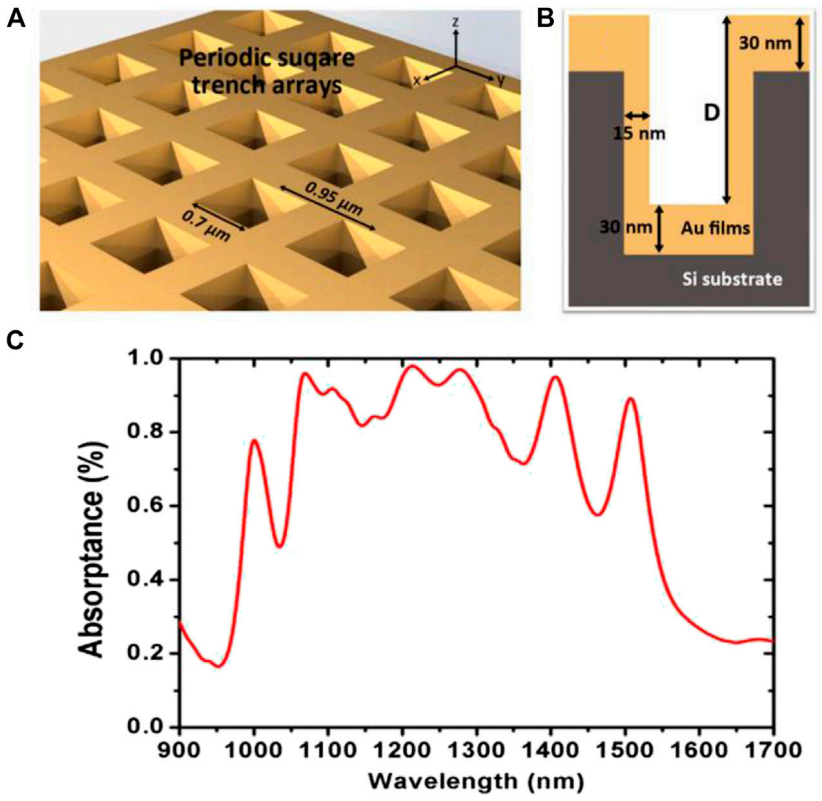

FIGURE 16 | The deep-trench microstructures **(A, B)** and corresponding response in the near infrared range from 1000 to 1500 nm with D = 2.4 μm **(C)**. *Source*: Reproduced from Ref. 36.

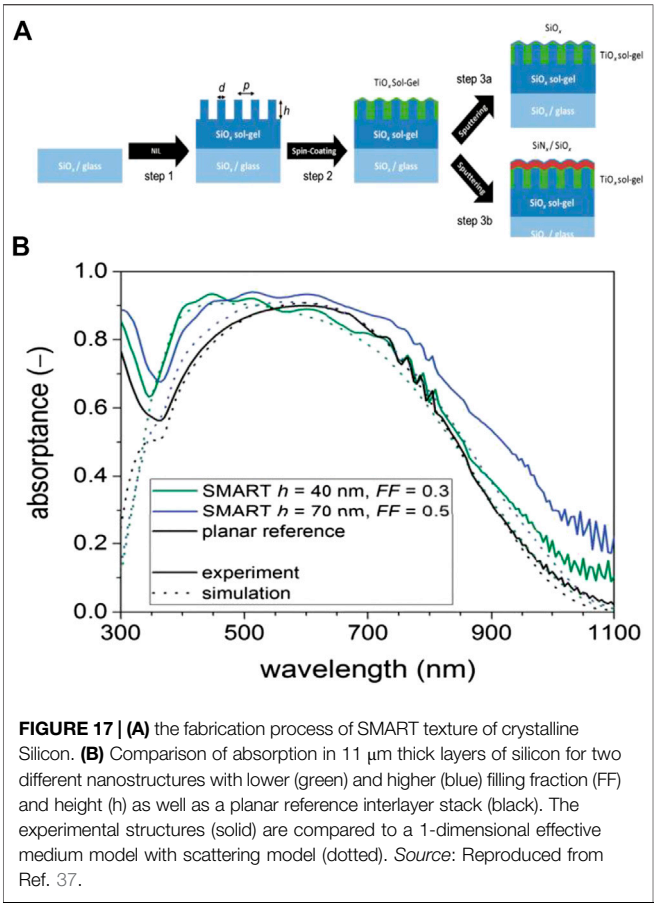

FIGURE 17 | (A) the fabrication process of SMART texture of crystalline Silicon. **(B)** Comparison of absorption in 11 μm thick layers of silicon for two different nanostructures with lower (green) and higher (blue) filling fraction (FF) and height (h) as well as a planar reference interlayer stack (black). The experimental structures (solid) are compared to a 1-dimensional effective medium model with scattering model (dotted). *Source*: Reproduced from Ref. 37.

nanotexture is imprinted into a high temperature stable silicon oxide (SiOx) sol-gel layer. Subsequently, the nanostructures are smoothed by spin-coating a titanium oxide (TiOx) sol-gel, which preferentially fills the void between the protrusions of the nanostructure. In the single-layer approach, a thin SiOx layer is sputtered on top of the smooth nanostructure. For the double-interlayer system, an additional silicon nitride (SiNx) layer is deposited prior to the SiOx layer. As a result, the absorption of the SMART texture structure is higher than that of the planar reference (**Figure 17B**).

PROSPECT

Many kinds of metasurface structures that could improve incident photons absorption are analyzed in this paper. Structures that are compatible with CMOS or other easy to mass produce processes are attractive structures to be adopted to make revolutionary changes to conventional SPAD. As a result, the metasurface integrated SPAD would greatly push forward its applications in the quantum information, single photons imaging, life medicine, and other low-level light detections.

In ultraviolet band detection, the underspectral transfer can be carried out by preparing a spectral conversion layer on the SPAD surface, which will be a good research direction for SPAD to perform underspectral conversion. There are now some crystal materials that can carry rare earth ions for photoelectric conversion, such as YAG:Ce [38] and $SrAl_2O_4$ [39, 40]. YAG:Ce can absorb photons at short wavelengths, transform it into photons of long wavelengths, achieve the ultimate efficiency improvement in ultraviolet band detection. Similarly, in the near-infrared and infrared bands, rare earth ions can also absorb multiple long-wave radiation emitted by photons and convert them into short-wave radiation, a process known as upper-conversion luminescence. This material is of great significance in laser technology, optical fiber communication technology, fiber optic amplifier, and other fields [41]. At present, other researchers have also researched conversion materials [42–44].

Furthermore, the metamaterial could be used for multispectral imaging, by integrating it on the CMOS SPAD image sensor. Recently, an array of high-transmission mosaic filters was developed, each of which was completed by a single-step lithography process and was implemented by a plasmonic metasurface [45]. Integrated on the CMOS-SPAD array, the mosaic filter was reconstructed at the microphoto level of an average of five photons per pixel, and multispectral data at low-light levels was obtained simultaneously using three-color active laser lighting or broadband white light. This represents the first single-photon color image reconstruction achieved using a SPAD image sensor integrated with a mosaic filter array.

AUTHOR CONTRIBUTIONS

TZ is the corresponding author of the article, who lead this scientific research work and wrote the paper. LC contributed to the study of the metasurface fabrication process. SZ contributed to the study of the metasurface structures. YY contributed to the study of the Introduction of the paper. CL contributed to the study of the prospect part of the paper. YS contributed partly to writing the introduction of the paper. RX contributed partly to writing about the nano conical array discussed in *Nano Conical Array* and the nanowire arrays discussed in *Nanowire Arrays*. YC contributed partly to writing about the nano spherical structure discussed in *Nano Spherical Structure*. YT contributed partly to writing the prospect part of the paper.

FUNDING

This work was supported by the National Key R&D Program of China (Grant No. 2018YFF0215304), the National Nature Science Foundation of China (NSFC) (Grant No. 61904169 and 61904168), the Zhejiang Provincial Natural Science Foundation of China (Grant No. LQ18F040001), the Technique Support Program of State Administration for Market Regulation (No. 2019YJ067), and the Major Scientific Research Project of Zhejiang Lab (2019DE0KF01).

REFERENCES

1. Han X, Feng L, Li Y, Zhang L, Song J, Zhang Y, et al. Experimental observations of boundary conditions of continuous-time quantum walks. *Chin Optic Lett* (2019) 17:052701. doi:10.3788/col201917.052701
2. Jung Lee H, Su Park H. Generation and measurement of arbitrary four-dimensional spatial entanglement between photons in multicore fibers. *Photon Res* (2019) 7:19–27. doi:10.1364/prj.7.000019
3. Curic D, Giner L, Lundeen JS. High-dimension experimental tomography of a path-encoded photon quantum state. *Photon Res* (2019) 7:A27–A35.
4. Tang C, Fang J, Wang L. *Current status and future trends of quantum information technology* (2017)
6. Hadfield RH. Single-photon detectors for optical quantum information applications. *Nat Photonics* (2009) 3(12):696–705. doi:10.1038/nphoton.2009.230
7. He W. *Design of ultraviolet single photon counting imaging system based on avalanche photodiode*. Nanjing: Southeast University (2018)
8. Ren M. *Study on high-speed single-photon detection and applications*. Wuhan: Central China Normal University (2013)
9. Qiao J, Mei F, Ye Y. Single-photon emitters in van der Waals materials. *Chin Optic Lett* (2019) 17:020011. doi:10.3788/col201917.020011
10. Ziaul Amin M, Mahbub Hossain M. Doping radius effects on an erbium-doped fiber amplifier. *Chin Optic Lett* (2019) 17:010602. doi:10.3788/col201917.010602
11. Rusby DR, Armstrong CD, Scott GG, et al. Effect of rear surface fields on hot, refluxing and escaping electron populations via numerical simulations. *High Power Laser Sci Eng* (2019) 7(3):e45. doi:10.1017/hpl.2019.34
12. Pan KQ, Yang D, Guo L. Enhancement of the surface emission at the fundamental frequency and the transmitted high-order harmonics by pre-structured targets. *High Power Laser Sci Eng* 7(2):e36. doi:10.1017/hpl.2019.20
13. Zang K, Jiang X, Huo Y. Silicon single-photon avalanche diodes with nano-structured light trapping. *Nat Commun* (2017) 8(1):22–27. doi:10.1038/s41467-017-00733-y
14. Jian M. *Design of single photon avalanche diodes*. Beijing: University of Science and Technology of China (2016)
15. Peng Y. *Analysis and design of a single photon avalanche diode*. Xiangtan: Xiangtan University (2019)
16. Liu X, Coxon PR, Peters M, Hoex B, Cole JM, Fray DJ. Black silicon: fabrication methods, properties and solar energy applications. *Energy Environ Sci* (2014) 7:3223–63. doi:10.1039/c4ee01152j
17. Liu R, Zhang F, Con C, Cui B, Sun B. Lithography-free fabrication of silicon nanowire and nanohole arrays by metal-assisted chemical etching. *Nanoscale Res Lett* (2013) 8:155. doi:10.1149/ma2010-02/18/1315
18. Han H, Huang Z, Lee W. Metal-assisted chemical etching of silicon and nanotechnology applications. *Nano Today* (2014) 9:271–304. doi:10.1117/12.2238480.5163995439001
19. Fan Y, Han P, Liang P, Xing Y, Ye Z, Hu S, Differences in etching characteristics of TMAH and KOH on preparing inverted pyramids for silicon solar cells, *Appl Surf Sci* (2013) 264:761–6. doi:10.1016/j.apsusc.2012.10.117
20. Campbell P, Green MA. Light trapping properties of pyramidally textured surfaces. *J Appl Phys* (1987) 62:243–9. doi:10.1063/1.339189
21. Khandelwal R, Plachetka U, Min B, et al. A comparative study based on optical and electrical performance of micro- and nano-textured surfaces for silicon solar cells. *Microelectron Eng* (2013) 111:220–3. doi:10.1016/j.mee.2013.03.162
22. Noor NAM, Mohamad SK, Hamil SS, Devarajan M, Pakhuruddin MZ. Effects of etching time towards broadband absorption enhancement in black silicon fabricated by silver-assisted chemical etching. *Optik* (2019) 176:586–92. doi:10.1016/j.ijleo.2018.09.096
23. Rahman T, Boden SA. Optical modeling of black silicon for solar cells using effective index techniques. *IEEE J. Photovolt* (2017) 7:1556–62. doi:10.1109/jphotov.2017.2748900
24. Huang Z, Geyer N, Werner P, De Boor J, Gösele U. Metal-assisted chemical etching of silicon: a review. *Adv Mater* (2011) 23:285–308. doi:10.1117/12.2238480.5163995439001
25. Pakhuruddin MZ, Dore J, Huang J, Varlamov S. Effects of front and rear texturing on absorption enhancement in laser-crystallized silicon thin-films on glass. *Jpn J Appl Phys* (2015) 54:13–27. doi:10.7567/jjap.54.08kb04
26. Ingenito A, Isabella O, Zeman M. Nano-cones on micro-pyramids: modulated surface textures for maximal spectral response and high-efficiency solar cells. *Prog Photovolt Res Appl* (2019) 23:1649–59. doi:10.1002/pip.2606
27. Toor F, Page MR, Branz HM, Yuan HC. 17.1%-Efficient multi-scale-textured black silicon solar cells without dielectric antireflection coating. *Conf Rec IEEE Photovolt Spec Conf* (2011) 12:20–4. doi:10.1109/pvsc.2011.6185835
28. Dimitrov DZ, Du CH. Crystalline silicon solar cells with micro/nano texture. *Appl Surf Sci* (2013) 266:1–4. doi:10.1016/j.apsusc.2012.10.08
29. Li Q, Gao J, Li Z. Absorption enhancement in nanostructured silicon fabricated by self-assembled nanosphere lithography. *Opt Mater* (2017) 70:165–70. doi:10.1016/j.optmat.2017.05.036
30. Qi H. *Study of nanophotonic structures based perfect absorbers*. Beijing: University of Electronic Science and Technology of China (2015)
31. Gong L. *The research on irregular nanowire array solar cells*. Beijing: Beijing University of Posts and Telecommunications (2016)
32. Chen L. *Studies on enhancement efficiency of thin film silicon solar cells with high-efficiency surface light-trapping structure*. Shangai: Shanghai Jiao Tong University (2017)
33. Zang K, Ding X, Jiang X. Surface textured silicon single-photon avalanche diode. In: *Proceedings of CLEO: Science Innovation* (2017)
34. Li R, Wang S, Chuwongin S. Nanoscale silver-assisted wet etching of crystalline silicon for anti-reflection surface textures. *J Nanosci Nanotechnol* (2013) 13:493–7. doi:10.1166/jnn.2013.6916
35. Chen Y. *Research on optimal design and application of perfect absorber based on surface plasmon resonance*. Wuhan: China Academy of Engineering Physics (2018)
36. Yang H, Liu X, Gao J. An extending broadband near-infrared absorption of Si-based deep-trench microstructures. *Optic Commun* (2017) 392:59–63. doi:10.1016/j.optcom.2017.01.041
37. Eisenhauer D, Jäger K, Köppel G, Rech B, Becker C. Optical properties of smooth anti-reflective three-dimensional textures for silicon thin-film solar cells. *Energy Proc* (2016) 102:121–134. doi:10.1016/j.egypro.2016.11.314
38. Shao G. *Investigation on the enhancement of conversion efficiency of solar cell*. Nanjing: Southeast University (2016)
39. Nazarov M, Brik MG, Spassky D. Structural and electronic properties of $SrAl_2O_4$:Eu2+ from density fonctional theory calculations. *J Alloys Compd* (2013) 573(10):6–10. doi:10.1016/j.jallcom.2013.04.004
40. Tai Y. *Dissertation guide for postgraduates*. Xi'an: Northwest University (2016)
41. Sanderson KD, Mills A, Parkin I. The use of titanium dioxide coatings deposited by APCVD on glass substrates to provide a dual action self-cleaning. In: 46th Annual society of vacuum coaters technical conference, San Francisco, United States (2003) 203–8.
42. Yu J, Zhao X, Lin L. Preparation and characterization of super-hydrophilic TiO_2/SiO_2 composite thin films. *J Inorg Mater* (2001) 16(3):529–44. doi:10.1016/s0254-0584(00)00364-3
43. Zywitzki O, Modes T, Sahm H. Structure and properties of cry stalline titanium oxide layers deposited by reactive pulsemagnetr on sputtering. *Surf Coat Technol* (2004) 180–181(3):538–43. doi:10.1016/j.surfcoat.2003.10.115
44. Wang H, Wang J, Wang H, Yang F. An anti-fog self-cleaning glass and preparation method. CN200610019338 (2004)
45. Shah YD, Connolly PWR. Ultralow-light-level color image reconstruction using high-efficiency plasmonic metasurface mosaic filters. *Optica* (2020) 7(6):632. doi:10.1364/optica.389905
46. Al-Rawhani MA, James B, Cumming David RS. Wireless fluorescence capsule for endoscopy using single photon-based detection. *Sci Rep* (2015) 5:1–9. doi:10.1038/srep18591

Conflict of Interest: The authors declare that the research was conducted in the absence of any commercial or financial relationships that could be construed as a potential conflict of interest.

frontiers in Physics

ORIGINAL RESEARCH
published: 03 December 2020
doi: 10.3389/fphy.2020.595642

Wideband Absorption at Low Microwave Frequencies Assisted by Magnetic Squeezing in Metamaterials

Zhenxu Wang[1], Jiafu Wang[1], Yajuan Han[1], Ya Fan[2], Xinmin Fu[1], Yongqiang Pang[3], Mingbao Yan[1], Yongfeng Li[1], Hua Ma[1], Zhuo Xu[3] and Shaobo Qu[1]**

[1]Department of Basic Science, Air Force Engineering University, Xi'an, China, [2]College of Information Counter, Air Force Early Warning Academy, Wuhan, China, [3]School of Electronics and Information Engineering, Xi'an Jiaotong University, Xi'an, China

In this paper, the magnetic squeezing effect in metamaterials is explored and applied to achieve wideband absorption in low-frequency microwave bands. To this end, a metamaterial absorber (MA) is proposed, which consists of a square lattice of a split ring resonator (SRR) placed on top of a magnetic absorbing material (MAM) layer backed by a conducting ground. In the positive resonance region of SRRs, a strong magnetic squeezing effect occurs and more concentrated magnetic field lines are confined within SRRs. This results in significant magnetic field enhancement within the MAM layer, which provides a prerequisite for high-efficiency absorption enhancement at low frequencies. To verify this method, we fabricated a prototype using a 3.0 mm thick silicone MAM sheet. Both the simulation and experiment results show that with the assistance of magnetic squeezing in the SRR array, the absorption at lower frequencies is significantly enhanced and is above 90% in 1.25–2.31 GHz under normal incidence. Furthermore, the MA exhibits satisfactory stability for different polarization states and incident angles due to the square lattice of the SRR array. This design method may find potential applications in fields such as electromagnetic compatibility, wireless communication, and others.

Keywords: metamaterial absorber, magnetic squeezing effect, low microwave frequency, wideband absorption, metamaterials

OPEN ACCESS

Edited by:
Xufeng Jing,
China Jiliang University, China

Reviewed by:
Xiangkun Kong,
Nanjing University of Aeronautics and Astronautics, China
Mohammad Rashed Iqbal Faruque,
National University of Malaysia, Malaysia

****Correspondence:***
Jiafu Wang
wangjiafu1981@126.com
Shaobo Qu
qushaobo@mail.xjtu.edu.cn

Specialty section:
This article was submitted to Optics and Photonics, a section of the journal Frontiers in Physics

Received: *17 August 2020*
Accepted: *22 September 2020*
Published: *03 December 2020*

Citation:
Wang Z, Wang J, Han Y, Fan Y, Fu X, Pang Y, Yan M, Li Y, Ma H, Xu Z and Qu S (2020) Wideband Absorption at Low Microwave Frequencies Assisted by Magnetic Squeezing in Metamaterials. Front. Phys. 8:595642. doi: 10.3389/fphy.2020.595642

1. INTRODUCTION

Metamaterials provide a series of novel design concepts achieving peculiar physical phenomena and effects that cannot be realized with natural materials, such as negative refractive index [1], electromagnetic (EM) wave cloaking [2, 3], and an inverse Doppler effect [4]. As a kind of special methodology, metamaterials have been widely used not only in the military field, for example, EM stealth [5–7], but also in the civil field, such as solar energy harvesting [8] and biological sensing [9]. Since Landy et al. proposed a late-model perfect metamaterial absorber (MA) which can obtain an absorptivity rate of 99% at a specific frequency [10], MAs with the framework of metal-substrate-metal have been rapidly developed [11–14], which were generally based on electric or magnetic resonances and had the property of flexible adjustable absorption frequency by changing the geometrical parameters of the unit cell. Besides, traditional radar absorbing materials (RAMs) are generally comprised of magnetic metals or ferrite nanocrystalline particles dispersed in a polymer matrix, and always have a high thickness and heavy weight. In contrast, MAs have the advantage of high absorptivity, thin thickness, and a flexible design. However, the bandwidth of this kind of MAs is too narrow.

Therefore, one common purpose in this topic is to broaden the bandwidth of the MAs and improve the absorption level simultaneously [15–18]. Thus, a great many research attempts have been implemented, including stacking multiple resonances together in the vertical direction [19], loading with lumped resistors [20], and applying spoof surface plasmon polariton (SSPP) [21, 22].

Nevertheless, the MAs still face two challenges before they can be applied in engineering. One is to resolve the contradiction that enables high-efficiency absorption in low frequency bands with thin thickness and light weight. The other is that the MAs in most literature aims to absorb EM waves with a normal or small incidence angle. But in practice, the incident angle is usually oblique or glancing. In this case, the absorption efficiency of the MAs decreases with the increase of the incident angle, leading to a poor absorption performance. In order to solve these two issues, a series of studies have been conducted. As in Ref. 23, a kind of two-dimensional MA was proposed, which can achieve an absorption peak in the P-band with an incident angle ranging from 0 to 45°. In Ref. [22], two hybrid plasmonic MAs, combining a plasmonic structure covering and various traditional absorbing materials were proposed, achieving high-efficiency absorption in the frequency bands of 4.1–35 and 4.7–31.2 GHz, respectively. In Ref. 24, a two-layer MA consisting of a non-planar metamaterial and a magnetic microwave absorbing material was proposed, and it can realize 90% absorptivity over the whole 2.0–18.0 GHz range. Nevertheless, this research just focused on one single subject. That is, MAs with not only wide-angle absorption, but also obtaining low-frequency absorption with limited thickness are important to be studied and suggest promising prospects in various applications.

In this paper, firstly, the magnetic squeezing effect in metamaterials is explored, which indicates that by virtue of the positive resonance region of the metamaterials, the magnetic field lines will be squeezed, resulting in significant magnetic field strength enhancement. Then, a kind of metamaterial absorber (MA) based on the effect is proposed, featuring wideband absorption in the low-frequency microwave bands with thin thickness and light weight. The MA consists of a square lattice of a split ring resonator (SRR), placed directly on the top of a grounded magnetic absorbing material (MAM) layer. In the positive resonance region of SRRs, a strong magnetic squeezing effect occurs. That is, more concentrated magnetic field lines are confined within the SRR arrays. This results in significant magnetic field enhancement within the MAM layer, which provides a prerequisite for high-efficiency absorption enhancement at low frequencies. To verify this, we fabricated a prototype using a 3.0 mm thick silicone MAM sheet. Both the simulation and experiment results show that under normal incidence, the 10 dB absorption band is 1.25–2.31 GHz. Furthermore, the lattice structure enables the MA to exhibit satisfactory stability for polarization states and incident angles. This design method may find potential applications in fields such as electromagnetic compatibility, wireless communication, and others.

2. MODEL ANALYSIS

The schematics and working principles of the proposed MA are shown in **Figure 1**. The MA consists of three layers: the metamaterial, MAM, and conducting ground layer. When the EM waves impinge on the structure, magnetic resonance occurs. In the positive resonance region, the phenomenon of magnetic squeezing will take place. The magnetic field lines will be confined within the SRR arrays and the magnetic field strength will be enhanced inevitably, as shown on the right side of **Figure 1**. In addition, by changing the geometrical parameters, the magnetic resonant frequency can be adjusted correspondingly and the positive resonance region can be changed into a low-frequency band. Therefore, derived from the high loss of MAM, low-frequency microwave absorption can be achieved. Also, the lattice structure enables the structure to have satisfactory stability for polarization and wide incident angles.

3. LOW-FREQUENCY WIDEBAND ABSORPTION

3.1. Unit Structure Design

As schematically depicted in **Figure 2**, the unit of the proposed MA is shown. The top layer is the SRR arrays etched on FR4 (ε_r = 4.3, the loss tangent is 0.025) with the period of P = 8.0 mm, and the gap between adjacent SRRs is s = 1.40 mm. The middle layer is the MAM with the thickness of d = 3.00 mm, and the bottom layer is the conducting ground. The other geometrical parameters are: l_1 = 6.60 mm, l_2 = 6.95 mm, h = 7.75 mm, r = 0.4 mm, g = 0.3 mm, and t = 0.8 mm.

Firstly, we simulated the reflectivity spectra of the MAM with different incident angles using CST Microwave Studio 2018. The boundary conditions along the x- and y-directions are the unit cell boundaries, while along the z-direction is open add space. As we all know, the reflectivity R(ω) and transmittance T(ω) can be obtained from the reflection and transmission coefficients $S_{11}(\omega)$ and $S_{21}(\omega)$. That is, $R(\omega) = |S_{11}(\omega)|^2$ and $T(\omega) = |S_{21}(\omega)|^2$. The absorption A(ω) can be calculated by $A(\omega) = 1 - T(\omega) - R(\omega) = 1 - |S_{11}(\omega)|^2 - |S_{21}(\omega)|^2$. Due to the specular reflection of the conducting ground, $S_{21}(\omega)$ would be nearly zero in the frequency range. So the absorption can be simplified to $A(\omega) = 1 - |S_{11}(\omega)|^2$. In other words, we can use reflectivity spectra to represent the absorption performance. **Figure 3A** shows the simulated reflectivity spectra of the MAM at different angles. It is obvious that there is only a reduction of 9 dB within a very narrow bandwidth and only for the specific incident angles. Self-evidently, only the MAM cannot meet the requirements of practical application.

In consideration of the high magnetic loss of the MAM, the absorption performance will be improved significantly if the magnetic field strength in the MAM can be enhanced greatly. In the previous work [25, 26], the SRRs or their derivatives were widely used to construct left-handed metamaterials by virtue of the negative effective permeability in the negative resonance region. Whereas, in the positive resonance region, the effective

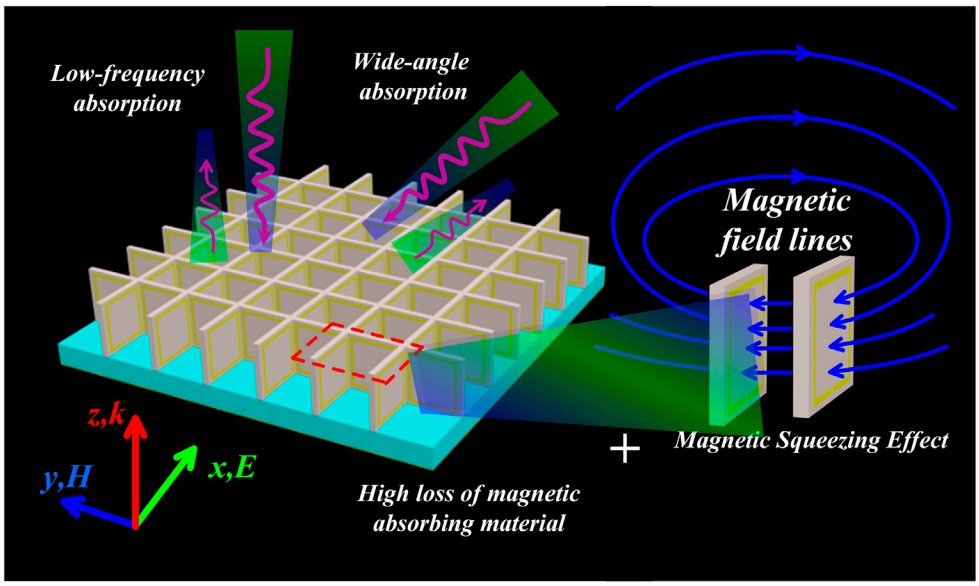

FIGURE 1 | The schematics and working principles of the proposed MA.

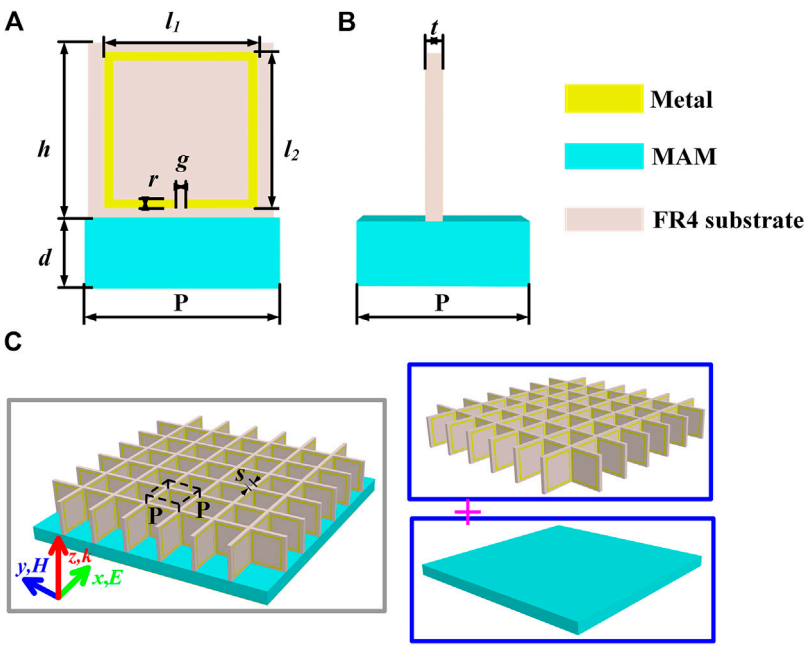

FIGURE 2 | Schematic illustration of the unit of proposed MA: **(A)** front view, and **(B)** side view. **(C)** Perspective view of the MA.

permeability will be larger than 1. In other words, the magnetic field strength within or even below the SRR will be enhanced greatly. Placing the MAM beneath the SRR, we can achieve high-efficiency absorption performance in low-frequency microwave bands. Just as **Figure 3B** shows, under normal incidence, the absorption rate of the proposed MA is enhanced significantly and the −10 dB frequency band is 1.25–2.31 GHz, compared with the MAM.

In addition, the reflectivity spectra of the proposed MA varied with different incident angles for TE and TM polarized waves are shown in **Figures 3C**,D. Clearly, under TE polarized waves, a 10 dB absorption band can be achieved in 1.25–2.31 GHz with an

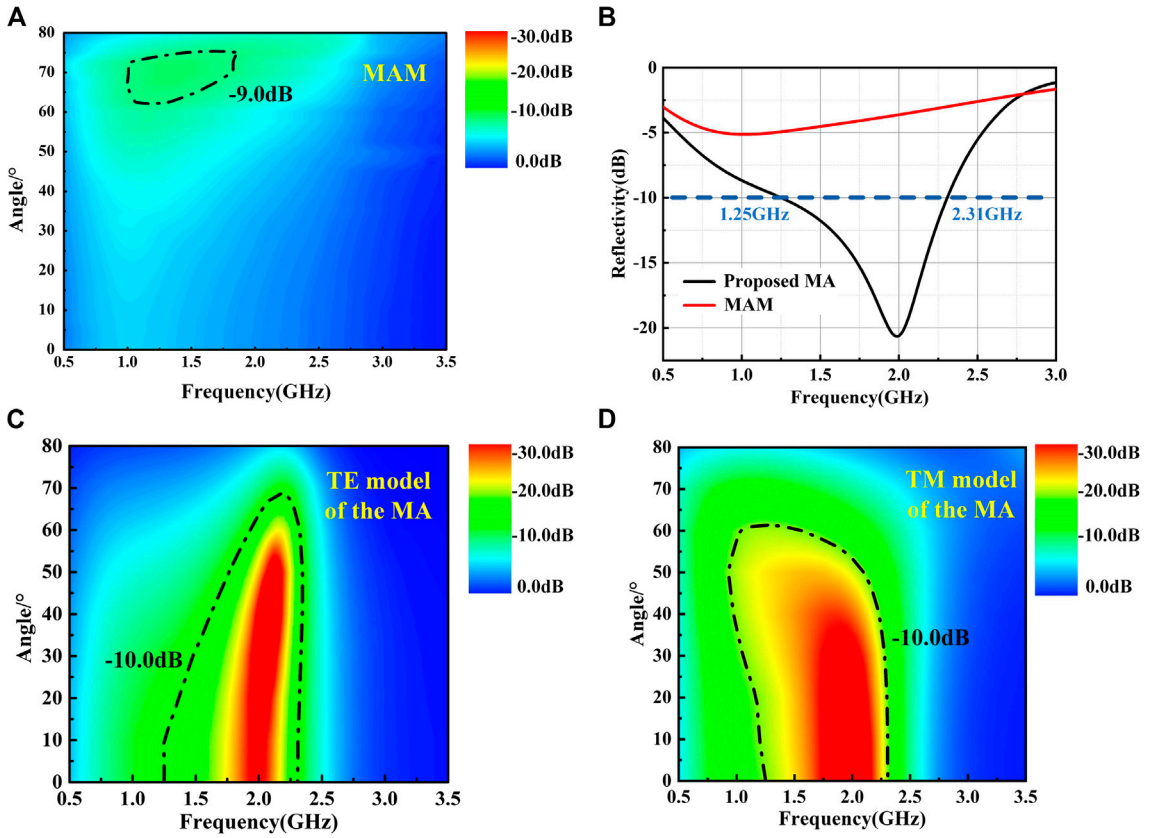

FIGURE 3 | (A) The simulated reflectivity spectra of the MAM at different angles. **(B)** The reflectivity of the comparison between the proposed MA and MAM under normal incidence. The simulated reflectivity spectra of the proposed MA at different angles under **(C)** TE polarized waves and **(D)** TM polarized waves.

incident angle ranging from 0 to 70°, and as for the TM polarized waves, the 10 dB absorption band gradually increases as the incident angle increases. Compared with **Figure 3A**, distinctly, the performances of the absorption bandwidth, absorption level, and angular domain have been improved significantly.

The design steps of our proposed MA can be summarized as follows: firstly, we analyzed and simulated the absorptive performance of the MAM, indicating that there is just a reduction of 9 dB within a very narrow bandwidth, only for the specific incident angles, and only the MAM cannot meet the requirements of practical application. Secondly, in consideration of the high magnetic loss of the MAM, the absorption performance can be improved significantly if the magnetic field strength in the MAM can be enhanced. By utilizing the positive resonance region of the SRRs and the magnetic squeezing effect, the magnetic field strength in the MAM will be greatly enhanced. Finally, the metamaterial absorber (MA) is proposed, which consists of SRR arrays placed on top of the MAM backed by a conducting ground.

3.2. Theoretical Analysis

When a kind of loss material is applied as the substrate, both the dielectric loss and the magnetic loss lead to high-efficiency absorption, following the relation: $P_{total} = P_E + P_M = (1/2)\omega\varepsilon''|\mathbf{E}|^2 + (1/2)\omega\mu''|\mathbf{H}|^2$ [27]. Here, **E** is the total electric field, ω and ε'' are the angular frequency and imaginary part of the permittivity, respectively. **H** is the total magnetic field, and μ'' is the imaginary part of the magnetic permeability. As previously analyzed, when the substrate is a MAM with high magnetic loss, by increasing the magnetic field strength in the MAM, the absorption efficiency will be significantly improved. Because the magnetic field is rotational and the magnetic field lines have to be closed to form a circulation, in the positive resonance region, the magnetic field lines tend to be squeezed within the MAM. On the other side, in the positive resonance region, the direction of magnetic field induced by SRR will be in accord with the incident magnetic field. That is to say, the magnetic field strength below the SRR structure will be enhanced greatly by superimposing them together. In **Figure 4A**, the retrieved effective permeability of the proposed MA is shown. Clearly, in the frequency band from 1.26 to 2.35 GHz, the real component of effective permeability is larger than one and the structure operates in the positive resonance region, which corresponds to the 10 dB absorptive frequency band shown in **Figure 3B**. Clearly, the frequency band of the positive resonance region is a little different from the absorbing frequency band, after comprehensive analysis, the reason can be concluded that the boundary conditions of the simulation and the retrieving effective permeability MATLAB

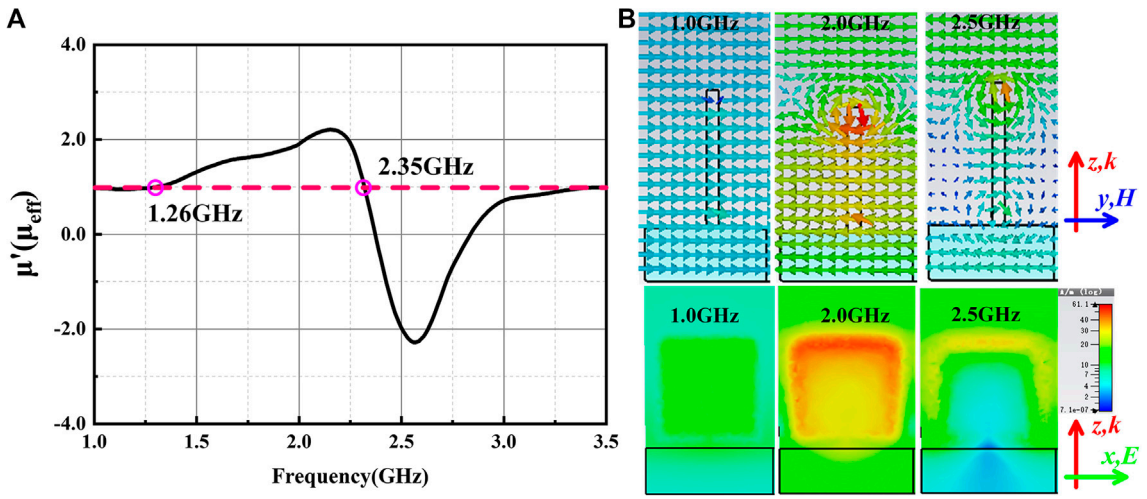

FIGURE 4 | (A) The retrieved effective permeability of the proposed MA. **(B)** Magnetic field distribution of 1.0, 2.0, and 2.5 GHz in the y-z and x-z planes for the normal incidence.

TABLE 1 | Simulated results of our proposed MA and recent works.

References	Absorption band (GHz)	Electrical thickness	Polarization sensitivity	Incident angle sensitivity
This work	**1.25–2.31**	**0.04λ_L**	**Insensitivity**	**0°-65°**
[29]	2.0–18.5	0.082λ_L	Insensitivity	0°–45°
[30]	6.08–13.04	0.07λ_L	Insensitivity	0°–45°
[31]	1.85–7.50	0.24λ_L	Insensitivity	0°–30°
[32]	2.0–4.4	0.02λ_L	Sensitivity	Not mentioned

procedure [28] are not the same, in other words, the conducting ground in the retrieving effective permeability MATLAB procedure is taken out. However, the purpose of retrieving effective permeability of the proposed MA is to verify that in the positive resonance region, the magnetic squeezing effect occurs, and further validating our scheme, in other words, the retrieved effective permeability is for reference only, therefore, the subtle differences between the frequency bands are acceptable.

In order to verify the analysis mentioned above, we monitored the magnetic field distribution at 1.0 GHz (the real component of effective permeability is approximately equal to 1), 2.0 GHz (the real component of effective permeability is larger than 1), and 2.5 GHz (the real component of effective permeability is negative) in the *y-z* and *x-z* planes with normal incident EM waves, just as **Figure 4B** shows. Clearly, at 2.0 GHz, which is in the positive resonance region, the magnetic field lines above the MA structure are confined within or below the MA, leading to significant magnetic field enhancement, which provides a prerequisite for low-frequency absorption. While at 2.5 GHz, which belongs to the negative resonance region, in contrast to the direction of the incident magnetic field, the direction of magnetic field induced by SRR will be in the opposite direction. That is, the magnetic field strength in the MAM will be weakened inevitably, as shown in **Figure 4B**, which will inevitably contribute to weaker absorption.

In addition, simulated results of our proposed MA in contrast to the recent works of broadband MAs are also presented in **Table 1**.

The comprehensive comparison concludes that our proposed MA achieves an optimal performance of low-frequency microwave absorption with comprehensive consideration of the absorption band and electrical thickness.

4. EXPERIMENT VERIFICATION

To verify our design concept, we fabricated and measured a prototype with dimensions of 600 × 600 mm^2. The prototype photograph is shown in **Figure 5A**. The components from top to bottom are: SRR arrays etched on FR4 dielectric, the MAM with 3.0 mm thickness and conducting ground. Firstly, the factory-made samples of SRR arrays are assembled. Then, the samples are glued onto the MAM and a plate of conducting ground. Under normal incidence, the comparison between the simulated and measured reflectivity curves (TE and TM polarized) are shown in **Figure 5B**. Furthermore, in order to obtain the reflection coefficient of oblique incidence, what we need to do is to adjust the angle disc to get the specific angle like the detail in **Figure 5A**, while the horn feed stays stationary. Hence, correspondingly, the angle of the incident wave is controlled. The reflectivity spectrum varied with different incident angles for the TE and TM polarized waves are shown in **Figures 5C**,D, respectively. Compared with **Figures 3C**,D, it is obvious that the agreements are very good considering the tolerance in the fabrication and assembly, which validates our scheme. Hence,

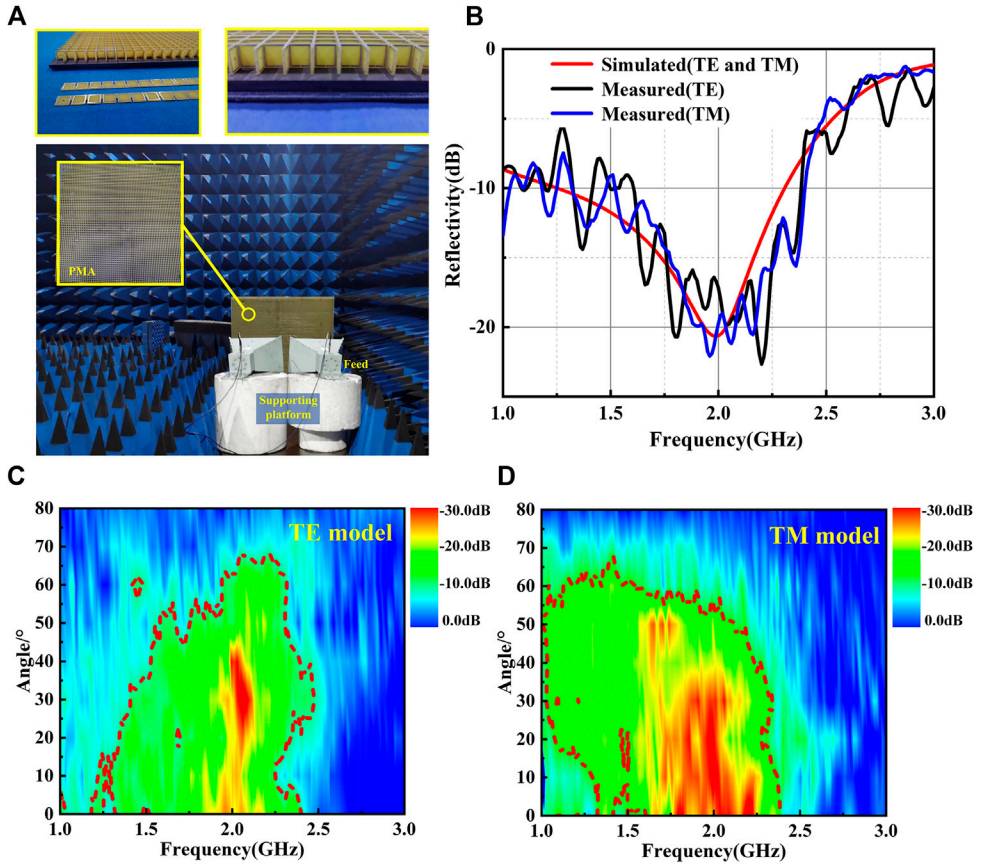

FIGURE 5 | (A) The fabricated prototype of the MA and the measured environment of oblique incidence. **(B)** Comparison between simulated and measured reflectivity spectra under normal incidence. Measured reflectivity spectrum varied with different incident angles under **(C)** TE and **(D)** TM polarized waves.

to some extent, we can agree that our proposed MA can achieve wide-angle microwave absorption in a low-frequency band.

5. CONCLUSION

In conclusion, we designed, fabricated, and measured a kind of MA, which included a top layer of SRR, a middle layer of MAM and a bottom layer of conducting ground. The MA can achieve wide-angle microwave absorption in 1.25–2.31 GHz under normal incidence by utilizing the phenomenon of magnetic squeezing. In the positive resonance region of SRRs, a strong magnetic squeezing effect occurs. That is, more concentrated magnetic field lines are confined within the SRR arrays. This results in significant magnetic field enhancement within the MAM layer, which provides a prerequisite for high-efficiency absorption enhancement at low frequencies. Furthermore, the lattice structure enables the MA to have satisfactory stability for polarization and wide incident angles. To verify our design concept, a prototype with dimensions of $600 \times 600\,mm^2$ was fabricated and measured, and the good agreement between simulated and measured results validates our scheme. This design method may find potential applications in fields such as electromagnetic compatibility, wireless communication, and others.

DATA AVAILABILITY STATEMENT

All datasets presented in this study are included in the article/supplementary material.

AUTHOR CONTRIBUTIONS

ZW: Conceptualization, Methodology, Software, Validation, Writing - original draft, Writing - review and editing. JW: Conceptualization, Investigation, Writing - review & editing. YH, YF, XF, YP, MY, YL, HM, ZX, and SQ: Supervision, Writing - review & editing.

FUNDING

The authors are grateful to support from the National Natural Science Foundation of China (Grant Nos.

61971435, 61801509, 61901508, 61671466, and 61971341), the Shaanxi Province Scientific and Technology Innovation Team Foundation of Shaanxi Province under Grant No. 2019JZ-40, and the National Key Research and Development Program of China (Grant No.: SQ2017YFA0700201).

REFERENCES

1. Smith DR, Padilla WJ, Vier DC, Nemat-Nasser SC, Schultz S. Composite medium with simultaneously negative permeability and permittivity. *Phys Rev Lett* (2000) 84:4184. doi:10.1103/physrevlett.84.4184.
2. Chen H, Wu BI, Zhang B, Kong JA. Electromagnetic wave interactions with a metamaterial cloak. *Phys Rev Lett* (2007) 99:063903. doi:10.1103/physrevlett.99.149901.
3. Huang C, Yang J, Wu X, Song J, Pu M, Wang C, et al. Reconfigurable metasurface cloak for dynamical electromagnetic illusions. *ACS Photonics* (2017) 5:1718–25. doi:10.1021/acsphotonics.7b01114.
4. Seddon N, Bearpark T. Observation of the inverse Doppler effect. *Science* (2003) 302:1537–40. doi:10.1126/science.1089342.
5. Hao J, Wang J, Liu X, Padilla WJ, Zhou L, Qiu M. High performance optical absorber based on a plasmonic metamaterial. *Appl Phys Lett* (2010) 96:251104. doi:10.1063/1.3442904.
6. Reinhard B, Schmitt KM, Wollrab V, Neu J, Beigang R, Rahm M. Metamaterial near-field sensor for deep-subwavelength thickness measurements and sensitive refractometry in the terahertz frequency range. *Appl Phys Lett* (2012) 100:221101. doi:10.1063/1.4722801.
7. Narayan S, Sangeetha B, Sruthi TV, Shambulingappa V, Nair RU. Design of low observable antenna using active hybrid-element FSS structure for stealth applications. *AEU - Int J Electron Commun* (2017) 80:137–43. doi:10.1016/j.aeue.2017.06.038.
8. Yong Z, Zhang S, Gong C, He S. Narrow band perfect absorber for maximum localized magnetic and electric field enhancement and sensing applications. *Sci Rep* (2016) 6:24063. doi:10.1038/srep24063.
9. Wu C, Neuner B, III, John J, Milder A, Zollars B, Savoy S, et al. Metamaterial-based integrated plasmonic absorber/emitter for solar thermo-photovoltaic systems. *J Optic* (2012) 14:024005. doi:10.1088/2040-8978/14/2/024005.
10. Landy NI, Sajuyigbe S, Mock JJ, Smith DR, Padilla WJ. Perfect metamaterial absorber. *Phys Rev Lett* (2008) 100:207402. doi:10.1103/physrevlett.100.207402.
11. Cheng Y, Zou Y, Luo H, Chen F, Mao X. Compact ultra-thin seven-band microwave metamaterial absorber based on a single resonator structure. *J Electron Mater* (2019) 48:3939–46. doi:10.1007/s11664-019-07156-z.
12. Bakir M, Karaaslan M, Ünal E, Akgöl O, Sabah C. Microwave metamaterial absorber for sensing applications. *Opto-Electron Rev* (2017) 25:318–25. doi:10.1016/j.opelre.2017.10.002.
13. Kim YJ, Hwang JS, Yoo YJ, Khuyen BX, Rhee JY, Chen X, et al. Ultrathin microwave metamaterial absorber utilizing embedded resistors. *J Phys D Appl Phys* (2017) 50:405110. doi:10.1088/1361-6463/aa82f4.
14. Cheng Y, Cheng Z, Mao X, Gong R. Ultra-thin multi-band polarization-insensitive microwave metamaterial absorber based on multiple-order responses using a single resonator structure. *Materials* (2017) 10:1241. doi:10.3390/ma10111241.
15. Zhao J, Cheng Y. Ultrabroadband microwave metamaterial absorber based on electric SRR loaded with lumped resistors. *J Electron Mater* (2016) 45:5033–9. doi:10.1007/s11664-016-4693-0.
16. Ramya S, Srinivasa Rao I. A compact ultra-thin ultra-wideband microwave metamaterial absorber. *Microw Opt Technol Lett* (2017) 59:1837–45. doi:10.1002/mop.30636.
17. Hoa NTQ, Lam PH, Tung PD. Wide-angle and polarization-independent broadband microwave metamaterial absorber. *Microw Opt Technol Lett* (2017) 59:1157–61. doi:10.1002/mop.30490.
18. Wang Q, Cheng Y. Compact and low-frequency broadband microwave metamaterial absorber based on meander wire structure loaded resistors. *AEU Int J Electron Commun* (2020) 120:153198. doi:10.1016/j.aeue.2020.153198.
19. Ding F, Cui Y, Ge X, Jin Y, He S. Ultra-broadband microwave metamaterial absorber. *Appl Phys Lett* (2012) 100:103506. doi:10.1063/1.3692178.
20. Nguyen TT, Lim S. Design of metamaterial absorber using eight-resistive-arm cell for simultaneous broadband and wide-incidence-angle absorption. *Sci Rep* (2018) 8:6633. doi:10.1038/s41598-018-25074-8.
21. Shen Y, Zhang J, Meng Y, Wang Z, Pang Y, Wang J, et al. Merging absorption bands of plasmonic structures via dispersion engineering. *Appl Phys Lett* (2018) 112:254103. doi:10.1063/1.5040067.
22. Shen Y, Zhang J, Wang W, Pang Y, Wang J, Ma H, et al. Integrating absorber with non-planar plasmonic structure for k-vector matching absorption enhancement. *J Appl Phys* (2018) 124:225101. doi:10.1063/1.5068717.
23. Fan Y, Zhang HC, Yin JY, Xu L, Nagarkoti DS, Hao Y, et al. An active wideband and wide-angle electromagnetic absorber at microwave frequencies. *Antennas Wirel Propag Lett* (2016) 15:1913–16. doi:10.1109/lawp.2016.2544399.
24. Li W, Wu T, Wang W, Guan J, Zhai P. Integrating non-planar metamaterials with magnetic absorbing materials to yield ultra-broadband microwave hybrid absorbers. *Appl Phys Lett* (2014) 104:022903. doi:10.1063/1.4862262.
25. Wang J, Qu S, Yang Y, Ma H, Wu X, Xu Z. Multiband left-handed metamaterials. *Appl Phys Lett* (2009) 95:014105. doi:10.1063/1.3170236.
26. Wang J, Qu S, Xu Z, Zhang J, Ma H, Yang Y, et al. Broadband planar left-handed metamaterials using split-ring resonator pairs. *Photonics Nanostruct - Fundam Appl* (2009) 7:108–113. doi:10.1016/j.photonics.2009.01.001.
27. Pozar DM. *Microwave engineering*. 4th ed. Hoboken, NJ: John Wiley & Sons (2012)
28. Smith DR, Vier DC, Koschny T, Soukoulis CM. Electromagnetic parameter retrieval from inhomogeneous metamaterials. *Phys Rev* (2005) 71:036617. doi:10.1103/physreve.71.036617.
29. Tayde Y, Saikia M, Srivastava KV, Ramakrishna SA. Polarization-insensitive broadband multilayered absorber using screen printed patterns of resistive ink. *Antennas Wirel Propag Lett* (2018) 17:2489–93. doi:10.1109/lawp.2018.2879274.
30. Kong X, Xu J, Mo J-J, Liu S. Broadband and conformal metamaterial absorber. *Front Optoelectron* (2017) 10:124–131. doi:10.1007/s12200-017-0682-z.
31. Bian B, Liu S, Kong X. Three-dimensional microwave broadband metamaterial absorber with broad transmission window based on the coupled symmetric split ring resonators. *J Electromagn Waves Appl* (2016) 30:2153–64. doi:10.1080/09205071.2016.1249417.
32. Zhang HB, Deng LW, Zhou PH, Zhang L, Cheng DM, Chen HY, et al. Low frequency needlepoint-shape metamaterial absorber based on magnetic medium. *J Appl Phys* (2013) 113:13903. doi:10.1063/1.4772622.

Conflict of Interest: The authors declare that the research was conducted in the absence of any commercial or financial relationships that could be construed as a potential conflict of interest.

frontiers in Physics

REVIEW
published: 08 December 2020
doi: 10.3389/fphy.2020.585881

Research on the Influence of Metamaterials on Single Photon LiDAR

*Yingying Hu†, Duoduo Xu†, Zehui Zhou†, Tianqi Zhao *, Yan Shi, Ying Tian, Rui Xu and Yi Chen*

School of Optics and Electronic Technology, China Jiliang University, Hangzhou, China

Single photon light detection and ranging (LiDAR) has the advantages of high angle and distance resolution, great concealment, a strong anti-active jamming capability, small volume, and light mass, and has been widely applied in marine reconnaissance, obstacle avoidance, chemical warfare agent detection, and navigation. With the rapid development of metamaterials, the performance of a single photon LiDAR system would be improved by optimizing the core devices in the system. In this paper, we first analyzed the performance index of the single photon LiDAR and discovered the potential of metamaterials in improving the system performance. Then, the influence of metamaterials on the core devices of the single photon LiDAR were discussed, including lasers, scanning devices, optical lenses, and single photon detectors. As a result, we have concluded that through effective light field modulation, metamaterial technology might enhance the performance innovation of the single photon LiDAR.

Keywords: single photon LiDAR, metamaterial, lidar, light field modulation, enhanced detection

OPEN ACCESS

Edited by:
Chee Leong Tan,
University of Malaya, Malaysia

Reviewed by:
Kun Song,
Northwestern Polytechnical University, China
Lin Chen,
Beijing Radiation Center (BRC), China

****Correspondence:***
Tianqi Zhao
18a0402151@cjlu.edu.cn

†These authors have contributed equally to this work

Specialty section:
This article was submitted to Optics and Photonics, a section of the journal Frontiers in Physics

Received: *21 July 2020*
Accepted: *28 September 2020*
Published: *08 December 2020*

Citation:
Hu Y, Xu D, Zhou Z, Zhao T, Shi Y, Tian Y, Xu R and Chen Y (2020) Research on the Influence of Metamaterials on Single Photon LiDAR. Front. Phys. 8:585881. doi: 10.3389/fphy.2020.585881

1. INTRODUCTION

Inspired by how bats fly, Christian Schuesmaier invented the first radar in the world in 1904. As the combination of traditional radar technology and modern laser technology, light detection and ranging (i.e., LiDAR) is an advanced remote sensing technology, which mainly uses the light reflected from obstacles to determine the actual position information of the target object. Compared with the conventional microwave radar, LiDAR has the advantages of higher angle and distance resolution, greater concealment, stronger anti-active jamming capabilities, better low-altitude detection performance, smaller volume, and lighter mass.

In recent years, LiDAR based on single photon detectors, i.e., single photon LiDAR, has gradually emerged and developed rapidly with the development of single photon detection technologies. With higher detection limit distance and resolution, the single photon LiDAR can achieve multidimensional data, such as azimuth-pitch angle-distance, range-speed-intensity, and display the data in the form of images to obtain radiation geometric distribution images, range-gate images, and velocity images, which has wide applications. First, it is an important means of reconnaissance [1]. For marine reconnaissance, LiDAR was used for the detection and location of water targets [2–5], wave detection [6, 7], and the reconnaissance of sea gas [8]. Then, for land reconnaissance, LiDAR was used for the global monitoring of Earth's ice sheet mass balance [9], aircraft height detection, and topographic surveys [10, 11]. Third, for atmospheric reconnaissance, LiDAR was used for cloud-aerosol detection [12, 13], checking wind speed, and measuring the real-time wind field [14]. For obstacle avoidance, LiDAR promotes the use of driverless cars [8, 15], unmanned ships [16, 17], and

unmanned erial vehicles [18, 19]. Besides, LiDAR can be used for chemical warfare agent detection [20] and navigation [21].

In the following, we analyze the performance index of a single photon LiDAR in section 2, study the influence of metamaterials on a single photon LiDAR in section 3, and finally underline the upcoming prospects for LiDAR in section 4.

2. THE PERFORMANCES INDEX OF SINGLE PHOTON LIDAR

2.1. Measurement Position Accuracy

For LiDAR, the higher the accuracy, the better. The data obtained by LiDAR can be used for obstacle identification, and dynamic object detection and location. If the accuracy is too poor, the above objectives cannot be achieved. However, high precision requires high object configuration requirements, which may have too large a volume. The factors affecting the measurement accuracy include noise, pulse width and time resolution, and the average signal photon number in echo signals.

Noise. The lower the noise, the higher the accuracy of the single photon LiDAR. Reducing the error caused by noise plays an important role in improving the measurement accuracy. The dark count of a single photon detector is a noise contributor which usually causes measurement errors [22]. For the single photon avalanche photodiode (SPAD), a type of single photon detector, the metamaterial integration technology provides a novel way to achieve high photon detection efficiency (PDE), without changing the device structure which obtains low dark counts and good time resolution [23].

Pulse width and time resolution. The pulse width of a laser usually refers to the duration when the laser power is maintained at a certain value. The time resolution of the detector is the minimum recognizable time interval of incident signals. With the increase of pulse width and poorer time resolution, the wider the range of distance statistical discrete distribution is, the lower the measurement accuracy. The pulse shaping technology by metamaterials enables narrower pulse width from the light source.

Average signal photon number in echo signals. When the echo signal is weak, the probability of target detection is low, while the measurement accuracy increases rapidly with the increase of echo signal strength [24, 25]. When the intensity of the echo signal reaches a critical value, the probability of the target detection tends to 1. It is worth mentioning that, compared with traditional SPAD, SPAD with metamaterials on the device surface have the advantage of higher PDE which promote higher probability of the target detection even on the condition of fewer photons in the echo signal. Besides, the meta lens technology could effectively focus photons in the echo signal on the detector.

2.2. Measurement Limit Distance

Different applications have different requirements for the detection range of LiDAR. For example, to be able to detect vehicles ahead on a highway, a telescope needs to be equipped with LiDAR for long-range ranging. The process of pulse laser ranging is generally as follows: launch laser pulse to the target under test, and a time probe for the launch of the laser pulse is recorded. After detecting the echo signal time, the measurement distance is calculated by the basic formula,

$$D = \frac{c \cdot t}{2} \tag{1}$$

where D is the distance between the detector and the detected target; t is the round trip time of laser pulse; and c is the speed of light [26]. The measurement limit distance of LiDAR is dependent on the effective time detection of the echo signal. Therefore, a single photon detector with stronger weak light detection capabilities and good time resolution makes a single photon LiDAR with further measurement limit distance, compared with conventional LiDAR. SPAD integrated with metamaterials is an important approach. Moreover, the vortex beam or polarized laser produced by the metamaterials technology endows the LiDAR system with stronger anti-interference abilities and further measurement limit distance.

2.3. Angular Resolution

Resolution refers to the ability to distinguish between the left and right adjacent targets at a certain distance. The smaller the angular resolution, the smaller the target that can be resolved, so that the measured point cloud data are more delicate. The angular measurement accuracy of general obstacle avoidance LiDAR is only about 0.1°, while the angular resolution of mapping LiDAR is generally 0.001° or even lower. When the mono-pulse method is used to measure the azimuth and pitch angle of the target, the angular resolution mainly depends on the antenna beamwidth and signal-to-noize ratio (SNR) [27]. The wider the beam width is, the stronger the directivity of the LiDAR beam is, and the better the resolution of corresponding direction is. The SNR also affects the resolution and plays an important role for the improvement of the measurement accuracy of diagonal resolution. Therefore, the wider the antenna beam and the higher the SNR, the higher the angular resolution of the LiDAR will be. H igher PDE can be achieved for SPAD integrated with metamaterials, which promotes higher SNR for the single photon LiDAR. In addition, the anti-interference light source and focusing lens realized by metamaterials technology also provides higher SNR.

2.4. Imaging Speed

Most imaging LiDAR uses the imaging technology of single pixel detector LiDAR. The scanning optical system points the transmitting pulse to the target, and the echo intensity reflects the specific reflectivity of the target. The scanner hits the beam at different positions on the target according to a certain scanning pattern, and the image of the target can be obtained through the receiving system. The image speed is usually limited by the scanning speed. Compared with a conventional mechanical scanning method, the laser beam steered by the metamaterials technology provides a possibility of faster scanning.

2.5. Cost

High performance LiDAR with fast imaging speed and long measuring distance, usually requires a lot of hardware with

high cost, including the manufacturing and functional components [28]. Single-photon LiDAR is widely used, such as human eye safety LiDAR [29] and atmospheric signal-to-noize ratio detection in laser remote sensing [30]. A wide range of applications makes the single photon LiDAR more valuable and promotes lower cost. Generally, metamaterial has supernormal physical properties that natural materials do not possess, and it can flexibly adjust and control the phase, amplitude, polarization, and other characteristics of electromagnetic waves through the micro-structure of the subwavelength, as well as being easy to integrate [31]. This means that metamaterial may contribute to the realization of small size, high integration, and low-cost single photon LiDAR.

3. APPLICATION OF METAMATERIAL IN SINGLE PHOTON LIDAR

The core optoelectronic devices in single photon LiDAR are a laser, an optical lens, a scanning device (just for the scanning type LiDAR), and a single photon detector. Because of the development of metamaterials [32–38], the performance of these core devices might be improved.

3.1. Light Source

Making full use of the designed metamaterial can help to effectively regulate the laser light source, such as wavelength, intensity, phase, and polarization. The second-order and third-order nonlinear optical effects in metamaterials have a good application prospect in the field of optical frequency conversion. Through frequency conversion, coherent radiation of various wavelengths can be obtained, which helps to coordinate the light sources of appropriate wavelengths and meet the needs of various practical applications [39]. The nonlinear optical efficiency of the metamaterial is determined by the macroscopic polarization of the metamaterial functional unit and the microscopic polarization of the constituent material. The control of the nonlinear optical field can be realized by designing the material, geometry, and spatial order of the metamaterial functional unit reasonably. It further overcomes the limitations of natural materials in this respect. Compared with 3D metamaterials which are always limited by nano-processing technology and high optical loss, 2D meta-surfaces are easier to process and have relatively low optical loss, so it attracts much attention in the aspect of nonlinear optical field regulation [40]. As a result, the wavelength range limited of the laser light source can be expanded to the ultraviolet and deep ultraviolet area, and make up the cost of expensive laser infrared or ultraviolet light [41–43].

Andrew Forbes demonstrated the first meta-surface laser in the world which produced "super-chiral light": light with super high angular momentum [44]. The new laser produced a new type of high-purity "distorted light" that had never been seen before, including the highest angular momentum reported by the laser. The researchers developed a nanostructured meta-surface that has the largest phase gradient produced to date and allows for high-power operation in a compact design, which is capable of generating a peculiar state of twisted structured light on demand. The meta-surface is composed of many tiny rods of nanomaterials that change the light transmission as it passes through. More importantly, this method is applicable to many laser architectures. For instance, the gain volume and meta-surface size can be increased to produce high-power large volume lasers, or reduce the laser system to a monolithic meta-surface design on the chip.

Based on the principle of linear filtering, the ultrashort pulse polarization can be controlled to a large extent by designing an ultrashort pulse meta-surface, so as to realize the expansion, compression, and remodeling of ultrashort pulse polarization [45]. Since the surface plasmon polaritons (SPPs) can shape the propagating optical spectrum, temporal control of the pulse shape of ultrashort pulses can be achieved through engineered resonances of plasmonic nanoparticles and lattice arrangements. As shown in **Figures 1A,B** a compact ultra-thin plasma meta-surface made of nanoparticles was proposed. Given the input pulses, the meta-surface filter was designed to output the specific pulses with narrower pulse width (**Figure 1C**). And the meta-surface filters are able to compress the different Gaussian pulses with different compression ratios. It is beneficial to realize the optical index of narrow pulse width and high peak power of the laser, thus improving the detection accuracy and broadening the detection range of LiDAR.

The orbital angular momentum shows the potential of improving resolution and an anti-jamming capability [46]. In the propagation process, the vortex beam always maintains the invariability of the hollow distribution, with spin and orbital angular momentum, and the spiral phase structure, which promotes the super-resolution imaging for LiDAR [47, 48]. Jin Han et al. designed and realized an intuitive and simple meta-surface method for generating and manipulating annular vortex beams [49].

The dynamic control of laser output polarization state is an ideal imaging application. Some researchers have used new methods to realize the direct polarization switching of lasers [50]. The laser is integrated with the semiconductor gain medium through a polarization-sensitive meta-surface to amplify the cavity mode and output the polarized laser. The meta-surface is used together with the output coupler reflector. The emitting laser is perpendicular to the outer cavity surface, and the output polarization state can be electrically switched separately. This design means that the laser output has the possibility of high switching speed, compactness, and power efficiency. The use of polarization technology improves the performance of the coherent detection system and promotes the development of high precision LiDAR.

A vertical cavity surface-emitting laser (VCSEL) is a kind of light source with the advantages of low power consumption, low-cost packaging, and ease of fabrication into arrays for wafer-scale testing. Kun Li et. al presented a monolithic, electrically-pumped tunable 1,060 nm VCSELs with a high-contrast grating (HCG) meta-structure as the highly reflective tunable mirror [51], as shown in **Figure 2**. Through electrical actuation of the HCG, the wavelength tuning of larger than 30 nm VCSELs is continuously realized. This is promising for the realization of a high-speed and

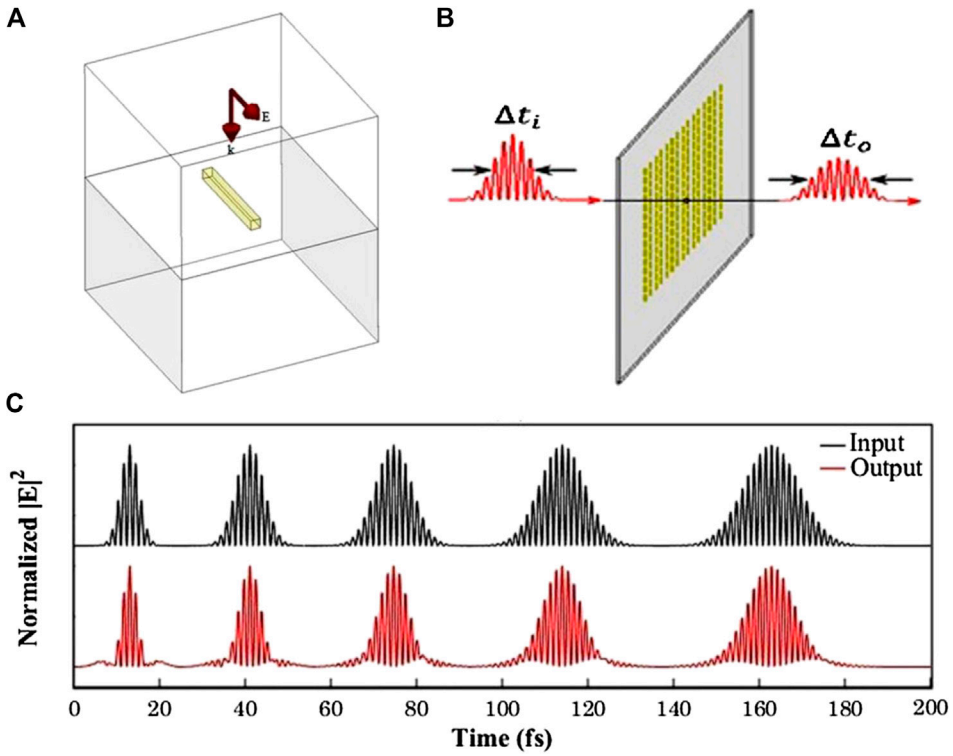

FIGURE 1 | (A) Unit cell of the periodic golden meta-surface on a fused silica substrate with a 2 nm titanium adhesion layer. **(B)** Pulse shaping schematic using a nano-plasmonic filter, which is a periodic golden meta-surface, Δt_i is the half-power pulse width of the input pulse, Δt_o is the half-power pulse width of the output pulse. **(C)** Input/output comparison for different pulse width at the central frequency of 370 THz. *Source*: reproduced from Ref. 45.

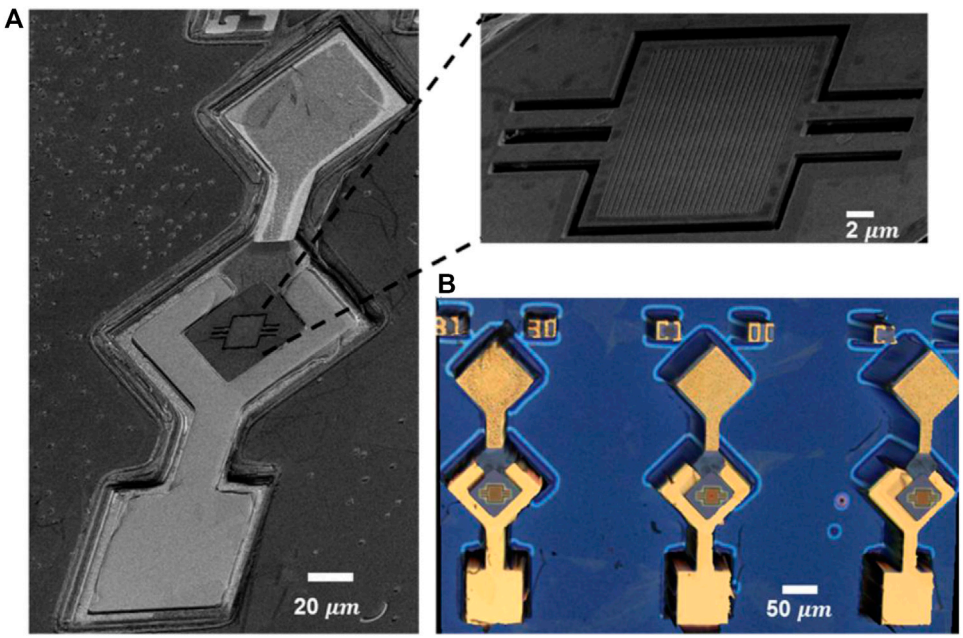

FIGURE 2 | (A) Scanning electron microscope (SEM) image of a typical HCG-VCSEL device, with a zoomed-in view of the fully suspended HCG surrounded by air. **(B)** 3D confocal optical image of the faburicated HCG-VCSEL array. *Source*: reproduced from Ref. 51.

widely variable wavelength tunable source with cost-effective fabrication processes for applications in LiDAR.

3.2. Scanning Structure and Scanning Mode

The space scanning methods of LiDAR can be divided into a non-scanning system and a scanning system [52]. Compared with the traditional mechanical controlling scanning method, the planar devices based on the meta-surface are small and could be easily controlled by the micro-electro-mechanical system (MEMS), which helps to remove the huge components, simplifying the system and lowering the cost [53].

For the non-scanning methods, some researchers have proposed the use of dielectric Huygens meta-surface structures to construct flat lenses and beam deflectors [54]. The device adopts a silicon nano-disk structure to suppress reflection loss. By locally changing the radius of the silicon nano-disk elements, phase transition mutation is realized and arbitrary wavefront control is realized. By experimentally studying the phase gradient, the researchers realized that the plane lens has the characteristic of beam deflection, and the resulting light is similar with that produced by the beam deflection device. Compared with traditional lenses, the design is compact, lightweight, and easier to handle in complex wavefront operations. In addition, controlling the phase and amplitude of light emitted by the elements (i.e., pixels) of an optical phased array is of paramount importance to realizing dynamic beam steering for LiDAR applications. A. C. Lesina presented a plasmonic pixel composed of a metallic nanoantenna covered by a thin oxide layer and a conductive oxide for use in a reflect array meta-surface (as shown in **Figure 3**), which predicted the control of the reflection coefficient phase over a range >330° with a nearly constant magnitude [55]. F. He proposed a silicon surface material that dynamically controls the output light angle [56]. The structure is an array of silicon nanopillars of different diameters with a thick glass substrate underneath. By adjusting the relative phase and intensity of the two incident beams, the angle of output light can be continuous tuned at ~10° as needed. Besides, the output beam has good stability and no distortion, suggesting potential applications in LiDAR.

3.3. Optical System

The function of a LiDAR transmitting optical system is to provide a high power laser, collimate and reshape the beam with an asymmetric shape, produce large divergence and astigmatism

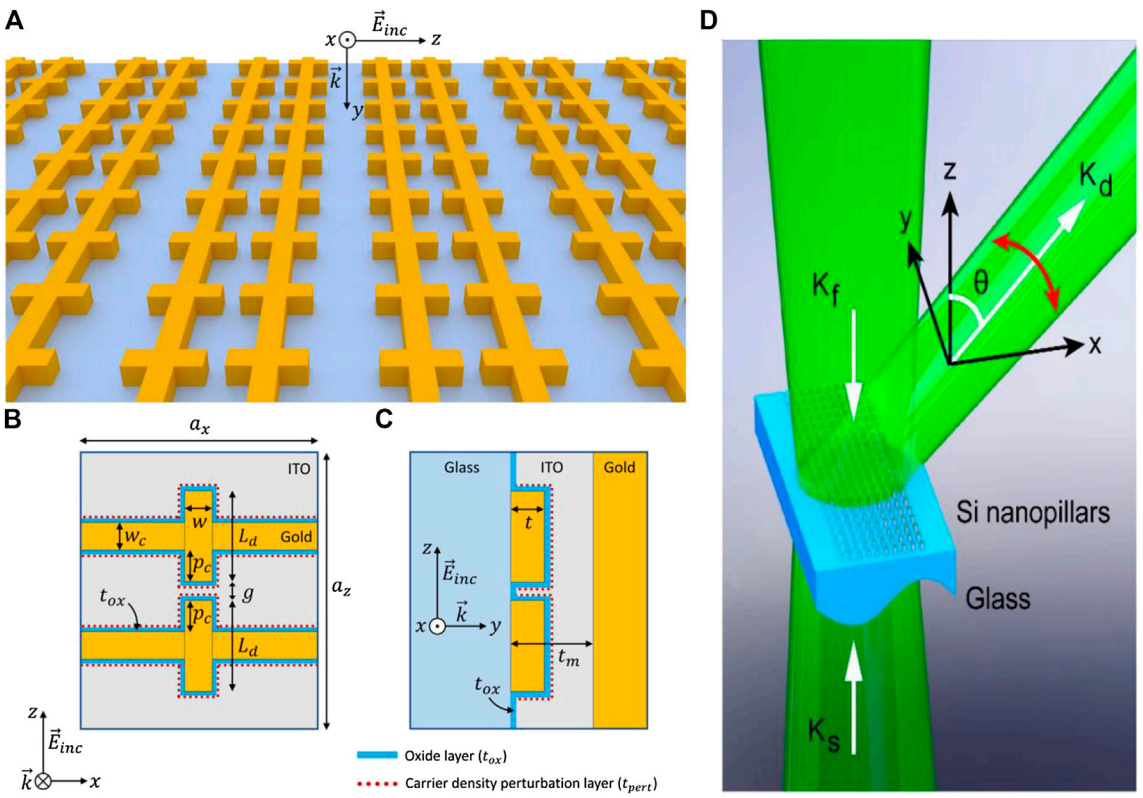

FIGURE 3 | (A) Meta-surface containing an array of plasmonic pixels (only glass substrate and gold nanoantennas are sketched). **(B)** Top view and **(C)** cross-sectional view of the proposed plasmonic pixel. The pixel has dimensions a_x by a_z, and contains a gold dipole nanoantenna which is formed by two branches of length L_d, width w, thickness t, and separated by a gap of size g. The pixel also contains two gold lines of width w_c. The thickness of the meta-surface (metalnanostructure + oxide + ITO) and ITO are denoted as t_m and t_{ox}, respectively. *Source*: reproduced from Ref. 55. **(D)** coherent illumination of a dielectric meta-surface for continuous beam steering. Two counterpropagating light beams (K_f and K_s) illuminate the meta-surface at normal incidence. The propagation angle θ of the output beam (K_d) deflected into free space can be continuously steered via adjusting the relative phase and intensity of the two incident beams. *Source*: reproduced from Ref. 56.

from the semiconductor laser, enhance the echo signal, improve signal-to-noize ratio, and measure the accuracy of the system [57]. The core element of the optical system is a different kind of lens. Because metamaterials can control electromagnetic waves arbitrarily, more attention has been paid to them. A metamaterial lens is one of its typical implementations [58]. Metamaterials can theoretically achieve arbitrary permittivity and permeability. When the electromagnetic impedance of the plate and vacuum is almost equal, it will reflect little electromagnetic waves, while the plate medium will not absorb electromagnetic waves at this time, which means that the conditions for lenses are available. In 2014, D. M. Lin proposed a medium-graded meta-surface optical lens, and successfully realized the production of gratings, lenses, and axicons on the SOI substrate, with the working band in visible light [59]. Using titanium dioxide "nanowires" with about 600 nm height, F. Capasso created a perfectly "flat" paper-thin "focusing lens" [60], as shown in **Figures 4A–F**. The metamaterial lens had an effective magnification of up to 170 times and had an excellent imaging resolution. It used nano-bricks stacked in an unusually neat arrangement with a negative refractive index. By changing the shape, size, and arrangement of the nanostructures (smaller than the wavelength of light), the light can be focused. In addition, a broadband achromatic dielectric meta lens was developed to eliminate the chromatic aberration, which can focus the entire spectrum with wavelengths over 1,200–1,650 nm at the same point (**Figures 4G,H**) [61].

By designing the meta-surface, the distribution of the phase, polarization, and intensity of the spatial light field is controlled locally by a thin layer of the subwavelength structure unit. It can effectively regulate the propagation property of light and expand the means and methods of people's regulation of the electromagnetic wave, so that the development of electromagnetic wave regulation device tends to be miniaturized, planarized, and conformed, and thus has an important application prospect. Huygens' principle and Fermat's principle can be used to calculate the phase distribution required by the metamaterial lens. An optical zoom method based on the wavelength regulation of the metamaterial lens was presented and the tomographic imaging method of the superstructure lens based on the elimination of spherical aberration was realized [62, 63]. However, once the micro-nano structure integrated on the metamaterial lens is prepared, it is usually difficult to change

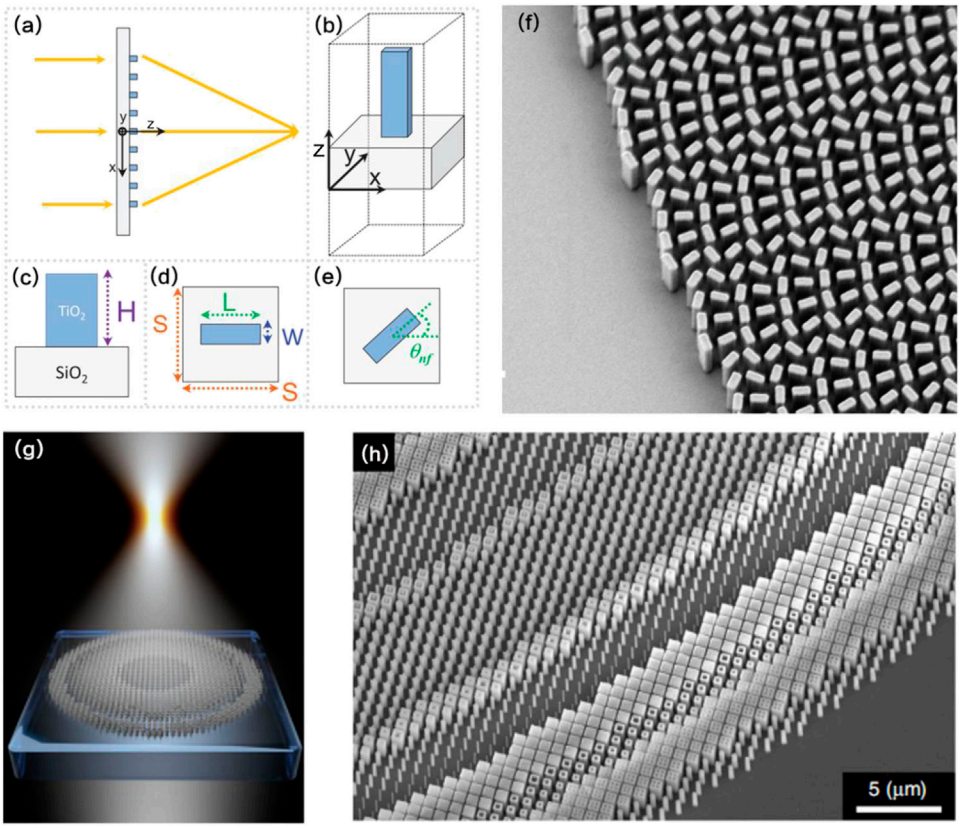

FIGURE 4 | (A) Schematic of the meta lens and its building block, the TiO_2 nanofin. **(B)** The meta lens consists of TiO_2 nanofins on a glass substrate. **(C,D)** Side and top views of the unit cell showing height H, width W, and length L of the nanofin, with unit cell dimensions S × S. **(E)** The required phase is imparted by the rotation of the nanofin by an angle θ_{nf}, according to the geometric Pancharatnam-Berry phase. **(F)** SEM micrograph of the fabricated meta lens. *Source*: reproduced from Ref. 60. **(G)** Schematic of a broadband achromatic meta lens composed of meta-units with complex cross sections, showing dispersionless focusing. **(H)** SEM images of fabricated meta-lenses using meta-units. *Source*: reproduced from Ref. 61.

its morphology or size, so it is impossible to control its focusing performance in real time. Recently, scientists have explored many ways to realize real-time regulation of the focusing performance of a superstructure lens, among which the most striking one is the combination of intelligent materials and a superstructure lens [64]. For example, K. Chen et al., invented a real-time local reconfigurable source Huygens meta lens in the 6.9 GHz working wave band [65], which, to the best of our knowledge, demonstrates for the first time that multiple and complex focal spots can be controlled simultaneously at distinct spatial positions and reprogrammable in any desired fashion, with a fast response time and high efficiency, as shown in **Figure 5**.

In the cases discussed above, the metamaterials give optical lenses the potential to push the limits and even disrupt things like camera lenses. In the future, camera lenses by metamaterials may become as thin as paper, and there will no longer be the inherent distortion and edge image attenuation problems of "convex lenses". Moreover, the lens cost of metamaterial lenses is much cheaper than that of traditional glass lenses, which is an extremely significant development for the industry. However, it is not without flaws. Currently, metamaterials usually regulate electromagnetic waves in a narrow band, which is determined by its principle. Although super lenses can realize sub-wavelength imaging, it has the great requirement for medium loss and absorption [66]. It has also been difficult to develop negative refractive index metamaterials, for the use in optical devices [67].

3.4. Single Photon Detection System

The single photon detector is the core device used for echo signal detection in a single photon LiDAR system. The main kinds of single photon detectors include photomultipliers (PMT), SPADs, and superconduct nanowire single photon detectors (SNSPD). Compared with the fragile PMT with high bias, SPAD has high quantum efficiency, small volume, low bias voltage, and low environmental requirements. SNSPD is a new technology developed in recent years, with a wide spectral response range, a high count rate and time resolution, and very low noise, which is applied in quantum communications. However, SNSPD has to work at a superconducting temperature (<4 K), which needs high-power mechanical refrigeration or liquid helium refrigeration. These supporting refrigeration devices have greatly increased the cost and volume, limiting the large-scale application. Therefore, SPAD is the mainstream single photon detector for LiDAR. However, the photon detection efficiency (PDE) of SPAD is not ideal. For example, the PDE of silicon-based SPAD is not with in the near-infrared wavelength, which limits the detection performance in the application of LiDAR. Recently, SPAD integrated with nano-structures was presented to overcome this drawback. SPAD integrated with a meta-surface not only performs well in PDE, but also holds other SPAD performance metrics well, such as dark count rate, after the pulse, and time resolution. Regardless of the influence of PDE on device structure, the SPAD structure can be independently designed to achieve low dark count rate and good time resolution. Therefore, meta-surface integration is a revolutionary technology

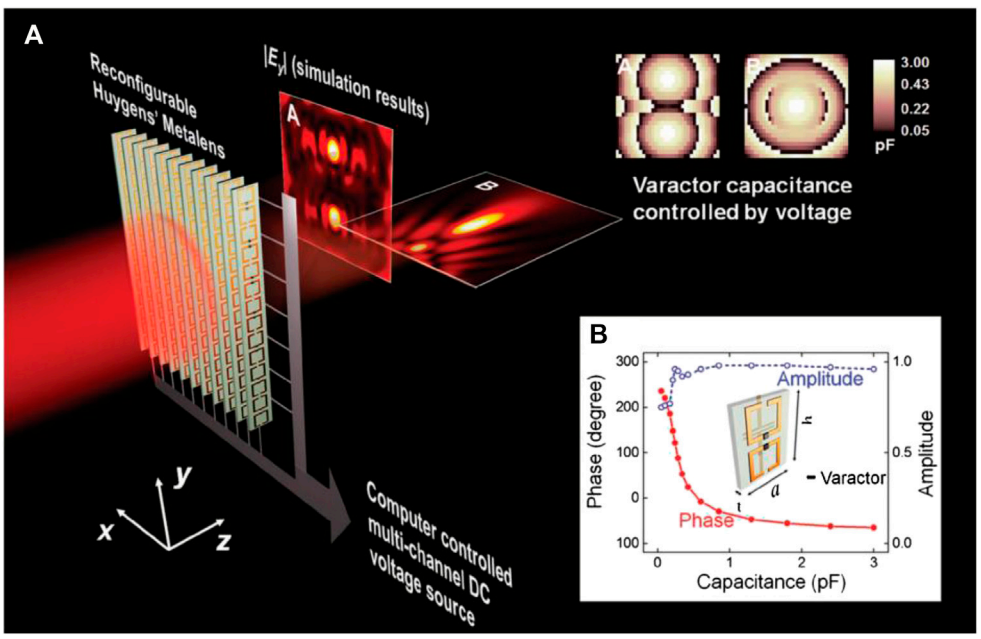

FIGURE 5 | Reconfigurable Huygens' meta lens and characteristics of meta-atom. **(A)** Active Huygens' meta lens for dynamic EM wave focusing, of which meta-atoms are biased by computer-controlled multichannel DC voltage sources. Upper-right inset: spatial distributions of capacitances used to achieve two focal spots either in *x*-*y* **(A)** or in *x*-*z* planes **(B)** based on full-wave simulation. **(B)** Capacitance-dependent phase and amplitude responses of EM wave transmission at the target frequency of 6.9 GHz for incident electric and magnetic fields which are parallel to *y*- and *x*-axes, respectively. *Source*: reproduced from Ref. 65.

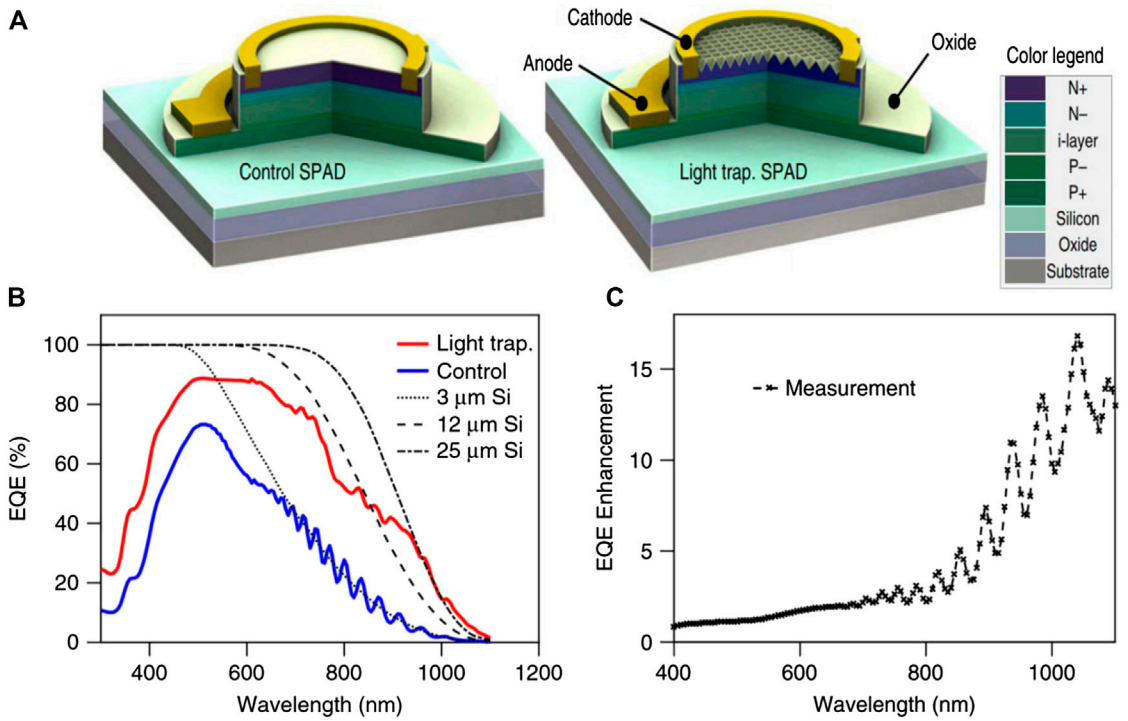

FIGURE 6 | (A) Three-dimensional (3D) cross-sectional schematics of layer configurations of control (left) and light-trapping SPADs (right). **(B)** EQE measurements of control (blue solid) and light-trapping SPADs (red solid); dashed black lines correspond to theoretical absorption of 3, 12, and 25 μm thick Si from left to right. **(C)** EQE enhancement: ratio of light-trapping SPAD EQE compared to control SPAD. *Source*: reproduced from Ref. 68.

for the development of SPAD. There are many kinds of meta-surface, including the inverse pyramid nano-structure array [68], nano cone array [69], nano pyramid array [70], nanowire arrays [71], nano dimples or convex balls array structure [72], and nanosphere shell structure array [73].

As an example of an inverse pyramid nano-structure array, a light-trapping SPAD with a typical mesa-type shallow-junction was fabricated using a complementary metal oxide semiconductor (CMOS) compatible process. Si epitaxial layers with a total thickness of 2.5 μm were grown on an SOI substrate. As shown in **Figure 6A**, the nano-structure was etched as an inverse pyramid, with an 850 nm period in a square lattice pattern. Unlike the resonance peaks found in the responsivity of resonant-cavity-enhanced (RCE) detectors, the light-trapping SPAD has broadband responsivity enhancement. The improvement of external quantum efficiency (EQE) is mainly due to the

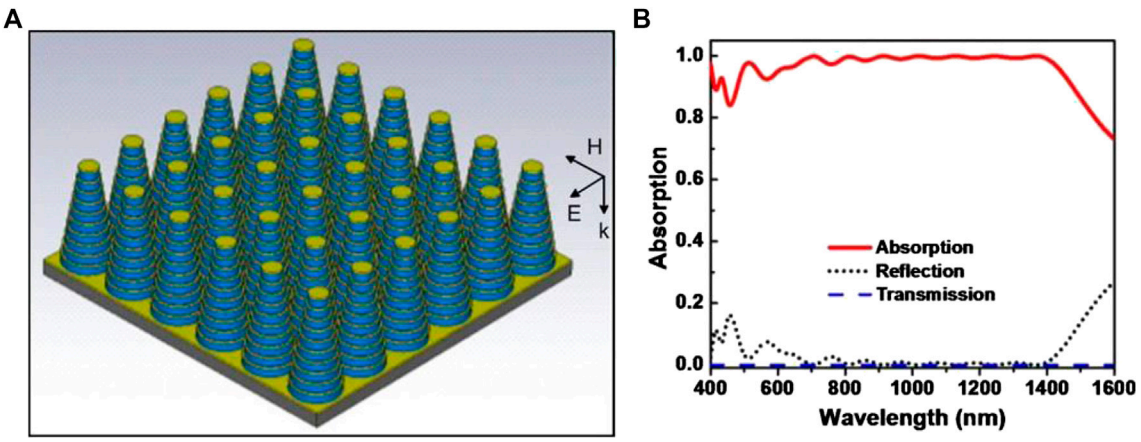

FIGURE 7 | (A) Schematic diagram of truncated cone-shaped metamaterial absorber. **(B)** The reflection, absorption, and transmission characteristics of the absorber. *Source*: reproduced from Ref. 74.

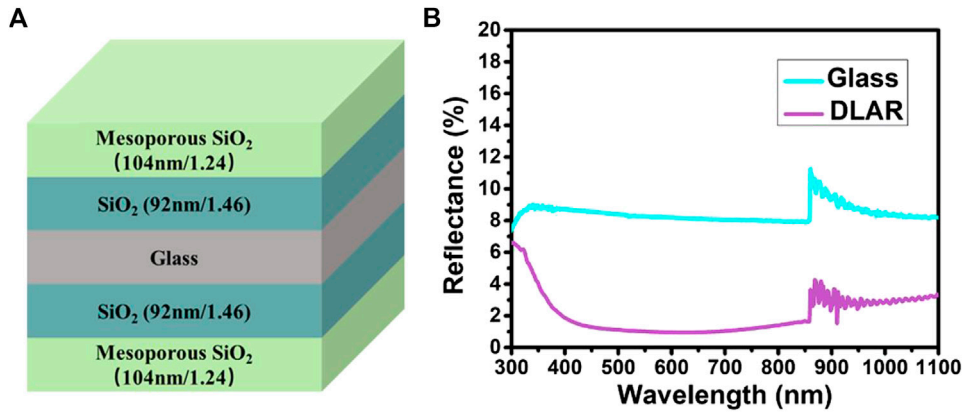

FIGURE 8 | (A) Structure of mesoporous DLAR coating. **(B)** Reflectance spectra of glass and DLAR coatings. *Source*: reproduced from Ref. 75.

enhanced anti-reflection effect and nano-structure diffraction [68]. As shown in **Figures 6B and 6C**, the enhancement effect of EQE is more obvious for longer wavelengths.

A truncated cone-shaped metamaterial absorber was designed using silicon and gold [74], as shown in **Figure 7**. This absorber can achieve an absorption bandwidth of 1,000 nm in the visible and near-infrared bands covering 480–1,480 nm. The material is a kind of multi-layer truncated cone, composed of metal dielectrics (such as gold and silicon) stacked with ultra-wideband metamaterial absorption structures arranged periodically. The number and diameter of the truncated cones in each basic unit are adjusted, and the width of the absorption band can be changed as needed. Through the interlayer exchange coupling of the electric field and the magnetic field in adjacent unit cells, the absorption efficiency can be improved. Under any severe conditions, the receiver has strong stability, the high absorption rate can still remain unchanged, and has good performance in terms of compact structure, large bandwidth, and polarization insensitivity.

Xu et al. presented a mesoporous double-layer antireflection (DLAR) coating [75]. The coating has good performance of high light transmittance and durability. It is a new type of layered structure, as shown in **Figure 8A**. The top silicon layer structure is composed of mesoporous dioxide with a pore diameter of 2–50 nm. The team prepared a metamaterial DLAR coating with an average transmittance of 99.02% in the visible light band from 380 to 780 nm (**Figure 8B**). In addition, the high porosity of the structure is conducive to obtaining a lower refractive index, which can harvest higher transmittance. With another layered structure, M. I. Fathima proposed a theoretical design of Effective Interface Antireflective coating (EIARC) which is based on the theory of Fabry-Perot-Interference filters [76]. In the anti-reflection coating, photons can be reflected multiple times to minimize reflection loss. This design is a combination of a spatial index layer and two multi-layer subsystems.

Zeng et al. designed a nanostructure fabricated by reactive ion etching (RIE) and wet etching on the surface of silicon [77]. The surface of the nanostructure is uneven, which produces multiple reflections on the surface, and forms an effective light-harvesting structure in the 300–800 nm band. As shown in **Figure 9**, the reflectivity of the nanostructure surface by wet etching (Pyramid sample) or RIE (Sample 20) is obviously lower than the blank surface. And sample 22 produced by wet etching and then RIE obtains the minimum reflectance of only 1.27%. W. Chen et al. further improved the anti-reflective properties of the nanostructures by changing reactive gas compositions comprising chlorine (Cl_2), sulfur hexafluoride (SF_6), and oxygen (O_2) for the RIE process [78].

Except physical processing technology, Chen-Chih Hsueh et. al fabricated uniform silicon nanowire (SiNW) arrays on the mono- and multi-crystalline wafers by employing the improved solution-processed metal-assisted chemical etching (MacEtch) method [79]. They demonstrated a good optical trapping effect and reflectance well below 6% over a broad wavelength range from 300 to 1,100 nm with good uniformity, as shown in **Figure 10**. The improved MacEtch concept is suitable for commercial mass production. However, it suffers from a lower effective lifetime, because the higher surface state causes higher surface recombination for the SiNW arrays wafer.

4. PROSPECT

The metamaterials technology promotes the development of the core devices of single photon LiDAR. First of all, the outstanding anti-reflective properties of the meta-surface promoted the development of SPAD with better performance matrix. The meta-surface could flexibly regulate the amplitude and phase of incident light through the subwavelength microstructure, so it has great application potential in the field of beam emission. An optical meta-surface uses the phase mutation of transmitted or reflected waves on the structural surface to effectively regulate the wave front of the incident wave, which can realize the regulation of beam deflection and polarization. In the future, the optical meta-surface could be further used to adjust waveforms to optimize beam transmission, laser amplification and frequency control, and conduct beam shaping to improve beam near-field control ability. Besides, the metamaterial lenses reveal an new industry development direction.

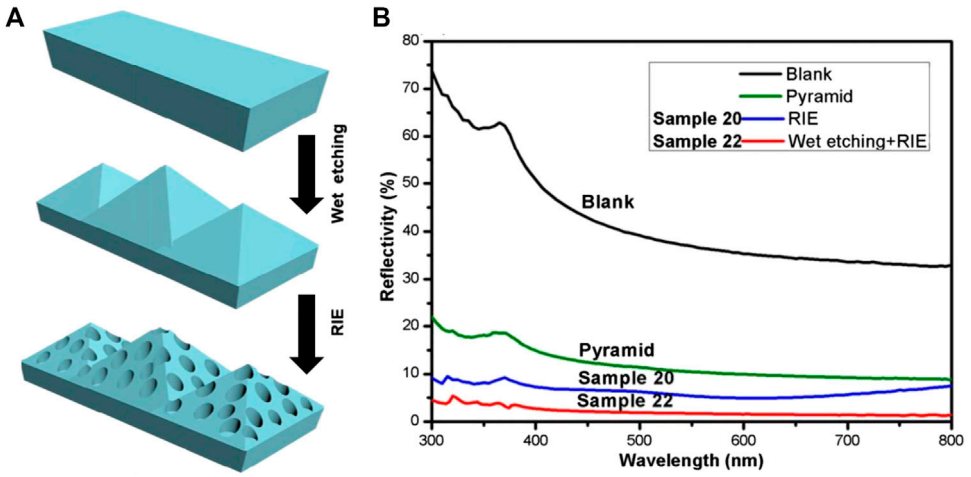

FIGURE 9 | (A) The surface of silicon etched by wet etching and RIE. **(B)** Reflectivity of different kinds of silicon surface. *Source*: reproduced from Ref. 77.

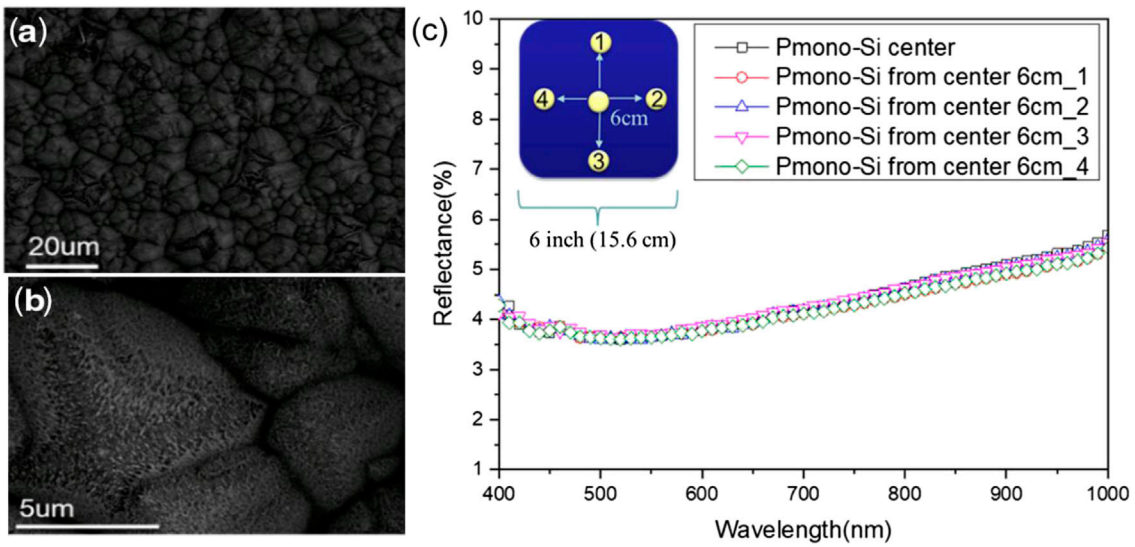

FIGURE 10 | (A,B) Pyramid/SiNW array structure on a P-type mono-crystalline wafer (top view of SEM images). **(C)** Total reflectance of different spots of 6-inch P-type mono-crystalline pyramid/SiNW array structure wafer. The inset marks the measured area at the center and 6 cm from the center. *Source*: reproduced from Ref. 79.

AUTHOR CONTRIBUTIONS

TZ is the corresponding author of the article, who lead this scientific research work and paper writing. YH contributed to the study of the performance index of single photon LiDAR, and the application of metamaterial in lenses. DX contributed to the study of the introduction and prospect part of the paper, and the application of metamaterial in lasers. ZZ contributed to the study of the basic architecture of LiDAR, and the application of metamaterial in scanning devices. YS partly contributed to the writing of the introduction of this paper (Section 1). RX partly contributed to the writing of the performance index of single photon LiDAR (Section 2). YC partly contributed to the writing of the application of metamaterial in single photon LiDAR (Section 3). YT partly contributed to the writing of the prospect part of the paper (Section 4).

FUNDING

This work was supported by the National Key R&D Program of China (Grant No. 2018YFF0215304), the National Nature Science Foundation of China (NSFC) (Grant Nos. 61904169 and 61904168), the Zhejiang Provincial Natural Science Foundation of China (Grant No. LQ18F040001), the Technique Support Program of State Administration for Market Regulation (No. 2019YJ067), and the Major Scientific Research Project of Zhejiang Lab (2019DE0KF01).

REFERENCES

1. Hou Y, Li D, Kong X, Chen S. Integrated electronic warfare-an assassin's mace in modern warfare. Beijing, China: National Defense Industry Press (2000) 56 p.
2. Nong G, Yue Y, Yang G, Sun W. Applications of satellite observation information in ocean surveillance and reconnaissance. *Ship Sci Tech* (2011) 144(z1):92–5. doi:1672-7649 (2011) S-0092-04
3. Zhang L, Liu Z, Li G, Cheng-Wen Z. Research on a new method of moving target positioning by reconnaissance missile at sea-taking compass+PD/HRLR combination as foundation. *Opt Optoelectron Technol* (2013) 11(4):77–81. doi:CNKI:SUN:GXGD.0.2013-04-017
4. Mingtao Z, Zhang J, Zhang J, Hang X, Mingjiang Z, Wang A, et al. Chaotic modulation lidar for underwater ranging. *Laser Optoelectron Prog* (2016) 53(5): 232–9. doi:10.3788/LOP53.051402
5. Fu C, Fang L, Xie L, Wang Y. Prototype design and water-land joint survey test of airborne dual-frequency lidar. *J PLA Univ Sci Tech* (2016) 17(6):520–5. doi:10.12018/j.issn.1009-3443.20160425003
6. Liu C, Mao Q, Chu X, Xie S, Wang F, Yan B. *The invention relates to a shipborne wave dynamic measuring device based on lidar*. CN109490906A (2019).
7. Jian H. *Research on detection of submarine through short scale ocean waves using a streak tube imgaging LiDAR*. Harbin, China: Harbin Institute of Technology (2014)
8. Wang C, Kong B, Yang J, Wang Z, Zhu H. An algorithm for road boundary extraction and obstacle detection based on 3D Lidar. *Pattern Recognit Artif Intell* (2020) 33(4):353–62. doi:10.16451/j.cnki.issn1003-6059.202004008
9. Yu A, Stephen MA, Li SX, Shaw GB, Seas A, Dowdye E, et al. Space laser transmitter development for ICESat-2 mission. *Proc SPIE* (2010) 7578:757809. doi:10.1117/12.843342
10. He S. *Linear light source terrain detection Sharm lidar*. CN207037090U (2018)
11. Qu S, Zhang X, Zhu C, Huo L, Liu H. Design and test of airborne LiDAR system for forest resources survey. *J Northwest For Univ* (2018) 33(4):175–82. doi:10.3969/j.issn.1001-7461.2018.04.29
12. Shangyong G, Xiong H, Zhaoai Y, Yongqiang C, Wenjie G, et al. Research development of space-borne lidar in foreign countries. *Laser Technol* (2016) 40(5):772–8. doi:10.7510/jgjs.issn.1001-3806.2016.05.032
13. Wu D, Wang J, Yan F. Estimation of air-sea gas transfer velocity using the CALIPSO lidar measurements. *Acta Opt Sin* (2012) 32(9):270–8. doi:10.3788/AOS201232.0928001
14. Shen F, Sun D, Wang Z, Xianghui X, Tingdi C, Xiankang D. Beam scanning and wind inversion technique of a Mobile Doppler Lidar. *Acta Opt Sin* (2012) 32(3):1–5. doi:10.3788/AOS201232.0312004
15. Zhang N, Bao X, Li H. Intelligent vehicle obstacle recognition based on lidar and camera fusion. *Sci Technol Eng* (2020) 20(4):1461–6. doi:CNKI:SUN:KXJS.0.2020-04-025
16. Zuang J, Jiao N, Yin F. Application of MMW radar and lidar in mass. *Ship Eng* (2019) 41(11):79–82. doi:10.13788/j.cnki.cbgc.2019.11.15
17. Bi X. *Lidar-based unmanned ship slam obstacle avoidance technology*. Dalian, China: Dalian Maritime University (2019).
18. Lai W, Liu Z, Ji K, Xu L, Zhang B. System design of autonomous patrol UAV based on lidar. *Microcontrollers Embedded Syst* (2020) 20(5):37–40. doi:CNKI:SUN:DPJY.0.2020-05-012
19. Quan Y, Li M, Zhen Z, Yuanshuo H. Modeling crown characteristic attributes and profile of larix olgensis using UAV-borne lidar. *J Northeast For Univ* (2019) 47(11):52–28. doi:10.13759/j.cni.dlxb.2019.11.011
20. You W, Chen D, Zeng Q. Research status of chemical warfare agent remote detection system in air force airfield. Proceedings of the 5th chemical prevention symposium of the Chinese Chemical Society. Kunming, China: Chinese Chemical Society (2001). p. 571–5.
21. Liu L, Cai X, Qiao L. Research of active imaging guiding lidar system. *Infrared Laser Eng* (2000) 29(2):36–40
22. Wu J, Pu G, Shen H, Yang X, Bu X. Analysis and research of laser ranging technology based on core instruments detection of SPAD. *Laser J* (2019) 40(9): 29–33. doi:10.3969/j.issn.1007-2276.2014.02.008
23. Ma J. *Design of single photon avalanche diodes*. Hefei, China: University of Science and Technology of China (2016).
24. Liu C, Chen Y, He W, Gu G, Chen Q. *Simulation and accuracy analysis of single photon ranging system*. *Infrared Laser Eng* (2014). 2(6):382–387. doi:10.3969/j.issn.1007-2276.2014.02.008
25. Zeng X, Song L, Wang J. *Detection simulation of dangerous space debris based on spaceborne single photon radar*. Science Technology and Engineering (2017). 17(10):219–224. doi:10.3969/j.issn.1671-1815.2017.10.038
26. Fu Z, Lin Y. Method to improve accuracy of pulse laser ranging. *Electro-Optic Tech Appl* (2011). 15(2):21–22. doi:10.3969/j.issn.1003-0522.2017.15.010
27. Radar Communication. The relationship between radar parameter measurement accuracy and resolution (2018) Available from: https://www.sohu.com/a/234896120_695278.
28. Lidar. Depth analysis of unmanned lidar (2018) Available from: https://www.sohu.com/a/227001488_100109901.
29. Liu J. *Design and performance study of single-photon detectors based on InGaAs(P)/InP APDs*. Jinan, China: Shandong university (2018).
30. Shangguan M. *Laser remote sensing with 1.5μm single photon detectors*. Hefei, China: University of Science and Technology of China (2017).
31. Liu Y. *Research on multiwavelength dispersion characteristics of optical metasurfaces*. Jinan, China: Shandong university (2019).
32. Qiao J, Mei F, Ye Y. Single-photon emitters in van der Waals materials. *Chin Optic Lett* (2019) 17:020011. doi:10.3788/COL201917.020011
33. Han X, Feng L, Li Y, Zhang L, Song J, Zhang Y. Experimental observations of boundary conditions of continuous-time quantum walks. *Chin Optic Lett* (2019) 17:052701. doi:10.3788/COL201917.052701
34. Amin MZ, Qureshi KK, Hossain MM. Doping radius effects on an erbium-doped fiber amplifier. *Chin Optic Lett* (2019) 17:010602. doi:10.3788/COL201917.010602
35. Lee HJ, Park HS. Generation and measurement of arbitrary four-dimensional spatial entanglement between photons in multicore fibers. *Photon Res* (2019) 7: 19–27. doi:10.1364/PRJ.7.000019
36. Curic D, Giner L, Lundeen JS. High-dimension experimental tomography of a path-encoded photon quantum state. *Photon Res* (2019) 7:A27–A35. doi:10.1364/PRJ.7.000A27
37. Rusby DR, Armstrong CD, Scott GG, King M, McKenna P, Neely D. Effect of rear surface fields on hot, refluxing and escaping electron populations via numerical simulations. *High Power Laser Sci Eng* (2019) 7(3):e45. doi:10.1017/hpl.2019.34
38. Pan KQ, Yang D, Guo L, Li ZC, Li SW, Zheng CY, et al. Enhancement of the surface emission at the fundamental frequency and the transmitted high-order harmonics by pre-structured targets. *High Power Laser Sci Eng* (2019) 7(2):e36. doi:10.1017/hpl.2019.20
39. Yao J. All solid state laser and nonlinear optical frequency conversion technology. Beijing, China: World Sci-Tech R & D (2002) 10 p.
40. Liu X, Deng J, Tang Y. Nonlinear photonic metamaterials. *Materials China* (2019) 38(4):342–51. doi:10.7502/j.issn.1674-3962.2019.04.03
41. Liu X, Tang J, Zhang Y. Nonlinear photonic metamaterials. Available from: https://kc.sustech.edu.cn/handle/2SGJ60CL/62527?mode=full&submit_simple=Show+full+item+record.
42. Sun Y, Duan Y, Cheng M. Triple wavelength-switchable lasing in yellow-green based on frequency mixing of self-Raman operation. *Acta Phys Sin* (2020) 69(12):124201. doi:10.7498/aps.69.20200324
43. Liu P, Wang T. Multi-wavelength thulium-doped mode-locking fiber laser based on nonlinear polarization rotation. *Photon Sin* (2016) 45(6):12–6. doi:10.3788/gzxb20164506.0614003
44. Sroor H, Huang YW, Sephton B. High-purity orbital angular momentum states from a visible metasurface laser. *Nat Photon* (2020) 14:498–503. doi:10.1038/s41566-020-0623-z
45. Eesa R, Kursat S. Femtosecond pulse shaping by ultrathin plasmonic metasurfaces. *J Opt Soc Am* (2016) 33(2):A1–7. doi:10.1364/JOSAB.33.0000A1
46. Xue H, Long L. Orbital angular momentum generation technology and its research progress in the field of radar imaging. Proceedings National antenna conference. Chengdu, China: Antenna Branch of China Electronics Association (2017).
47. Liang C. *Research on the focusing characteristics and application of vortex beams*. Guangzhou, China: South China Normal University (2011).
48. Chen Y, Dong X. Research on radar correlation imaging technology based on orbital angular momentum. *Electron Design Eng* (2018) 6(2): 109–14. doi:10.3969/j.issn.1674-6236.2018.06.024
49. Han J, Intaravanne Y, Ma A, Wang R, Li S, Li Z, et al. Optical metasurfaces for generation and superposition of optical ring vortex beams. *Electron Design Eng* (2020) 14:2000146. doi:10.1002/lpor.202000146

50. Tang D, Chen L, Jia L, Zhang X. Achromatic metasurface doublet with a wide incident angle for light focusing. *Optics Express* (2020) 38:392197. doi:10.1364/OE.392197
51. Kun L, Chase C, Rao Y, Chang-Hasnain CJ. Widely tunable 1060-nm high-contrast grating VCSEL. Compound semiconductor week; 2016 Jun 26–30; Toyama, Japan. IEEE (2016). p. 1–2
52. Bai X. *Application status and prospect of lidar technology*. Beijing, China: Beijing Institute of Technology (2015).
53. Roy T, Zhang S, Jung IW, Troccoli M, Capasso F, Lopez D. Dynamic metasurface lens based on MEMS technology. *APL Photon* (2017) 3: 021302. doi:10.1063/1.5018865
54. Özdemir A, Hayran Z, Takashima Y, Kurt H. Polarization independent high transmission large numerical aperture laser beam focusing and deflection by dielectric Huygens' metasurfaces. *Opt Commun* (2017) 401:46–53. doi:10.1016/j.optcom.2017.05.031
55. Lesina AC, Goodwill D, Eric B, Lora R, Berini P. Optical beam steering for LIDAR via tunable plasmonic metasurface. *IEEE J Sel Top Quant Electron* (2020) 27(1):9166964. doi:10.1109/PN50013.2020.9166964
56. He F, MacDonald KF, Fang X. Continuous beam steering via controlling light with light on a dielectric metasurface. 2019 conference on lasers and electro-optics Europe & European quantum electronics conference; 2019 Oct 17; Munich, Germany. IEEE (2019) 1 p.
57. Xiao J. *Application of metamaterial on beamscanning of microstrip leaky wave antenna*. Chengdu, China: School of Physical Electronics (2015).
58. Qi M. *Manipulations of electromagnetic waves by metamaterial lens and metasurface and their applications*. Nanjing, China: Southeast University (2016).
59. Lin DM, Fan PY, Hasman E, Brongersma ML. Dielectric gradient metasurface optical elements. *Science* (2014) 345(6194):298–302. doi:10.1126/science.1253213
60. Capasso F. Metalenses at visible wavelengths: diffraction-limited focusing and subwavelength resolution imaging. *Science* (2016) 352(6290):1190–4. doi:10.1126/science.aaf6644
61. Shrestha S, Overvig AC, Lu M, Stein A, Yu N. Broadband achromatic dielectric metalenses. *Light Sci Appl* (2018) 7:85. doi:10.1038/s41377-018-0078-x
62. Li T, Chen C, Zhu S. A new method of tomography based on spherical aberration (2019) CN109752842A.
63. Li T, Chen C, Zhu S, Wang S, Zhu S. Optical zoom method based on superstructure lens using wavelength regulation (2018) CN108241208A.
64. Jin M. *Design and implementation of colorful display and metalens based on optical metasurfaces*. Harbin, China: Harbin Industrial University (2019) .
65. Chen K, Feng Y, Monticone F, Zhao J, Zhu B, Jiang T, et al. A reconfigurable active huygens metalens. *Adv Mater* (2017) 29(17):1606422. doi:10.1002/adma.201606422
66. Jia L. *Application of metamaterial in optical transmission*. Nanjing, China: Nanjing University of Aeronautics and Astronautics (2014) .
67. Liu X. Negative refractive index metamaterials to achieve light enhancement eliminate the related research and development of the main obstacles. *Opt Instrum* (2010) 4(1):57–57. doi:CNKI:SUN:GXYQ.0.2010-04-017
68. Zang K, Jiang X, Huo Y, Ding X, Morea M, Chen X, et al. Silicon single-photon avalanche diodes with nano-structured light trapping. *Nat Commun* (2017) 8: 628. doi:10.1038/s41467-017-00733-y
69. Li Q, Gao J, Li Z, Yang H, Liu H, Wang X, et al. Absorption enhancement in nanostructured silicon fabricated by self-assembled nanosphere lithography. *Opt Mater* (2017) 70:165–70. doi:10.1016/j.optmat.2017.05.036
70. Qi H. *Study of nanophotonic structures based perfect absorbers*. Chengdu, China: University of Electronic Science and Technology of China (2015) .
71. Gong L. *The research on irregular nanowire array solar cells*. Beijing, China: Beijing University of Posts and Telecommunications (2016).
72. Zang K, Ding X, Jiang X, Huo Y, Morea M, Chen X, et al. Surface textured silicon single-photon avalanche diode. 2017 conference on lasers and electro-optics (CLEO); 2017 May 14–19; San Jose, CA. IEEE (2017) p. 1–2. Available from: https://ieeexplore.ieee.org/stamp/stamp.jsp?tp=&arnumber=8084082
73. Chen Y. *Research on optimal design and application of perfect absorber based on surface plasmon resonance*. Chengdu, China: China Academy of Engineering Physics (2018).
74. Hoa NTQ, Lam PH, Tung PD, Tuan TS, Nguyen H. Numerical study of a wide-angle and polarization-insensitive ultrabroadband metamaterial absorber in visible and near-infrared region. *IEEE Photon J* (2016) 11(1): 4600208. doi:10.1109/JPHOT.2018.2888971
75. Xu Y, Zhang J, Ai L, Lou X, Lin S, Lu Y, et al. Fabrication of mesoporous double-layer antireflection coatings with near-neutral color and application in crystalline silicon solar modules. *Sol Energy* (2020) 201:149–56. doi:10.1016/j.solener.2020.02.098
76. Ismail Fathima M, Joseph Wilson KS. Efficiency enhancement of silicon solar cell using effective Interface face method in antireflective coating layers. *Int J Mod Phys C* (2020) 31:1–7. doi:10.1142/S012918312050076X
77. Zeng Y, Fan X, Chen J, He S, Yi Z, Ye X, et al. Preparation of composite micro/nano structure on the silicon surface by reactive ion etching: enhanced anti-reflective and hydrophobic properties. *Superlattices Microstruct* (2018) 117: 144–154. doi:10.1016/j.spmi.2018.03.035
78. Chen WH, Hong FCN. 0.76% absolute efficiency increase for screen-printed multicrystalline silicon solar cells with nanostructures by reactive ion etching. *Sol Energy Mater Sol Cells* (2016) 157:48–54. doi:10.1016/j.solmat.2016.05.046
79. Hsueh C-C, Thiyagu S, Liu C-T, Syu H-J, Yang S-T, Lin C-F. Application of silicon nanostructure arrays for 6-inch mono and multi-crystalline solar cell. *Nanoscale Res Lett* (2019) 14:212. doi:10.1186/s11671-019-3030-y

Conflict of Interest: The authors declare that the research was conducted in the absence of any commercial or financial relationships that could be construed as a potential conflict of interest.

frontiers in Physics

REVIEW
published: 29 January 2021
doi: 10.3389/fphy.2020.586087

A Review on Metasurface: From Principle to Smart Metadevices

*Jie Hu, Sankhyabrata Bandyopadhyay, Yu-hui Liu and Li-yang Shao**

Department of Electrical and Electronic Engineering, Southern University of Science and Technology, Shenzhen, China

Metamaterials are composed of periodic subwavelength metallic/dielectric structures that resonantly couple to the electric and magnetic fields of the incident electromagnetic waves, exhibiting unprecedented properties which are most typical within the context of the electromagnetic domain. However, the practical application of metamaterials is found challenging due to the high losses, strong dispersion associated with the resonant responses, and the difficulty in the fabrication of nanoscale 3D structures. The optical metasurface is termed as 2D metamaterials that inherent all of the properties of metamaterials and also provide a solution to the limitation of the conventional metamaterials. Over the past few years, metasurfaces; have been employed for the design and fabrication of optical elements and systems with abilities that surpass the performance of conventional diffractive optical elements. Metasurfaces can be fabricated using standard lithography and nanoimprinting methods, which is easier campared to the fabrication of the counterpart 3 days metamaterials. In this review article, the progress of the research on metasurfaces is illustrated. Concepts of anomalous reflection and refraction, applications of metasurfaces with the Pancharatanm-Berry Phase, and Huygens metasurface are discussed. The development of soft metasurface opens up a new dimension of application zone in conformal or wearable photonics. The progress of soft metasurface has also been discussed in this review. Meta-devices that are being developed with the principle of the shaping of wavefronts are elucidated in this review. Furthermore, it has been established that properties of novel optical metasurface can be modulated by the change in mechanical, electrical, or optical stimuli which leads to the development of dynamic metasurface. Research thrusts over the area of tunable metasurface has been reviewed in this article. Over the recent year, it has been found that optical fibers and metasurface are coagulated for the development of optical devices with the advantages of both domains. The metasurface with lab-on fiber-based devices is being discussed in this review paper. Finally, research trends, challenges, and future scope of the work are summarized in the conclusion part of the article.

Keywords: metasurface, wavefront modulation, flexible metasurface, reconfigurable metasurface, meta-device, lab on fiber

OPEN ACCESS

Edited by:
Xufeng Jing,
China Jiliang University, China

Reviewed by:
Jifeng Liu,
Dartmouth College, United States
Venu Gopal Achanta,
Tata Institute of Fundamental Research, India

****Correspondence:***
Li-yang Shao
shaoly@sustech.edu.cn

Specialty section:
This article was submitted to Optics and Photonics, a section of the journal Frontiers in Physics

Received: *22 July 2020*
Accepted: *30 September 2020*
Published: *29 January 2021*

Citation:
Hu J, Bandyopadhyay S, Liu Y, Shao L (2021) A Review on Metasurface: From Principle to Smart Metadevices. Front. Phys. 8:586087. doi: 10.3389/fphy.2020.586087

INTRODUCTION

Over the past 2 decades, metamaterials [41, 192] have attracted lots of interests owing to their remarkable electromagnetic features. Metamaterials are arrays of special-shaped scattering elements rationally designed, and exhibit some special electromagnetic responses, for instance, negative-index media [139, 143], zero-index materials [196] and ultra-high-index materials [117, 136]. The two-dimensional counterpart of metamaterials, metasurface [74, 104, 107] is much easier to be fabricated and utilized. It can exhibit the amazing capacity of electromagnetic wavefront manipulation, which is mainly introduced by the interaction between an electromagnetic wave and these meta-atoms structures as well as their functional arrangements. Over recent years, metasurface paradigm is considered as an important way to engineer electromagnetic wave, including wavefront shaping [63, 162], polarization conversion [168, 194]and radiation control or energy concentration [18, 79]. With these versatile electromagnetic properties, metasurface has attracted enormous attention from the research communities. Based on strong wavefront modulation capability of metasurface within the sub-wavelength scale, many mete-devices have been demonstrated in the last ten years, such as meta-lens [16, 21, 94, 155], invisible cloak [50, 126], absorber [52, 98, 169], vortex beam generator [176], holography [43, 113, 193] and so on.

it was observed that the dynamic performance of the metasurface is essential for modern-day science and technological applications but conventional metasurface limits its operation in terms of tunability and reconfiguration. Conventional metasurface provides static and predefined optical functions that are normally being governed by the geometry, shape, and arrangements of meta-atoms. Over the past few years researchers put an effort to develop flexible and reconfigurable metasurfaces, where the shape, size, and arrangements of the meta-atoms can be tuned or altered with external stimuli [33, 45, 85]. And many researchers are devoting themselves to access reprogrammable metasurface [83, 87, 103].

Progressive research on metasurface has enormously expanded its application domain over the past decade or so. In this article, a primary focus is being given to the applications of metasurface through wavefront engineering. We have reviewed recent works in the area of metasurface based arbitrary wavefront modulation, and in due course, the review is being extended with flexible and reconfigurable metasurface and meta-devices. The principles of operation of the device, applications along with their extraordinary advantages, fabrication challenges, and prospects are being discussed in a detailed manner. In the aspect of fabrication of new and novel optical devices, metasurface and optical fiber integrated [124, 125] for the development of novel "lab-on-fiber" structures are also illustrated in this paper, which possess enormous potentials for future applications. The review work is concluded with a summarization of the challenges and prospects of this research area.

THE PRINCIPLE OF METASURFACE FOR WAVEFRONT MODULATION

The regulation of electromagnetic waves with traditional optical components, such as lenses and prisms, is realized through the accumulation of phase delay in the process of light propagation, which greatly limits the reduction and integration of optical devices. Control of phase and amplitude plays a crucial part in wavefront modulation. Those traditional optical elements, as well as diffractive elements such as gratings and holograms, are bulky for optical set-up. Whereas, metasurface can modify the amplitude and impart an abrupt phase shift to the incident wave within the sub-wavelength scale through the light-matter interaction, and thus realize the wavefront modulation much more efficiently. In the past few years, several excellent review papers have summarized the development of this field [34, 165]. There are three main types of mechanism for metasurface to manipulate the phase variation under certain polarization states, including resonances with linearly polarized (LP) light, Pancharatnam–Berry (PB) phase for circularly polarized (CP) light, and Huygens' principle with polarization independence [146].

Wavefront Engineering of Linearly Polarized Light

Fermat's principle states that light travels along an extremum path. In 2011, Nanfang Yu et al. put forward generalized laws of refraction and reflection in succession, adapted Fermat's principle to a larger class of interfaces where the presence of antennas may provide abrupt phase jump to incident waves [176]. They derived the general relation between an incident and scattered waves as

$$\begin{cases} n_t \sin(\theta_t) - n_i \sin(\theta_i) = \dfrac{\lambda_0}{2\pi} \dfrac{d\phi(x)}{dx} \\ n_i \sin(\theta_r) - n_i \sin(\theta_i) = \dfrac{\lambda_0}{2\pi} \dfrac{d\phi(x)}{dx} \end{cases} \tag{1}$$

where n_i and n_t are the refractive indices on the two sides of the interface, λ_0 is the free space wavelength, θ_i, θ_r and θ_t are the incident, reflected, and transmitted angles, as shown in **Figure 1A**, and $d\phi/dx$ indicates the gradient of the phase discontinuity along with the interface, provided by the meta-atoms of the metasurface. **Equation 1** implies that both the refracted and reflected beam can have an arbitrary direction, provided that a suitable constant gradient of phase discontinuity along the interface ($d\phi/dx$) is introduced. By engineering a phase discontinuity along an interface, one can fully steer light and accomplish unparalleled control of anomalous reflection and refraction described by the generalized Snell's law. Implementation of this idea was accomplished by V-shaped gold nanoantennas which were used as a gradient metasurface. As shown in **Figure 1B**, V-shaped resonators support "symmetric" and "antisymmetric" modes, which are excited by electric-field components along ŝ and â axes, respectively. By changing the length and the opening angle of plasmonic nanorods, one can get an abrupt phase shift over a π phase range as well as different amplitudes, as shown in **Figure 1C**.

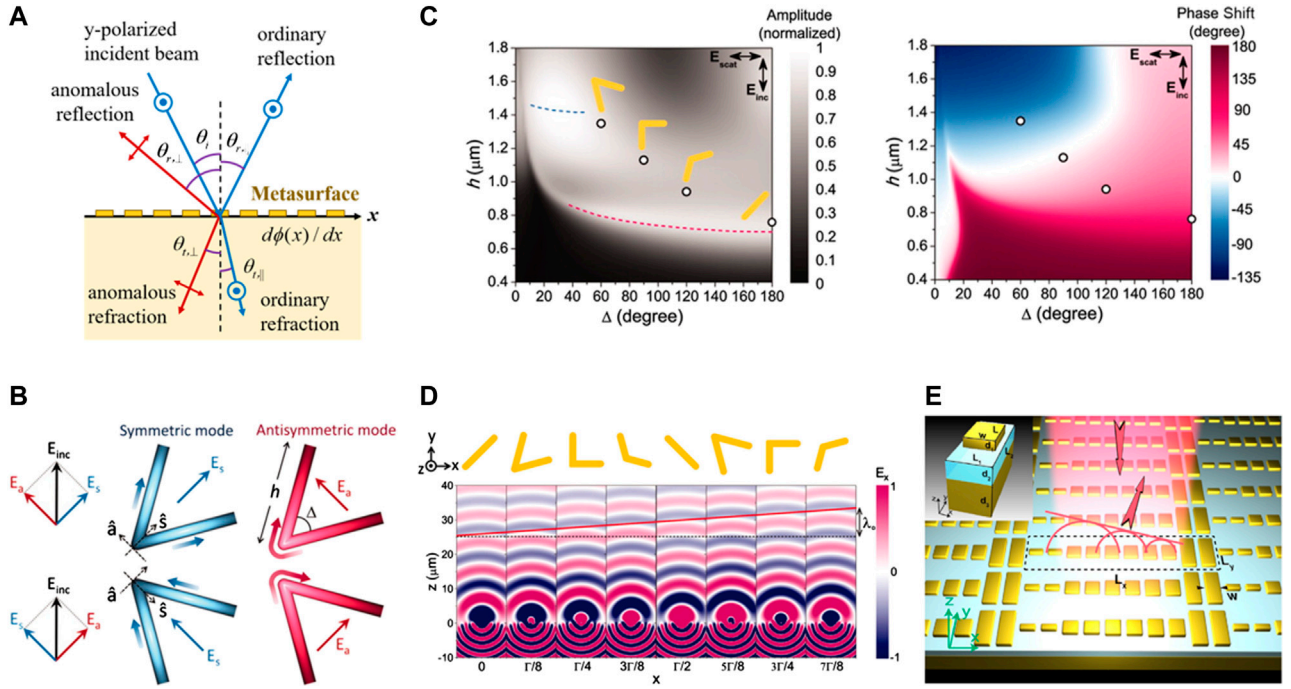

FIGURE 1 | (A) Generalized Snell's law of refraction and reflection: Schematic of anomalously refracted and reflected beams for cross-polarized scattered beams. **(B)** V-shaped nanoantenna supports symmetric and antisymmetric modes, which are excited by cross-polarized components of the incident light. There is a π phase difference between the mirror structures [176]. **(C)** Simulated amplitude and phase shift of the cross-polarized scattered light for V-shaped nanoantennas with different length and opening angle of gold nanorods at wavelength of 8 μm [176]. **(D)** Anomalous refraction phenomenon caused by phase discontinuities with a gradient metasurface consisting of V-shaped nanoantenna array [176]. **(E)** Anomalous refraction phenomenon caused by metasurface operating in reflection with a back ground plane [141]. Figure reproduced with permission from: **(B)**–**(D)**, © 2011, American Association for the Advancement of Science (AAAS); **(E)**, © 2012, American Chemical Society (ACS).

However, to achieve full phase regulation, the phase shift range must be no less than 2π phase coverage. Yu et al. realized that, for linearly polarized incident light, a 90° rotation of the V-shaped antennas allowed the remaining π range to be accessed in the cross-polarized scattered waves [111, 175, 176]. As shown in **Figure 1D**, if each second source at a position x of the interface carries an abrupt phase variation over 2π phase coverage, the abnormal refraction and reflection can be observed. Reference to the theory of gradient metasurface, many other structure designs such as C-shaped antennas [96], nanorods [58] and nanobricks [121], were proposed later and demonstrated to have full phase control capability. What's more, by adjusting the size of the unit cell, these electromagnetic responses were achieved in different frequency ranges, such as visible-band [93], near-infrared [74] and mid-infrared frequencies [176]. However, these proposed designs were realized by cross-polarized components coupled to the scattering field. The maximum coupling efficiency between the two polarizations was extremely limited within a single metasurface, and thus, only a small amount of incident electromagnetic energy can interact with the metasurface while a large amount of energy radiated outside in an ordinary way [109]. In order to improve the efficiency, gradient metasurfaces operating in reflection with a back ground plane were proposed [121, 122, 141], as shown in **Figure 1E**. This type of metasurface consisted of metallic nanoantennas array separated from a metallic ground film with a thin dielectric layer, namely Metal-Insulator-Metal (MIM) structures. Thanks to the strong coupling between the top antennas layer and the ground metallic plane, magnetic resonances as gap modes inside the dielectric spacer were excited, and thus phase delay up to 2π can be achieved.

Modualtion of Circularly Polarized Light Through Pancharatnam–Berry Phase

The metasurfaces discussed in the previous subsection are designed for linearly polarized waves, which is incapable for controlling CP waves. Recently, Pancharatnam–Berry phase metasurfaces [57] attracted intense attention due to their strong capabilities in modulating CP waves. Consider two arrays of identical scattering elements placed on the x-y plane, and the structures in one group are rotated at an angle of θ with respect to the counterparts in the other group. Then illuminating the two scatter arrays by the same CP beam, only one difference can be observed between the spin-flipped components of waves scattered by these two arrays of meta-atoms, which is a phase factor $e^{i2\theta}$, independent of the scatter details and the frequency. This phenomenon is called PB phase, which can be created by any anisotropic optical antennas. From the mathematical derivation, assuming that the incident CP wave is left-handed circular

polarized (LCP) light $E_i = E_{LCP} = \begin{pmatrix} 1 \\ i \end{pmatrix}$ (or = $E_{RCP} = \begin{pmatrix} 1 \\ -i \end{pmatrix}$ for right-handed circular polarized (RCP) light), the scattered light E_s from an anisotropic antenna with an orientation angle of θ can be described as Refs. 49 and 174.

$$E_s = \begin{pmatrix} \cos\theta & -\sin\theta \\ \sin\theta & \cos\theta \end{pmatrix} \begin{pmatrix} t_o & 0 \\ 0 & t_e \end{pmatrix} \begin{pmatrix} \cos\theta & \sin\theta \\ -\sin\theta & \cos\theta \end{pmatrix} \times E_i = \frac{t_o + t_e}{2} E_{LCP} + \frac{t_o - t_e}{2} \exp(\pm i2\theta) E_{RCP} \quad (2)$$

where t_o and t_e are the scattering coefficients for the two orthogonal linear polarization components of the incident light along the two axes of the scattering elements. From the **Eq. 2**, it is clear that the scattered light consists of two circular polarization states: one component has the same handedness as the incident CP beam without any phase delay (as shown by the first term of the above equation), and the other component is cross-polarization with a phase delay of $\pm 2\theta$ (as shown by the second term of the above equation). The sign "+" and "−" represent the phase delay for the incident LCP and RCP light, respectively, as shown in **Figure 2A** [57]. Because the phase delay is linear to the orientation angle of the scattering elements, it can provide continuous phase control from 0 to 2π very easily, by rotating the anisotropic meta-atoms from 0 to π, such as C-shaped split-ring resonators, nanorods, and nanoslits [58, 145, 179]. Although PB phase metasurface can regulate CP beams, the conversion efficiencies of earlier published works were very low. It was demonstrated that the maximum conversion efficiency of a single layer ultrathin PB phase metasurface was limited by 25% [31]. To improve the working efficiency, MIM structures working in reflection style were proposed and proved to be an effective approach [193]. On the other hand, if the metasurface contains both electric and magnetic resonators, resulting in constructive interference at the transmission side and destructive interference at the reflection side, and thus a transmissive ultrathin PB metasurface with an ultra-high efficiency can be achieved [102] as shown in **Figure 2B**.

Huygens' Principle With Polarization Independence

Different from those designs based on phase compensation on different polarization states mentioned above, Huygens' metasurface considers the impedance matching on the interface with polarization insensitivity [116], and simultaneous excitation of electric and magnetic dipole moments are achieved. According to the surface equivalence principle [116, 133], it was understood that both electric and magnetic surface currents were required on the interface to create the desired field distribution and meet the boundary conditions, as shown in **Figure 2C**. Consequently [116],

$$\begin{cases} \vec{J}_s = \hat{n} \times \left(\vec{H}_2 - \vec{H}_1 \right) \\ \vec{M}_s = -\hat{n} \times \left(\vec{E}_2 - \vec{E}_1 \right) \end{cases} \quad (3)$$

where $\vec{J}_s$ and $\vec{M}_s$ are the required electric and magnetic surface currents. The specially designed subwavelength metallic texture was usually fabricated on the dielectric substrate to get the required surface impedance of each unit. A general method was proposed to convert the desired transmission/reflection phase distributions to the required surface profiles of Huygens' metasurface [108]. Minimization of the transmission loss was accomplished by high contrast transmits/reflect arrays and it was developed by using a significant high index layer [4, 5].

In particular, metallic metasurface has a large ohmic loss in optical frequencies, which significantly limits and even degrades its performance. Thus, in this regime, high-index dielectric resonators with low loss (dielectric metasurface) was a hot topic in this decade [6, 93, 167, 177]. Electric and magnetic resonances are excited in dielectric metasurface, which can be classified as Mie resonances [36, 39, 53, 115], replacing the plasmonic resonances in metallic counterparts, and thus cause the dielectric metasurface to produce electromagnetic response, including amplitude modulation, abrupt phase jump production and so on [4, 134].

THE APPLICATIONS: WAVEFRONT ENGINEERING WITH METASURFACE

Since the advent of the metasurface, it has demonstrated excellent wavefront shaping ability, which makes it a promising application in many fields. After sorting the theory and techniques of metasurface to control the phase and amplitude under different polarization states, a detailed review of their applications in the domain of photonics devices is being discussed in this section.

Meta-Lens

Metasurface can provide abrupt phase mutations to incident electromagnetic waves within sub-wavelength scales. In the previous section, we have discussed the abnormal refraction and reflection of incident light caused by these abrupt phase variations along the interface of the two medium. The light beam can be twisted, focused; and special optical beams like optical vortex beam [10, 134, 178], and Bessel beam [14] can be generated with a controlled phase profile of the metasurface. Phase profile engineering is the basic tool that has being used over the years to control the shape of the incident wave and a detailed discussion over creation of the phase profile for meta-lens are being given in this section.

Assuming the electromagnetic energy was focused at a distance of "*f*", as shown in **Figure 3A**, the phase distribution (in the x-y plane) for transmitted or reflected wave should be arranged as the **Eq. 4** below [174] to compensate for the optical path difference:

$$\phi(x, y) = \frac{2\pi}{\lambda} \left(\sqrt{x^2 + y^2 + f^2} - f \right) \quad (4)$$

Based on the concept of optical phase discontinuities, Capasso et al. demonstrated a meta-lens at Telecom wavelength with V-shaped nanoantennas, as shown in **Figure 3A** [2]. However, the focusing efficiency was approximately 1% only. Complementary V-shaped apertures were also proposed to

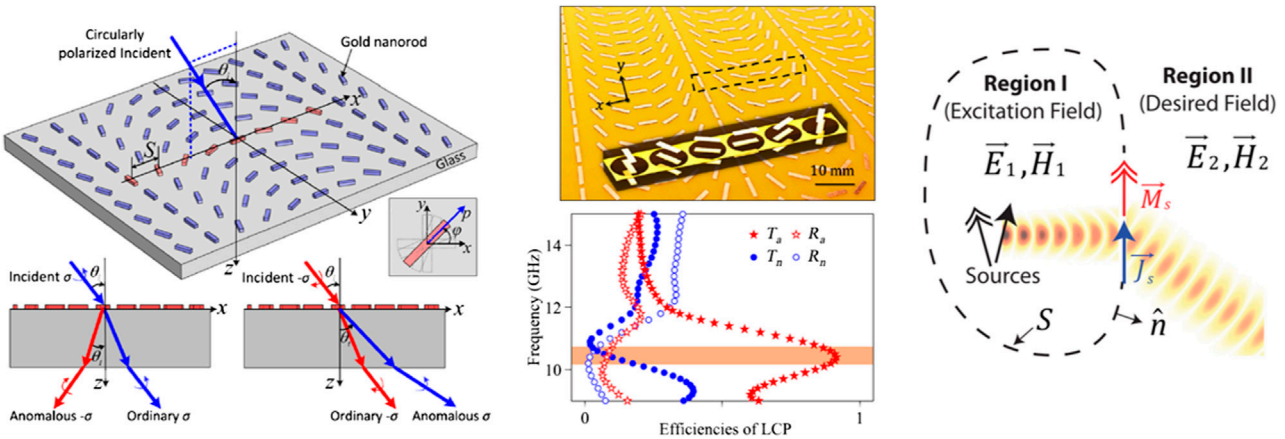

FIGURE 2 | (A) Schematic diagram of normal and anomalous refraction by Pancharatnam–Berry metasurface when illuminated by LCP and RCP light, respectively, [57]. **(B)** Picture of fabricated Pancharatnam–Berry metasurface exhibiting both electric and magnetic responses and its ultra-high transmissive conversion efficiency [102]. **(C)** The surface equivalence principle is employed to find the fictitious electric and magnetic surface currents that satisfy the boundary conditions [116]. Figure reproduced with permission from: **(A)**, © 2012, American Chemical Society (ACS); **(B)**, © 2017, American Physical Society (APS); **(C)**, © 2013, American Physical Society (APS).

realize meta-lens in the optical regime, but the efficiency was not improved [112]. MIM structure-based meta-lens were demonstrated to improve the focusing efficiency, in the near infrared [123] and mid-infrared regimes [183]. Because of the large ohmic loss of metal in optical frequencies, which limits the efficiency to a certain extent, many metallic meta-lens were designed to work in larger wavelength regime, such as Terahertz, millimeter-wave or microwave regime [24, 27, 92].

Recently, dielectric metasurfaces were developed to circumvent the significant Ohmic losses at optical frequencies [89, 173, 189, 197]. Our group compared the resonance performance in metallic and all-dielectric metasurface in a detailed way [51]. In 2014, utilizing the spin-dependent properties of PB phase, Lin et al. proposed a transmissive metalens composed of thousands of Si nanobeam nanoantennas. Via rational structural tuning, the metalens was designed to exhibit a focal length 100 μm with an NA = 0.43 at wavelength of 500 nm. When shining the metalens with RCP light through the substrate, the transmissive light was converted to LCP focal spot with a size of 670 nm, which was close to diffraction limit [93]. Later on, Capasso et al. successfully realized the fabrication of high-aspect-ratio titanium dioxide (TiO_2) metasurface, as shown in **Figure 3B**. Based on the geometric PB phase, they demonstrated three metalenses with large NA (0.8) working at wavelengths of 660, 532, and 405 nm with corresponding efficiencies of 66, 73, and 86% [72]. In their following work, a polarization-insensitive metalens working at these three wavelengths was demonstrated, which had large NA (0.85) and high efficiency (over 60%). Importantly, the focusing ability of the incident light was down to diffraction-limited spots (~0.64 λ), which were very promising [73].

Since these metalenses operate based on the phase jump governed by resonance conditions, the dispersion effect of the metalens limits their operation in a broad range of frequency. Thus, minimization or removal of chromatic aberrations of metalenses has been a serious matter of concern in the case of designing and fabrication of the metalens. Avayu et al. designed a multi-layer structure by vertically stacking independent metasurfaces and demonstrated a triply working wavelength achromatic metalens in the visible range (450, 550, and 650 nm) [9]. Capasso and his co-workers combined multiple dielectric resonators into meta-atoms and realized an achromatic metalens at three discrete wavelengths (1,300, 1,550 and, 1,800 nm) [71]. Similarly, Yu et al. utilized this combining method with new meta-unit geometries that can fulfill the space to a much greater degree, and realized a polarization-independent metalens with focusing efficiencies over 20% within a broadband of 1,200–1,650 nm [137], as shown in **Figure 3C**. Employing both low-Q-factor resonance induced phase and geometric phase that compensate with each other, an achromatic metalens working in a large wavelength band (1,200–1,680 nm) with the efficiency of ~12% was demonstrated experimentally [156]. Achromatic metalens consists of GaN-based integrated resonator meta-atom was designed and fabricated, which proved to eliminate chromatic aberration in visible wavelength (400–660 nm) with an average efficiency of ~40% [155]. Recently, tunable dielectric meta-lenses were also proposed [6, 68] to provide more usage of meta-device with higher freedom. In the later part of this review, we will discuss about these reconfigurable metasurface.

Metasurface Holography

Metasurface can also realize the holograms by tailoring the amplitude and phase of the electromagnetic wave simultaneously. In 2013, Shalaev et al. proposed a complementary V-shaped groove array fabricated in a 30 nm gold film on a glass substrate and demonstrated the holographic image of the word “PURDUE” illuminated by a visible laser of 676 nm, as shown in **Figure 4A** [113]. Based on PB phase arrangement, three-dimensional holography for a jet was

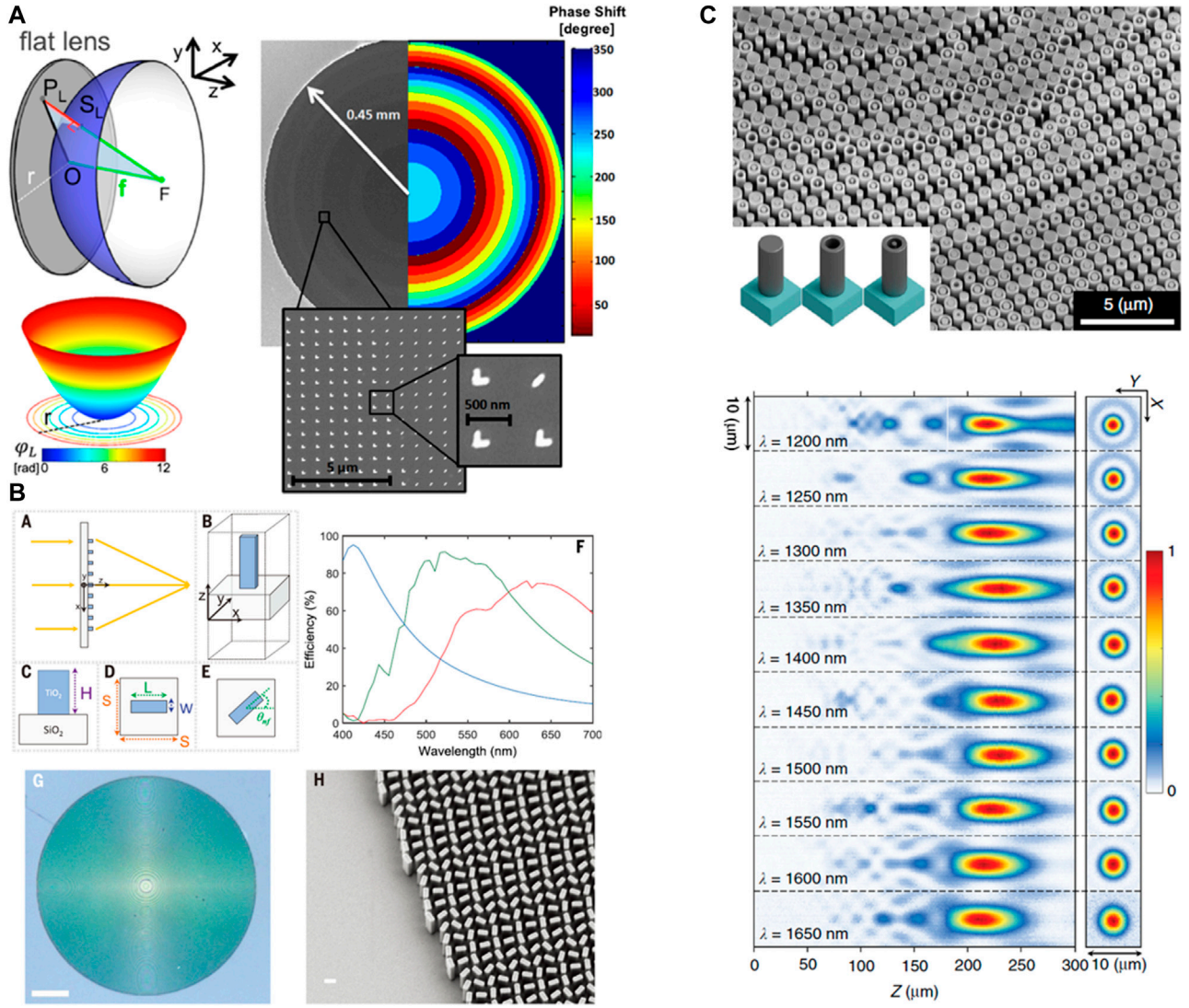

FIGURE 3 | (A) Design schematic diagram of phase distribution of metalens as well as metallic metalens consists of V-shaped nanoantennas with different lengths and opening angles of plasmonic nanorods [2]. **(B)** Dielectric metalens consists of high-aspect-ratio titanium dioxide (TiO2) nanobricks with different orientations [72]. **(C)** Dielectric metalens working in a large wavelength range (1,200–1,650 nm) with super meta-atoms composed of multi-resonators [137]. Figure reproduced with permission from: **(A)**, © 2012, American Chemical Society (ACS); **(B)**, © 2016, American Association for the Advancement of Science (AAAS); **(C)**, © 2018, Nature Publishing Group (NPG).

experimentally demonstrated with metallic nanorods metasurface, which had a large field of view estimated as 40° [58]. Single-layered plasmonic metasurfaces generally suffered from low efficiency, MIM reflection configuration was utilized and realized a high efficiency (80%) reflective metasurface hologram of Einstein's portrait at the working wavelength of 825 nm, as shown in **Figure 4B** [193]. Another method to improve the efficiency of the transmissive metasurface hologram is using the dielectric Huygen's metasurface, which has been experimentally demonstrated to reach ultra-high diffraction efficiency over 99% at the wavelength of 1,600 nm with silicon nanopillar design [152].

These metasurface holograms mentioned above, in which the meta-atoms were designed for one specific wavelength, were single-color holograms. By combining the multiple resonators with various resonance wavelengths into each meta-unit cell, the matasurface designs can control multi-wavelength beam simultaneously. Based on this methodology, Tsai and co-workers realized binary-phase holograms working for three primary colors (red, green, and blue) with aluminum MIM design, as shown in **Figure 4C** [60]. Similarly, Choudhury et al. designed super-unit cells consisting of three silver nanoslits with different sizes and orientations, and thus re-built transmissive three-color hologram [26].

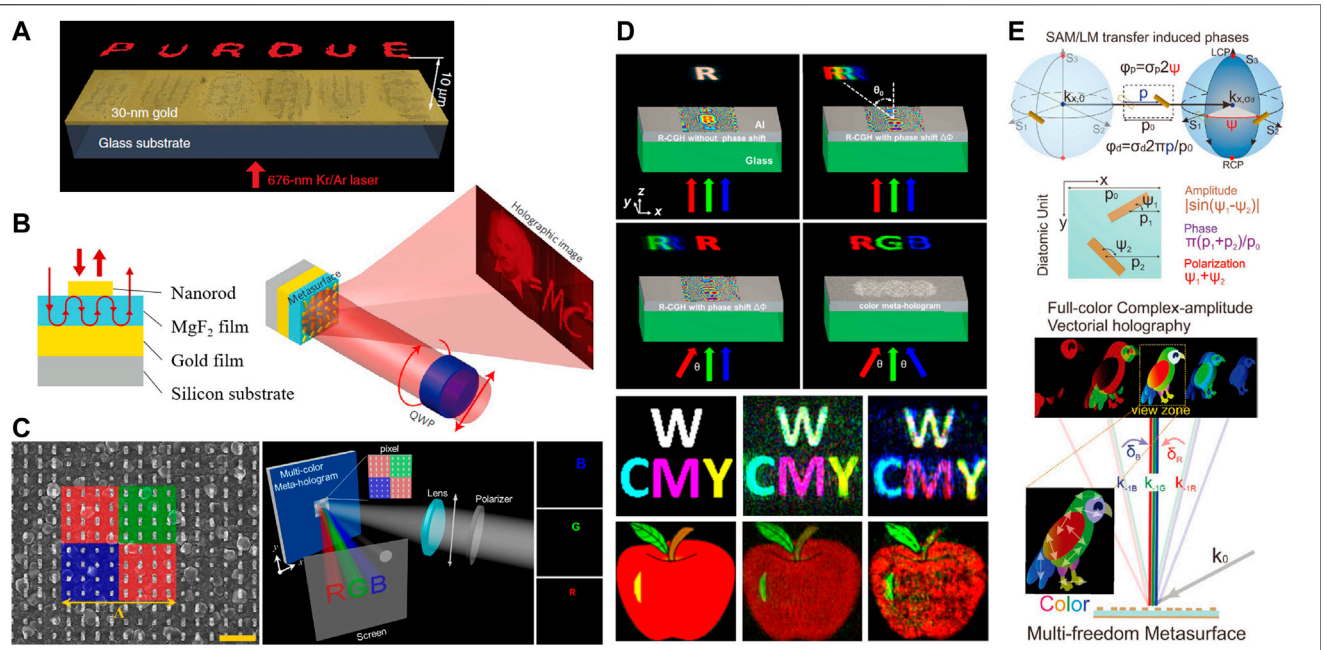

FIGURE 4 | (A) Complementary V-shaped metallic grooves produce a single-color holographic image of the word "PURDUE" [113]. **(B)** Metasurface hologram with Metal-Insulator-Metal (MIM) structure design for improving the efficiency and shows an Einstein's portrait [193]. **(C)** Metasurface with super meta-atoms composed of multi-resonators designed for RGB three-primary colors and demonstrates three-colors metasurface hologram [60]. **(D)** Metasurface hologram with off-axis illumination method realizes the decoding of three primary color components, and further generates their secondary superimposed colors (such as cyan, magenta, yellow, and white) [145]. **(E)** Design principle of the multi-freedom metasurfaces for full-color meta-hologram [29]. Figure reproduced with permission from: **(A)**, © 2013, Nature Publishing Group (NPG); **(B)**, © 2012, Nature Publishing Group (NPG); **(C)**, © 2015, American Chemical Society (ACS); **(D)**, © 2016, American Chemical Society (ACS); **(E)**, © 2020, Wiley.

Further on, via modulation of the intensity and phase of RGB (red, green, and blue) laser, (also called color mixing), three-color metasurface holograms can evolve into a full-color hologram. Wan et al. and Li et al. used the off-axis illumination method, that is using three beams of laser (red, green, and blue) to illuminate the metasurface with different tilted incident angles, thus decode three primary color components, and can further generate their secondary superimposed colors (such as cyan, magenta, yellow, and white) [90, 145], as shown in **Figure 4D**. The full-color metasurface holograms were demonstrated by using dielectric metasurfaces, such as silicon nanoblocks [11, 147], silicon nanodisks [188], titanium dioxide (TiO_2) nanodisks [161] and even graphene oxides [91]. In a very recent work, multi-freedom metasurfaces were proposed, which can modulate phase, amplitude, and polarization simultaneously and independently. Li's group combined the frequency-independent PB phase and detour phase and realized a complex-amplitude vectorial hologram at various wavelengths, thus a full-color meta-hologram was demonstrated, as shown in **Figure 4E** [29].

Metasurface Based Invisible Cloak

A cloak is a device with the ability to render objects invisible to incoming waves. Transformation optics and metamaterials are offering powerful tools for the development of cloaking devices [17, 81, 142]. Though the concept of the invisible cloak was successfully demonstrated with metamaterials,in practical aspects, development of 3-dimensional cloak with 3D metamaterials is extremely difficult. An alternative approach was first introduced with waveguide based cloaking and it played an important crucial role over a "quasi-conformal mapping technique" where the cloak concealed an object by restoring a wavefront as it was being reflected from a flat surface. This concept was defined as "carpet cloaking" and was demonstrated accordingly [38]. The realization of ultra-thin carpet cloaking was feasible due to the ultra-thin engineered metasurface based structure. Metasurfaces provided an efficient way of designing three-dimensional arbitrary shaped carpet cloaks with ultrathin thicknesses and low loss. The multi-layers structure of metasurface was proposed to offer the broadband performance of the cloak [148]. Metallic resonator with discontinuous phase was fabricated over a polyimide substrate. An excellent wavefront manipulation was demonstrated and it was employed over a surface with a triangular bump [158]. The schematic representation of the metasurface carpet clock was shown in **Figure 5A**. The cloaking layer was fabricated with a standard lithography process, and low loss flexible polyimide layer was used as the spacer medium. Terahertz time-domain spectroscopy with an angular scanning system was used for terahertz cloak demonstration.

The dispersion of materials is always the main challenge in optical components for broadband carpet cloaking. A novel metasurface was proposed recently for carpet cloaking with linear polarization at visible wavelengths from 650 to 800 nm.

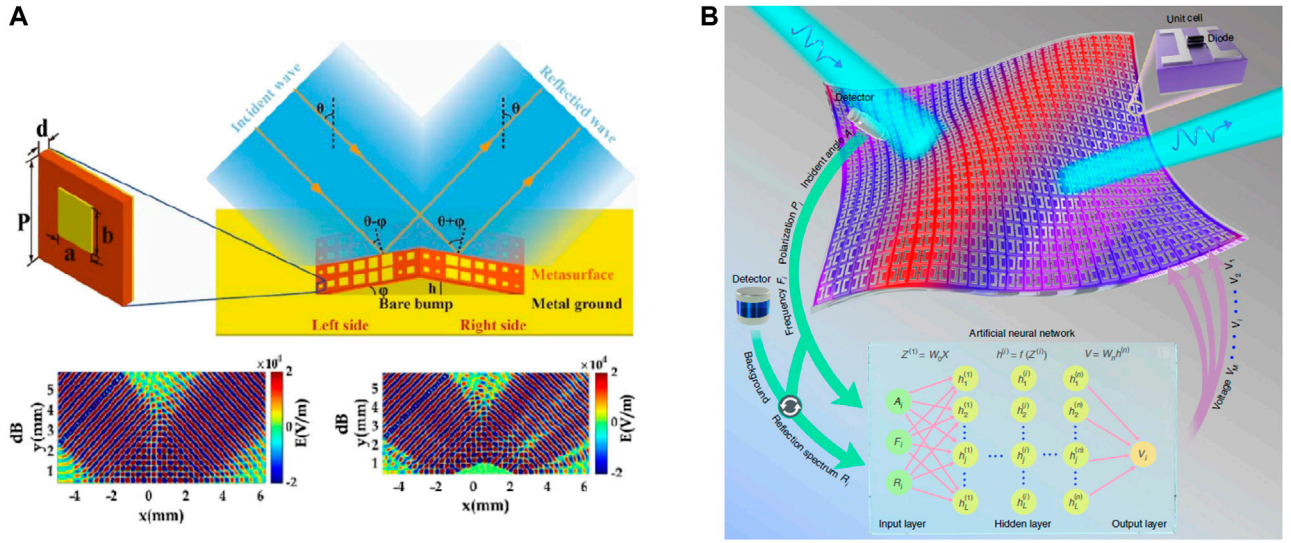

FIGURE 5 | (A) Schematic representation of the metasurface based carpet cloak [158]. **(B)** Deep-learning-enabled self-adaptive metasurface cloak [126]. Figure reproduced with permission from: **(A)**, © 2017, Optical Society of America (OSA); **(B)**, © 2020, Nature Publishing Group (NPG).

In this proposed structure, a thin slot of waveguide based metasurface was presented [50]. Very recently, a metasurface featuring machine learning algorithm was used as an adaptive cloaking system. This work shows the development of next-generation invisible cloak with artificial intelligence. An effective tunable metasurface loaded with varactor diodes was used for the fabrication of invisible cloak in the microwave range, as shown in **Figure 5B**. The metasurface cloak can respond swiftly, on a millisecond timescale with a change in incident wave and surrounding medium by a pre-trained artificial neural network which was a fundamental building block of deep learning [126].

A TREND: FROM SLAB METASURFACE TO FLEXIBLE METASURFACE

The metasurfaces are required to operate in many other different surfaces apart from large planar wafers for the application of various practical requirements, as well as cooperating with different devices. Thus, the realization of flexible (or soft) metasurface becomes one of the emerging topics nowadays. Soft Metasurfaces are normally being fabricated with metal, metal-dielectric structures, or only dielectric materials deposited over a flexible substrate [12, 22, 69], which are now considered to be the competitive platform for controlling the optical properties of the output light with mechanical force [20]. Meta-structures recently are being developed over flexible polymer [66], 2D materials [61, 99], or carbon nanofilms [138]. To expand the potential application range of flexible metasurface, our group fabricated metastructures on low-cost aluminum foils, which were widely used in food packaging [54]. Numerous modern-day engineering and scientific applications were being carried out over the curvature surface and non-planar surface where the planar sensor/device was outperformed due to the necessary efficiency [66]. Flexible metasurfaces were realized on low surface energy polymers, like polydimethylsiloxane (PDMS). PDMS can adhere to all surfaces in a conformal manner onto curved surfaces, epidermis, and packaging materials [67, 181]. **Figure 6A** represents the schematic representation of flexible metasurface with PDMS polymer. In this particular case, an amorphous Silicon nano post and a thin layer of Al_2O_3 were embedded in a low index flexible PDMS substrate. The thin dielectric metasurface layer conformed to the flexible substrate can modulate the optical response of the flexible substrate.

Soft-metasurface with a randomized phase distribution was employed for diffuse terahertz wave scattering. The distinctly patterned gold layer was deposited over the polyimide substrate for the fabrication of the structure [185]. **Figure 6B** represents the microscopic view of the sample as well as its reflection amplitudes with different modes. The energy of surface plasmon polarition of Bloch wave was tuned by flexible meta structures. The tunable plasmonic response was achieved with two layers of gold nanoribbon arrays [99]. The performance of graphene nanoribbon arrays in soft metasurface based plasmonic structures was also investigated in a detailed manner [153]. Randomly distributed meta elements over the polyimide thin films were employed to develop low scattering surface for possible EM stealth technology [187].

Modern and advanced micro and nanofabrication technologies are the basic fabrication tools that are being used for the development of soft and flexible metamaterials [144]. Photolithography, electron-beam lithography, and focused-ion-beam lithography are the most commonly used lithography for patterning nanostructures over the metasurfaces [49, 140, 174]. The resonance pattern over a flexible substrate can be accomplished with electron beam lithography [176], focused

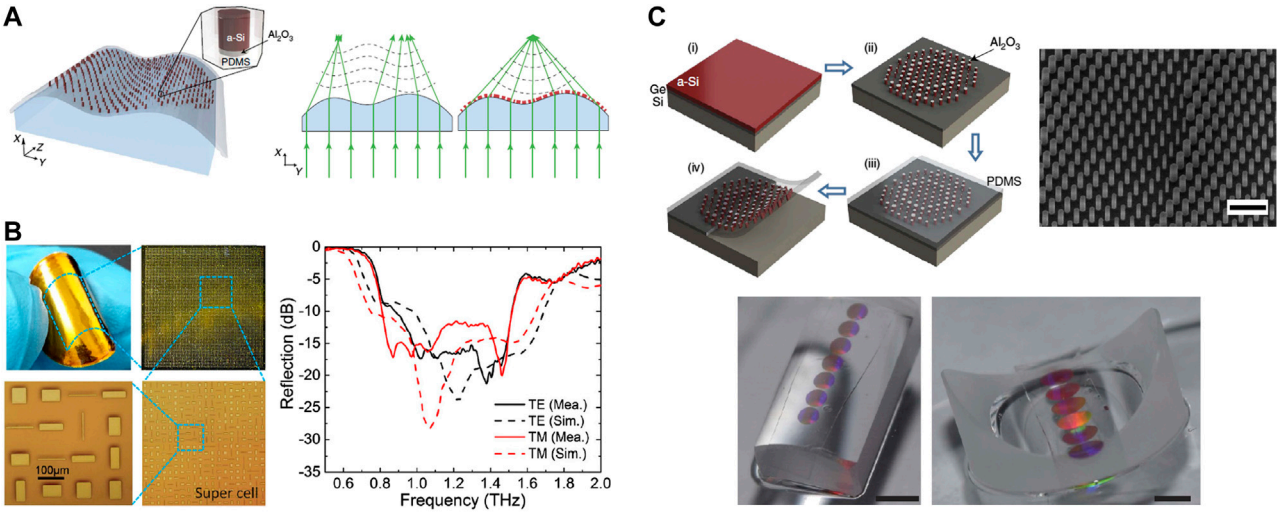

FIGURE 6 | (A) Soft metasurface conformed to the surface of a transparent object with arbitrary geometry to re-shape the wavefront and realize the focusing of transmissive electromagnetic wave [66]. **(B)** Microscopic pictures of the soft metasurface and its reflection spectrum of transverse electric (TE) and transverse magnetic (TM) modes of the electromagnetic waves within THz frequency domain [185]. **(C)** Process of developing the soft metasurface via transfer printing [66]. Figure reproduced with permission from: **(A)–(C)**, © 2016, Nature Publishing Group (NPG).

ion beam lithography [40, 113], plasmonic lithography [101], probe scanning lithography [62], laser writing lithography [44, 186] and plasmonic lithography [101]. Nanostencil lithography [105, 149] has enabled nanopatterning on a wider range of flexible nonplanar substrates with a simple fabrication process. The softness of the photonics device can be assessed by "mechanical flexibility". Flexibility is normally measured with the maximum possible deformation without any damage in the structure. Yield strength can measure mechanical flexibility and it is defined as maximum allowed strain with deformation of the photonic device. The minimization of the strain of the photonic device layer with deformation force is the key parameter for the fabrication. Minimization of strain can be attained by adopting the so-called "neutral plane" configuration. At the neutral plane, the strain response of the structure vanishes [55].

The transfer of resonance pattern over the flexible substrates needs to be released from the hard substrate which seems to be a delicate part in the designing [45, 66, 84]. Transfer of the metasurface layer over the flexible substrate can be done by transfer printing (or called stamp printing). Two mostly used processes are a) direct flip transfer and b) stamp assisted transfer. Monolithic patterning of soft photonic devices is used often as they provide ease of fabrication, improved yield, and large area patterning capability. The encapsulated devices are peeled off from the rigid handler to complete the fabrication process of the soft photonic devices, as shown in **Figure 6C**. The sacrificial layer used for successful detachment of flexible metasurface from a rigid substrate. A diluted ammonia solution was used to remove the sacrificial layer from the fabricated structure. Similarly, Ambhire et al. also proposed "Pattern and Peel" method, using PDMS as the sacrificial layer, to fabricate the metasurface on an elastomeric substrate (PDMS) [3]. What's more, they also showed reconfiguration or tunability of the resonance by stretching PDMS layer, and thus realized a kind of reconfigurable metasurface, which will be covered in detailed in next section with various types.

RECONFIGURABLE METASURFACE: AN ENCOURAGING IMPROVEMENT FROM STATIC

The optical properties of the metasurface are related to engineered structure. Size, shape, and the inter meta-atomic distances as well as the optical parameters of materials control and dictate the optical characteristics of the metasurface. However, traditional metasurfaces are difficult to be tuned after being fabricated, which considerably limit the degree of freedom for full-wave controls. As such, it is highly desirable to realize dynamic metasurfaces, whose functionalities can be actively tunable with controlled external factors. Recent few years, there have been some impressive works published. In this part, the reconfigurable metasurface is being discussed in detail.

Mechanical Force in Soft Metasurface

Geometric arrangements of resonant building blocks with a fixed material composition drive the performance of the metasurface. The performance of metasurface can be tuned by varying the shape, size, and spatially arrangements of the constituent meta-atoms. Mechanical force is the main influence on the tuning of the optical properties of the tunable metasurface. Novel aspects of manipulating light could be achieved with the ability to bend, stretch, and roll of the device on flexible substrates and which promises a new wave of device designs and functionalities [69, 144, 174].

Unique and typical characteristics that are being found in metasurface through mechanical deformation is mostly due to the flexible substrates [69, 130, 144]. PDMS, a silicon-based organic polymer is being widely used as an elastomeric substrate due to its low optical loss and excellent elasticity during reversible deformation. Transmittivity of flexible metasurface was demonstrated in detail, and an excellent control over the optical properties by mechanical tuning was shown. **Figure 7A** depicts that the metasurface exhibits remarkable resonance shifts with mechanical tuning [45]. The interparticle distance was used to modulate the optical properties of metasurface with mechanical stretching. The gap between successive resonators was found to be varied from 10 to 140 nm with 0–100% applied strain over PDMS substrates [97]. The mechanical flexibility of engineered metasurface was explored in tuning the focal length of meta-lens. All-dielectric material metalens was demonstrated where amorphous silicon post was developed over the PDMS substrate [68]. The mechanically tunable lens in visible wavelength was also demonstrated with significant efficiency in controlling the focal length. The lattice constant of Au nanorod was tuned which is fabricated over PDMS substrate [33]. Polarization of the incident wave can be tuned with chirality of the metasurface, and nanostructures with chiral geometries exhibit strong polarization rotation. Plasmonic nano colloids with rotary optical activity were developed with twisted PDMS substrate and multilayers of metal nanoparticles [76].

From Microelectromechanical Systems to Programmable Metasurface

Microelectromechanical systems (MEMS) offers a method to realize the structural reconfiguration of the metasurface, thus modifying the electromagnetic response. Metasurface based mid-IR flat lens was developed for active beam steering [128]. The design of microcantilever arrays in metasurface allowed the structure can be tuned between the "touch" and "separate" by the electrostatic force [28, 120, 190]. **Figure 7B** presents a MEMS metasurface with micro-cantilever, which realizes structural tunability with electricity. There were significant shifts of resonance wavelength as one end of unfixed open ring resonators gradually warps. Discrete structures, which stood on substrates with different properties, offered the possibility of modification [182]. As shown in **Figure 7C**, the metasurface composes of two types of slabs. One kind of slabs patterned on a rigid substrate and the other one was suspended, which can be shifted by a micromachined actuator. However, recently explored MEMS metasurfaces generally work in the Terahertz band, microwave regime, and range with longer wavelengths, which have a large size with a dimension of tens of micrometers or even larger. For those more compact meta-structures working in a higher-frequency region, one needs to explore special sophisticated methods, such as Nanoelectromechanical systems technology. Further on, blending self-feedback and programming algorithms into the metasurface, programmable metasurface can be achieved. More recently, Cui et al. utilized the diodes and field-programmable gate array, which embedded into the metasurface, to store a bulk of coding sequences as well as corresponding electromagnetic responses, and realized a smart metasurface [103]. **Figure 7D** presents the appearance of this reprogrammable metasurface. Adaptive single-beam, multi-beam manipulation, and other dynamic reactions were demonstrated successfully. In recent years, with the rise of artificial intelligence, concepts such as machine learning have emerged in many fields. With the aid of machine learning, reprogrammable metasurface will also be more intelligent [87]. This is undoubtedly a promising direction in the field of metasurface research.

Structures With Tunable Materials

The reconfigurable metasurface mentioned above is achieved by changing the structure (shape, arrangement). Utilizing those tunable materials, as a part of the structure design, can also be a strategy to realize the modification of metasurface. Phase-change materials (PCMs), such as the GeSbTe (short for GST) alloys, suffer from significant optical parameters variation between the amorphous and crystalline states, and thus recently being used to modify the optical properties of metasurface [15, 25, 30]. Galarreta et al. embedded a thin layer of GST into silicon nanodisks and realized the modification of resonance [129]. In addition to the amorphous and crystalline states, stepwise intermediates states were also demonstrated [154].

Graphene has received a lot of attention since its discovery. It can also be used to achieve reconfigurable metasurfaces due to its adjustable band gap and excellent optical properties. A monolayer graphene sheet was patterned on the silicon photonic crystal-like substrate and realized tunable induced transparency via the electrical method [23]. Fan et al. used a pump beam to excite the graphene and enhanced the initially weak magnetic resonances significantly [35]. Similarly, giving stimuli according to other embedded materials sensitive to a thermal, electric, or optical stimulus can also get a tunable metasurface. For example, silicon illuminated with infrared pump beam can produce photocurrent and tune the resonance of metallic metasurface [42]. Recently, ferromagnetic particles were mixed in the 3D-printed soft materials and realized the actively controlling of the shape under applied magnetic fields [77], which can be also referred to in the metasurface design.

Fluidic Unit Cell Metasurface

Microfluidic technology [13, 106] enables people to control liquids in various fields within micro-/nanoscale, which matches the structural dimensions of the metasurface well. Recent few years, the combination of microfluidic and metasurface is emerging gradually [184]. Injecting liquid into a sub-wavelength periodic channel structure, i.e., "liquid cell metasurface", and using the fluidity of the liquid or liquid material, personalized micro-structure units can be created to customize the metasurface optical response. Besides, more applications are required to be completed in a liquid environment, such as bio-sensing, bio-detection, and bio-imaging. Different optical responses can be obtained by injecting different solutions into the water-cell metasurface microstructure. Most water-cell metasurfaces are used as

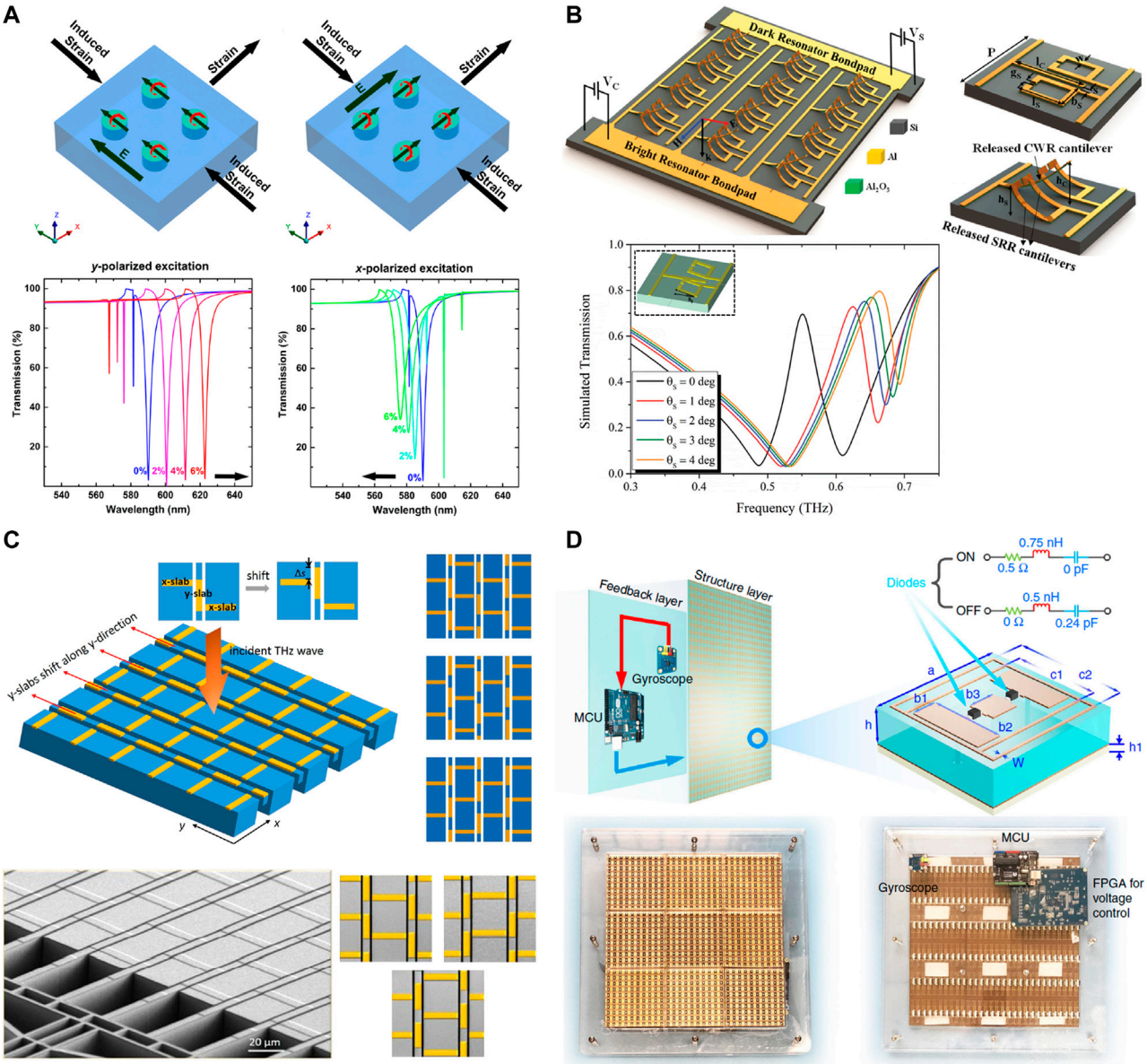

FIGURE 7 | (A) Stretch the flexible metasurface and realize remarkable resonance shifts [45]. **(B)** MEMS metasurface with cantilevers allow structures can be tuned via electricity voltage. There are significant shifts of resonance wavelength as one end of unfixed open ring resonators gradually warps [120]. **(C)** The reconfigurable metasurface with suspended MEMS structure design and its three reconfigurable states [182]. **(D)** Schematic diagram and actual appearance of programmable metasurface [103]. Figure reproduced with permission from: **(A)**, © 2016, American Chemical Society (ACS); **(B)**, © 2016, Wiley; **(C)**, © 2017, Nature Publishing Group (NPG); **(D)**, © 2019, Nature Publishing Group (NPG).

sensors to detect incoming samples. For example, a THz system that combines highly sensitive and non-invasive detection of biological samples with metasurfaces and microfluidics was developed recently [59], and an ultra-sensitive fluid sensor capable of determining the type and concentration of chemical reagent with high accuracy was demonstrated successfully [1]. All of these have laid the foundation for accurate detection in the future medical chemistry and other fields. While the liquid-metal is a substance with fluidity, metallicity, and thermal expansion characteristics. Mercury (Hg) was first used in the metasurface molecules in the microwave band to regulate the propagation of waves, as shown in **Figure 8A** [70]. However, Hg is highly toxic and thus be replaced by some alloys such as eutectic gallium-indium (EGaIn). In **Figure 8B**, by injecting EGaIn into PDMS mold, the first THz liquid-metal-cell metasurface was born [150, 151]. Later, the metasurface composed of small tubes infused with liquid-metal EGaIn and copper wire pairs completed the tuning of switching the electromagnetically induced transparency (EIT)-like response [164]. The liquid-metal alloy EGaIn was injected into the microfluidic channel on the PMMA substrate, and the

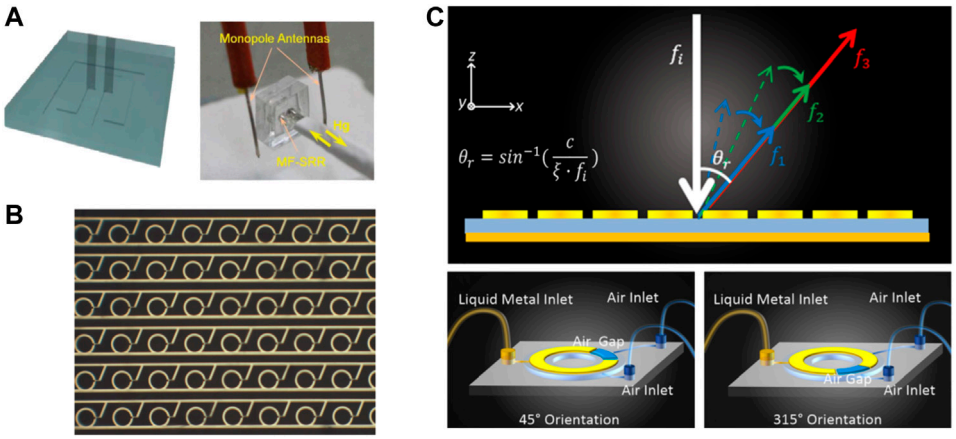

FIGURE 8 | Structures of liquid-metal-cell metamaterials. **(A)** Reconfigurable electromagnetic metamaterials using Hg in metamolecular [70]. **(B)** Reconfigurable THz metamaterial device with EGaIn in microchannels [150]. **(C)** Individually modulating ring-resonator-array metamaterial using liquid-metal Galinstan [166]. Figure reproduced with permission from: **(A)**, © 2009, AIP Publishing; **(B)**, © 2014, Optical Society of America (OSA); **(C)**, © 2017, AIP Publishing.

shear of the resonance frequency from 10.96 to 10.61 GHz was completed while maintaining the absorption rate up to 98% [95]. As for more precise reconfiguration, a metasurface for periodically distributed ring resonators was designed as shown in **Figure 8C**, which can modulated the shape of the liquid-metal Galinstan, a gallium indium tin alloy, in each ring resonator individually, and then dynamically adjusted the light reflection [166]. According to the thermal expansion of liquid-metal mercury, different broadband THz metasurface absorbers were proposed and can be customized at different temperatures [180].

Metasurface in Fluid-Background

The fluid-background metasurface is a solid-liquid mixed metasurface. The developed metasurface is immersed in water, alcohol, liquid crystal (LC), or even a solution of suspended nanoparticles, to achieve the corresponding purpose of induced tuning optic waves. Water is the most abundant liquid resource on earth. Because it is cheap and non-toxic, and can be miscible with a large number of liquids, it is a very common liquid surrounding material and different structures were proposed over the years [32, 56]. Ethanol [75], glucose solution [195], sucrose solution [114], etc. are also often used as background material. By adjusting the concentration of the solution covering the solid metasurface, the refractive index of the solution is changed, and then the dielectric constant is changed, and finally, the optical response is adjusted [114]. In recent years, LC has attracted much attention as a promising background material of metasurface. It has both crystallinity and fluidity at room temperature. By changing the external conditions, the orientation of the LC molecules can be redirected to achieve a tunable optical response. The excellent characteristics of LC make it applicable in many fields. Liu's group has designed several reconfigurable chiral metasurface absorbers by using a LC layer as an insulator layer. In one structure, the circular dichroism of the incident light will be modulated with the different alignments of the LC molecules, which could achieve the effect of reversing circular dichroism [172]. Other plasmonic LC reconfigurable chiral metasurfaces of sandwich-structure, as shown in **Figure 9A**, were simulated to spin-selectively absorb CP light at multiband frequencies [160] and efficiently [171]. Recently, THz beam was manipulated by programmable LC background metasurfaces, as shown in **Figure 9B**. In this article, the "0" and "1" encoding technology was used to switch the state of different arrays to redirect the LC molecules in it, thereby changing the refractive index of different regions, and finally realize the dynamic manipulation of the THz wave, and its maximum deflection angle reached 31.2% [159]. Similarly, a digital metasurface device for light projection display was demonstrated with each pixel is electrically reconfigurable [82]. A LC plasma metasurface was also developed to display electronically adjustable color labels [135]. Metasurfaces with LC as the surrounding material was used as all-optical switches [8] and switches of controlling the generation of second harmonics of metasurface [127]. In terms of controlling electromagnetic radiation, the LC-based metasurface was also designed to successfully achieve dynamic thermal camouflage, as shown in **Figure 9C**, which provides a new development direction for the future thermal metasurface with emissivity engineering [100]. Nanoparticle solutions can also be used a background materials as same as LC. The orientation of the nanoparticles suspended in the solution can be redirected and rearranged by tuning the external factors, and thus the light will be controlled [48].

A NEW PLATFORM: METASURFACE ON FIBER

After the demonstration of the powerful capability of electromagnetic wave manipulation by metasurface, it has been successfully applied to optical fibers, bringing immense advantages over its domain of applications. Thus amalgamation of metasurface and optical fibers provide a powerful platform for the development of novel optical components. With the emergence of "Lab of Fiber", micro-,

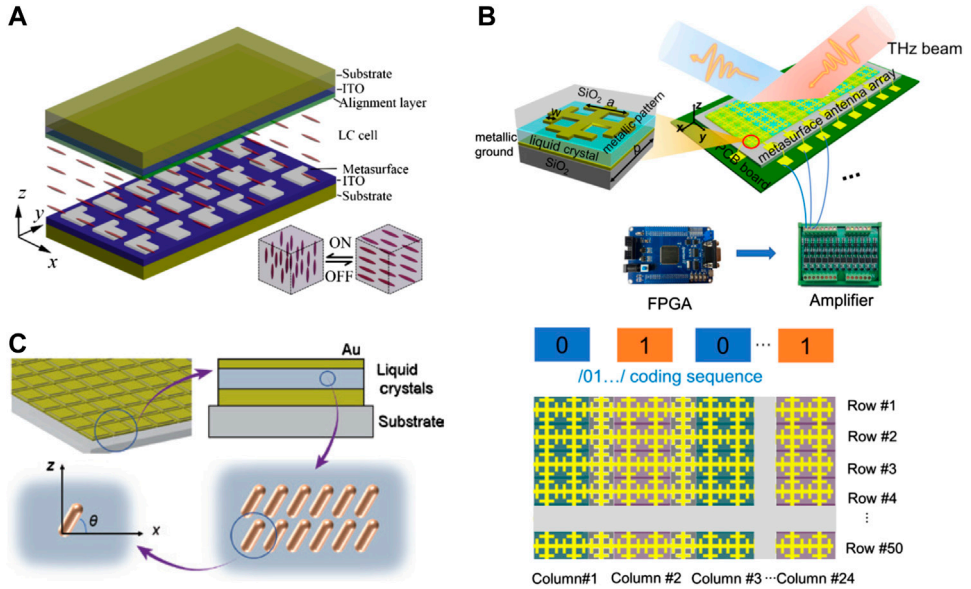

FIGURE 9 | Structures of LC background metamaterials. **(A)** Reconfigurable spin-selectively multiband absorber based on LC chiral metasurface [160]. **(B)** Codeable LC metamaterial for controlling THz beam [159]. **(C)** Metal-LC-Metal platform with dynamic thermal camouflage function [100]. Figure reproduced with permission from: **(A)**, © 2018, Optical Society of America (OSA); **(B)**, © 2020, AIP Publishing; **(C)**, © Walter de Gruyter GmbH 2020.

nano-structure, and metasurface are fabricated on/in/around the optical fiber to realize specific functions [37, 125, 163, 191].

Optical fiber devices decorated with micro-structures and functional materials have been studied for decades. Still, the surface decoration based on traditional self-assembly is almost out-of-order and uncontrollable. Thus, the ability to fabricate controllable structures on optical fiber will help the further expansion of the application. However, considering that most of the micro- and nanofabrication methods arising from the microelectronic industry operate on large planar substrates, fabrication of metasurface on the fiber is difficult. Researchers are contributing their wisdom to combine fiber optics with metasurfaces.

One primitive approach is self-assembly lithography. Since the nanospheres float in a regular arrangement at the interface between air and non-polar solvent, which is also called Langmuir-Blodgett procedure [7]. Pisco et al. used self-assembled polystyrene nanospheres as a mask and fabricated round hole periodic structure on the facet of fiber [118], as shown in **Figure 10A**. Similarly, a polymer solution with water droplets assembled as a close pack array inside was also used. The template was accomplished with evaporation of the water. They realized a round-hole periodic structure on the facet of fiber with the help of the holder [119]. Further on, this kind of regularly arranged nanostructures templates was used as Kaleidoscope shadow masks when illuminated with different incident angles, and thus makes it possible to fabricate more periodic structures [110], as shown in **Figure 10B**.

However, self-assembly lithography can only satisfy a limited number of simple structures. For more complicated structures, one needs to explore a more competent method for an advanced level of fabrication. Principe et al. utilized a holder to clamp the single-mode fiber and deposited a gold layer on the facet of fiber via electron beam evaporation, subsequently fabricated a rectangular groove array, which covered the entire core regime, with focused-ion-beam nanofabrication processed directly [125]. As shown in **Figure 10C**, the rectangular grooves with different lengths on the fiber end-facet produced various phase jumps, and the anomalous transmission in optical fiber was firstly demonstrated on this fiber meta-tip. Later, controlled absorption was also demonstrated in the optical fiber system with a similar method, and can be further used in logical operation [163].

This direct lithography method ensures that the shape of the fabricated metasurface structure can meet the requirements to a greater extent as one wishes. However, the resolution of standard UV lithography is over 1 μm while the size of the meta atoms on fiber end-facet is approximately ~100 nm or even smaller. E-beam lithography and FIB are normally used for the fabrication of the metasurface on fiber. What's more, compared with flat wafers, optical fibers are less compatible and controllable in lithography process. The scalability issue of the fabrication of metasurface are limited by the following factors: 1) The flatness and smoothness of the surface of the fiber tip; 2) The stability of the position of the fiber, as special mount is required to put the fiber vertically below the electron beam, a slight shift of the fiber from its position could affect the designing in a massive manner; 3) The size and pattern of the meta-atoms, which also greatly affect the speed and efficiency of the fabrication. It needs to be mentioned that both e-beam lithography and FIB fabrications methods are not industrial grade. So specific optimization processes are required to be followed for each of the specific fabrications. The fabrication of meta atoms over the planar device is a bit easier to optimize

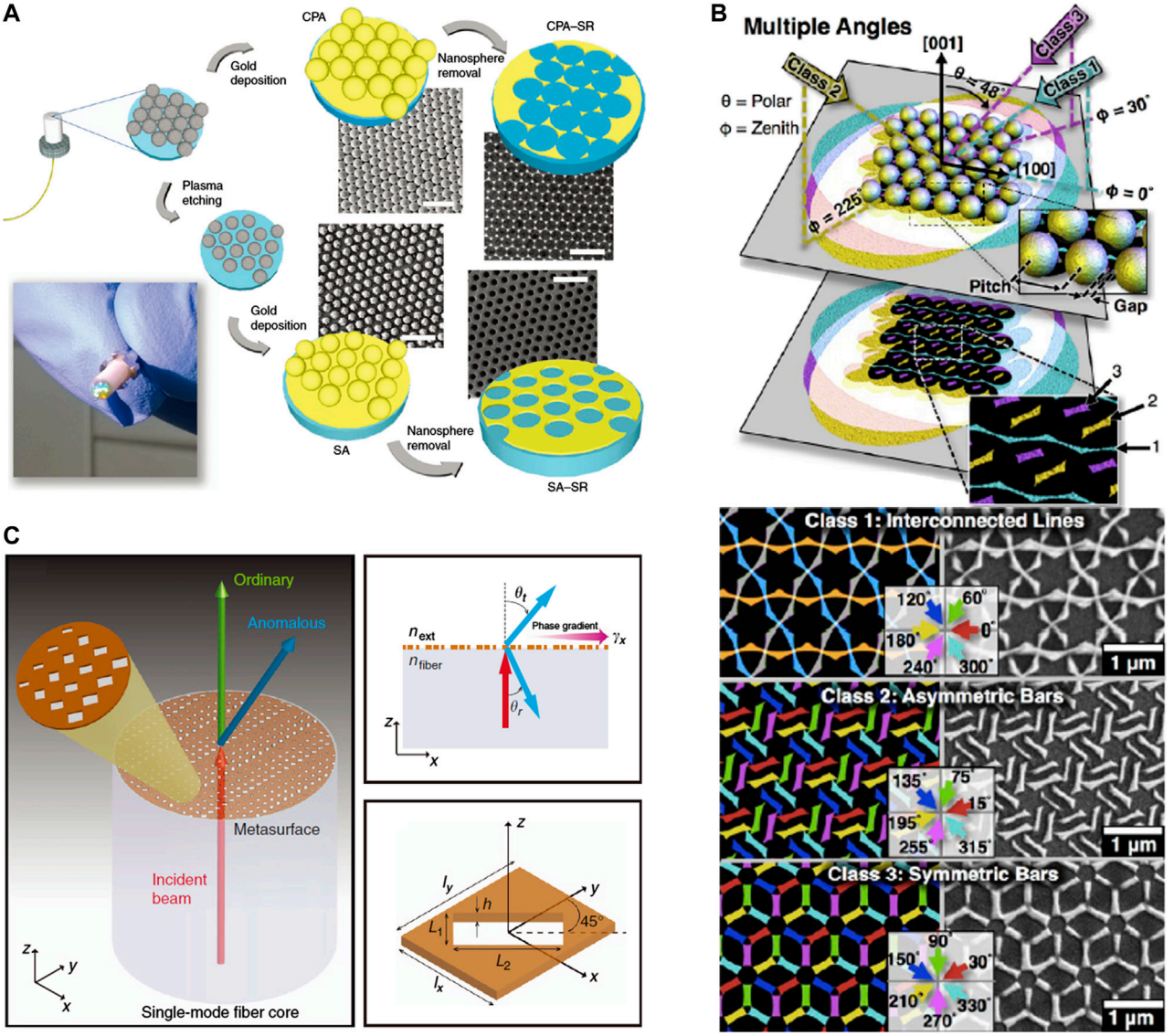

FIGURE 10 | (A) Fabrication process of meta-structure on the fiber end-facet via self-assembly lithography [118]. **(B)** Meta-structures fabricated with Kaleidoscope shadow masks [110]. **(C)** Anomalous transmission on fiber meta-tip [125]. Figure reproduced with permission from: **(A)**, © 2017, Nature Publishing Group (NPG); **(B)**, © 2014, American Chemical Society (ACS); **(C)**, © 2017, Nature Publishing Group (NPG).

than that required for optical fiber. As a result, it would be extremely inefficient to make these nano-structures directly on optical fibers.

Recently, transfer of nano-structure from a large wafer onto the fiber end-facet became a potential method to make metasurface on fiber [157]. Juhl et al. utilized UV-curable hybrid polymer to transfer the gold nanoantennas array from silicon wafer to the fiber tip completely, due to the soft and quickly-dry of UV-curable hybrid polymer [65]. Although it still takes a lot of labor and resources to make fine patterns on the wafer in advance, the transfer of the metasurface from the wafer to the fiber is not really difficult. As long as the wafer template is available, mass production of fiber meta-tips may become feasible. In addition, it is also promising to transfer these elaborate structures to the side-surface of the fiber by rolling the fiber and combining with this kind of transcription process.

Nanoinstile lithography, roll to roll printing techniques are used to make the process more appropriate but till today the fabrication of the meta-atoms over the fiber remains a challenge. To date, the metasurface is only developed on the flat end-facet of the fiber, almost no metasurface around the arc surface of the fiber has been demonstrated, let alone those inside of the photonic crystal fiber. In a word, there is still a long way to realize the integration of metasurface into an optical fiber system.

CONCLUSIONS AND OUTLOOK

As the latest generation of optical devices, the compactness of metasurface is unmatched by traditional optical devices. Metasurface can perform wavefront regulation at the sub-wavelength scale and has attracted extensive attention since its adventless than a decade ago. In this review, we have summarized the basic principles of metasurface in the reshaping of electromagnetic waves based on the phase and amplitude modulation, as well as its mainstream applications. Considering metasurface analogues are so attractive due to their amazing optical properties, metasurfaces are combined on another powerful optical device: optical fibers. This part of the explorations was also reviewed in this paper. From here, we can see that the working environment of a metasurface is by no means limited to large flat wafers. It needs to be integrated with other components, work on any surface, and adapt to a variety of environments. Thus, we retrospect that pioneering research works about flexible metasurface and reconfigurable metasurface.

It should be noted that, due to the vastness and rapid development of this field involved as well as our limited cognition and energy, it is impossible for cover all important aspects within this review, such as nonlinear metasurfaces [19, 78, 80, 170], hyperbolic metasurfaces [46, 64, 88]and so on. Some branches are just mentioned briefly. However, they are immensely important and play a crucial rule in their respective applications but a detailed discussion is out of scope of this particular review article. Before conclusion of this review, we would like to comment on future prospects of metasurface. From a functional device perspective, if the metasurface is only satisfied with the realization of functions on large flat wafers, it is not only unrealistic, but also has no future.

A simple way to make the study of metasurface more practical is to combine it with other more mature fields and functional devices. Due to the author's long working experience in the field of optical fiber, more attention is paid to the combination of this aspect. To date, there are only some simple metasurface diagrams developed on the flat end-facet of the fiber, or the so-called meta-tips. There is almost no metasurface developed around the arc surface of the fiber, let alone the metasurface inside of the photonic crystal fiber. More recently, Steiner and co-workers proposed a 'self-rolled multilayer metasurfaces' based on templates that can roll themselves up [12]. This method is similar to the Nano-imprint lithography [47, 131, 132], while implemented on the soft materials. Referring to this approach, metasurface may be developed around the arc surface of the fiber easily. In addition, the microstructure on the fiber is mostly used in the near-infrared communication band, which greatly limits the size of the microstructure to the sub-micron scale. At present, it can only be achieved by electron beam exposure, which heavily aggravates the difficulty of mass processing. If one could successfully implement the integration of metasurface into an optical fiber system and realize the lab on/around/in fiber, it would be a large step in optical devices. Although there are still more efforts required.

On the other hand, the integration of metasurface with other emerging concepts is also a promising direction. With the rise of artificial intelligence, various concepts such as artificial intelligence algorithms and data mining are expected to make metasurfaces more powerful [87, 103]. More recently, metasurface was utilized in the field of quantum optics, and the quantum behavior of superposition and correlation between homologous multi-photon pairs was experimentally verified [86]. This paper verified the feasibility of high dimensional quantum entanglement chip. We believe that with the joint efforts of many researchers, the research of metasurface will make swift progress, radiate to more fields, and promote the development of science and technology.

AUTHOR CONTRIBUTIONS

JH wrote most content of this review article; SB and YL helped JH to finish the whole review; LS supervised the whole work. All the authors reviewed the manuscript.

FUNDING

This work was supported in part by the Post-doctoral research fund and Start-up Funding of Southern University of Science and Technology under Grant No. Y01236128.

REFERENCES

1. Abdulkarim YI, Deng L, Karaaslan M, Altintas O, Awl HN, Muhammadsharif FF, et al. Novel metamaterials-based hypersensitized liquid sensor integrating omega-shaped resonator with microstrip transmission line. *Sensors.* (2020) 20(3):943. doi:10.3390/s20030943
2. Aieta F, Genevet P, Kats MA, Yu N, Blanchard R, Gaburro Z, et al. Aberration-free ultrathin flat lenses and axicons at telecom wavelengths based on plasmonic metasurfaces. *Nano Lett.* (2012) 12(9):4932–6. doi:10.1021/nl302516v
3. Ambhire SC, Palkhivala S, Agrawal A, Gupta A, Rana G, Mehta R, et al. "Pattern and Peel" method for fabricating mechanically tunable terahertz metasurface on an elastomeric substrate. *Opt Mater Express.* (2018) 8(11):3382–91. doi:10.1364/ome.8.003382
4. Arbabi A, Horie Y, Bagheri M, Faraon A. Dielectric metasurfaces for complete control of phase and polarization with subwavelength spatial resolution and high transmission. *Nat Nanotechnol.* (2015) 10(11):937–43. doi:10.1038/nnano.2015.186
5. Arbabi A, Horie Y, Ball AJ, Bagheri M, Faraon A. Subwavelength-thick lenses with high numerical apertures and large efficiency based on high-contrast transmitarrays. *Nat Commun.* (2015) 6:7069. doi:10.1038/ncomms8069
6. Arbabi E, Arbabi A, Kamali SM, Horie Y, Faraji-Dana M, Faraon A. MEMS-tunable dielectric metasurface lens. *Nat Commun.* (2018) 9(1):812. doi:10.1038/s41467-018-03155-6
7. Ariga K, Yamauchi Y, Mori T, Hill JP. 25th anniversary article: what can be done with the Langmuir-Blodgett method? Recent developments and its critical role in materials science. *Adv Mater.* (2013) 25(45):6477–512. doi:10.1002/adma.201302283

8. Atorf B, Muhlenbernd H, Zentgraf T, Kitzerow H. All-optical switching of a dye-doped liquid crystal plasmonic metasurface. *Opt Express.* (2020) 28(6): 8898–908. doi:10.1364/OE.383877
9. Avayu O, Almeida E, Prior Y, Ellenbogen T. Composite functional metasurfaces for multispectral achromatic optics. *Nat Commun.* (2017) 8:14992. doi:10.1038/ncomms14992
10. Bao Y, Ni J, Qiu CW. A minimalist single-layer metasurface for arbitrary and full control of vector vortex beams. *Adv Mater.* (2020) 32(6):e1905659. doi:10.1002/adma.201905659
11. Bao Y, Yu Y, Xu H, Guo C, Li J, Sun S, et al. Full-colour nanoprint-hologram synchronous metasurface with arbitrary hue-saturation-brightness control. *Light Sci Appl.* (2019) 8:95. doi:10.1038/s41377-019-0206-2
12. Bermúdez-Ureña E, Steiner U. Self-rolled multilayer metasurfaces. *ACS Photonics.* (2019) 6(9):2198–204. doi:10.1021/acsphotonics.9b00816
13. Bhatia SN, Ingber DE. Microfluidic organs-on-chips. *Nat Biotechnol.* (2014) 32(8):760–72. doi:10.1038/nbt.2989
14. Cai BG, Li YB, Jiang WX, Cheng Q, Cui TJ. Generation of spatial Bessel beams using holographic metasurface. *Opt Express.* (2015) 23(6):7593–601. doi:10.1364/OE.23.007593
15. Cao T, Cao Y, Fang L. Reconfigurable parity-time symmetry transition in phase change metamaterials. *Nanoscale.* (2019) 11(34):15828–35. doi:10.1039/c9nr01828j
16. Chen BH, Wu PC, Su VC, Lai YC, Chu CH, Lee IC, et al. GaN metalens for pixel-level full-color routing at visible light. *Nano Lett.* (2017) 17(10):6345–52. doi:10.1021/acs.nanolett.7b03135
17. Chen H, Zheng B, Shen L, Wang H, Zhang X, Zheludev NI, et al. Ray-optics cloaking devices for large objects in incoherent natural light. *Nat Commun.* (2013) 4:2652. doi:10.1038/ncomms3652
18. Chen L, Ma Q, Jing HB, Cui HY, Liu Y, Cui TJ. Space-energy digital-coding metasurface based on an active amplifier. *Phys Rev Appl.* (2019) 11(5):054051. doi:10.1103/PhysRevApplied.11.054051
19. Chen S, Reineke B, Li G, Zentgraf T, Zhang S. Strong nonlinear optical activity induced by lattice surface modes on plasmonic metasurface. *Nano Lett.* (2019) 19(9):6278–83. doi:10.1021/acs.nanolett.9b02417
20. Chen WT, Zhu AY, Capasso F. Flat optics with dispersion-engineered metasurfaces. *Nat Revi Mater.* (2020) 5:604–20. doi:10.1038/s41578-020-0203-3
21. Chen X, Huang L, Muhlenbernd H, Li G, Bai B, Tan Q, et al. Dual-polarity plasmonic metalens for visible light. *Nat Commun.* (2012) 3:1198. doi:10.1038/ncomms2207
22. Chen Y, Ai B, Wong ZJ. Soft optical metamaterials. *Nano Converg.* (2020b) 7(1):18. doi:10.1186/s40580-020-00226-7
23. Chen ZH, Tao J, Gu JH, Li J, Hu D, Tan QL, et al. Tunable metamaterial-induced transparency with gate-controlled on-chip graphene metasurface. *Opt Express.* (2016) 24(25):29216–25. doi:10.1364/OE.24.029216
24. Cheng Q, Ma M, Yu D, Shen Z, Xie J, Wang J, et al. Broadband achromatic metalens in terahertz regime. *Sci Bull.* (2019) 64(20):1525–31. doi:10.1016/j.scib.2019.08.004
25. Choi C, Lee SY, Mun SE, Lee GY, Sung J, Yun H, et al. Metasurface with nanostructured Ge2Sb2Te5 as a platform for broadband-operating wavefront switch. *Adv Opt Mater.* (2019) 7(12):1900171. doi:10.1002/adom.201900171
26. Choudhury S, Guler U, Shaltout A, Shalaev VM, Kildishev AV, Boltasseva A. Pancharatnam-Berry phase manipulating metasurface for visible color hologram based on low loss silver thin film. *Adv Opt Mater.* (2017) 5(10): 1700196. doi:10.1002/adom.201700196
27. Chu H, Qi J, Qiu J. An efficiently-designed wideband single-metalens with high-efficiency and wide-angle focusing for passive millimeter-wave focal plane array imaging. *Opt Express.* (2020) 28(3):3823–34. doi:10.1364/OE.385498
28. Cong L, Pitchappa P, Lee C, Singh R. Active phase transition via loss engineering in a terahertz MEMS metamaterial. *Adv Mater.* (2017) 29(26): 1700733. doi:10.1002/adma.201700733
29. Deng ZL, Jin M, Ye X, Wang S, Shi T, Deng J, et al. Full-color complex-amplitude vectorial holograms based on multi-freedom metasurfaces. *Adv Funct Mater.* (2020) 30(21):1910610. doi:10.1002/adfm.201910610
30. Ding F, Yang Y, Bozhevolnyi SI. Dynamic metasurfaces using phase-change chalcogenides. *Adv Opt Mater.* (2019) 7(14):1801709. doi:10.1002/adom.201801709
31. Ding X, Monticone F, Zhang K, Zhang L, Gao D, Burokur SN, et al. Ultrathin pancharatnam-berry metasurface with maximal cross-polarization efficiency. *Adv Mater.* (2015) 27(7):1195–200. doi:10.1002/adma.201405047
32. Ebrahimi A, Withayachumnankul W, Al-Sarawi S, Abbott D. High-sensitivity metamaterial-inspired sensor for microfluidic dielectric characterization. *IEEE Sensor J.* (2014) 14(5):1345–51. doi:10.1109/jsen.2013.2295312
33. Ee HS, Agarwal R. Tunable metasurface and flat optical zoom lens on a stretchable substrate. *Nano Lett.* (2016) 16(4):2818–23. doi:10.1021/acs.nanolett.6b00618
34. Estakhri NM, Alù A. Recent progress in gradient metasurfaces. *J Opt Soc Am B.* (2015) 33(2):A21. doi:10.1364/josab.33.000a21
35. Fan Y, Shen N-H, Zhang F, Zhao Q, Wei Z, Zhang P, et al. Photoexcited graphene metasurfaces: significantly enhanced and tunable magnetic resonances. *ACS Photonics.* (2018) 5(4):1612–8. doi:10.1021/acsphotonics.8b00057
36. Fu YH, Kuznetsov AI, Miroshnichenko AE, Yu YF, Luk'yanchuk B. Directional visible light scattering by silicon nanoparticles. *Nat Commun.* (2013) 4:1527. doi:10.1038/ncomms2538
37. Galeotti F, Pisco M, Cusano A. Self-assembly on optical fibers: a powerful nanofabrication tool for next generation "lab-on-fiber" optrodes. *Nanoscale.* (2018) 10(48):22673–700. doi:10.1039/c8nr06002a
38. Gharghi M, Gladden C, Zentgraf T, Liu Y, Yin X, Valentine J, et al. A carpet cloak for visible light. *Nano Lett.* (2011) 11(7):2825–8. doi:10.1021/nl201189z
39. Ginn JC, Brener I, Peters DW, Wendt JR, Stevens JO, Hines PF, et al. Realizing optical magnetism from dielectric metamaterials. *Phys Rev Lett.* (2012) 108(9): 097402. doi:10.1103/PhysRevLett.108.097402
40. Gorkunov MV, Rogov OY, Kondratov AV, Artemov VV, Gainutdinov RV, Ezhov AA. Chiral visible light metasurface patterned in monocrystalline silicon by focused ion beam. *Sci Rep.* (2018) 8(1):11623. doi:10.1038/s41598-018-29977-4
41. Grimberg R. Electromagnetic metamaterials. *Mater Sci Eng, B.* (2013) 178(19): 1285–95. doi:10.1016/j.mseb.2013.03.022
42. Gu J, Singh R, Liu X, Zhang X, Ma Y, Zhang S, et al. Active control of electromagnetically induced transparency analogue in terahertz metamaterials. *Nat Commun.* (2012) 3:1151. doi:10.1038/ncomms2153
43. Guo X, Pu M, Guo Y, Ma X, Li X, Luo X. Flexible and tunable dielectric color meta-hologram. *Plasmonics.* (2019) 15(1):217–23. doi:10.1007/s11468-019-01025-5
44. Guo Y, Yan L, Pan W, Shao L. Scattering engineering in continuously shaped metasurface: an approach for electromagnetic illusion. *Sci Rep.* (2016) 6:30154. doi:10.1038/srep30154
45. Gutruf P, Zou C, Withayachumnankul W, Bhaskaran M, Sriram S, Fumeaux C. Mechanically tunable dielectric resonator metasurfaces at visible frequencies. *ACS Nano.* (2016) 10(1):133–41. doi:10.1021/acsnano.5b05954
46. High AA, Devlin RC, Dibos A, Polking M, Wild DS, Perczel J, et al. Visible-frequency hyperbolic metasurface. *Nature.* (2015) 522(7555):192–6. doi:10.1038/nature14477
47. Hirai Y, Tanaka Y. Application of nano-imprint lithography. *J Photopolym Sci Technol.* (2002) 15(3):475–80. doi:10.2494/photopolymer.15.475
48. Hou B, Xu G, Wong H, Wen W. Tuning of photonic bandgaps by a field-induced structural change of fractal metamaterials. *Opt Express.* (2005) 13(23): 9149–54. doi:10.1364/opex.13.009149
49. Hsiao H-H, Chu CH, Tsai DP. Fundamentals and applications of metasurfaces. *Small Methods.* (2017) 1(4). doi:10.1002/smtd.201600064
50. Hsu L, Ndao A, Kante B. Broadband and linear polarization metasurface carpet cloak in the visible. *Opt Lett.* (2019) 44(12):2978–81. doi:10.1364/OL.44.002978
51. Hu J, Lang T, Hong Z, Shen C, Shi G. Comparison of electromagnetically induced transparency performance in metallic and all-dielectric metamaterials. *J Lightwave Technol.* (2018) 36(11):2083–93. doi:10.1109/jlt.2018.2804336
52. Hu J, Lang T, Shen C, Shao L. Combined Mie resonance metasurface for wideband terahertz absorber. *Appl Sci.* (2018) 8(9):1679. doi:10.3390/app8091679
53. Hu J, Lang T, Shi GH. Simultaneous measurement of refractive index and temperature based on all-dielectric metasurface. *Opt Express.* (2017) 25(13): 15241–51. doi:10.1364/OE.25.015241

54. Hu J, Lang T, Xu W, Liu J, Hong Z. Experimental demonstration of electromagnetically induced transparency in a conductively coupled flexible metamaterial with cheap aluminum foil. *Nanoscale Res Lett.* (2019) 14(1):359. doi:10.1186/s11671-019-3180-y
55. Hu J, Li L, Lin H, Zhang P, Zhou W, Ma Z. Flexible integrated photonics: where materials, mechanics and optics meet [Invited]. *Opt Mater Express.* (2013) 3(9):1313. doi:10.1364/ome.3.001313
56. Hu X, Xu G, Wen L, Wang H, Zhao Y, Zhang Y, et al. Metamaterial absorber integrated microfluidic terahertz sensors. *Laser Photon Rev.* (2016) 10(6): 962–9. doi:10.1002/lpor.201600064
57. Huang L, Chen X, Muhlenbernd H, Li G, Bai B, Tan Q, et al. Dispersionless phase discontinuities for controlling light propagation. *Nano Lett.* (2012) 12(11):5750–5. doi:10.1021/nl303031j
58. Huang L, Chen X, Mühlenbernd H, Zhang H, Chen S, Bai B, et al. Three-dimensional optical holography using a plasmonic metasurface. *Nat Commun.* (2013) 4(1):2808. doi:10.1038/ncomms3808
59. Huang ST, Hsu SF, Tang KY, Yen TJ, Yao DJ. Application of a terahertz system combined with an X-shaped metamaterial microfluidic cartridge. *Micromachines.* (2020) 11(1):74. doi:10.3390/mi11010074
60. Huang YW, Chen WT, Tsai WY, Wu PC, Wang CM, Sun G, et al. Aluminum plasmonic multicolor meta-hologram. *Nano Lett.* (2015) 15(5):3122–7. doi:10.1021/acs.nanolett.5b00184
61. Islam MS, Sultana J, Biabanifard M, Vafapour Z, Nine MJ, Dinovitser A, et al. Tunable localized surface plasmon graphene metasurface for multiband superabsorption and terahertz sensing. *Carbon.* (2020) 158:559–67. doi:10.1016/j.carbon.2019.11.026
62. Jakšić Z, Vasiljević-Radović D, Maksimović M, Sarajlić M, Vujanić A, Djurić Z. Nanofabrication of negative refractive index metasurfaces. *Microelectron Eng.* (2006) 83(4–9):1786–91. doi:10.1016/j.mee.2006.01.197
63. Jang M, Horie Y, Shibukawa A, Brake J, Liu Y, Kamali SM, et al. Wavefront shaping with disorder-engineered metasurfaces. *Nat Photon.* (2018) 12:84–90. doi:10.1038/s41566-017-0078-z
64. Jiang L, Zeng S, Xu Z, Ouyang Q, Zhang DH, Chong PHJ, et al. Multifunctional hyperbolic nanogroove metasurface for submolecular detection. *Small.* (2017) 13(30):1700600. doi:10.1002/smll.201700600
65. Juhl M, Mueller JPB, Leosson K. Metasurface polarimeter on optical fiber facet by nano-transfer to UV-curable hybrid polymer. *IEEE J Sel Top Quant Electron.* (2019) 25(3):1–7. doi:10.1109/jstqe.2019.2893757
66. Kamali SM, Arbabi A, Arbabi E, Horie Y, Faraon A. Decoupling optical function and geometrical form using conformal flexible dielectric metasurfaces. *Nat Commun.* (2016) 7:11618. doi:10.1038/ncomms11618
67. Kamali SM, Arbabi E, Arbabi A, Faraon A. A review of dielectric optical metasurfaces for wavefront control. *Nanophotonics.* (2018) 7(6):1041–68. doi:10.1515/nanoph-2017-0129
68. Kamali SM, Arbabi E, Arbabi A, Horie Y, Faraon A. Highly tunable elastic dielectric metasurface lenses. *Laser Photon Rev.* (2016) 10(6):1002–8. doi:10.1002/lpor.201600144
69. Kang L, Jenkins RP, Werner DH. Recent progress in active optical metasurfaces. *Adv Opt Mater.* (2019) 7(14):1801813. doi:10.1002/adom.201801813
70. Kasirga TS, Ertas YN, Bayindir M. Microfluidics for reconfigurable electromagnetic metamaterials. *Appl Phys Lett.* (2009) 95(21):214102. doi:10.1063/1.3268448
71. Khorasaninejad M, Aieta F, Kanhaiya P, Kats MA, Genevet P, Rousso D, et al. Achromatic metasurface lens at telecommunication wavelengths. *Nano Lett.* (2015) 15(8):5358–62. doi:10.1021/acs.nanolett.5b01727
72. Khorasaninejad M, Chen WT, Devlin RC, Oh J, Zhu AY, Capasso F. Metalenses at visible wavelengths: diffraction-limited focusing and subwavelength resolution imaging. *Science.* (2016a) 352(6290):1190–4. doi:10.1126/science.aaf6644
73. Khorasaninejad M, Zhu AY, Roques-Carmes C, Chen WT, Oh J, Mishra I, et al. Polarization-insensitive metalenses at visible wavelengths. *Nano Lett.* (2016b) 16(11):7229–34. doi:10.1021/acs.nanolett.6b03626
74. Kildishev AV, Boltasseva A, Shalaev VM. Planar photonics with metasurfaces. *Science.* (2013) 339(6125):1232009. doi:10.1126/science.1232009
75. Kim HK, Lee D, Lim S. A fluidically tunable metasurface absorber for flexible large-scale wireless ethanol sensor applications. *Sensors.* (2016) 16(8):1246. doi:10.3390/s16081246
76. Kim Y, Yeom B, Arteaga O, Jo Yoo S, Lee SG, Kim JG, et al. Reconfigurable chiroptical nanocomposites with chirality transfer from the macro- to the nanoscale. *Nat Mater.* (2016) 15(4):461–8. doi:10.1038/nmat4525
77. Kim Y, Yuk H, Zhao R, Chester SA, Zhao X. Printing ferromagnetic domains for untethered fast-transforming soft materials. *Nature.* (2018) 558(7709): 274–9. doi:10.1038/s41586-018-0185-0
78. Koshelev K, Tang Y, Li K, Choi D-Y, Li G, Kivshar Y. Nonlinear metasurfaces governed by bound states in the continuum. *ACS Photonics.* (2019) 6(7): 1639–44. doi:10.1021/acsphotonics.9b00700
79. Lawrence N, Trevino J, Dal Negro L. Aperiodic arrays of active nanopillars for radiation engineering. *J Appl Phys.* (2012) 111(11):113101. doi:10.1063/1.4723564
80. Lee J, Tymchenko M, Argyropoulos C, Chen PY, Lu F, Demmerle F, et al. Giant nonlinear response from plasmonic metasurfaces coupled to intersubband transitions. *Nature.* (2014) 511(7507):65–9. doi:10.1038/nature13455
81. Leonhardt U. Optical conformal mapping. *Science.* (2006) 312(5781):1777–80. doi:10.1126/science.1126493
82. Li J, Yu P, Zhang S, Liu N. Electrically-controlled digital metasurface device for light projection displays. *Nat Commun.* (2020) 11(1):3574. doi:10.1038/s41467-020-17390-3
83. Li L, Jun Cui T, Ji W, Liu S, Ding J, Wan X, et al. Electromagnetic reprogrammable coding-metasurface holograms. *Nat Commun.* (2017) 8(1): 197. doi:10.1038/s41467-017-00164-9
84. Li L, Lin H, Qiao S, Huang YZ, Li JY, Michon J, et al. Monolithically integrated stretchable photonics. *Light Sci Appl.* (2018a) 7:17138. doi:10.1038/lsa.2017.138
85. Li L, Lin H, Qiao S, Zou Y, Danto S, Richardson K, et al. Integrated flexible chalcogenide glass photonic devices. *Nat Photon.* (2014) 8(8):643–9. doi:10.1038/nphoton.2014.138
86. Li L, Liu Z, Ren X, Wang S, Su VC, Chen MK, et al. Metalens-array-based high-dimensional and multiphoton quantum source. *Science.* (2020) 368(6498): 1487–90. doi:10.1126/science.aba9779
87. Li L, Ruan H, Liu C, Li Y, Shuang Y, Alu A, et al. Machine-learning reprogrammable metasurface imager. *Nat Commun.* (2019) 10(1):1082. doi:10.1038/s41467-019-09103-2
88. Li P, Dolado I, Alfaro-Mozaz FJ, Casanova F, Hueso LE, Liu S, et al. Infrared hyperbolic metasurface based on nanostructured van der Waals materials. *Science.* (2018) 359(6378):892–6. doi:10.1126/science.aaq1704
89. Li S, Zhou C, Ban G, Wang H, Lu H, Wang Y. Active all-dielectric bifocal metalens assisted by germanium antimony telluride. *J Phys Appl Phys.* (2019) 52(9):9. doi:10.1088/1361-6463/aaf7f3
90. Li X, Chen L, Li Y, Zhang X, Pu M, Zhao Z, et al. Multicolor 3D meta-holography by broadband plasmonic modulation. *Sci Adv.* (2016) 2(11): e1601102. doi:10.1126/sciadv.1601102
91. Li X, Ren H, Chen X, Liu J, Li Q, Li C, et al. Athermally photoreduced graphene oxides for three-dimensional holographic images. *Nat Commun.* (2015) 6: 6984. doi:10.1038/ncomms7984
92. Li X, Xiao S, Cai B, He Q, Cui TJ, Zhou L. Flat metasurfaces to focus electromagnetic waves in reflection geometry. *Opt Lett.* (2012) 37(23): 4940–2. doi:10.1364/OL.37.004940
93. Lin D, Fan P, Hasman E, Brongersma ML. Dielectric gradient metasurface optical elements. *Science.* (2014) 345(6194):298–302. doi:10.1126/science.1253213
94. Lin RJ, Su VC, Wang S, Chen MK, Chung TL, Chen YH, et al. Achromatic metalens array for full-colour light-field imaging. *Nat Nanotechnol.* (2019) 14(3):227–31. doi:10.1038/s41565-018-0347-0
95. Ling K, Kim HK, Yoo M, Lim S. Frequency-switchable metamaterial absorber injecting eutectic gallium-indium (EGaIn) liquid metal alloy. *Sensors.* (2015) 15(11):28154–65. doi:10.3390/s151128154
96. Liu L, Zhang X, Kenney M, Su X, Xu N, Ouyang C, et al. Broadband metasurfaces with simultaneous control of phase and amplitude. *Adv Mater.* (2014) 26(29):5031–6. doi:10.1002/adma.201401484
97. Liu W, Shen Y, Xiao G, She X, Wang J, Jin C. Mechanically tunable sub-10 nm metal gap by stretching PDMS substrate. *Nanotechnology.* (2017) 28(7): 075301. doi:10.1088/1361-6528/aa5366
98. Liu X, Fan K, Shadrivov IV, Padilla WJ. Experimental realization of a terahertz all-dielectric metasurface absorber. *Opt Express.* (2017) 25(1):191–201. doi:10.1364/OE.25.000191

99. Liu X, Huang Z, Zhu C, Wang L, Zang J. Out-of-Plane designed soft metasurface for tunable surface plasmon polariton. *Nano Lett.* (2018) 18(2):1435–41. doi:10.1021/acs.nanolett.7b05190
100. Liu Y, Song J, Zhao W, Ren X, Cheng Q, Luo X, et al. Dynamic thermal camouflage via a liquid-crystal-based radiative metasurface. *Nanophotonics.* (2020) 9(4):855–63. doi:10.1515/nanoph-2019-0485
101. Luo J, Zeng B, Wang C, Gao P, Liu K, Pu M, et al. Fabrication of anisotropically arrayed nano-slots metasurfaces using reflective plasmonic lithography. *Nanoscale.* (2015) 7(44):18805–12. doi:10.1039/c5nr05153c
102. Luo W, Sun S, Xu H-X, He Q, Zhou L. Transmissive ultrathin pancharatnam-berry metasurfaces with nearly 100% efficiency. *Phys Rev Appl.* (2017) 7(4): 044033. doi:10.1103/PhysRevApplied.7.044033
103. Ma Q, Bai GD, Jing HB, Yang C, Li L, Cui TJ. Smart metasurface with self-adaptively reprogrammable functions. *Light Sci Appl.* (2019) 8:98. doi:10.1038/s41377-019-0205-3
104. Maci S, Minatti G, Casaletti M, Bosiljevac M. Metasurfing: addressing waves on impenetrable metasurfaces. *IEEE Antenn Wireless Propag Lett.* (2011) 10: 1499–502. doi:10.1109/lawp.2012.2183631
105. Makarov SV, Milichko V, Ushakova EV, Omelyanovich M, Cerdan Pasaran A, Haroldson R, et al. Multifold emission enhancement in nanoimprinted hybrid perovskite metasurfaces. *ACS Photonics.* (2017) 4(4):728–35. doi:10.1021/acsphotonics.6b00940
106. Mark D, Haeberle S, Roth G, von Stetten F, Zengerle R. Microfluidic lab-on-a-chip platforms: requirements, characteristics and applications. *Chem Soc Rev.* (2010) 39(3):1153–82. doi:10.1039/b820557b
107. Meinzer N, Barnes WL, Hooper IR. Plasmonic meta-atoms and metasurfaces. *Nat Photon.* (2014) 8(12):889–98. doi:10.1038/nphoton.2014.247
108. Mohammadi Estakhri N, Alù A. Manipulating optical reflections using engineered nanoscale metasurfaces. *Phys Rev B.* (2014) 89(23):235419. doi:10.1103/PhysRevB.89.235419
109. Monticone F, Estakhri NM, Alu A. Full control of nanoscale optical transmission with a composite metascreen. *Phys Rev Lett.* (2013) 110(20): 203903. doi:10.1103/PhysRevLett.110.203903
110. Nemiroski A, Gonidec M, Fox JM, Jean-Remy P, Turnage E, Whitesides GM. Engineering shadows to fabricate optical metasurfaces. *ACS Nano.* (2014) 8(11):11061–70. doi:10.1021/nn504214b
111. Ni X, Emani NK, Kildishev AV, Boltasseva A, Shalaev VM. Broadband light bending with plasmonic nanoantennas. *Science.* (2012) 335(6067):427. doi:10.1126/science.1214686
112. Ni X, Ishii S, Kildishev AV, Shalaev VM. Ultra-thin, planar, Babinet-inverted plasmonic metalenses. *Light Sci Appl.* (2013) 2(4):e72. doi:10.1038/lsa.2013.28
113. Ni X, Kildishev AV, Shalaev VM. Metasurface holograms for visible light. *Nat Commun.* (2013) 4(1):2807. doi:10.1038/ncomms3807
114. Peng R, Liu J, Xiao D, Fang X, Yin S, Yin Z, et al. Microfluid-enabled fine tuning of circular dichroism from chiral metasurfaces. *J Phys Appl Phys.* (2019) 52(41):415102. doi:10.1088/1361-6463/ab3129
115. Person S, Jain M, Lapin Z, Saenz JJ, Wicks G, Novotny L. Demonstration of zero optical backscattering from single nanoparticles. *Nano Lett.* (2013) 13(4):1806–9. doi:10.1021/nl4005018
116. Pfeiffer C, Grbic A. Metamaterial Huygens' surfaces: tailoring wave fronts with reflectionless sheets. *Phys Rev Lett.* (2013) 110(19):197401. doi:10.1103/PhysRevLett.110.197401
117. Pimenov A, Loidl A. Experimental demonstration of artificial dielectrics with a high index of refraction. *Phys Rev B.* (2006) 74(19):193108. doi:10.1103/PhysRevB.74.193102
118. Pisco M, Galeotti F, Quero G, Grisci G, Micco A, Mercaldo LV, et al. Nanosphere lithography for optical fiber tip nanoprobes. *Light Sci Appl.* (2017) 6(5):e16229. doi:10.1038/lsa.2016.229
119. Pisco M, Galeotti F, Quero G, Iadicicco A, Giordano M, Cusano A. Miniaturized sensing probes based on metallic dielectric crystals self-assembled on optical fiber tips. *ACS Photonics.* (2014) 1(10):917–27. doi:10.1021/ph500126v
120. Pitchappa P, Manjappa M, Ho CP, Singh R, Singh N, Lee C. Active control of electromagnetically induced transparency analog in terahertz MEMS metamaterial. *Adv Opt Mater.* (2016) 4(4):541–7. doi:10.1002/adom.201500676
121. Pors A, Albrektsen O, Radko IP, Bozhevolnyi SI. Gap plasmon-based metasurfaces for total control of reflected light. *Sci Rep.* (2013) 3:2155. doi:10.1038/srep02155
122. Pors A, Bozhevolnyi SI. Plasmonic metasurfaces for efficient phase control in reflection. *Opt Express.* (2013) 21(22):27438–51. doi:10.1364/oe.21.027438
123. Pors A, Nielsen MG, Eriksen RL, Bozhevolnyi SI. Broadband focusing flat mirrors based on plasmonic gradient metasurfaces. *Nano Lett.* (2013) 13(2): 829–34. doi:10.1021/nl304761m
124. Principe M, Consales M, Castaldi G, Galdi V, Cusano A. Evaluation of fiber-optic phase-gradient meta-tips for sensing applications. *Nanomater Nanotechnol.* (2019) 9. doi:10.1177/1847980419832724
125. Principe M, Consales M, Micco A, Crescitelli A, Castaldi G, Esposito E, et al. Optical fiber meta-tips. *Light Sci Appl.* (2017) 6(3):e16226. doi:10.1038/lsa.2016.226
126. Qian C, Zheng B, Shen Y, Jing L, Li E, Shen L, et al. Deep-learning-enabled self-adaptive microwave cloak without human intervention. *Nat Photon.* (2020) 14(6):383–90. doi:10.1038/s41566-020-0604-2
127. Rocco D, Carletti L, Caputo R, Finazzi M, Celebrano M, De Angelis C. Switching the second harmonic generation by a dielectric metasurface via tunable liquid crystal. *Opt Express.* (2020) 28(8):12037–46. doi:10.1364/OE.386776
128. Roy T, Zhang S, Jung IW, Troccoli M, Capasso F, Lopez D. Dynamic metasurface lens based on MEMS technology. *APL Photonics.* (2018) 3(2): 021302. doi:10.1063/1.5018865
129. Ruiz de Galarreta C, Sinev I, Alexeev AM, Trofimov P, Ladutenko K, Garcia-Cuevas Carrillo S, et al. Reconfigurable multilevel control of hybrid all-dielectric phase-change metasurfaces. *Optica.* (2020) 7(5):476. doi:10.1364/optica.384138
130. Sain B, Meier C, Zentgraf T. Nonlinear optics in all-dielectric nanoantennas and metasurfaces: a review. *Adv Photonics.* (2019) 1(02):024002. doi:10.1117/1.Ap.1.2.024002
131. Scheerlinck S, Dubruel P, Bienstman P, Schacht E, Van Thourhout D, Baets R. Metal grating patterning on fiber facets by UV-based nano imprint and transfer lithography using optical alignment. *J Lightwave Technol.* (2009) 27(10):1415–20. doi:10.1109/jlt.2008.2004955
132. Schift H, Park S, Gobrecht J. Nano-imprint-molding resists for lithography. *J Photopolym Sci Technol.* (2003) 16(3):435–8. doi:10.2494/photopolymer.16.435
133. Selvanayagam M, Eleftheriades GV. Discontinuous electromagnetic fields using orthogonal electric and magnetic currents for wavefront manipulation. *Opt Express.* (2013) 21(12):14409–29. doi:10.1364/OE.21.014409
134. Shalaev MI, Sun J, Tsukernik A, Pandey A, Nikolskiy K, Litchinitser NM. High-efficiency all-dielectric metasurfaces for ultracompact beam manipulation in transmission mode. *Nano Lett.* (2015) 15(9):6261–6. doi:10.1021/acs.nanolett.5b02926
135. Sharma M, Hendler N, Ellenbogen T. Electrically switchable color tags based on active liquid-crystal plasmonic metasurface platform. *Adv Opt Mater.* (2020) 8(7). doi:10.1002/adom.201901182
136. Shen JT, Catrysse PB, Fan S. Mechanism for designing metallic metamaterials with a high index of refraction. *Phys Rev Lett.* (2005) 94(19):197401. doi:10.1103/PhysRevLett.94.197401
137. Shrestha S, Overvig AC, Lu M, Stein A, Yu N. Broadband achromatic dielectric metalenses. *Light Sci Appl.* (2018) 7:85. doi:10.1038/s41377-018-0078-x
138. Sirmaci YD, Tang Z, Fasold S, Neumann C, Pertsch T, Turchanin A, et al. Plasmonic metasurfaces situated on ultrathin carbon nanomembranes. *ACS Photonics.* (2020) 7(4):1060–6. doi:10.1021/acsphotonics.0c00073
139. Smith DR, Pendry JB, Wiltshire MC Metamaterials and negative refractive index. *Science.* (2004) 305(5685):788–92. doi:10.1126/science.1096796
140. Su VC, Chu CH, Sun G, Tsai DP Advances in optical metasurfaces: fabrication and applications [Invited]. *Opt Express.* (2018) 26(10): 13148–82. doi:10.1364/OE.26.013148
141. Sun S, Yang KY, Wang CM, Juan TK, Chen WT, Liao CY, et al. High-efficiency broadband anomalous reflection by gradient meta-surfaces. *Nano Lett.* (2012) 12(12):6223–9. doi:10.1021/nl3032668
142. Valentine J, Li J, Zentgraf T, Bartal G, Zhang X An optical cloak made of dielectrics. *Nat Mater.* (2009) 8(7):568–71. doi:10.1038/nmat2461

143. Valentine J, Zhang S, Zentgraf T, Ulin-Avila E, Genov DA, Bartal G, et al. Three-dimensional optical metamaterial with a negative refractive index. *Nature.* (2008) 455(7211):376–9. doi:10.1038/nature07247
144. Walia S, Shah CM, Gutruf P, Nili H, Chowdhury DR, Withayachumnankul W, et al. Flexible metasurfaces and metamaterials: a review of materials and fabrication processes at micro- and nano-scales. *Appl Phys Rev.* (2015) 2(1): 011303. doi:10.1063/1.4913751
145. Wan W, Gao J, Yang X Full-color plasmonic metasurface holograms. *ACS Nano.* (2016) 10(12):10671–80. doi:10.1021/acsnano.6b05453
146. Wan W, Gao J, Yang X Metasurface holograms for holographic imaging. *Adv Opt Mater.* (2017) 5(21):011303. doi:10.1002/adom.201700541
147. Wang B, Dong F, Li QT, Yang D, Sun C, Chen J, et al. Visible-frequency dielectric metasurfaces for multiwavelength achromatic and highly dispersive holograms. *Nano Lett.* (2016) 16(8):5235–40. doi:10.1021/acs.nanolett.6b02326
148. Wang C, Yang Y, Liu Q, Liang D, Zheng B, Chen H, et al. Multi-frequency metasurface carpet cloaks. *Opt Express.* (2018) 26(11):14123–31. doi:10.1364/OE.26.014123
149. Wang H, Liu SC, Balachandran B, Moon J, Haroldson R, Li Z, et al. Nanoimprinted perovskite metasurface for enhanced photoluminescence. *Opt Express.* (2017) 25(24):A1162–A1171. doi:10.1364/OE.25.0A1162
150. Wang J, Liu S, Guruswamy S, Nahata A Reconfigurable terahertz metamaterial device with pressure memory. *Opt Express.* (2014) 22(4): 4065–74. doi:10.1364/OE.22.004065
151. Wang J, Liu S, Vardeny ZV, Nahata A Liquid metal-based plasmonics. *Opt Express.* (2012) 20(3):2346–53. doi:10.1364/OE.20.002346
152. Wang L, Kruk S, Tang H, Li T, Kravchenko I, Neshev DN, et al. Grayscale transparent metasurface holograms. *Optica.* (2016) 3(12):1504. doi:10.1364/optica.3.001504
153. Wang L, Liu X, Zang J Mechanically tunable terahertz graphene plasmonics using soft metasurface. *2D Mater.* (2016) 3(4):041007. doi:10.1088/2053-1583/3/4/041007
154. Wang Q, Rogers ETF, Gholipour B, Wang C-M, Yuan G, Teng J, et al. Optically reconfigurable metasurfaces and photonic devices based on phase change materials. *Nat Photon.* (2015) 10(1):60–5. doi:10.1038/nphoton.2015.247
155. Wang S, Wu PC, Su VC, Lai YC, Chen MK, Kuo HY, et al. A broadband achromatic metalens in the visible. *Nat Nanotechnol.* (2018) 13(3):227–32. doi:10.1038/s41565-017-0052-4
156. Wang S, Wu PC, Su VC, Lai YC, Hung Chu C, Chen JW, et al. Broadband achromatic optical metasurface devices. *Nat Commun.* (2017) 8(1):187. doi:10.1038/s41467-017-00166-7
157. Wang Y, Liu F, Zhang X Flexible transfer of plasmonic photonic structures onto fiber tips for sensor applications in liquids. *Nanoscale.* (2018) 10(34): 16193–200. doi:10.1039/c8nr05871g
158. Wei M, Yang Q, Zhang X, Li Y, Gu J, Han J, et al. Ultrathin metasurface-based carpet cloak for terahertz wave. *Opt Express.* (2017) 25(14):15635–42. doi:10.1364/OE.25.015635
159. Wu J, Shen Z, Ge S, Chen B, Shen Z, Wang T, et al. Liquid crystal programmable metasurface for terahertz beam steering. *Appl Phys Lett.* (2020) 116(13):131104. doi:10.1063/1.5144858
160. Xiao D, Liu YJ, Yin S, Liu J, Ji W, Wang B, et al. Liquid-crystal-loaded chiral metasurfaces for reconfigurable multiband spin-selective light absorption. *Opt Express.* (2018) 26(19):25305–14. doi:10.1364/OE.26.025305
161. Xiaofang Su XS, Li G, Yang H, Zhao Z, Yu F, Chen X, et al. A visible high efficiency and polarization-insensitive 34-level dielectric metasurface hologram. *RSC Adv.* (2017) 7(42):26371–6. doi:10.1039/c7ra03672h
162. Xie Y, Wang W, Chen H, Konneker A, Popa BI, Cummer SA Wavefront modulation and subwavelength diffractive acoustics with an acoustic metasurface. *Nat Commun.* (2014) 5:5553. doi:10.1038/ncomms6553
163. Xomalis A, Demirtzioglou I, Plum E, Jung Y, Nalla V, Lacava C, et al. Fibre-optic metadevice for all-optical signal modulation based on coherent absorption. *Nat Commun.* (2018) 9(1):182. doi:10.1038/s41467-017-02434-y
164. Xu J, Fan Y, Yang R, Fu Q, Zhang F Realization of switchable EIT metamaterial by exploiting fluidity of liquid metal. *Opt Express.* (2019) 27(3):2837–43. doi:10.1364/OE.27.002837
165. Xu Y, Fu Y, Chen H Planar gradient metamaterials. *Nat Rev Mater.* (2016) 1(12):16067. doi:10.1038/natrevmats.2016.67
166. Yan LB, Zhu WM, Wu PC, Cai H, Gu YD, Chin LK, et al. Adaptable metasurface for dynamic anomalous reflection. *Appl Phys Lett.* (2017) 110(20):201904. doi:10.1063/1.4983782
167. Yang Y, KravchenkoII, Briggs DP, Valentine J All-dielectric metasurface analogue of electromagnetically induced transparency. *Nat Commun.* (2014) 5:5753. doi:10.1038/ncomms6753
168. Yang Y, Wang W, Moitra P, Kravchenko II, Briggs DP, Valentine J Dielectric meta-reflectarray for broadband linear polarization conversion and optical vortex generation. *Nano Lett.* (2014) 14(3):1394–9. doi:10.1021/nl4044482
169. Yao Y, Shankar R, Kats MA, Song Y, Kong J, Loncar M, et al. Electrically tunable metasurface perfect absorbers for ultrathin mid-infrared optical modulators. *Nano Lett.* (2014) 14(11):6526–32. doi:10.1021/nl503104n
170. Ye W, Zeuner F, Li X, Reineke B, He S, Qiu CW, et al. Spin and wavelength multiplexed nonlinear metasurface holography. *Nat Commun.* (2016) 7: 11930. doi:10.1038/ncomms11930
171. Yin S, Ji W, Xiao D, Li Y, Li K, Yin Z, et al. Intrinsically or extrinsically reconfigurable chirality in plasmonic chiral metasurfaces. *Optic Commun.* (2019) 448:10–4. doi:10.1016/j.optcom.2019.05.006
172. Yin S, Xiao D, Liu J, Li K, He H, Jiang S, et al. Reconfigurable chiral metasurface absorbers based on liquid crystals. *IEEE Photonics J.* (2018) 10(6):1–9. doi:10.1109/jphot.2018.2878775
173. Yoon G, Kim K, Huh D, Lee H, Rho J Single-step manufacturing of hierarchical dielectric metalens in the visible. *Nat Commun.* (2020) 11(1): 2268. doi:10.1038/s41467-020-16136-5
174. Yu N, Capasso F Flat optics with designer metasurfaces. *Nat Mater.* (2014) 13(2):139–50. doi:10.1038/nmat3839
175. Yu N, Genevet P, Aieta F, Kats MA, Blanchard R, Aoust G, et al. Flat optics: controlling wavefronts with optical antenna metasurfaces. *IEEE J Sel Top Quant Electron.* (2013) 19(3):4700423. doi:10.1109/jstqe.2013.2241399
176. Yu N, Genevet P, Kats MA, Aieta F, Tetienne JP, Capasso F, et al. Light propagation with phase discontinuities: generalized laws of reflection and refraction. *Science.* (2011) 334(6054):333–7. doi:10.1126/science.1210713
177. Yu YF, Zhu AY, Paniagua-Domínguez R, Fu YH, Luk'yanchuk B, Kuznetsov AI High-transmission dielectric metasurface with 2π phase control at visible wavelengths. *Laser Photon Rev.* (2015) 9(4):412–8. doi:10.1002/lpor.201500041
178. Yue F, Wen D, Xin J, Gerardot BD, Li J, Chen X Vector vortex beam generation with a single plasmonic metasurface. *ACS Photonics.* (2016) 3(9): 1558–63. doi:10.1021/acsphotonics.6b00392
179. Zeng J, Li L, Yang X, Gao J Generating and separating twisted light by gradient-rotation split-ring antenna metasurfaces. *Nano Lett.* (2016) 16(5): 3101–8. doi:10.1021/acs.nanolett.6b00360
180. Zhang H-F, Wang Z-L, Hu C-X, Liu H-B A tailored broadband terahertz metamaterial absorber based on the thermal expansion feature of liquid metal. *Results Phys.* (2020) 16:102936. doi:10.1016/j.rinp.2020.102937
181. Zhang H, Feng L, Liang Y, Xu T An ultra-flexible plasmonic metamaterial film for efficient omnidirectional and broadband optical absorption. *Nanoscale.* (2019) 11(2):437–43. doi:10.1039/c8nr05276j
182. Zhang M, Zhang W, Liu AQ, Li FC, Lan CF Tunable polarization conversion and rotation based on a reconfigurable metasurface. *Sci Rep.* (2017) 7(1): 12068. doi:10.1038/s41598-017-11953-z
183. Zhang S, Kim MH, Aieta F, She A, Mansuripur T, Gabay I, et al. High efficiency near diffraction-limited mid-infrared flat lenses based on metasurface reflectarrays. *Opt Express.* (2016) 24(16):18024–34. doi:10.1364/OE.24.018024
184. Zhang W, Song Q, Zhu W, Shen Z, Chong P, Tsai DP, et al. Metafluidic metamaterial: a review. *Adv Phys X.* (2018) 3(1):1417055. doi:10.1080/23746149.2017.1417055
185. Zhang Y, Liang L, Yang J, Feng Y, Zhu B, Zhao J, et al. Broadband diffuse terahertz wave scattering by flexible metasurface with randomized phase distribution. *Sci Rep.* (2016) 6:26875. doi:10.1038/srep26875
186. Zhang Z, Luo J, Song M, Yu H Large-area, broadband and high-efficiency near-infrared linear polarization manipulating metasurface fabricated by orthogonal interference lithography. *Appl Phys Lett.* (2015) 107(24): 241904. doi:10.1063/1.4937006
187. Zhao J, Sima B, Jia N, Wang C, Zhu B, Jiang T, et al. Achieving flexible low-scattering metasurface based on randomly distribution of meta-elements. *Opt Express.* (2016) 24(24):27849–57. doi:10.1364/OE.24.027849

188. Zhao W, Jiang H, Liu B, Song J, Jiang Y, Tang C, et al. Dielectric Huygens' metasurface for high-efficiency hologram operating in transmission mode. *Sci Rep.* (2016) 6:30613. doi:10.1038/srep30613
189. Zhao W, Li X, Li S, Ge Z, Liu M, Li Z, et al. Sub-wavelength focusing based on all-dielectric polarization-independent metalens. *Int J Mod Phys B.* (2018) 32(29):18321. doi:10.1142/s0217979218503216
190. Zhao X, Schalch J, Zhang J, Seren HR, Duan G, Averitt RD, et al. Electromechanically tunable metasurface transmission waveplate at terahertz frequencies. *Optica.* (2018) 5(3):303. doi:10.1364/optica.5.000303
191. Zhao Y, Zhang J, Du J, Wang J Meta-facet fiber for twisting ultra-broadband light with high phase purity. *Appl Phys Lett.* (2018) 113(6):061103. doi:10.1063/1.5043268
192. Zheludev NI, Kivshar YS From metamaterials to metadevices. *Nat Mater.* (2012) 11(11):917–24. doi:10.1038/nmat3431
193. Zheng G, Muhlenbernd H, Kenney M, Li G, Zentgraf T, Zhang S Metasurface holograms reaching 80% efficiency. *Nat Nanotechnol.* (2015) 10(4):308–12. doi:10.1038/nnano.2015.2
194. Zhu HL, Cheung SW, Chung KL, Yuk TI Linear-to-circular polarization conversion using metasurface. *IEEE Trans Antenn Propag.* (2013) 61(9):4615–23. doi:10.1109/tap.2013.2267712
195. Zhu Y, Li Z, Hao Z, DiMarco C, Maturavongsadit P, Hao Y, et al. Optical conductivity-based ultrasensitive mid-infrared biosensing on a hybrid metasurface. *Light Sci Appl.* (2018) 7:67. doi:10.1038/s41377-018-0066-1
196. Ziolkowski RW Propagation in and scattering from a matched metamaterial having a zero index of refraction. *Phys Rev E–Stat Nonlin Soft Matter Phys.* (2004) 70(4):046608. doi:10.1103/PhysRevE.70.046608
197. Zuo R, Liu W, Cheng H, Chen S, Tian J Breaking the diffraction limit with radially polarized light based on dielectric metalenses. *Adv Opt Mater.* (2018) 6(21):1800795. doi:10.1002/adom.201800795

Conflict of Interest: The authors declare that the research was conducted in the absence of any commercial or financial relationships that could be construed as a potential conflict of interest.

Advantages of publishing in Frontiers

OPEN ACCESS
Articles are free to read for greatest visibility and readership

FAST PUBLICATION
Around 90 days from submission to decision

HIGH QUALITY PEER-REVIEW
Rigorous, collaborative, and constructive peer-review

TRANSPARENT PEER-REVIEW
Editors and reviewers acknowledged by name on published articles

Frontiers
Avenue du Tribunal-Fédéral 34
1005 Lausanne | Switzerland

Visit us: www.frontiersin.org
Contact us: frontiersin.org/about/contact

REPRODUCIBILITY OF RESEARCH
Support open data and methods to enhance research reproducibility

DIGITAL PUBLISHING
Articles designed for optimal readership across devices

FOLLOW US
@frontiersin

IMPACT METRICS
Advanced article metrics track visibility across digital media

EXTENSIVE PROMOTION
Marketing and promotion of impactful research

LOOP RESEARCH NETWORK
Our network increases your article's readership